CRANFIELD UNIVERSITY

Dries Verstraete

The Potential of Liquid Hydrogen for long range aircraft propulsion

SCHOOL OF ENGINEERING

Ph. D. Thesis

CRANFIELD UNIVERSITY
SCHOOL OF ENGINEERING

Ph. D. Thesis

Academic Year 2008-2009

Dries Verstraete

The Potential of Liquid Hydrogen for long range aircraft propulsion

Supervisor: Dr. Ken Ramsden

April 2009

Abstract

The growth of aviation needed to cater for the needs of society might be undermined by restrictions resulting from the environmental implications of air traffic. Hydrogen could provide an excellent alternative to ensure a sustainable future for aviation. Several challenges remain to be addressed though before its adoption can become reality. The liquid hydrogen tanks are one of the areas where considerable research is needed. Further insight into unusual restrictions on aircraft classes that would be thought of as ideal candidates for hydrogen is also required. Hydrogen fueled very large long range transport aircraft for instance suffer from the 80 m airport box constraint which leads to a strong decrease in performance compared to other aircraft classes.

In this work 3 main tools are developed to look into some of these issues. An aircraft conceptual design tool has been set up to allow a comparison between kerosene and hydrogen on a common and hence fair basis. An engine performance assessment routine is also developed to allow the coupling of the design of engine and aircraft as one integrated system. As the link between both subsystems is the liquid hydrogen tank, a detailed design method for the tanks has also been created.

With these tools it has been shown that the gravimetric efficiency for large transport aircraft varies by only a few percent for a wide range of fuel masses and aircraft diameters with values in the order of 76 to 80 %. The performance of the long range transport aircraft itself however varies strongly from one class to another. For aircraft with a passenger load around 400 passengers, takeoff weight reductions around 25% can be obtained for similar operating empty weights and fuel weights of about 30% of the equivalent kerosene fuel weight. For 550 passenger aircraft however, the takeoff weight reduction reduces strongly due to the need for a triple deck fuselage and the resulting increase in fuselage mass. Whereas for the first category of aircraft, a 3 to 6 times higher fuel price per energy content can be afforded for similar direct operating costs, this cost advantage is reduced by about a third for the 550 passenger aircraft. A twin fuselage configuration alleviates the geometrical restrictions and restores the potential for an aircraft family but does not yield strong weight reductions.

In a subsequent study, the implications of unconventional engine cycles as well as drag reduction resulting from natural laminar flow through surface cooling should be assessed using the developed set of tools as this will reveal the full potential of hydrogen as an aviation fuel.

This page is intentionally left blank

Acknowledgments

> Exaggerated concern about what others are doing can be foolish. It can paralyze effort and stifle a good idea. One finds that in the history of science almost every problem has been worked on by somebody else. This should not discourage anyone from pursuing his own path. – *Theodore Von Karman*

The road has been rather long and winding. Along that road many people have crossed and reached out with some help, a nice word, some encouragement, some distraction. My acknowledgment goes out to all of you. However, some people definitely deserve more than just a general word of appraisal.

First of all, I want to express my deepest gratitude to my supervisor Ken Ramsden for his continuous support, his expertise in many areas and his ever so good advice. But also for the encouraging words, the entertaining lunches and the ’war stories’ during conference dinners. And last but most definitely not least for his patience towards me throughout the course of the Ph. D.

Patrick Hendrick guided me in my first steps into the field of aircraft propulsion and has always been a mentor, an understanding and patient boss: always confident in me and providing support whenever needed.

The support of many people from the staff of Cranfield University was also vital for the completion of this long term project. I would especially like to show my appreciation for Peri Pilidis, Stephen Ogaji, Frank Noppel and Panos Laskaridis from the ’engineering side’ of the University. However at least as important was the support from the ’administrative and practical side’. Thank you Mary Howe, Gillian Hargreaves and Nicola Datt for providing me with solutions to administrative issues. Beyond all doubt, Anita Beal deserves an honorable mention for running the ’Students Off Site’ department so efficiently and always pointing me in the right direction.

A cordial thank you to the colleagues from the Aero-Thermo-Mechanics Laboratory of the Université Libre de Bruxelles is certainly also in place.

Andreas Westenberger from Airbus Deutschland is also acknowledged for the provision of the reports from the Cryoplane study.

At last my family deserves recognition for their lifelong support. Thank you for always being there for me and helping me through the rocky passages of this long and sometimes quite intense experience. I ll never forget you were always there for me. Thank you moetjeke, Wout, Joost and Kaspertje.

This page is intentionally left blank

Table of Contents

List of Figures

Chapter 1. Introduction **1**

Chapter 2. Effect of hydrogen on aircraft and engine design and performance **23**

Chapter 3. Liquid hydrogen tanks **39**

Chapter 4. Large long range transport aircraft with hydrogen fuel **73**

Appendix A. Some aspects of hydrogen in aviation **133**

This page is intentionally left blank

List of Tables

Nomenclature

Abbreviations and chemical formulae

AAMB	Aircraft Applied Maintenance Burden	[$]
APU	Auxiliary Power Unit	
AR	Aspect Ratio	
ASP	Airframe Study Price	[$]
BC	Bussiness Class	
BFL	Balanced takeoff field length	[m]
BH	Block hour	[hr]
BPR	ByPass Ratio	
CDT	Compressor Delivery (or Discharge) Temperature	[K]
CEA	Chemical Equilibrium with Applications	
CEF	Cost Escalation Factor	
CF	Cost Factor	
CFD	Computational Fluid Dynamics	
CGR	Climb Gradient	
CH_4	Methane	
CIAM	Central Institute of Aviation Motors	
CPI	Consumer Price Index	
CR	Contraction Ratio of the nacelle forebody	
CO	Carbon monoxide	
CO_2	Carbon dioxide	
CTE	Coefficient of Thermal Expansion	
DAM	Double Aluminized Mylar	
DOC	Direct Operating Costs	
DRA	Discontinuous Reinforced Aluminum	
DRC	Discontinuous Reinforced metallic Composite	
DSN	Double Silk Net	
EAMB	Engine Applied Maintenance Burden	[$]
EAS	Equivalent Air Speed	
EH	Engineering Hours	[h]
EI	Emission Index	[g/kg fuel]
EQHHPP	Euro-Quebec Hydro-Hydrogen Pilot Project	
ESA	European Space Agency	
ESFC	Energy Specific Fuel Consumption	[m/s]

ESP	Engine Study Price	[$]
FAR	Fuel-to-Air Ratio	
FC	First Class	
FC	Flight Cycle	
FH	Flight Hour	[hr]
GE	The General Electric company	
HC	HydroCarbons	
HD	High Density	
HPC	High Pressure Compressor	
HPT	High Pressure Turbine	
H_2O	Water vapor	
IPC	Intermediate Pressure Compressor	
IPT	Intermediate Pressure Turbine	
LCC	Life Cycle Cost	[$]
LCH_4	Liquid methane	
LD	Lower deck	
LHV	Lower Heating Value	[kJ/kg]
LH_2	Liquid Hydrogen	
LNG	Liquefied Natural Gas	
LOX	Liquid Oxygen	
LPC	Low Pressure Compressor	
LPT	Low Pressure Turbine	
KOH	Potassium hydroxide	
KSPA	Kuibyshev Scientific Production Association	
MAC	Mean Aerodynamic Chord	[m]
Max Cont	Maximum Continuous engine rating	
MD	Middle deck	
MFR	Mass Flow Ratio of the nacelle forebody	
MH	Manufacturing Hours	[hr]
MLI	Multi Layer Insulation	
MMC	Metal Matrix Composites	
MMH	Maintenance Man Hours	[hr]
NACA	National Advisory Committee for Aeronautics	
NASA	National Aeronautics and Space Administration	
NaCl	Natrium chloride	
NaOH	Natrium hydroxide	
NO_X	Nitrogen oxides	
NO	Nitrogen monoxide	
NO_2	Nitrogen dioxide	
N_2O	Nitrous oxide	
NTP	Normal temperature and pressure	

NTU	Number of transfer units	
OPR	Overall Pressure Ratio	
O_3	Ozone	
OH^-	Hydroxyl	
PLF	Pressure Loss Factor	
PMC	Polymer Matrix Composites	
PV	Photovoltaic	
SF	Scaling factor	
SFC	Specific Fuel Consumption of the turbofan	[g/kN/s]
SLS	Sea Level Static	
SLI	Space Launch Initiative	
SO_X	Sulphuric oxides	
SO_2	Sulphuric dioxide	
TBC	Thermal Barrier Coating	
TH	Tooling Hours	[hr]
TIT	Turbine Inlet Temperature	[K]
TNT	Trinitrotoluene	
TO	Take-Off	
UD	Upper deck	
UHC	Unburned HydroCarbons	
USAF	United States Air Force	
USD	United States dollar	
YC	Economy Class	

Notations

a	Diffusivity	[m^2/s]
a	Lift curve slope	
a_0	2D Lift curve slope	
A_{surf}	Turbine blade surface area	[m^2]
A_g	Turbine exit flow area	[m^2]
b	Span	[m]
Bi	Biot number	
c	Chord	[m]
C_D	Drag coefficient	
C_L	Lift coefficient	
C	Coefficient	
$\overline{c}$	Mean aerodynamic chord	[m]
c_p	Specific heat at constant pressure	[J/kg/K]
d	Diameter	[m]
e_w	Welding efficiency	
E	Endurance	[hrs]

E	Tank energy	[W]
f	Fineness ratio	
F_N	Net thrust	[kN]
g	Gravitational acceleration	[m/s^2]
h	Height	[m]
h	Specific enthalpy	[J/kg]
h_g	Convective heat transfer coefficient	[W/m^2/K]
H	Vertical nacelle separation distance	[m]
k	Empirical coefficient	
k	Thermal conductivity	[W/m/K]
K	Correction factor for mass determination	
K_{cool}	Cooling flow factor	
l	Length	[m]
L/D	Lift to Drag ratio	
M	Mach number	
$\dot{m}$	Massflow rate	[kg/s]
M_{DD}	Drag divergence Mach number	
M_{ff}	Fuel fraction of mission segment	
n	Load factor	
N	Total amount of layers of the MLI	
N_t	Layer density of the MLI	[layers/cm]
$\overline{N}$	Effective ultimate design factor	
Nu	Nusselt number	
P	Power	[W]
P_{dyn}	Dynamic landing gear load	[kg]
p_s	Static pressure	[Pa]
p_t	Total pressure	[Pa]
pax	Passengers	
Pr	Prantl number	
q	Heat flux	[W/m^2]
Q	Heat input in the tank	[W]
r	Radius	[m]
R	Range	[km]
R	Thermal resistance	[K/W]
R	Specific gas constant for air or combustion gases	[J/kg/K]
Ra	Rayleigh number	
R_i	Wing mass inertial relief factor	
Re	Reynolds number	
RoC	Rate of Climb	[ft/min]
S	Area	[m^2]
St	Stanton number	

t	Thickness	[m]
t/c	Thickness to chord ratio	
t	Time	[s]
T	thrust	[kN]
T_C	Cold boundary temperature	[K]
T_H	Hot boundary temperature	[K]
T_s	Static temperature	[K]
T_t	Total temperature	[K]
u	Specific internal energy	[J/kg]
U	Mean circumferential speed	[m/s]
v	Speed	[m/s]
V	Volume	[m^3]
$\overline{V}$	Volume coefficient	
w	Width	[m]
W	Mass	[kg]
x	Tail arm	[m]
X	Horizontal nacelle separation distance	[m]
α	Angle of attack	[°]
α	Thermal expansion coefficient	
α_3	Turbine blade outlet angle	[°]
β	Fuselage width to wing span ratio	
β	Thermal expansion coefficient	
γ	Isentropic expansion coefficient	
Δp	Maximum working pressure differential	[N/m^2]
ϵ	Emittance	
ϵ	Heat exchanger effectiveness	
ϵ_0	Turbine blade cooling effectiveness	
ϵ_f	Turbine blade film cooling effectiveness	
η_{CC}	Combustion chamber efficiency	
η_{int}	Turbine blade cooling internal cooling efficiency	
η_{is}	Turbomachinery isentropic efficiency	
η_{grav}	Tank gravimetric efficiency	
η_{pol}	Turbomachinery polytropic efficiency	
Θ_{300}	Combustion chamber loading	
θ	Boattail angle of the aft nacelle	[°]
λ	Taper ratio	
Λ	Sweep angle	[°]
μ	Dynamic Viscosity	[Pas]
ν	Kinematic Viscosity	[m^2/s]
π	Compressor pressure ratio	

ρ	Density	[kg/m^3]
σ	Working stress	[N/m^2]
σ	Stefan-Boltzmann constant	[W/m^2/K^4]
τ	Ratio of tip t/c to root t/c	
ϕ	Energy derivative	[Pa/J/m^3]
χ	Factor to account for primary cooling flows	
ψ	Turbine cooling air fraction	
Ψ	Entropy function	

Subscripts and superscripts

a	Air
a	Allowable
ad	Adiabatic
af	Airframe material
aft	Aft
airco	Air conditioning, pressurization and oxygen supply
app	Approach
APU	Accessory drives and APU
atm	atmosphere
av	Avionics
avg	Average
bl	Blockage
BPR	ByPass ratio
c	Chord
c	Coolant
cc	combustion chamber
c/4	Quarter chord
cl	Climb
cov	Box covers and spanwise shear webs
cr	Cruise
crew	Crew
crit	Critical
cyl	Cylindrical
D	Dive
deck	Deck
deice	De-icing
des	Design
dim	Dimensioning
dis	discharge
duct	Nacelle duct type

e	Empty
eff	effective
elec	Electrics
emp	Empennage
eng	Engine
equiv	Equivalent
exp	Exposed
ext	External
f	Fuel
fix eq	Fixed equipment
foam	Foam
for	Forward
fore	Forebody of the nacelle
fus	Fuselage
g	Gas
gg	Gas generator
GH2	Gaseous hydrogen
hld	High-lift devices
hl	Highlight
HL	Hinge line
HP	High Pressure
h	tank head
ht	Horizontal tail
hyd	Hydraulics and pneumatics
ieng	Inboard engine
in	inlet
ips	Ideal primary structure
l	Limit
lam	Laminar
LH2	Liquid hydrogen
life	Engine life
lg	Landing gear
LP	Low Pressure
m	Main
M	Mach
man	Manoeuvre
max	Maximum
mzf	Maximum zero fuel
n	Nose
nac	Nacelle
o	Outside

oe	Operational empty
oeng	Outboard engine
oper it	Operational items
out	outlet
p	Pressure
pl	Payload
prop	Propulsion system group
r	Root
rad	Radiation
recov	Recovery
ref	Reference
rib	Ribs
sc	Surface controls
skin	Skin
str	Structure
t	Tip
tot	Total
tail	Tail
tank	Tank
tot	Total
turb	Turbulent
ult	Ultimate
vt	Vertical tail
w	Wing
wa	Wall
W	Wave
wet	Wetted
y	Year

CHAPTER 1

Introduction

From its very earliest days about a century ago, the aviation industry has undergone a steady and fast growth which is predicted to continue in the long-term for all of its segments (Airbus (2007) and Boeing (2008)). After a temporary setback at the beginning of this century, the aeronautical sector seems to be recovering with passenger numbers on record levels and aircraft load factors as high as ever. Projected traffic increases lie in the order of 5% for passenger travel and slightly higher values for cargo transport despite the challenges arising from the slowing world economy and high fuel prices (Airbus (2007), Boeing (2008) and Rolls-Royce (2007)). Partially due to the increasing tendency to travel in the developing countries and emerging economies, aviation continues to be one of the fastest growing industry branches and is forecasted to expand faster than the average world economy over the next 15 to 20 years. This growth and the replacement of older aircraft results in the need of around 25000 new airplanes in the coming 15 to 20 years (Airbus (2007) and Boeing (2008)).

The increasing public awareness and attention of policy makers and media to the impact of anthropogenic emissions of greenhouse gases on the climate might however undermine this foreseen growth as it is very unlikely that aviation will be privileged and exempted from emission trading schemes. Even though advances in aeronautical technology have lead and will continue to lead to a significant improvement in the energy efficiency of transport aircraft, there is no realistic prospect that those gains will be sufficient to compensate for the anticipated traffic growth even if the aviation industry imposed very ambitious targets upon itself. On that account aviation faces a mounting conflict to sustain growth in a way that meets the needs of society while aiding to protect the environment (amongst others Cordina (2002), Green (2003), Green (2006), Greener by Design (2005), Greener by Design (2007) and Smith (2005)).

As hydrogen is a versatile and, most importantly, clean energy carrier which can be produced from many sources in various ways, it can, along with electricity, "satisfy all the energy needs and form an energy system that would be permanent and independent of energy sources" (Sherif et al., 2003a). Being 'green', hydrogen might aid in the sustainable development and growth of aviation. Consequently hydrogen holds great promise for meeting the challenges related to energy supply and climate change. Its utilization as a fuel for long range transport aircraft is therefore investigated in this work.

Section 1.1 addresses why hydrogen is appealing for a sustainable development of the aviation industry. As the idea of adopting hydrogen as an aviation fuel is not new, an overview of previous work on hydrogen fueled aircraft and engines is then given (section 1.2). This work is concerned with passenger transport aircraft, so the survey focusses on this particular sector too. The numerous studies on supersonic aircraft or unmanned aerial vehicles, for instance, are for this reason not reviewed here. After this digest, the objectives and scope of this thesis are detailed in section 1.3. Finally the structure of the thesis and the contents of the various chapters is given (section 1.4).

1.1 Why is hydrogen attractive for aviation?

Even though a secure supply of fuel at a stable price is of paramount importance for most industry branches it is even more the case for aviation since it is a highly competitive sector in which fuel costs represent a big share of the overall costs. As such fuel price fluctuations can have a significant impact on the economic success of aeronautical companies. As hydrogen can be produced from any primary energy source, its adoption would reduce the dependence on (imported) fossil fuel energy and could enable a stable fuel price level. Due to the absence of carbon particles the adoption of hydrogen might also enable an environmentally benign aeronautical industry even though an increased contrail cover due to the higher water vapor emissions could reduce the environmental benefit or even annul it. Both potential problems facing the aviation industry in its current form are briefly addressed below.

1.1.1 Security of fuel supply

Today the fossil fuel resources are concentrated in a few regions, with the Middle East holding over 40 % of the total and about two thirds of the known conventional oil reserves (BACAS (2006) and Schnieder & McKay (2001)). Currently, this concentration already creates geopolitical tensions and problems. These will most likely dramatically increase when depletion of the reserves is faced if alternative solutions are not developed and implemented by that time. After all both the United States and Europe will see an increased dependency on imported oil (DOE/EIA (2008) and EC (2003)). The import of 'foreign' oil for Europe is for instance forecasted to grow from around 75% in 2003 to over 85 % in 2020 (EC, 2003).

An energy carrier which could be produced from any primary energy source - especially from renewables - would therefore improve the reliability and security of the energy supply. This is not only true for aviation but also for the complete energy sector as such. However, the situation for the aeronautical sector is slightly different, as less alternative energy sources are at our disposal. For 'ground-based' applications, electricity could namely be a viable alternative or complement to hydrogen. The use of hydrogen as an energy carrier would furthermore facilitate the valorisation of energy sources far remote from the consumers as (gaseous) hydrogen could be more easily stored and transported than electricity. This could thus enable the exploitation of remote energy sources, as solar energy, even in deserted areas (BACAS (2006)).

However, the adoption of hydrogen as an alternative to fossil fuel energy strongly depends upon the price level of both hydrogen and fossil fuels. This depends on its turn mainly upon the speed of depletion of the fossil fuel sources and the total quantity of hydrogen produced. When fossil fuel reserves will be exhausted is nonetheless hard to judge and a considerable variation of the estimated reserves exists over time and between experts. Values ranging from approximately 1000 million barrels of proven reserves (EIA, 2009) to an ultimately recoverable amount between 2150 and 3500 million barrels are found in literature (IEA (2008) and Benner & van Geuns (2008)). This large deviation is mainly explained by the different assumptions made for the potential new discoveries and the variations in expectations of the ultimate recovery factors of conventional resources[1]. Even though resources might be abundant over the next decades, the unlimited availability of oil till the point of depletion is not a certitude. The level of demand could after all be higher than the rate at which they can be exploited if investments are not made in due time (IEA, 2008).

The wide range of forecasts on fossil fuel recources leads to an even bigger spread in the prediction of the fuel prices of both hydrogen and kerosene. All things considered forecasts are not able to take the offer-demand mechanism of the market into account which for instance lead to the peak in crude oil prices lately, exceeding $ 100 per barrel. As far as hydrogen fuel prices is concerned, the price scatter is even bigger since its level strongly depends upon the efficiency of the (future) production method. As an indication, according to Oelkers & Prenzel (2001) prices for kerosene and liquid hydrogen will be the same around 2037, after which hydrogen would be cheaper. Schnieder & McKay (2001), on the other hand predict equal prices for both fuels as early as 2020. Taxes upon emissions of CO_2 could for that matter significantly impact these forecasts moving the 'break-even point' forward in time (Svensson (2005) and Westenberger (2003b)).

In conclusion, it is virtually impossible to predict the timeframe in which hydrogen will become competitive with kerosene as an aviation fuel seen the large number of uncertainties. However, at a given moment in time, it will most likely happen. Besides future economical benefits hydrogen also offers the potential to improve the reliability of the energy supply chain as well as a reduction of the depency on fossil fuels and the related geopolitical tensions. Finally, the adoption of hydrogen as an energy carrier in general and an aviation fuel in specific, facilitates the diversification of the energy production sources, which entails a longer term price stabilization. An excessive increase in price of one primary energy source would namely be less imperishable as the switch towards another supply would be possible.

---

[1] The ultimate recovery factor is defined as the percentage of oil in place that can economically be extracted.

1.1.2 Reduction of the environmental impact of aviation

The combustion of hydrocarbon fuels generates several 'pollutants' that can either impact the earths radiative balance or alter the chemical composition of the atmosphere. As such aircraft have an impact on the climate of our planet which will become more important over the next decades seen the considerable growth predicted for aviation. Together with the risen public awareness on the problem of global warming and the emission of greenhouse gases, questions are raised whether the environmental impact of the aeronautical sector could limit the expansion of air travel (amongst others Antoine & Kroo (2005), Green (2006)). Even though the adoption of hydrogen as an aeronautical fuel does not completely eliminate the environmental impact of aviation, it could enable a long-term sustainable future for aviation as is shown below by a comparison of the emissions of kerosene and hydrogen fueled aircraft and their impact on the environment.

1.1.2.1 Emissions of pollutants from kerosene fueled aircraft

The combustion of a hydrocarbon fuel as kerosene produces carbon dioxide (CO_2), water vapor (H_2O), carbon monoxide (CO), oxides of nitrogen (NO_X), soot, aerosols and unburned hydrocarbons (UHC). The total fraction of combustion products in the exhaust amounts to about 8.5% of which the majority are the so-called primary emissions CO_2 and H_2O. The products of non-ideal combustion only constitute about 0.4% of this fraction (Penner et al., 1999). Typical emission index (EI) levels of the main greenhouses gases emitted by aircraft engines are given in Table 1.1.

Table 1.1. Typical emission index levels (g/kg fuel) for different engine operating regimes, adopted from Penner et al. (1999).

Species	Idle	Take-off	Cruise
CO_2	3160	3160	3160
H_2O	1230	1230	1230
CO	20 (10-65)	1	1-3.5
HC (as CH_4)	4 (0-12)	0.5	0.2-1.3
NO_X (as NO_2)			
- Short Haul	4.5 (3-6)	32 (20-65)	7.9-11.9
- Long Haul	4.5 (3-6)	27 (10-53)	11.1-15.4
SO_XO (as SO_2)	1.0	1.0	1.0

Carbon Dioxide is an inherent consequence of the combustion of any hydrocarbon and the quantity of emitted CO_2 is linearly related to the fuel consumption of the engines as shown by the constant EI in Table 1.1. Aviation is currently responsible for roughly 2% of all anthropogenic CO_2 emissions (Penner et al. (1999) and Sausen et al. (2005)) but this share is likely to increase significantly in the future seen the forecasted growth of aviation. As CO_2 has an atmospheric lifetime of 50-200 years (Green, 2006), its effect on the earths radiative balance does not depend on the location of the emissions and the accumulated emissions over the last century need to be considered when assessing the radiative forcing. It is this long lifetime that makes carbon dioxide such a strong greenhouse gas.

Water Vapor is the second primary combustion product of aviation kerosene. Water emitted in the (lower) troposphere precipitates quickly after release. In the stratosphere, however, the lifetime of water can be up to one year with a consequent higher radiative forcing (Svensson & Singh, 2004). When emitted in the lowermost stratosphere, accumulation times of water are nonetheless still considered to be small (Ponater et al., 2006), which makes that the direct contribution to the climate impact from water released from aviation can be considered as marginal ((Penner et al., 1999) and Sausen et al. (2005)). Indirectly water vapor however also contributes through the formation of contrails and possible cirrus clouds as described below (Schumann, 2005).

Soot and Aerosols only have a small contribution to the global warming effect of aviation. Their mass concentrations are namely very small and will continue to be so, even at a very high rate of growth of the aviation sector (Penner et al., 1999). Soot emissions tend to warm the atmosphere whereas aerosols do the opposite. The latter also play an important role in the formation of (aviation) cirrus clouds as nuclei for condensation. As such they lead to an increased cloud cover and can furthermore alter the radiative properties of natural cirrus clouds (Schumann, 2005).

Nitrous oxides (NO_X) primarily form through the dissociation of atmospheric nitrogen at temperatures higher than about 1850 K and the recombination with dissociated oxygen to NO, that is further oxidized to NO_2[2] (Lefebvre, 1999). NO and NO_2 are considered together and called NO_X. NO_X concentrations increase exponentially with temperature and linearly with residence time (Lefebvre, 1999). At ground level NO_X emissions lead to an increase of ozone concentrations, which may entail respiratory illness, headaches, ... (Lefebvre, 1999). Upon emission in the upper troposphere up to altitudes of about 15 km, NO_X has an indirect climate effect as it provokes the formation of ozone, which is a greenhouse gas. At higher altitudes, in the stratosphere, NO_X emissions cause on the other hand ozone depletion, which inflicts increased ground-level ultra-violet radiation (Gauss et al. (2006) and Singh (2004)). NO_X emissions furthermore also reduce concentrations of methane, which leads to a cooling of the atmosphere and therefor partially balances its effect on ozone formation (Gauss et al. (2006) and Sausen & Schumann (2000)).

Contrails or condensation trails are line-shaped ice-clouds that can appear in aircraft wakes when the atmospheric conditions are right. Their formation depends on many variables including ice microphysics, chemical reactions in the wake, wake dynamics, atmospheric dispersion rates and engine technology (amongst others Meerkötter et al. (1999), Noppel (2007), Marquart et al. (2003), Penner et al. (1999), Ponater et al. (2002), Schumann (2005) and Stordal et al. (2005)). Depending on the atmospheric conditions during the flight, the contrail can either evaporate quickly or persist for time periods up to several hours. The ice crystals in contrails scatter terrestrial long wave radiation back to the surface of the earth and reflect the short wave solar radiation. As the former effect is predominant, they lead to a warming of the earths surface (Ponater et al. (2002)

---

[2] Besides atmospheric NO_X , several other forms exist. A small part of NO_X forms from nitrogen present in the fuel, so-called fuel NO_X. Further NO_X formation mechanisms are related to the formation of nitrous oxides (N_2O) and so-called prompt NO (Lefebvre, 1999).

and Schumann (2005)). Although they have a global heating effect, contrails reduce local temperatures during the day and increase them at night (Ponater et al., 2002). The radiative forcing of contrails depends on their global coverage and is currently believed to consitute about 20% of the total climate impact of aviation (Sausen et al., 2005). This is expected to increase considerably due to the foreseen traffic growth (Marquart et al., 2003).

Contrail cirrus clouds develop from contrails when the ambient humidity is not high enough for natural ice-cloud formation. The added moisture and nuclei from the engine exhaust change the meteorological conditions so that contrails can develop into clouds with similar radiative properties as contrails[3]. Despite large uncertainties in understanding the formation of contrail cirrus clouds, their radiative forcing is believed to be several times larger than that of the contrails the clouds originated from (Sausen et al., 2005).

All the aforementioned effects are summarized in Figure 1.1 which shows the original estimates from Penner et al. (1999) and updates based on improved understanding resulting from the TRADEOFF research project (European Commission, Framework Program V). Although the current level of scientific knowledge and understanding of atmospheric climate science does not allow precise estimates of the radiative forcing of contrails and cirrus, the figure shows that they might cause a radiative forcing bigger than that of all other aviation pollutants combined.

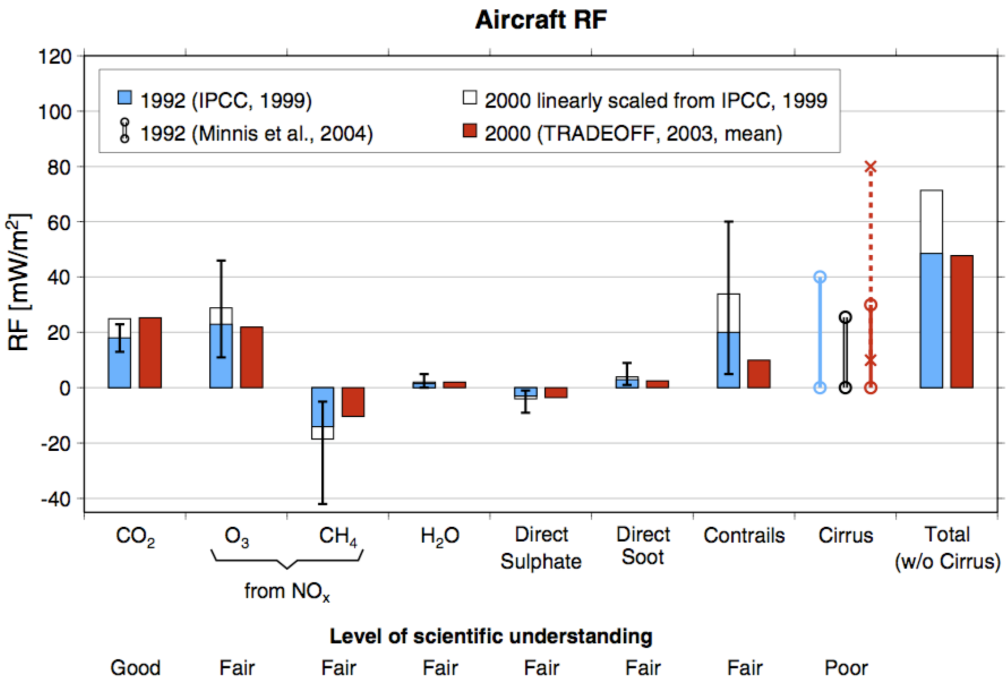

Figure 1.1. Radiative forcing from aviation in 1992 and 2000, adopted from Sausen et al. (2005).

---

[3] The particles emitted by aircraft can even cause the formations of cirrus long after the aircraft has passed. This happens if the background atmosphere changes in the mean time to a supersaturated state that enables cloud formation. The aerosols can also modify the micro-physical properties of clouds, alter particle sizes and forms,... (Sausen et al. (2005) and Stordal et al. (2005)).

1.1.2.2 Emissions of pollutants from hydrogen fueled aircraft

When burning hydrogen the only primary combustion product is water vapor and the only secondary emissions of any significance are oxides of nitrogen. The emissions of CO_2, CO, soot, SO_X and unburned hydrocarbons are completely eliminated solely by the nature of the fuel. As hydrogen is a pure fuel without many contaminants, the number of particles in the exhaust of the engine will also be strongly reduced.

Water vapor emissions from hydrogen are approximately 2.6 times higher compared to a typical kerosene fuel, on an equal energy content basis (Ponater et al. (2006) and Westenberger (2003b)). Due to this increased rate of water emissions in the upper troposphere-lower stratosphere region by the adoption of a cryoplane fleet, the amount of water accumulated in this region can no longer be neglected, as shown on Figure 1.2[4]. Nonetheless, the direct contribution of water vapor is still small compared to the overall climate effect of aviation.

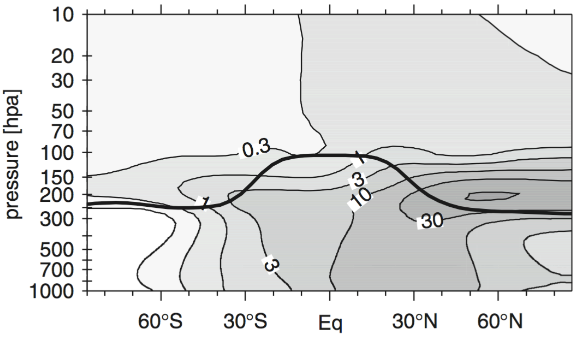

Figure 1.2. Annual mean increase of water vapor mixing ratio (in nmol/mol) due to emissions of a purely LH_2 fueled air fleet using the 2015 inventory, adopted from Ponater et al. (2006).

Nitrous oxides emissions could be significantly reduced when adopting hydrogen as a fuel as a direct consequence of the combustion-related properties of hydrogen (see Table A.1). The wide flammability limits of hydrogen, and more particularly the low lean blowout limit, namely enable operation of the hydrogen combustion chambers at lower equivalence ratios, compared to conventional kerosene combustion chambers, as indicated on Figure 1.3(a). The high burning velocity of hydrogen further enhances this effect as it results in a shorter combustion chamber and in consequence reduced cooling requirements (Svensson & Singh, 2004). The injection of hydrogen as a gas in the combustion chamber and its high diffusivity are final contributors to its low-NO_X potential. Both effects after all enable the avoidance of local fuel rich regions which lead to hot spots. Various programs have shown that single digit NO_X emission index numbers are possible in practical combustion chambers (amongst others Brand et al. (2003), Dahl & Suttrop (1998), Marek et al. (2005), Ziemann et al. (1998)). This is shown on Figure 1.3(b).

---

[4] Ponater et al. (2006) indicate that a wide variety in the radiative forcing of water vapor due to hydrogen fueled aircraft exists in literature. They attribute this to a difference in the assumed strength in water vapor sink (through condensation and subsequent sedimentation) and background water vapor concentrations around the tropopause.

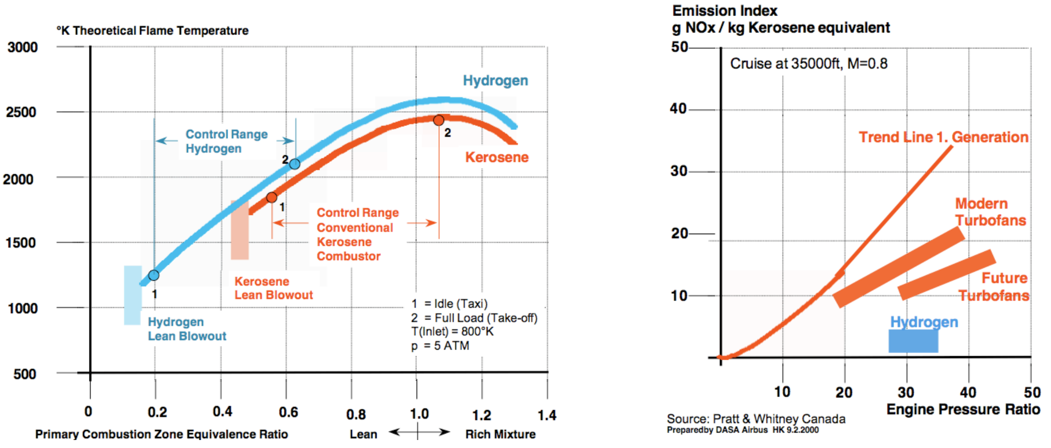

(a) Combustor primary zone temperature (b) Low-NO_X potential of H_2 combustion

Figure 1.3. Temperature characteristics and low NO_X potential of hydrogen combustion chambers, adopted from (Faass, 2001).

Contrails and contrail cirrus are the main contributors to the climate impact of hydrogen fueled aircraft. Due to the increased amount of water vapor emissions, cryoplanes would lead to the formation of contrails over a wider range of altitudes than kerosene-fueled aircraft, for a similar propulsive efficiency of the engines (Marquart et al. (2001), Noppel (2007) , Ponater et al. (2006), Svensson & Singh (2004), Svensson et al. (2004)). A typical annual mean contrail cover for a pure cryoplane fleet is shown on Figure 1.4. However, the absence of particles in the engine exhaust when using hydrogen fuel would lead to contrails and cirrus clouds that have less but larger ice crystals, hence modifying the radiative forcing of the clouds (Noppel (2007) , Ponater et al. (2006), Svensson & Singh (2004)). Ponater et al. (2006, pg. 6941) claim that "the net effect of cryoplane contrails" (on the warming of the atmosphere) "is likely to be less positive than for contrails from conventional aircraft, because smaller optical depth dominates over higher occurrence frequency on a global scale".

The current understanding of the climate impact of hydrogen fueled aviation is summarized on Figure 1.5[5]. The figure shows the separate contributions of CO_2, O_3, contrails and H_2O vapor for 4 different transition scenarios. *Ker* indicates the standard future projection of aircraft emissions of a pure kerosene fleet. In *Cryo1* a smooth stepwise transition approach, beginning in 2015 in the European Union is assumed, followed by a transition start in North America 5 years later and another 5 years later for South America, Asia and the Middle East. In all regions, small aircraft are replaced first, followed by long-range aircraft some 10 years later. *Cryo2* assumes a faster world-wide transition of small and medium-sized aircraft in 2015 and of large aircraft in 2025, leading to a complete switch to hydrogen fuel in 2050. Finally for *Cryo3* the world-wide transition starts in 2020 continuing as fast as *Cryo2* towards the end of the period (Ponater et al., 2006).

As shown on the figure, the contributions of aviation CO_2, ozone and contrails reduce for

---

[5] In this figure, the surface temperature changes are used as a metric rather than radiative forcing since they account for the delay between forcing and response due to the thermal inertia of the climate system (Ponater et al., 2006).

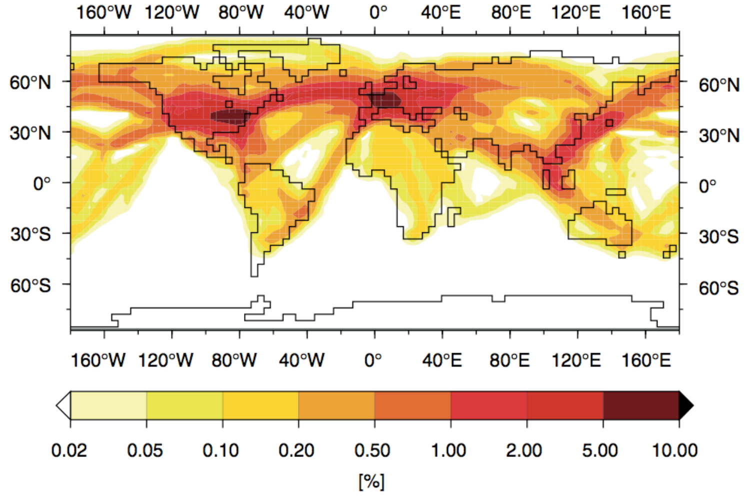

Figure 1.4. Annual mean contrail cover from a purely LH_2 fueled air fleet for a predicted 2015 traffic inventory, adopted from Ponater et al. (2006).

each of the transition scenarios compared to the pure kerosene scenario. The increase in CO_2 radiative forcing reflects the large lifetime of the pollutant and the consequent huge delay between changes in emissions and the corresponding climate forcing. Due to the reduced NO_X emissions of cryoplanes, the contribution from ozone drops sharply for each of the transition scenarios[6]. Contrail radiative forcing is slightly smaller for each of the transition scenarios due to the aforementioned effects, but still increases as the effect of increasing air traffic dominates over the benefits from adopting cryoplanes. Finally, water vapor radiative forcing increases sharply for the cryoplane cases but stays the smallest contributor for each of the scenarios.

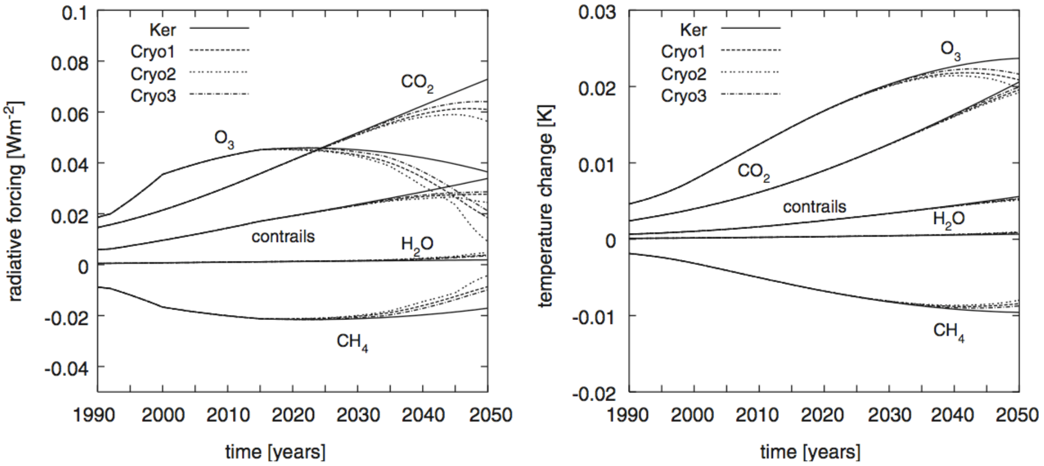

Figure 1.5. Global mean radiative forcing (in W/m^2) and temperature change (K) due to conventional air traffic and cryoplane transition scenarios up to 2050, adopted from Ponater et al. (2006).

---

[6] Ponater et al. (2006)) assumed an advance in combustion chamber technology leading to reduced NO_X emissions for both kerosene and hydrogen fueled engines.

A few notes need to be added to this climate change assessment though, as raised by Ponater et al. (2006). First of all, the absence of aviation induced cirrus in the analysis is noted as an important limit to the current assessment. However, the authors "deem the scientific basis" of contrail cirrus formation "to draw quantitative conclusions to be insufficient for assessment purposes"(Ponater et al., 2006, pg. 6941). They however "suggest an even enhanced environmental benefit of cryoplanes: These do not emit particles (meaning no indirect effect due to background aerosol accumulation) and cause contrails with smaller optical depth and, potentially, a shorter lifetime[7]" (Ponater et al., 2006, pg. 6941). Measurements in contrails from a cryoplane prototype would however be necessary in order to evaluate model calculations. Furthermore, the authors also note that "the assumption of a linear dependency between emissions and radiative impact for spatially in-homogeneous climate forcings as contrails or aircraft induced ozone may only be justified as long as the air traffic density pattern with respect to latitude and altitude does not substantially change with time"(Ponater et al., 2006, pg. 6941). According to the authors these shortcomings seem to be acceptable as they lead to uncertainties within the range given by Penner et al. (1999).

As a final note, Ponater et al. stress that the advantage of the absence of CO_2 emissions would become more obvious for longer time horizons. If constant fuel consumptions and emissions are assumed for a period of 50 years from 2050 onwards, the total radiative forcing would be reduced by between 50% and 60% whereas the reduction of the temperature change would increase from 10% in 2050 to about 45% in 2100 (Ponater et al., 2006).

1.2 Previous work on hydrogen fueled aircraft and engines

Hydrogen has been considered as an alternative to hydrocarbon fuels for almost as long as powered aviation exists. As early as 1918, P. Meyer wrote an article entitled "Is There Any Available Source of Heat Energy Lighter than Gasoline?" which the NACA adopted as Technical Note 136 in the early 1920s (Meyer, 1923). Meyer drew attention to hydrogen indicating it has a higher heat content per mass than any other known fuel. He however only considered it in gaseous form under pressure and remarked that the containers had to be strong and heavy, which counterbalanced the energy advantage (Meyer (1923)).

The research on hydrogen fuel for aviation continued during World War II when Simon befuddled the fuel experts in the United States by suggesting that liquid hydrogen should be used to increase aircraft range. This lead to an investigation of the application of liquid hydrogen to aircraft and rockets. As hydrogen's very low density made its application in volume-limited airplanes appear totally impractical these studies did not go in detail. The very low availability of hydrogen as a liquid and its handling hazards were furthermore used as arguments against it (Sloop, 1978). Interest in hydrogen was however not lost completely in the United States. It resurfaced towards the end of the war when researchers at Wright Field looked into future projects (Sloop, 1978).

---

[7] As the larger size particles are heavier they could fall out of zones with ice supersaturation quicker than ice particles in contrails from kerosene fueled aircraft.

In the mean time, von Ohain was the first person to actually use hydrogen as an aviation fuel. In 1937 he successfully ran a hydrogen fueled gas turbine engine, rig testing the He S-1 experimental engine, a radial turbojet which delivered a thrust of 250 lbs (Conner, 2001). Von Ohain chose gaseous hydrogen combustion as it allowed an early demonstration of the jet engine principle whereas the gasoline-fueled combustion chamber still required extensive further development before becoming practical. As such Von Ohain proved his concept and obtained the necessary budgets for continuing the work on the gasoline-fueled combustor. Besides being the first person to ever run a turbojet aero-engine he unintentionally became the pioneer of hydrogen fueled aviation.

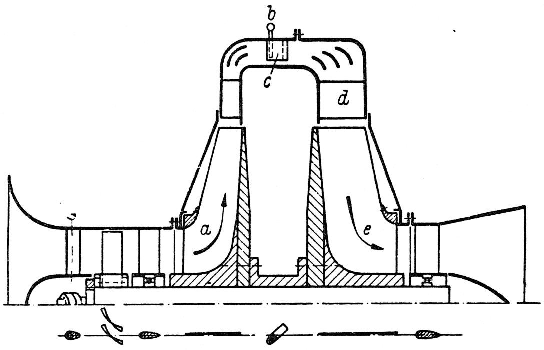

Figure 1.6. He S-1 radial turbojet with hydrogen, adopted from Conner (2001).

About two decades later the United States Air Force asked Pratt & Whitney Aircraft in 1956 to look into the possibility of using LH_2 as a fuel for aircraft engines. The study consisted among others out of the testing of the J57 engine modified for hydrogen and the development of a hydrogen-fueled demonstration engine (Sloop, 1978). Figure 1.7 shows a schematic drawing of the J57 engine adapted to use hydrogen fuel.

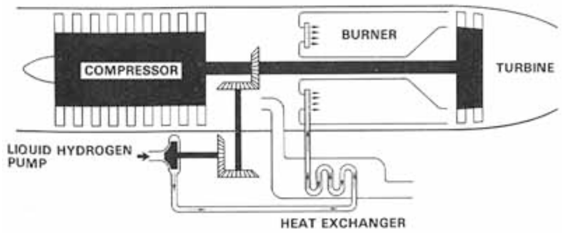

Figure 1.7. Sketch of the J57 engine modified to use H_2 fuel, adopted from Sloop (1978).

As the military was on a quest for longer range and higher cruising altitudes, testing with hydrogen was at the same time performed at the NASA Lewis Research Centre (Conrad (1979), Dahl & Suttrop (2000) and Sloop (1978)). The poor combustion efficiency of hydrocarbon fuelled combustors at altitude namely resulted in operational ceilings around 21000 meters while the goal was set at 30500 meters. Around early 1955, Silverstein saw the synergies between high altitude aircraft and the superior combustion characteristics of hydrogen and thought it would be possible to cope with its low density (Sloop, 1978). At high altitudes and low speeds, big wings are after all needed and these require a proportionately large fuselage leading to substantial available volumes. According to Silverstein, this could favor the use of low-density liquid hydrogen, provided lightweight hydrogen tanks proved feasible. Together with Hall, he looked into the possibilities in more detail, which lead to a report on the advantages and issues of hydrogen for high-altitude flight, issued in April 1955 (Silverstein & Hall, 1955).

Of the problems associated with the use of hydrogen for aircraft, the authors identified hydrogen tanks as the major problem. Looking at the technology of long-range missiles, they proposed liquid hydrogen tanks constructed as cylindrical balloons of light-gage metal which rely on internal pressure to maintain shape (see Figure 1.8). Their tank was 25 m long, 3 m in diameter with a volume of 175 m^3 and could store 11300 kg of liquid hydrogen. The estimated tank mass was 10 percent of the fuel mass (Silverstein & Hall, 1955). As the feasibility of a lightweight, insulated tank was a key assumption, a more detailed study was carried out on this subject. The conclusions of the study were that a tank with a mass less than 15 percent of the liquid hydrogen was possible with hydrogen vaporization rates of less than 30 percent of the hydrogen consumption during cruise (Sloop, 1978).

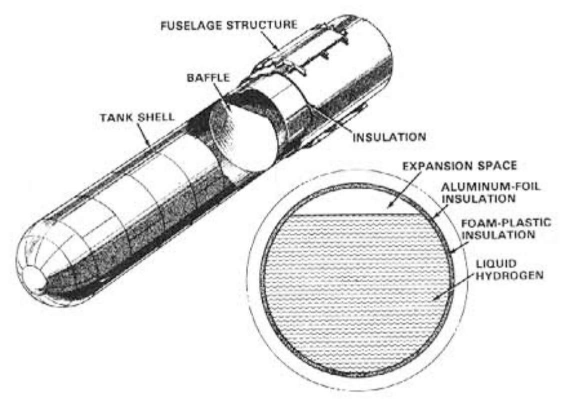

Figure 1.8. Liquid hydrogen tank suitable for aircraft as envisioned by Silverstein & Hall, adopted from Sloop (1978).

Using this basic hydrogen-tank design, Silverstein and Hall analyzed the use of liquid hydrogen for 3 types of aircraft (Silverstein & Hall, 1955). Their subsonic reconnaissance airplane had a gross mass of 40000 kilograms with hydrogen tanks in both wings and fuselage. The operational altitude was set at 24000 meters and the aircraft could make observations up to 13500 kilometers from its base. Advanced turbojet engines weighing about half those in use at that time were assumed. Silverstein & Hall concluded from their study that "within the state of the art and the progress anticipated, aircraft designed for liquid-hydrogen fuel may perform several important missions that comparable aircraft using hydrocarbon (JP-4) fuel cannot accomplish." They also concluded that a "substantial applied research and development effort will be required in many technical fields to achieve the goal outlined" (Silverstein & Hall, 1955).

Simultaneously, six type of injectors for burning gaseous hydrogen were investigated in September 1955, with a subsequent evaluation of three different turbojet engines in altitude test chambers (J-47, J-65-B-3 and J71-A-11). These tests showed superior combustion efficiencies with prototype hydrogen injectors compared to production JP-combustors at altitudes above 22-24 kilometers. The hydrogen was extremely stable and an extended relight capability was demonstrated albeit at a relatively low combustion efficiency (Dahl & Suttrop (2000) and Sloop (1978)) .

As laboratory testing did not prove whether it was realizable to use liquid hydrogen in an aircraft, Project Bee was set up in 1955. A modified Curtiss Wright J-65 turbojet engine and a hydrogen supply system were installed into a B-57B twin-engine bomber and flown (see Figure 1.9). The airplane was equipped with a hydrogen fuel system that was isolated from its regular fuel system and the left-engine was adapted to operate on hydrogen as well as kerosene. During takeoff and climb kerosene was used. After reaching level flight at about 16400 meters, the engine was switched to hydrogen fuel in two steps. First the hydrogen lines were purged and the engine was operated on both fuels for two minutes. Then it was changed to hydrogen alone. After approximately 20 minutes, the fuel flow was turned back to kerosene and the airplane returned to its base (Sloop, 1978). The aircraft was successfully flown in February 1957 with over 40 fuel transitions. Helium in the right wing tip mounted tank was used to pressurize the left wing tip mounted hydrogen tank, forcing the hydrogen through a heat exchanger to gasify it with ram air (Dahl & Suttrop (2000) and Sloop (1978)).

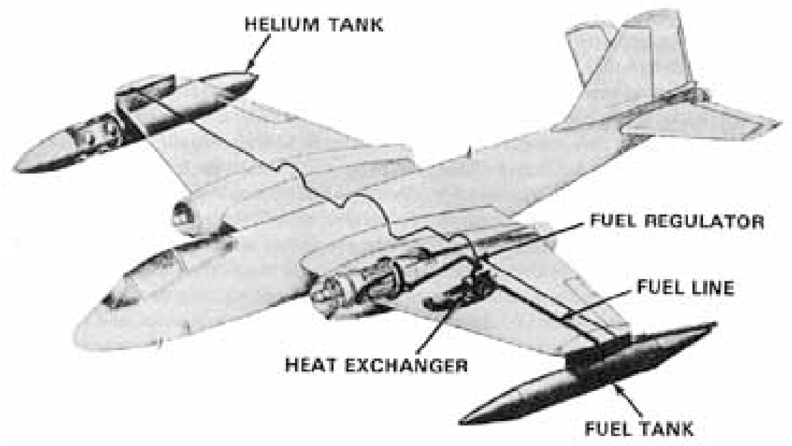

Figure 1.9. The liquid hydrogen fueled B-57 airplane, adopted from Sloop (1978).

Project Bee showed that technological progression was still due and that some technical problems required a solution before application to civil aviation would be possible. Already at that time, it was concluded from the tests that engine modifications to exploit the hydrogen characteristics had to be looked into. One particular problem that appeared during the tests was the considerable fluctuation in engine speed during the transition to hydrogen. It was believed that unsteady boiling in the heat exchanger leading ro rapid changes in hydrogen flow to the engine was at the origin of this issue. Project Bee was stopped in 1958 as studies indicated excessive costs to equip all aircraft bases for hydrogen (Sloop, 1978).

In the 1970's, hydrogen gained renewed attention as a consequence of the oil crisis. Due to this crisis the world realized for the first time that fossil fuel availability might be restricted. The energy security issue resulted in several studies by the General Electric company (GE) and NASA on hydrogen as an aviation fuel. GE looked into hydrogen for aircraft propulsion systems and evaluated unconventional cycles. The influence of the unconventional engines upon aircraft mission performance was also predicted and assessed (Payzer & Renninger, 1979).

Simultaneously, various other studies were conducted under the auspices of the NASA Langley Research Center (Brewer et al. (1975a), Brewer et al. (1975b), Brewer et al. (1978) and Brewer (1991)). In these studies both subsonic and supersonic aircraft were designed to use synthetic aviation grade kerosene (synjet), liquid hydrogen and liquid methane. Subsonic aircraft from short range passenger aircraft (130 pax - 1500 nm) to very long range transport aircraft (400 pax - 5500 nm to 10000+ nm) were designed for all three fuels. The studies showed that LH_2 was an outstanding alternative fuel for use in future transport aircraft for most of the envisaged aircraft designs. Although the benefit was larger for missions which require large fuel loads, the study showed that LH_2-fueled aircraft require less resource energy than the corresponding SynJet and the LCH_4 vehicles throughout almost the entire spectrum of sizes which were studied.

Besides the preliminary designs of the different aircraft, detailed investigations on the fuel systems and subsystems as well as the fuel containment system were also conducted as part of the research. For all these systems, the critical components were identified and a design of these components is presented. A big effort was placed on the design of the cryogenic liquid hydrogen tanks with a detailed design of the tank structure as well as the insulation. Some work on airport requirements for LH_2 and safety aspects of the use of hydrogen fuel was also performed. Brewer and his team furthermore identified several possible unconventional engine designs to exploit the heat sink of the liquid hydrogen. Besides compressor pre- and inter-cooling, cooling of the turbine cooling air with hydrogen and regenerative fuel heating, where the fuel is heated in the exhaust pipe before it is injected in the combustor, were presented as promising technologies to further improve the overall engine cycle efficiency. A hydrogen expander cycle, where accessory power would be provided by using a hydrogen expansion turbine, was assessed too. The latter two concepts showed the highest improvement in direct operating costs for the baseline cycle whereas the concepts that uses cooling of the turbine cooling air was identified as being very promising if higher turbine inlet temperatures were used (Baerst & Riple (1979) and Brewer et al. (1978)).

In 1976, The Rand Corporation reported the results of an investigation on alternative fuels for very large transport aircraft (Gebman & Stanley (1976) and Mikolowsky & Noggle (1976)). The alternative fuels were considered to reduce potential energy problems of the USAF fleet which was a direct consequence of the oil crisis in the early seventies. A variety of candidate applications for the very large airplanes were considered[8], which lead to a design radius of 3600 nm, flown at Mach 0.80 at 30000 ft with a payload of 350000 lb. All considered fuels had to be created on a coal basis as significant coal reserves are available in the U.S. Besides synthetic jet fuel, liquid hydrogen, liquid methane and nuclear fuel were selected for the aircraft designs and both life cycle-cost and life-cycle total energy consumption estimates were used as figure of merit for the comparison between the different alternatives. For both figures of merit the LH_2 fueled very large aircraft showed poorer performance than the other candidate fuels, due to the energy intensiveness of the considered hydrogen production processes, particularly the liquefaction process (Mikolowsky & Noggle, 1976). The aircraft was however both lighter and more efficient in terms of direct energy consumption. Mikolowsky & Noggle (1976) nonetheless

---

[8] Amongst others, a strategic airlifter, tanker, missile launcher, tactical battle planform and command, control and communications platform mission were taken into consideration.

recognized that hydrogen is the only candidate alternative fuel that can readily be derived from renewable energy sources and, in view of this, liquid hydrogen could according to them be expected to eventually be employed as a fuel for aircraft as well as other modes of transportation. They also acknowlegde the distinct benefits of LH_2 over the other candidates as far as pollutant emissions and noise footprint are concerned.

A couple of years later, NASA-Langley also investigated the potential of liquid hydrogen and liquid methane as an aircraft fuel, when produced from coal. Witcofski (1981a) concluded that liquid methane can be produced cheaper and more efficient than (synthetic) aviation kerosene or liquid hydrogen but that the liquid hydrogen fuelled aircraft consume slightly less energy than the other fuels. This energy consumption advantages increases with increasing mission range. As shown on Figure 1.10, the aircraft onboard energy consumption favors for the liquid hydrogen fuelled case when the design range is bigger than 4000 km. When the energy required to produce the fuel is also taken into account, a range in excess of 8000 km is needed before coal-derived LH_2 aircraft are more energy efficient. Witcofski (1981a) furthermore decides that it is technically feasible to provide hydrogen liquefaction, storage, distribution and fueling facilities at a major air terminal. The time required to refuel a liquid hydrogen fueled aircraft was found to be in the same order of that required to refuel with conventional aviation fuel.

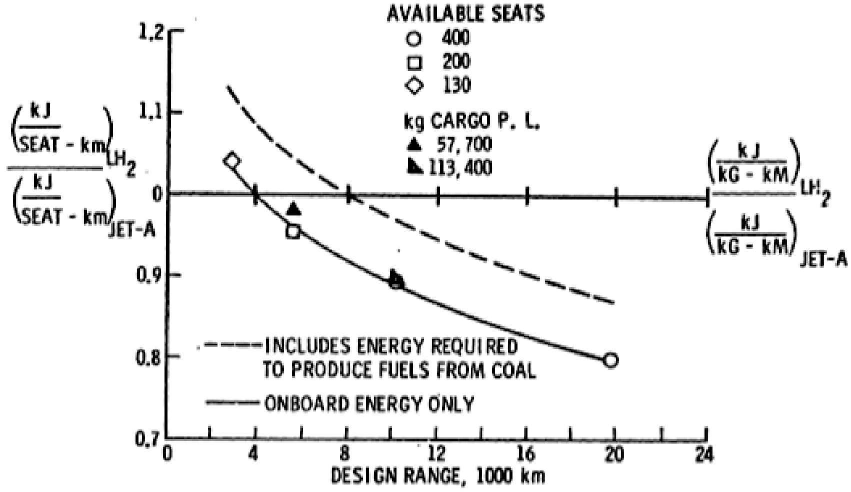

Figure 1.10. Relative energy consumption of LH_2 and Jet-A transport aircraft, adopted from Witcofski (1981a).

In 1982, Lockheed-Georgia undertook a similar study as the one that was reported by The Rand Corporation in 1976 using the same design mission and considering the same alternative fuels. As Muehlbauer (1982) projected an initial operational capability around 2000, advanced technologies were taken into account for each alternate fuel. Three criteria were used for selecting optimum aircraft designs: minimum ramp (gross) weight, minimum fuel and minimum trip costs for which different utilizations and fleet sizes were subsequently considered. It was found that the minimum ramp weight and trip cost aircraft designs coincided, so that only two categories of aircraft were subsequently considered. The study showed that the LH_2 aircraft were 23 and 26 % lighter in ramp weight than the corresponding (synthetic) JP aircraft. The extra R& D cost required for the liquid hydrogen aircraft however results in acquisition costs that are 1 % less and 7 % greater than those for the JP aircraft (Muehlbauer, 1982). The influence of the fuel price on the trip costs of the different aircraft was also investigated and it was found that the JP-fueled aircraft suffer greater relative penalties with higher fuel prices than liquid-hydrogen fueled aircraft as shown on Figure 1.11. According to Muehlbauer (1982) liquid hydrogen fuel therefore appears to be more promising than either synthetic jet propulsion fuel or nuclear power in advanced-technology aircraft, envisioned for the future.

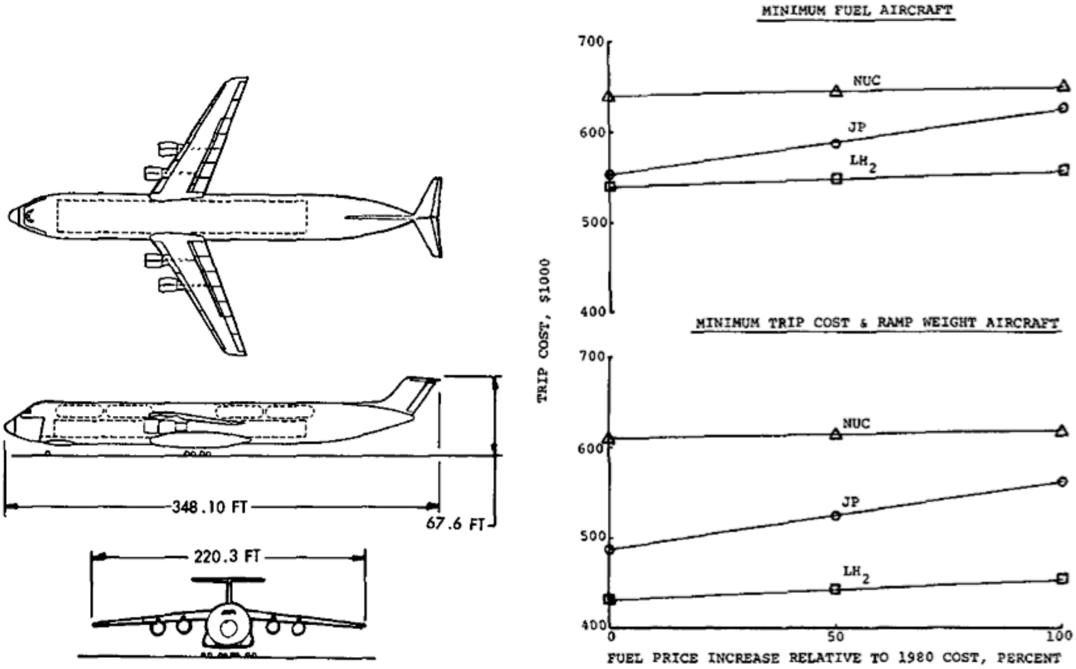

(a) Minimum Ramp weight and trip cost LH_2 a/c (b) Fuel price effect

Figure 1.11. Geometrical characteristics and fuel price influence, adopted from Muehlbauer (1982).

In the 1980's, the practical side of the development was tackled again when the TRUD consortium performed the first test where an engine was fuelled with hydrogen during the whole flight (Sosounov & Orlov, 1990). Kuibyshev Scientific Production Association (KSPA) and the Central Institute of Aviation Motors (CIAM) jointly developed an experimental Tu-155 aircraft, which is based on the Tu-154 passenger aircraft. The starboard NK-88 engine was converted to a dual fuel engine, burning either kerosene and LH_2 or kerosene and liquid natural gas (Kaminski-Morrow (2009) and Sosounov & Orlov (1990)). The Tu-155 has an 18 m^3 liquid hydrogen tank installed in the rear fuselage (in blue on Figure 1.12) and the entire fuel section is, for safety reasons, either filled with nitrogen or constantly purged with air from the air condition system of the aircraft. An additional helium system is installed for pipeline purging as well as control of the hydrogen fuel system valves. The first Tu-155 flight was achieved on April, 15^{th} 1988 and lasted for about 21 minutes. Several flights were accomplished without any shutdowns or operational system issues for both LH_2 and LNG (Sosounov & Orlov, 1990).

Figure 1.12. The hydrogen fueled Tupolev TU-155 aircraft, adopted from Kaminski-Morrow (2009).

During the 1990s further research on hydrogen fuelled aircraft was performed motivated by both environmental concerns as well as the dwindling fossil fuel sources. Airbus Germany and the Russian Aircraft manufacturer Tupolev teamed up to approach these issues from a system perspective including various fields which are affected by the introduction of hydrogen as an aviation fuel (Klug (1997) and Klug & Grassl (1993)). In January 1992, on the other hand, the Euro-Quebec Hydro-Hydrogen Pilot Project (EQHHPP) was initiated. This 4 year program was aimed at reducing the NO_X emissions of burning hydrogen and providing guidelines for the development of real aero engine combustion chambers. Both analytical modeling as well as experimental tests were performed on low-NO_X hydrogen combustion chambers for aero engines. Besides this, hydrogen safety, regulations, acceptability and socio-economic aspects were studied and several demonstration projects were set up, mainly concerning the utilisation of hydrogen in flight and ground transportation (Drolet et al. (1996) and Ziemann et al. (1998)).

In 2000, a system analysis of liquid hydrogen fueled aircraft, called the Cryoplane study[9], was untertaken under the Competitive and Sustainable Growth Programme funded by the European Commission (Framework Programme 5). The main objective of the study was to provide a sound basis for initiating larger scale activities preparing for the development and introduction of LH_2 as an aviation fuel. Aircraft were designed for all aircraft categories in commercial operation and safety, airport and environmental compatibility and medium/long term scenarios for a smooth transition from kerosene to hydrogen in aviation were investigated in this 26 months study lead by Airbus Deutschland (Westenberger, 2003b). Figure 1.13(a) shows the hydrogen fueled aircraft for some of the investigated categories.

The study concluded that the energy consumption of the LH_2 fuelled conventional aircraft would increase by 9 to 14 % depending on the aircraft category (see Figure 1.13(b)). This increase is mainly attributed to the bigger wetted area of the aircraft due to H_2 storage in bulky pressure vessels inside or on top of the fuselage. Due to this additional tank

---

[9] The same name was used for this project as for the Airbus-Tupolev project. In this work the name Cryoplane is used mainly for this project however. When the Airbus-Tupolev project is referred to it is explicitly mentioned.

structure, the operating empty weight of the aircraft also increases by roughly 23 %. The maximum take-off weight will on its turn vary between plus 4.4 % to minus 14.8 % depending on the aircraft configuration and mission. All this leads to an increase of the operating costs by 4 to 5 % caused by the fuel only. The study also revealed that the potential for very large long range aircraft was limited due to size restrictions imposed by the airport 80 m gatebox which leads to a sharp increase in energy consumption for this configuration, as shown on Figure 1.13(b). This is mainly a consequence of the triple deck design that is needed to accommodate both fuel and passengers in a fuselage limited to 80 m length. Besides conventional aircraft, various unconventional configurations have also been assessed. However, none of the investigated unconventional configurations provided a clear advantage (Westenberger, 2003b).

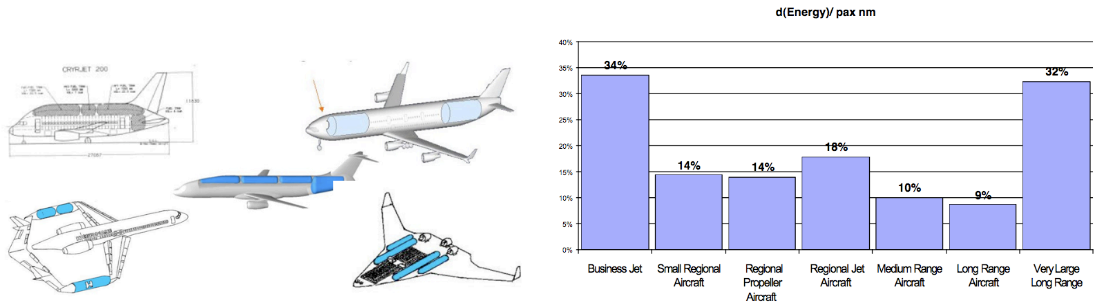

(a) Aircraft configurations

(b) Energy conssumption

Figure 1.13. Configurations and energy consumption from the Cryoplane study, adopted from Westenberger (2003b).

A detailed analysis of conventional engines has confirmed that hydrogen-fuelled engines will be equally or slightly more efficient than kerosene engines in terms of energy consumed when designed for the same takeoff thrust. A redesign of the fuel supply and injection system is mandatory while an adaptation of the control system may also be needed. Different design principles for the heat exchanger, needed in the hydrogen fuel supply system, have been assessed. The investigation showed that the hydrogen-air heat exchanger is feasible but requires further research for its design and implementation into the power plant. For unconventional engine configurations, on the other hand, small but non negligeable benefits have been found by the utilization of the cooling capacity of liquid hydrogen. Due to the favorable combustion characteristics of hydrogen, substantial improvements in NO_X emissions have furthermore been quantified in the study (Westenberger, 2003b).

As the Cryoplane study was meant to be a complete system analysis, several additional aspects of the introduction of hydrogen fuel in aviation were also assessed. Safety aspects specific for aviation have been looked at coming to the conclusion that hydrogen will not be less safe than conventional aircraft fuel. Environmentally, great benefits have been identified looking at the long-term benefits of hydrogen as an alternative fuel when produced using renewable energy sources. Extensive computer simulations within the project have shown that contrails produced by hydrogen fuelled aircraft will, despite the higher cloud coverage due to the higher water vapour content of the exhaust gasses, contribute less to the anthropogenic greenhouse effect than conventional kerosene fueled aircraft, due to a smaller optical thickness of the contrails. It is furthermore shown that the effect of hydrogen fueled transport aircraft can be significantly reduced by flying at a lower cruise altitude (and thus paying a small fuel cost penalty).

In 2002, two extra studies were reported by NASA which both looked at unconventional configurations. In Guynn & Olson (2005), an aircraft with high bypass ratio turbofans installed over the wing for noise shielding was investigated. As such the noise level was brought down by approximately 53 % compared to current aircraft, partially due to the higher bypass ratio and partially due to the shielding effect. To make the aircraft, besides less noisy, also less polluting, hydrogen was adopted as a fuel. The main reason for this choice was, according to Guynn & Olson (2005), the reduction of emissions at the airport. The study was part of NASA's Revolutionary Aerospace Systems Concepts program and was called Quiet Green Transport program. The most critical technology was not related to the aircraft itself but to the provision of economical and environmentally friendly hydrogen to the airport.

The emissionless aircraft study from NASA and MSC Technology on the other hand set itself the aim to completely eliminate all aircraft emissions (Alexander et al., 2002). To reach this objective, the power and propulsion system of the aircraft is based on planar solide oxide fuel cells powering electric motors, which drive fans for propulsion. A bottoming cycle is added utilizing turbines coupled to generators to convert the exhaust heat of the high temperature fuel cells into additional electric power. The liquid water reaction product of the fuel cells is retained onboard the aircraft until its mission is completed. It is shown in the study that even at a near term technology level, practical operating ranges can be attained without exceeding the maximum takeoff weight of its hydrocarbon fuelled counterpart[10]. However, the aircraft range would be limited to around 2200 nm for this technology level. The long-term scenario on the other hand lead to a maximum range of almost 4850 nm. For both technology levels, the study identified a strong influence of weight reduction factors on the archievable range for the mission.

Besides these studies several reports on supersonic aircraft or on unmanned aerial vehicles, from small over-the-hill type to high altitude long endurance vehicles, are available. Some studies on fuel cell propulsion for general aviation airplanes have also recently been published (Menard (2006), Romeo et al. (2007) and Wentz et al. (2005)). As they fall outside the scope of this work, the results of these studies are not reported here.

1.3 Objectives and scope of this thesis

The expansion of the aeronautical sector could be restricted by its impact on the environment as the forecasted growth will outweigh the predicted technological progress to reduce emissions. Unless a solution is found to enable a sustainable future for aviation that does not impose an unsupportable burden on the atmosphere, aviation might not be able to cater for the needs of society. As a clean energy carrier hydrogen could provide

---

[10] The maximum designed landing weight must be looked at for the emissionless aircraft as the water produced by the fuel cells is retained onboard, thereby increasing the weight of the aircraft during the mission. A maximum weight of 655626 lb was imposed.

the means to alleviate the impact of aviation on the environment and could at the same time ensure the long term energy supply for all industry branches in general and aviation in particular. However, as shown by the overview of previous work on hydrogen fueled transport aircraft several technical challenges and questions will have to be addressed before hydrogen can become a real option for aviation and some classes of aircraft are subjected to severe limitations.

One particular class of aircraft that, despite what may be believed at first sight, is submitted to restrictions that limit the capabilities for hydrogen fuel is the very large long range transport aircraft class. As shown in the Cryoplane study (Astaburuaga et al. (2001) and Westenberger (2003b)), this class of aircraft is very hard to convert to hydrogen in a conventional configuration. The geometrical restrictions imposed by the 80 m airport box constraint and the need to house the hydrogen tanks in the fuselage namely lead to a triple deck design. Airbus however indicates a shift towards high-capacity long range aircraft to cope with the increasing congestion of airspace and airports and predicts a potential for over 1000 airplanes of the large long range type in the coming two decades (Airbus, 2007). This is clearly reflected by the recent introduction into service of the Airbus A380. Even though Boeing not explicitly mentions this shift, they foretell a similar number of large long range aircraft (Boeing, 2008).

From the early start of research into hydrogen fueled aircraft, the investigations point towards the need for lightweight yet highly insulated fuel tanks designed for lifetimes, numbers of cycles and weight goals that are unmet by existing liquid hydrogen tanks. Most studies indicate that the key challenge for hydrogen to be a viable candidate, left alone an economically competitive one, is as such related to the design of the tanks. As the tanks not only depend on the particular aircraft configuration, through the ratio of surface area to fuel volume imposed by the fuselage diameter, but also on the fuel consumption, by a reduction of the pressure of the two-phase mixture of liquid and gaseous hydrogen inside them, a particular design is required for each aircraft type and maybe even for each aircraft-engine combination. As such the fuel tank ’couples’ engine and aircraft to an even higher extent than is already the case for kerosene fueled aircraft.

In the light of the issues and challenges that were revealed by the review of studies concerning liquid hydrogen in subsonic civil transport, the aim of this thesis is therefore an investigation of two main areas:

- The design of the liquid hydrogen tanks and the key factors that play a role on the configuration that is best suited for large long range transport aircraft. For this design, the focus will lie on selection of appropriate materials on the one hand and the tradeoff between mechanical and thermal tank characteristics on the other hand.
- The design of an unconventional twin fuselage configuration that could restore the potential of liquid hydrogen for large long range transport aircraft. After all, the larger the fuel mass of the mission is, the larger the (theoretical) gains from the adoption of hydrogen could be.

To carry out the designs for these two areas several tools are developed to enable a comparison between kerosene and hydrogen fueled aircraft on the one side and conventional and unconventional aircraft configurations for hydrogen on the other side.

- A design method for liquid hydrogen tanks, taking thermal, mechanical and mass properties of the materials into account as well as the mission for which the tank will be utilized and the geometrical restrictions imposed by the aircraft.
- A conceptual aircraft design tool that is sufficiently detailed to allow trade-off studies between configurations of aircraft and between kerosene and hydrogen fuel.
- A turbofan design and performance analysis routine that can be integrated with the aircraft conceptual design tool to analyze the impact of the engine configuration on the 'optimal' design point for the aircraft.

1.4 Structure of the thesis

The remainder of this work is divided into 4 chapters and 3 appendices.

Chapter 2 completes the literature survey on liquid hydrogen for large long range transport aircraft by addressing its particular effects on the design of both aircraft and engine and how these are accounted for in the developed tools.

Chapter 3 looks into detail at the design of the liquid hydrogen tanks. The selection of materials, the thermal and mechanical sizing as well as the volume determination are covered extensively. Once all methods are described two widely different applications are investigated to analyze the implications of the selected aircraft type on the design of the tank.

In Chapter 4 the results of the different case studies on large long range aircraft that were executed in the frame of this study are given. Two classes of long range aircraft are covered by conventional designs and a twin fuselage design is presented for the very large (550 pax) long range aircraft.

Conclusions are drawn from the results on both the tank and the long range aircraft in Chapter 5. Several areas for extensions of the models and continuation of the work are highlighted as well.

Besides the main chapters 3 detailed appendices are included.

Appendix A touches on some aspects of hydrogen in aviation that are not the main focus of this work but are still considered to be important. After a review of the main properties of hydrogen, some production and liquefaction methods are discussed and notes on airport storage as well as safety and handling of hydrogen are given.

The different models of the conceptual aircraft design routine developed in Matlab® are consecutively described in Appendix B. The determination of geometrical, mass and aerodynamic properties of the aircraft is described. Load and balance, performance and direct operating cost computations are also treated.

The final appendix gives an overview of the turbofan design and performance tool set up in Ecosimpro^{TM}. The appendix details the calculation of the thermodynamic properties and the component building blocks. The set up of a model for design point and off-design calculations is also specified and in a last section the gas path analysis method used in this work is described.

Even though the tools reported in the last two appendices were vital to obtain the results presented in this thesis, they are placed in appendices as they are not essential to the understanding of the different results and design studies. As the design of the liquid hydrogen is a relatively new field and contributes significantly to the understanding of the design trade-offs as well as the results, the developed tank sizing method is covered in the main text rather than in an appendix.

CHAPTER 2

Effect of hydrogen on aircraft and engine design and performance

The utilization of hydrogen instead of kerosene onboard aircraft has a distinct effect on the design and performance of both the aircraft itself as well as its engines. After all, hydrogen has characteristics that are significantly different than those of kerosene. Some are beneficial, some not at all, as will be shown in this chapter based on the properties of hydrogen. A more general discussion of the properties themselves can be found in Appendix A. The scope of this chapter is limited to characteristics that affect the aircraft and the engine.

Section 2.1 describes the effect that hydrogen has on the aircraft. After this the influence on the engine is reported in section 2.2. After the most important implications have been identified, the required modifications to the design tools developed in this work to account for the peculiar aspects of hydrogen are reported. Both the aircraft (subsection 2.3.1) and the engine (subsection 2.3.2) are treated. The developed tools themselves are not described in this chapter. They can be found in Appendices B and C. Here only changes needed when switching to hydrogen are given.

2.1 Effect on aircraft design and performance

The impact of the adoption of hydrogen as a fuel on aircraft design and performance is summarized in Table 2.1, which is adopted from Brewer (1991). The left column of the table gives properties of hydrogen whereas the right column denotes the anticipated effect of that particular property on the design and the performance of the aircraft in comparison to aircraft designed for kerosene fuel.

The main advantage of hydrogen as an aircraft fuel lies in its very high heat of combustion. As shown in the table the lower heating value of hydrogen is approximately 2.8 times higher than that of kerosene. If all other factors remain the same, a hydrogen fueled aircraft would require about 2.8 times less fuel to fly the mission compared to its kerosene fu-

Table 2.1. Effect of H_2 on aircraft design and performance, adopted from Brewer (1991).

Property	Effect (relative to kerosene
High heat of combustion	Fuel weight reduced by factor of 2.8
	Quieter aircraft
High specific heat	Fuel cools engine and vehicle hot parts
	High TIT and OPR
	Further reduced specific fuel consumption
	Further weight savings
Low density	Lesser weight of the fuel requires about 4.15 times more volume, this leads to
	Lower L/D
	Low wing loading at takeoff
Cryogenic	requires
	Airtight insulation system
	Heavy tank and fuel system
	Special tank fill and vent procedures
	Constant tank pressure to minimize boil-off

eled counterpart. A 'snowball' effect can however be anticipated where each saved pound of fuel mass leads to a cumulating weight benefit (Brewer, 1991). Due to this reduced fuel load the aircraft will be able to perform its mission with a lower gross weight, which enables the use of smaller and thus also quieter engines.

The engines of a hydrogen fueled airplane will not only be smaller, they could also become more efficient due to the high specific heat capacity of hydrogen and its low storage temperature. Exploiting the heat sink offered by the cryogenically stored LH_2 could improve engine performance as will be shown in the next section. However the aircraft performance can also benefit from this cooling capacity. For super- and hypersonic aircraft the cold hydrogen can be used to cool the structures of the aircraft subjected to aerodynamic heating. For subsonic aircraft, on the other hand, the drag can be reduced by cooling through hydrogen to ensure laminar flow (Brewer (1991), Cunnington & Parmley (1980) and Theisen & Brewer (1979)). Through hydrogen a drag reduction near 27% can be obtained with an easier and more reliable system[1] than suction which furthermore does not require power (Theisen & Brewer, 1979). According to Brewer (1991), about 75% of the wing chord, 20% of the fuselage and the complete engine nacelles can all be cooled to the required temperatures with the flow rates required during climb and cruise. Skin cooling should however only be used when moisture is either already frozen or moisture content is small to prevent frost buildup on the surfaces. According to Brewer (1991), this nonetheless does not restrict its use for the last climb phases or throughout the whole cruise flight.

The next property listed in Table 2.1 is the main disadvantage of hydrogen for aeronautical

---

[1] The system is more reliable as it is not prone to fouling by bugs or dirt that can block the suction holes of 'conventional' systems.

applications. Due its low density hydrogen requires about 4 times more volume than an equivalent kerosene mission fuel. In view of this the designer "must exercise ingenuity to find an aircraft configuration which will accommodate the fuel volume" (Brewer, 1991, p. 15). As a consequence of the cryogenic nature of the liquid hydrogen the tanks must moreover have a low surface-to-volume ratio to limit boil-off and tank and insulation weight. The low density bulky fuel storage will furthermore generally lead to a slightly lower lift-to-drag ratio for the aircraft and a lower wing loading than found on aircraft using conventional fuels (Brewer, 1991). The fuel should thus preferably be stored in the fuselage to reduce the surface-to-volume ratio of the tanks. As a result, the fuselages are generally larger and accordingly have a higher wetted area. As the wing size can be reduced due to the lower weight, a penalty in lift-to-drag ratio is by and large found. The low wing loading (at takeoff) on the other hand follows from the low fuel weight. The wing loading at landing should namely by in the same order of other aircraft to obtain similar approach speeds. Brewer (1991) also notes that the shorter span of cryoplanes offers distinct handling benefits for airport maneuvering.

The last property of hydrogen in the table, its cryogenic nature, is as already explained an advantage and a disadvantage at the same time. As mentioned, the heat sink of the cryogenic liquid clearly offers an advantage. The need for a minimal heat input into the tank and the implications this has on the tank attachment and support structure are on the other hand undoubtedly is not beneficial. Additionally, the thermal expansion and contraction of tank and structure should be accounted for. According to Brewer (1991), a flight weight cryogenic insulation system does on its own not pose a problem. The required useful life, the need to absorb shocks from numerous landings and the requirement for accessibility are the key challenges related to the insulation. As the tank will be heavier and bulkier than kerosene tanks, a part of the weight advantage stemming from the high heat of combustion is thus lost.

2.2 Effect on engine design and performance

Combustion gases of hydrogen clearly have a different composition than those of a hydrocarbon fuel. Carbon dioxide is absent whereas the amount of water vapor downstream of the combustion chamber increases. As water vapor has a high specific heat, the specific heat of hydrogen combustion gases increases compared to equivalent gases from hydrocarbon combustion. As a consequence of this higher specific heat, the turbine expansion is modified which results in an energy specific fuel consumption benefit for hydrogen in the order of 3% (for a hydrogen injection temperature of 298 K and equal thrust). The energy specific fuel consumption or ESFC is defined as:

$$ESFC = SFC \cdot LHV = \frac{\dot{m}_f \cdot LHV}{F_N} \tag{2.1}$$

where SFC is the (thrust) specific fuel consumption, $\dot{m}_f$ the fuel flow rate, LHV the lower heating value and F_N the net thrust produced by the engine. The ESFC is defined to enable the comparison between fuels with a different lower heating value. It is a measure of how efficient the energy present in the fuel is converted into thrust.

The ESFC advantage (at constant thrust and a high fuel injection temperature) is similar for both takeoff and cruise and depends on the fuel injection temperature as shown in Corchero & Montañés (2003). It is a direct consequence of the changed composition of the combustion gases. This can be explained based on Figure 2.1. The figure shows the specific heat at constant pressure and the isentropic expansion coefficient, γ, for air, kerosene combustion gases and hydrogen combustion gases. The fuel-to-air ratios used to generate the curves are taken from typical takeoff conditions for a high bypass ratio GE90-like engine for both fuels. As the conclusions from the figure are valid in general and do not depend on the specific engine type nor the operating conditions, details on these are omitted here. They are presented in Verstraete et al. (2005a).

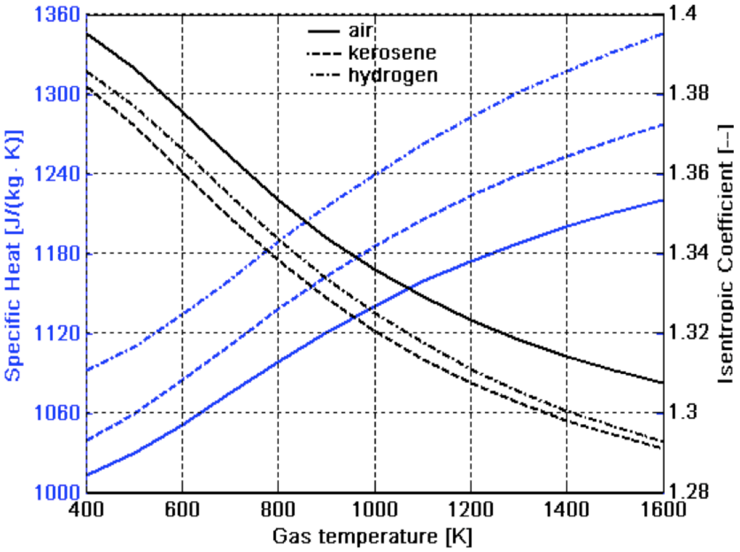

Figure 2.1. Changes in combustion gas properties when using hydrogen, as presented in Verstraete et al. (2005a).

As can be seen from Figure 2.1, the specific heat for hydrogen combustion gases is higher than that of kerosene which leads to a slightly lower temperature drop for a given turbine work (or enthalpy drop). As shown by the following equation, this effect is partially balanced by the slightly lower gas flow rate due to the smaller fuel flow rate of hydrogen. The effect of the composition change is however predominant.

$$P_{turb} = \left(\dot{m}_a + \dot{m}_f\right) \cdot c_p \cdot \left(T_{t,in} - T_{t,out}\right)$$

where P_{turb} is the turbine output power, $T_{t,in}$ and $T_{t,out}$ the total temperature at the turbine inlet and outlet and $\dot{m}$ the mass flow rates or air (a) and fuel (f).

Besides the effect of the specific heat, γ also varies. As γ is higher when burning hydrogen, the required temperature drop can be obtained with a smaller pressure drop, which leaves more energy in the gases after the turbine and leads to a higher thrust.

$$\frac{T_{t,out}}{T_{t,in}} = \left(\frac{p_{t,out}}{p_{t,in}}\right)^{\frac{\gamma-1}{\gamma}}$$

where p_t stands for total pressure. As a consequence the engine can either run colder for a given thrust output or can be made smaller. A tradeoff between engine life (through the turbine inlet temperature) and size (and drag) thus has to be made.

The performance of hydrogen fueled engines can however be further improved in addition to this composition effect, as was already indicated in the previous section. The cooling capacity of the cryogenic liquid hydrogen can be used to yield a higher engine performance in a so-called unconventional cycle. Even though several of these unconventional cycles have also gained significant attention lately for kerosene fuel (see for instance Doulgeris (2008)), the availability of hydrogen is definitely beneficial. Its high heat sink would namely reduce the demands on the heat exchanger effectiveness for an equal performance improvement compared to kerosene. The heat exchanger size and mass can therefore be reduced. Almost all studies that have been executed on unconventional hydrogen cycles fall back on four main cycles (amongst others Baerst & Riple (1979), Boggia (2000), Boggia et al. (2001), Brewer (1991) and Payzer & Renninger (1979)):

- pre-heating of the fuel from the exhaust gases,
- cooling of the compressor air with hydrogen fuel,
- cooling the turbine cooling air with the fuel and
- a hydrogen topping cycle

As the pre- or intercooled and the turbine cooling air cooling cycle seem more promising than the other cycles as far as a 'practical' adoption on an aircraft is concerned, only those two are briefly reviewed here. More information on the other cycles can amongst others be found in Boggia (2000) and Boggia et al. (2001).

A first possible way of exploiting the peculiars of hydrogen is cooling the compressor air, which leads to a reduction of the compressor work. If the limit on the overall pressure ratio (OPR) of the engine is furthermore set by material limitations (e.g. the desire to use lighter or cheaper materials) compressor cooling can allow the adoption of a higher OPR for a given compressor outlet (delivery) temperature CDT. As a higher pressure is available at the low pressure turbine (LPT) inlet, a higher bypass ratio can be adopted (Boggia et al., 2001).

Boggia (2000) shows for instance that inter-cooling through a heat exchanger mounted in front of the booster leads to an increase in OPR from 28.5 to 35.6 for a given CDT and TIT. For the V2527-A5 engine investigated in that particular work this meant the installation of one additional high pressure compressor stage and it allowed an increase in bypass ratio (BPR) from 4.8 to 5.2. Both the cruise and takeoff thrust were raised by about 7% which lead to a decrease in TSFC of 6 and 5%. To install the heat exchanger and higher bypass ratio fan, the length and the diameter of the engine 'go up' and hence the engine is heavier leading to a slight reduction in thrust to weight ratio.

The main challenge of inter-cooling with hydrogen is related to the freezing of the moisture in the air which could block the heat exchanger passages depriving the engine from air. Nonetheless, Payzer & Renninger (1979) conclude that it is feasible to design a hydrogen air intercooler without freezing issues. Similar conclusions are drawn from a recent study performed for ESA on advanced hydrogen-air heat exchangers for oxygen collection in a two-stage-to-orbit launch vehicle (Hendrick et al. (2008a) and Hendrick et al. (2008b)).

A second promising way to exploit the heat sink is to cool the bleed air, used to cool the turbine blades and vanes. A lower temperature of the cooling air would after all yield a more effective blade cooling. An increase in turbine inlet temperature (TIT) would therefore be possible while preserving the engine life[2]. The possibility to increase the TIT is however limited by the cooling of the walls of the combustion chamber (Boggia, 2000). Even though hydrogen fuel will lead to a reduction in the combustion chamber liner cooling air due to the reduced emissivity of the gases (and hence reduced heat transfer through radiation), the maximum allowable increase in TIT is still judged to be around 140 K for the V2527-A5 engine (from 1472 to 1613 K) at takeoff (Boggia et al., 2001).

Due to the higher TIT more energy is available at the inlet of the LPT which means that the BPR can again be increased. The BPR can be raised from 4.8 to 6.5 for the V2527-A5 engine, which is a significantly higher increase than for the inter-cooled concept described previously. Despite the 2 extra LPT stages needed to drive the higher BPR fan, the thrust-to-weight ratio remained virtually constant. The thrust namely increased by 28% due to the increase in bypass ratio. The TSFC on the other hand remained similar to the conventional hydrogen fueled engine.

The main challenges for this new cycle are related to the significant redesign of the cooling air routing. Possibly even more demanding are the severe thermal gradients that the blades would have to sustain due to the lower cooling air (Baerst & Riple, 1979). This will most definitely be the main challenge for the extreme case of turbine cooling proposed in Brewer (1991) and Payzer & Renninger (1979): using hydrogen directly in the blade and as such completely eliminating turbine cooling air. Besides the low cycle fatigue issues this would entail, safety issues however also arise as the gas temperature in the turbines is higher than the auto-ignition temperature of hydrogen (858 K). A small leak or diffusion through the blades would hence lead to a fire in the turbine section. Material embrittlement of the severely loaded turbine blades and disks will also be a key challenge which could be solved by the use of an intermittent inert coolant at the price of an increase in weight.

2.3 Modifications required in conceptual aircraft design calculations

As described in the previous section, the adoption of hydrogen as a fuel has consequences for the design of both the aircraft as well as its engines. To assess the difference between both fuels on a fair basis a common tool is needed to the highest possible extent. After all this ensures that the same models and assumptions are used for both fuels and prevents biasing of one fuel over the other. As part of this thesis two tools have been developed for that purpose. The first routine tackles the conceptual design of the aircraft whereas the

---

[2] An increase of about 20 K in metal temperature implies halving of the turbine life (Hendrick, 2006).

second is oriented towards the design and performance assessment of gas turbine (turbofan) engines. The models used in the various parts of the tools are not described here. They can be found in Appendices B and C. Appendix B describes the modular conceptual aircraft design routine that has been developed in Matlab®. Appendix C deals with the design point and off-design modeling of the engines in Ecosimpro^{TM}. Both appendices primarily report the models for the kerosene fueled aircraft and engines.

As Matlab® and Ecosimpro^{TM} can be coupled, the design of the engine could be integrated into the conceptual aircraft design. This is not attempted here for various reasons. First of all, using both tools separately rather than grouped will ensure stability of operation of both tools. Convergence problems in one model will not provoke errors in the other. More importantly however, it is believed that more can be learned from keeping both tools separate. As hydrogen fueled aircraft, despite the long history indicated in the introduction, are a far from mature field, it is important to allow a 'quest' for new synergies and to gain understanding in the close coupling of the design of engine and aircraft. Decoupling also guarantees that modifications to one tool have no implications for the other.

Below, the modifications required to convert the tools from kerosene to hydrogen fuel are concisely reported. First the modifications needed for the aircraft design part are detailed. Then the changes to the turbofan design and performance model are given.

2.3.1 Modifications to the conceptual aircraft design tool

Due to the highly iterative nature of aircraft design and to allow an easier modification of some of the models when switching from kerosene to hydrogen, a modular approach was adopted for the conceptual design of the aircraft, as shown on Figure 2.2. Even though the adoption of hydrogen as an aircraft fuel requires significant modifications to the conventional aircraft architecture, the number of models that have to be adapted on the aircraft level is relatively limited.

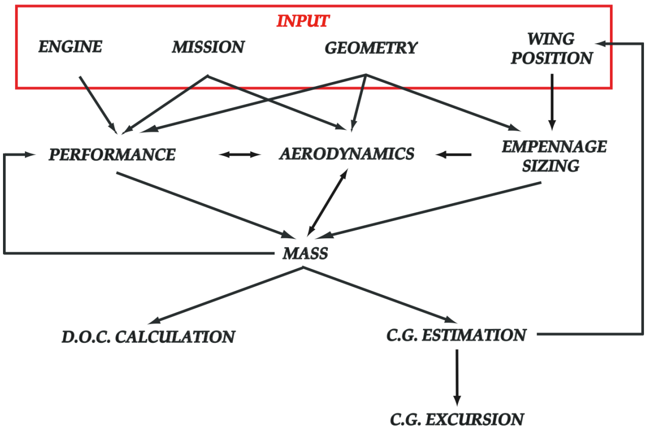

Figure 2.2. The structure of the conceptual aircraft design tool.

The main modification to the existing aircraft architecture is the storage of the fuel in highly insulated fuel tanks located inside the fuselage instead of in the wings. As the design of the tanks is a key challenge to enable hydrogen flights for transport aircraft, the tanks themselves are not reported here. Their design is described in Chapter 3 as a detailed investigation on the applicable materials, structures, . . . has been performed.

Besides the tanks the main differences between both fuels lie in the geometry and mass of the fuselage and wing and in the direct operating cost of the aircraft. These are subsequently reported below.

2.3.1.1 Fuselage geometry and mass

As the fuel tanks are located in the fuselage, both its geometry and mass will be affected. For the long range aircraft under consideration the fuel needs to be stored in two separate tanks[3]. The first tank is located between the cockpit and the cabin, whereas the second tank is integrated into the tail cone. This configuration allows a proper allocation of the aircraft center of gravity but does not allow to shift fuel from one tank to the other to reduce trim drag as is according to Raymer (1989) done on some current kerosene fueled aircraft. The fuel mass is namely relatively small so that the center of gravity movement will be limited. More importantly however, moving the fuel from one tank to the other will result in boil-off and loss of the cryogenic hydrogen and should thus be avoided (Allidieris & Janin, 2002b).

As the tank separates the cockpit from the cabin, a passageway might be needed by creating a cutout in the tank as shown on Figure 2.3. Even though this will imply a weight penalty for the tanks, it is not believed to be much heaver than the alternative of not providing access between cabin and cockpit (Astaburuaga et al., 2001). After all, an extra door, extra lavatories and other facilities need to be provided to the cockpit in that case. Astaburuaga et al. (2001) also argument that the captain needs to be able to inspect his cabin. According to Roskam (2002) (personal communication) there is no such regulation at all and the ability to inspect the cabin could either be delegated to the cabin crew or be done through a camera system. Torenbeek & Jesse (2001) also indicate that a purser with a higher legal authority can take up a part of the cabin-related tasks of the captain in a twin fuselage aircraft. Here it is left open what option to decide on.

As the two tanks will provide extra (point) loads to the fuselage structure, the remainder of the fuselage needs to be beefed up slightly to be able to cope with those. According to Brewer (1991) this leads to an increment of around 6 % of the fuselage mass. As a detailed layout of the fuselage structure is outside the scope of this work, this value is adopted here.

The main change for the fuselage as far as design related calculations are concerned is the change in fuselage length with the fuel mass. As the weight of the aircraft is determined iteratively, the length of the fuselage needs to be updated in every step. This is done automatically by moving the passenger cabin aft and forth and adding a cylindrical plug aft of the cabin to house a part of the aft tank if its length is too high to allow it to fit in the tail cone completely.

---

[3] As the federal aviation requirements stipulate that each engine has to be fed from its own dedicated tank during takeoff, a bulkhead is foreseen in each tank so that it is physically split in two (Brewer, 1991).

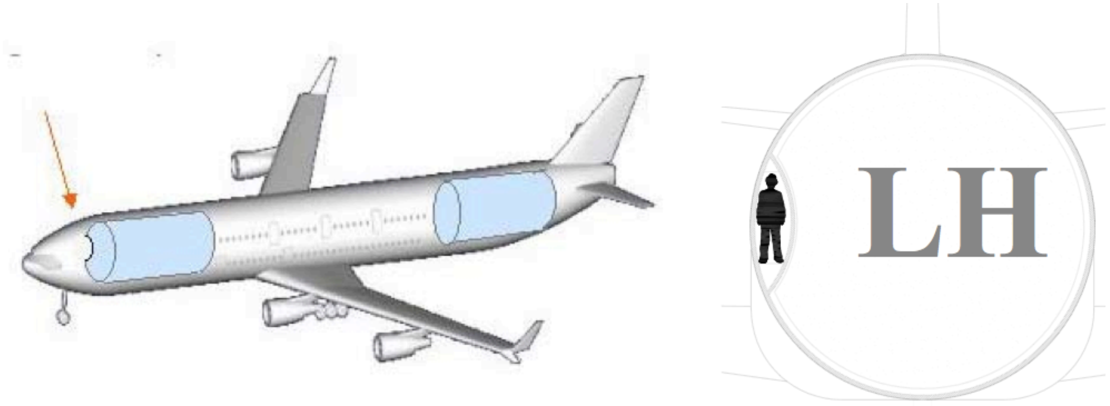

Figure 2.3. A cutout in the tank to provide access to the cabin, adopted from Astaburuaga et al. (2001).

2.3.1.2 Wing mass and flutter

As the fuel is no longer stored in the wing, the wing mass will be affected. After all for kerosene the fuel mass opposes the bending moment on the wing root due to the lift generated by the wing. This wing root bending moment alleviation will no longer be present when using hydrogen which will result in an increase in wing mass. In this work this has been accounted for by selection of proper correlations (from Jenkinson et al. (1999) and Howe (2000)) as reported in Appendix B. Both adopted correlations utilize a bending relief factor, originally implemented to account for the presence of wing mounted engines. Adaptation of the correlations to take the absence of fuel in the wing into account is straightforward and is thus not reported here (see Appendix B).

The fact that the fuel no longer is stored inside the wing however also has a consequence that is not so easy to account for. The fuel mass namely acts as a damper to aerodynamically induced vibrations of the wing, called flutter. As no data was found in literature describing the influence of fuel on wing flutter, this is not accounted for directly. Flutter correlations found in literature for kerosene fueled aircraft are generally based on statistics and can thus not be easily adapted to hydrogen fueled aircraft. However, the adopted correlations principally impose an upper limit on the usable lift coefficient (see Appendix B). As the fuel damping effect no longer is present it can be expected that flutter will occur at lower lift coefficients for hydrogen fueled aircraft. A variety of 'reduction factors' is thus applied in the hydrogen fueled case studies as reported in the next chapter. A rigorous analysis is however required for more detailed restrictions on the design space.

2.3.1.3 Impact of hydrogen on direct operating costs of the aircraft

As it is virtually impossible to accurately predict future fuel prices for both kerosene and hydrogen, this is bypassed here by assessing a range of prices for both fuels and calculating the direct operating costs (DOC) for all of them. This allows to determine the hydrogen price for a given kerosene price that results in the same direct operating costs.

However, not only the fuel cost will be different between kerosene and hydrogen. The aircraft acquisition and maintenance cost will most likely also change as a consequence of the differences between both fuels. This is accounted for in two different ways. In a first step, a general factor is imposed on the airframe acquisition and maintenance cost for the hydrogen fueled aircraft. This method has the advantage of simplicity and allows to get ballpark numbers for what if scenarios. It is assumed that the airframe maintenance and acquisition cost for hydrogen fueled aircraft is either 10% or 50% higher than the cost for the equivalent kerosene aircraft. The latter value is very unlikely but nonetheless gives an upper limit of the expected changes and indicates trends.

In a second step, the DOC calculation method from Burns (1994) is used to determine the aircraft acquisition cost as recommendations for its application to hydrogen fueled as well as unconventional aircraft are reported in Sefain (2005). These recommendations can be found in section of appendix B. As shown in the appendix, several factors need to be adapted which makes the method sensitive to the assumptions made for these factors. The method additionally requires the specification of a number of aircraft to be built which calls for further judging. Both methods are therefor used side by side.

2.3.2 Modifications to the turbofan design and performance tool

The thermodynamic changes by switching from kerosene to hydrogen are accounted for by importing the proper combustion gas properties data into the tool. This will not be reported here as it is described in Appendix C. Below the implications of the fuel switch on the amount of cooling air required to maintain the turbine metal temperature to a certain value are described first. A next subsection reports how the influence of the fuel injection temperature on the engine performance is taken into account. Finally the change in combustion chamber length is commented upon.

2.3.2.1 Cooling air

The cooling air fraction ψ for kerosene fuel is determined from the model given in Wilcock et al. (2005) as explained in section C.3.9. The model was adopted as it avoids the need for detailed calculations while still resulting in sufficiently accurate results to model the influence of an increase in turbine inlet temperature on the engine performance. In Wilcock et al. (2005), the following equation is proposed to calculate ψ:

$$\psi = \frac{\dot{m}_c}{\dot{m}_{tot}} = \frac{K_{cool}}{1+B} \cdot \left(\frac{\epsilon_0 - \epsilon_f \cdot \left[1 - \eta_{int} \cdot (1-\epsilon_0)\right]}{\eta_{int} \cdot (1-\epsilon_0)} \right) \tag{2.2}$$

where ϵ_0 is the blade cooling effectiveness, K_{cool} the cooling flow factor, η_{int} the internal cooling efficiency, ϵ_f the film cooling effectiveness and B a factor to account for the Biot number of both the blade metal Bi_{met} and the thermal barrier coating (TBC) Bi_{TBC}.

As explained in the Appendix the cooling flow factor K_{cool} was tuned in Wilcock et al. (2005) to engine data and values are proposed for the factor for different technology levels (see Table C.2). The factor is according to Wilcock et al. (2005) given as

$$K_{cool} = \left(1+\chi\right) \cdot \frac{A_{surf}}{A_g} \cdot \frac{c_{p,g}}{c_{p,c}} \cdot St_g \tag{2.3}$$

where A_{surf} denotes the blade surface area, A_g the exit flow area normal to the axial direction, $c_{p,g}/c_{p,c}$ is the gas to coolant specific heat ratio. χ is a factor to allow for other primary cooling flows (mainly end wall cooling), but does not consider secondary cooling flows for sealing, ... (Wilcock et al., 2005). St_g finally is the Stanton number of the gas flow:

$$St_g = \frac{h_g \cdot A_g}{\dot{m}_g \cdot c_{p,g}}$$

where $\dot{m}_g$ denotes the total combustion gas flow rate and h_g the mean convective heat transfer coefficient in the turbine.

As the combustion gases are different between hydrogen and kerosene, the amount of turbine cooling air needed might be affected. After all, the different composition of the gases would, according to Brewer (1991), lead to an increase in turbine life of about 25 to 30%. The changed combustion gases will however also modify the heat transfer which should be accounted for in the design. There is no carbon dioxide present which leads to a reduced luminosity of the combustion gases. However, there is a significantly higher water vapor level in the combustion gases. Chiesa et al. (2005) argue that replacing CO_2 by water vapor has no significant effect on the heat transfer at 1000°C and 10 bar. However, the turbines will operate at a wide range of temperatures and pressures, so a first order calculation to verify this statement is made here. To fully assess the difference a full blown CFD simulation should be made on a realistic geometry for different operating conditions. This is however considered to fall outside the scope of this work.

A simplified verification can be made by introducing the definition of the Stanton number in the definition of the cooling factor:

$$K_{cool} = \left(1+\chi\right) \cdot \frac{A_{surf}}{\dot{m}_g \cdot c_{p,g}} \cdot h_g \tag{2.4}$$

which shows that, for constant operating conditions (temperature, pressure and mass-flow rate) and the same turbine geometry (A_{surf}) K_{cool} is proportional to the convective heat transfer coefficient:

$$K_{cool} \propto h_g$$

The mean convective heat transfer coefficient can be determined from correlations depending on the geometry and the flow type (laminar or turbulent). Several correlations for gas turbines can be found in literature (amongst others Harasgama (1995), Louis (1978) and Rubini (2005)). In a rigorous assessment, different correlations should be used for the leading edge, the pressure side and the suction side and the transition from laminar to turbulent flow has to be taken into account (Rubini, 2005). As this requires detailed knowledge of the turbine which is not available here, two different correlations are adopted. Only turbulent flow is considered as this leads to a conservative estimate (Rubini, 2005).

The first correlation is taken from Rubini (2005) where the author indicates that it leads to a slight overestimation (and thus is conservative):

$$Nu_g = 0.235 \cdot Re_g^{0.64} \tag{2.5}$$

where Nu_g is the Nusselt number of the combustion gases and Re_g the Reynolds number. The Nusselt number is defined as

$$Nu_g = \frac{h_g \cdot c}{k_g}$$

where k_g is the thermal conductivity of the gas and the chord c is the representative length for the heat transfer phenomenon under investigation. The Reynolds number is on the other hand defined as

$$Re_g = \frac{\rho \cdot v \cdot c}{\mu_g}$$

where ρ is the density, v the airspeed and μ_g the dynamic viscosity of the fluid.

The second correlation used to verify the statement from Chiesa et al. (2005), is the correlation the authors used at 1000°C and 10 bar, which is derived from Louis (1978):

$$h_g = 0.285 \cdot \frac{\left(\rho \cdot v\right)^{0.63} \cdot c_p^{1/3} \cdot k_g^{2/3}}{d_{equiv}^{0.37} \cdot \mu^{0.7}} \tag{2.6}$$

where d_{equiv} is the equivalent diameter based on the wetted area of the turbine blade, ρ the density of the gases, v the main stream speed based on the cascade exit and c_p the specific heat at constant pressure.

Assuming that the operational conditions do not change when switching from one fuel to the other and that the turbine geometry does not change either, the ratio of the convective heat transfer coefficients can be determined. As the various properties of the combustion gases depend on the fuel to air ratio, a constant ratio for the FAR of the different fuels is assumed. Based on simulations of a GE90 like engine (see Verstraete et al. (2005a)) the ratio is set to

$$\frac{FAR_{kero}}{FAR_{H_2}} = 2.86$$

The results of the calculations are given for a wide range of turbine temperatures and fuel to air ratios (of kerosene) in Tables 2.2 and 2.3. Table 2.2 gives the results based on the correlation from Rubini (2005) whereas Table 2.3 is based on the correlation from Louis (1978). Even though not all combinations of TIT and FAR are realistic, the wide range is chosen deliberately to see the variations in the values with increasing temperature for a given fuel-to-air ratio or vice versa. After all, changing the overall pressure ratio of the engine will change the compressor delivery temperature which results in a variation of the amount of fuel required to obtain a given TIT.

A comparison between tables 2.2 and 2.3 shows that there is a big variation between the results for both correlations. The correlation from Louis (1978) in table 2.3 leads to a difference in cooling air requirements that can be neglected. It is only slightly over 1% higher for

Table 2.2. Ratio of cooling air for H_2 to cooling air for kerosene from equation (2.5).

TIT	**FAR**					
	0.005	**0.010**	**0.015**	**0.020**	**0.025**	**0.030**
1200	1.011	1.022	1.032	1.043	1.053	1.063
1300	1.012	1.024	1.036	1.047	1.059	1.07
1400	1.013	1.025	1.037	1.049	1.061	1.072
1500	1.013	1.025	1.037	1.049	1.061	1.073
1600	1.014	1.028	1.041	1.054	1.067	1.080
1700	1.014	1.028	1.042	1.056	1.069	1.082
1800	1.014	1.029	1.043	1.056	1.070	1.083
1900	1.016	1.031	1.046	1.061	1.075	1.089
2000	1.016	1.031	1.046	1.061	1.075	1.09

Table 2.3. Ratio of cooling air for H_2 to cooling air for kerosene from equation (2.6).

TIT	**FAR**					
	0.005	**0.010**	**0.015**	**0.020**	**0.025**	**0.030**
1200	1.002	1.005	1.007	1.009	1.011	1.013
1300	1.002	1.005	1.007	1.009	1.011	1.014
1400	1.002	1.004	1.007	1.009	1.011	1.013
1500	1.003	1.005	1.008	1.010	1.013	1.015
1600	1.002	1.004	1.006	1.009	1.011	1.013
1700	1.002	1.004	1.006	1.008	1.010	1.012
1800	1.002	1.005	1.007	1.009	1.012	1.014
1900	1.002	1.004	1.006	1.008	1.010	1.012
2000	1.002	1.005	1.007	1.010	1.012	1.014

extremely high fuel-to-air ratios. Table 2.2 on the other hand shows cooling air fractions that can be around 4% to 6% higher for typical operating conditions of modern turbofans. The increase is still moderate but can be considered to influence the engine performance. It should definitely be accounted for in a real engine design. The difference in the results for both correlations indicate that further research into this aspect is mandatory. To be conservative, the cooling factor K_{cool} is increased by a factor 1.06 compared to the values given for kerosene fuel in table C.2.

2.3.2.2 Hydrogen fuel injection temperature

In the description of the combustion chamber modeling in section C.3.4, the energy input of the (kerosene) fuel is implicitly considered to consist solely of its lower heating value (equation C.13). This assumption is valid since the fuel will be injected at temperatures near to its reference temperature (298.15 K) and the specific heat of kerosene is very small

(Hendrick, 2006). The error committed in neglecting the enthalpy of the fuel will therefor be negligible.

With hydrogen this is however not the case. Hydrogen namely has a very high specific heat, in the order of 10000 to 22000 J/kg/K (as shown on Figure A.2 in Appendix A and in ESDU (1961)). As it is stored at 20 K the hydrogen could furthermore also be injected at temperature much below the reference temperature at which the lower heating value has been defined. There is however a lower limit on the injection temperature that stems from the fuel controller for which the injection temperature needs to be higher than 150 to 250K, according to Corchero & Montañés (2003). Simon et al. (1994) also indicate that 150K is a compromise to ensure stable combustion while limiting the heat exchanger dimensions whereas Brand et al. (2003) mention that it is the lower limit to avoid large fluctuations in density and viscosity as well as partial liquefaction during expansion in the injector. In any case, the hydrogen needs to be pumped from the tank to the appropriate injection pressure through both a boost pump located in the tank and an engine-mounted pump (Allidieris & Janin (2002a) and Brewer (1991)) which will make its temperature rise. It is furthermore very likely that the fuel will be passed through and oil cooler and a heat exchanger to reduce the temperature of the air bled for cabin pressurization as shown on Figure 2.4 (Brewer, 1991). All of these will rise the temperature of the hydrogen from about 20 K close to the 150 K minimum.

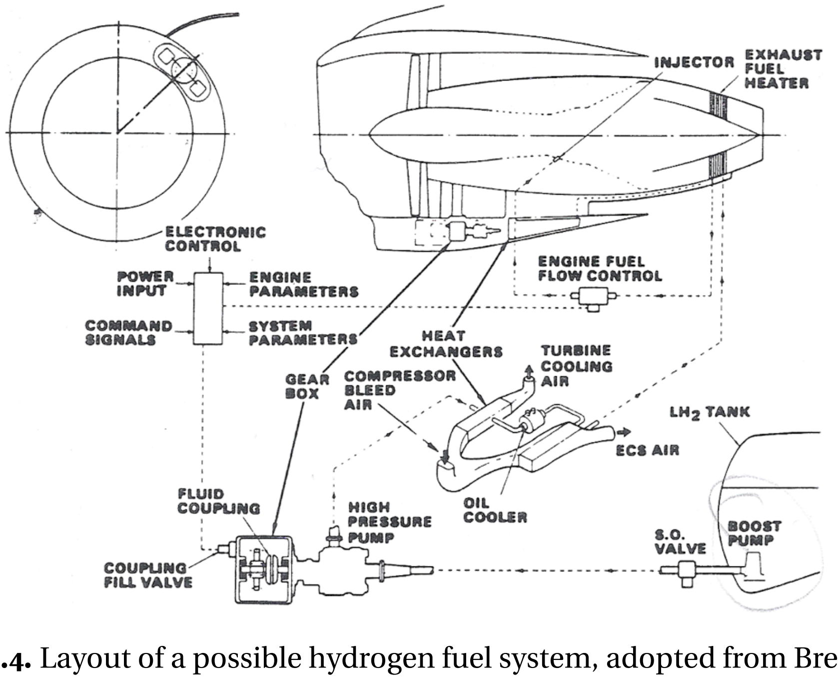

Figure 2.4. Layout of a possible hydrogen fuel system, adopted from Brewer (1991).

In unconventional cycles a combustion chamber injection temperature as high as 600 K could be reached through the introduction of heat exchangers in strategic locations to improve the engine performance (Boggia (2000), Boggia et al. (2001), Brewer (1991) and Svensson (2005)). For both extremes, the enthalpy of the hydrogen fuel flow thus has to be considered in the calculations, as is also pointed out in Corchero & Montañés (2003). The enthalpy difference is adopted here from NIST (2007). As the combustion gas properties were derived for normal hydrogen through CEA, the enthalpy difference is also taken for the normal hydrogen for reasons of consistence. As explained in Appendix A, an error is introduced by this assumption which is however small for the temperature range envisaged in this work.

2.3.2.3 Combustion chamber length

As the flame speed of hydrogen is several times higher than that of kerosene (see Appendix A), the combustion chamber length could be significantly reduced to bring NO_X emissions down to a level that is substantially lower than for kerosene combustion chambers as shown in Chapter 1. NO_X levels are after all proportional to the residence time in the combustion chamber, whereas they increase exponentially with flame temperature (Lefebvre, 1999). As hydrogen has very wide flammability limits which allow lean burning in the combustion chamber much more easily than for kerosene, NO_X emissions would be lower than for kerosene even if the relative residence time would be increased (see Figure 1.3). Nonetheless the length should be reduced to exploit this to the fullest.

As the final length of the combustion chamber is hard to predict, the fraction of the total engine length that is allocated to the combustion chamber in the gaspath analysis is not changed here. All in all, this is slightly conservative as it will increase the hydrogen fueled engine length slightly thereby increasing its drag. The influence on the final results will however be small.

2.4 Conclusions

This chapter gives a general overview of the implications of the adoption of hydrogen on the aircraft and engine design and performance. It is shown that the utilization of hydrogen as a fuel entails both benefits as well as drawbacks. The main benefits for both engine and aircraft are related to the high lower heating value of the fuel. This results on the one hand in a lower fuel mass and as a consequence also in a lower structural and overall mass of the aircraft. It allows on the other hand to use smaller and quieter engines.

The main drawback of hydrogen is its low density, even if stored as a cryogenic liquid. This results in bulky and heavy fuel tanks that need to be accommodated in the fuselage rather than in the wing. For the long range transport aircraft under investigation the preferred storage option is to locate one tank in front of the passenger cabin and one aft of the cabin. This is done to obtain an appropriate location of the center of gravity. Both Astaburuaga et al. (2001) and Brewer (1991) use a distribution of about 40% of the fuel in the front tank and 60 % in the aft tank. This will be retained here.

After this general overview, the required modifications to the tools developed for the conceptual design of the aircraft and the performance assessment of the engines are detailed. The tools themselves are not detailed here. A description of them can be found in Appendix B and C. The main changes for the aircraft are the longer fuselage length to accommodate the fuel tanks and a slight increase in wing weight due to the absence of the wing root bending moment alleviation by the fuel. As it is outside the scope of this work to assess the impact of the absence of the fuel in the wing on wing flutter, the design point of the studies will be located away from the boundary imposed for kerosene fueled aircraft. A similar simplification is adopted to account for the effect of hydrogen (and kerosene) fuel price. The price of both fuels is varied and the equivalent price, leading to the same DOC is determined. As these DOC depend on aircraft acquisition cost which will be different, two different approaches for this 'problem' have been proposed as well.

CHAPTER

3

Liquid hydrogen tanks

As was pointed out in the very first studies on liquid hydrogen for aviation, one of the key factors to enable the utilization of hydrogen as an aircraft fuel is the design of adequate hydrogen tanks (Silverstein & Hall, 1955). Even nowadays, the design and development of durable, lightweight, highly insulated cryogenic propellant storage and feed systems is still regarded as one of the crucial technical challenges confronting use of LH_2 in operational aircraft (Allidieris & Janin (2002b), Brewer (1991) and Mital et al. (2006)). After all, this type of tank currently does not exist as cryogenic LH_2 tanks for space applications are designed for a very short tank lifetime and a limited number of cycles. Space tanks furthermore require the propellant to be stored and maintained for a relatively short period, as it is consumed rather quickly. Because of the short cycle time, a higher boiloff rate is acceptable for the tank. Space shuttle operation, for instance, accepts a loss rate of approximately 1.6 % of LH_2 by weight per hour. For an aircraft operation, however, acceptable boiloff rates are in the order of 0.1 % by weight per hour or less (Mital et al., 2006). Automotive applications are, on the other hand, much less influenced by weight limitations, which leads to relatively heavy designs that are not suited for aeronautical applications. Some preliminary designs have been done for reusable space vehicles (Heydenreich (1998), Robinson (1994) and Robinson et al. (2002)), but to the authors knowledge, none have been built and successfully tested for several cycles so far.

Liquid hydrogen tanks furthermore intensify the link between aircraft and engine, who's designs are already closely coupled for conventional aircraft and fuels. It is thus considered mandatory to have a sufficiently detailed tank model that allows to perform the proper tradeoff studies. After all, the tank design depends on both aircraft and engine. The aircraft (fuselage) namely sets an upper limit on the tank diameter whereas the aircraft-engine combination will determine the amount of fuel to be stored and hence the tank length (for a given diameter). The fuel flow rate required by the engine will furthermore play a key role in the optimum tank design as it sets the required insulation thickness, as will be shown in this chapter.

Below, the routine developed to analyse the trade-offs in cryogenic LH_2 aircraft tanks is described. In sections 3.1, 3.2 and 3.3, the structure of the tank as well as the insulation and tank wall materials are selected based on a literature review of conceptual tank designs. Then, the sizing methods adopted in this work are given (section 3.4). The mechanical and thermal design methods are described and the tank pressure rise and volume determination are elucidated (section 3.5). In a final section (3.6) designs are presented for a regional airliner and for the large long range transport aircraft which form the subject of the next chapter of this thesis.

3.1 Selection of the tank configuration

Several different types of cryogenic hydrogen tanks can be envisaged for aeronautical applications. As it is not feasible within the scope and timeframe of this work to make an analysis of all possible types, a preselection is made first. Even though hydrogen could be stored as a gas under pressure, as a hydride or in slush form[1], here only liquid hydrogen will be considered. All other storage forms appear to be impractical for the type of aircraft under investigation because of their excessive weight or volume (Allidieris & Janin (2002a), Allidieris & Janin (2002b), Brewer (1991), Mital et al. (2006) and Westenberger (2003b)).

Two possible types of liquid storage are nonetheless possible: a supercritical liquid or a saturated liquid. To store the hydrogen as a supercritical liquid, pressures over 13 bar are needed to obtain a single phase fluid. The heavier tank design as well as the more complex ground operations at higher pressure lead to the rejection of supercritical hydrogen in the Cryoplane project (Westenberger (2003b)). When stored as a supercritical liquid, the storage pressure furthermore increases about 10 times faster for a given heat input Allidieris & Janin (2002b). Therefore, the only remaining possibility is to store the hydrogen as a saturated liquid, at a combination of temperature and pressure where the vapor is saturated and in equilibrium with its liquid.

3.1.1 Integral or non-integral tanks

Even though, compared to kerosene, a relatively small mass of fuel needs to be embarked for a given mission due to the high lower heating value of hydrogen, its low density will result in the need for a large tank volume. Successful configurations will require innovative designs with small frontal and surfaces areas as well as minimal weight. At first sight, either integral or non-integral tanks could nonetheless provide these features.

---

[1] In the Cryoplane project, the consequences of the adoption of slush hydrogen on aircraft design, performance and economics were assessed based on a practical slush of 50 % solid in terms of mass at a temperature of -260°C (Westenberger, 2003b). Due to the higher density, a 20 % smaller tank volume was possible compared to LH_2 while the higher heat capacity of the slush also allows to reduce the insulation thickness and weight. However, due to the higher production costs (in the order of 8 to 17 %) and the correspondingly higher fuel cost, a direct operating cost reduction compared to LH_2 was not clearly identifiable. It was therefore concluded that the use of slush hydrogen does not offer a convincing advantage to justify major dedicated efforts.

Non-integral tanks serve only as fuel containers and are mounted within and supported by a conventional fuselage skin/stringer/frame structure. Consequently, they only have to bear the loads associated with the fuel containment, i.e. pressurization and fuel dynamic loads, plus thermal stresses.

Integral tanks, on the other hand, form an integral part of the basic airframe structure. They must thus be capable to withstand all the usual fuselage axial, bending and shear stresses resulting from the critical aircraft loading conditions in addition to the above loads. Since the external surface of the integral tank design is not protected by the fuselage structure, as it is in the non-integral case, a protective layer needs to be provided over the insulation. This extra shield brings protection from aerodynamic heating as well as from the air loads, which could otherwise inflict structural damage on the insulation.

As shown in Table 3.1, the potential of integral tanks is superior to that of the non-integral tanks. The integral design namely has a greater structural efficiency, which yields a direct weight saving for the aircraft. It additionally has a higher volumetric efficiency, leading to a lower drag and thus a further weight saving. In addition, the tank/fuselage structure as well as the insulation of the integral design is more readily accessible for inspection and repair. Any repairs required for the non-integral type would necessitate removal from the airplane. Local repairs on the integral tank can, on the other hand, be carried out by simply removing the skin in the area requiring attention (and the thermal protection system if external insulation is adopted) (Brewer, 1991). For all these reasons, the integral tank concept is selected in this work as was also the case in and Allidieris & Janin (2002b), Allidieris & Janin (2002a), Brewer (1991), Brewer et al. (1975a), Brewer et al. (1975b) and Brewer et al. (1978).

Table 3.1. Comparison of tank structural concepts, adopted from Brewer (1991).

	Nonintegral	**Integral**
Fuel weight fraction (lb/lb of LH_2)		
Tank[a]	0.113	0.196
Thermal protection system	0.079	0.060
Heat shield	0	0.060
Fuselage structure	0.152	0
Total	0.344	0.316
Volumetric efficiency[b]	0.855	0.927
Accessibility for inspection / repair	removal of tank	removal of heat shield

[a] Based on a 40000 psi (275.8 MPa) allowable stress

[b] Volume available for LH_2 divided by volume of fuselage section

3.1.2 Tank shape

As the integral tank concept is selected, the geometry of the tank needs to be adapted to the shape of the fuselage in a way that provides a good use of the total free space.

Therefore, only spherical or cylindrical tank shapes with a diameter equal to the fuselage diameter are possible[2]. Spherical shaped tanks provide minimum surface area for a given volume, which minimizes the passive heat flux into the tank and thus also the boil-off of LH_2. However, the spherical shape poses manufacturing problems and has a higher frontal surface area, resulting in higher drag forces compared with a cylindrical-shaped tank (Mital et al., 2006).

Cylindrical tank shapes are on the other hand easier to manufacture but have a higher surface area to volume ratio thus resulting in a higher passive heat load into the tank. As they are however easier to integrate into the tubular fuselage, they offer a higher volumetric efficiency. For those reasons, cylindrically shaped tanks are adopted in this work. As the aft tank is located in the tail cone, it will however not be purely cylindrical but conical to comply with the shape of the aft fuselage. A weight penalty and increase in length is applied to the aft tank to account for this, based on Brewer (1991).

3.1.3 Internal or external insulation?

If cryogenic insulation is applied to the inside of the tanks, the tank walls will remain at near-ambient temperature, which minimizes the differential thermal expansion relative to the warm aircraft skin and primary structure. Similarly, the problems of attachment and support for the tanks are simplified. The difficulty for internal insulation is that the insulation system must be impermeable to GH_2. As the insulation is continuously exposed to hydrogen, diffusion of GH_2 to the tank wall would namely raise the thermal conductivity of the insulation to that of GH_2, thereby crippling its effectiveness.

If the insulation is applied to the exterior surface of the tanks, the tank structure will significantly expand and contract as LH_2 is introduced and used. Attachment problems for the structural support system are therefore severe, not only because of the dimensional changes that must be accounted for, but also because of the potential for thermal leaks. External insulation is also more susceptible to mechanical damage. In addition, it must be impervious to air. Although this is a far less demanding requirement to meet than that faced by internal insulation, it is still mandatory to prevent cryo-pumping, a process that ultimately would result in air filling the insulation, which destroys its effectiveness.

Brewer and his team (Brewer (1991) and Brewer et al. (1978)) selected an external isolation because of the difficulty of meeting the requirement for a liner impervious to gaseous hydrogen if internal insulation is used. Air Liquide also only considered external insulation for the Cryoplane project (Allidieris & Janin, 2002b). The same approach will therefore be adopted here.

---

[2] In the initial phases of the Cryoplane project, tanks on top of the fuselage and in the wing were proposed. This solution maximized the carrying capacity but was rejected later on in the project, as the shapes are not well adapted to the pressurization requirement and would lead to heavy and thick tank walls and many stiffeners (Allidieris & Janin, 2002a).

3.2 Selection of the tank materials

The hydrogen fuel is thus considered to be stored in integral, cryogenic LH_2 tanks with external insulation. However, the design of a lightweight cryogenic LH_2 storage tank involves many challenges in selecting the proper materials. The main challengers are concisely reviewed below. Then, a selection of classes of materials is made for both the tank wall as well as the insulation. Finally, the materials that will be analyzed in detail are picked from the previously selected groups of materials.

3.2.1 Key challenges for cryogenic LH_2 tanks

The key material issues for cryogenic hydrogen tanks include the temperature at which the hydrogen needs to be stored, permeation of hydrogen through the tank walls and hydrogen embrittlement issues. The importance and the implications of these key challenges are briefly commented upon below.

3.2.1.1 Cryogenic Temperature

The normal boiling point of liquid hydrogen is -252°C thus the LH_2 inside the tank needs to be kept at the lowest possible temperature to minimize boil-off. Vaporization of the fuel namely implies a loss of usable fuel as the pumps inside the tanks should be designed to cope with liquid only to ensure continuity of the fuel flow (Allidieris & Janin (2002b) and Brewer (1991)). The boil-off furthermore leads to an increase in pressure inside the tanks which will only be designed for a relatively low burst pressure to keep the weight as low as possible.

During both the ground operations as well as the flight, the temperature difference between the inside and the outside of the tank is thus expected to be in the order of 250-300°C. A lightweight, low-conductivity insulation is obviously necessary to maintain such a large temperature gradient. After all, for long duration flights, excessive boiloff is undesirable and could limit the aircraft range. In addition, the tank and any connecting lines or attachments will need to be completely isolated from the outside atmosphere because all gases, with the exception of helium, solidify at the temperatures of LH_2 and raise the potential for obstructing the flow lines and other components (Brewer et al., 1978). Finally, frost buildup on the aircraft skin needs to be avoided too, as it would lead to a significant increase of the aircraft drag.

3.2.1.2 Permeation

As hydrogen molecules are very small, they are extremely prone to permeating through the tank wall. According to Mital et al. (2006), the permeation by hydrogen might be the most critical issue in the tank design. Metallic tanks are an obvious solution to this problem, as hydrogen permeates through metals at a much slower rate than through the nonmetallic materials. However, the mass of a metallic tank will be higher than that of its composite counterpart, which could limit the payload capability and/or range of the aircraft. A polymer matrix composite (PMC) tank using a thin liner would also solve the permeability problem, but weight could still be an issue (Mital et al., 2006). Furthermore, the coefficient of thermal expansion mismatch between the composite tank wall and the metallic layer will make them to contract differently, possibly inducing stresses. This could result in separation of the liner from the tank and/or fracture of the liner or tank[3]. Lately, there have been some studies to evaluate polymeric films and coatings that could be applied to the composite inner skin and act as a barrier to contain the LH_2 in the tank (Mital et al., 2006).

3.2.1.3 Hydrogen embrittlement

Many materials become embrittled when exposed to hydrogen in large concentrations and under tensile stresses. As the material becomes more brittle, its reliable load-carrying capacity and ductility are reduced. As hydrogen embrittlement can result in cracking at stress levels significantly below yield stresses, a catastrophic failure could occur without significant deformation or obvious deterioration of the structural components. Even though all materials are to some extent susceptible to hydrogen embrittlement, high-strength alloys and in particular high-strength steels are known to be very prone to this type of material deterioration (Stroe (2005) and Thompson (1980)). Aluminum, on the other hand, is one of the few metals known to show only minimal susceptibility to hydrogen embrittlement due to its face-centered cubic structure, which minimizes the solubility of hydrogen and reduces the speed at which hydrogen molecules move through the lattice (Dieters (1986), NASA (1997), Zielinski (2001) and LLNL (2008)).

The low strength aluminum alloys 2024 and 6061 are for instance particularly recommended in the nuclear industry (LLNL, 2008) as materials for high-pressure hydrogen gas pressure vessels. The 5086 (Al-Mg) alloy is recommended in NASA (1997) for use with liquid hydrogen as the material remains ductile at the low temperatures associated with the cryogenic storage of the liquid hydrogen. The alloy is also recommended in the Cryoplane project even though alloy 5083 is claimed to have better characteristics after welding (Allidieris & Janin, 2002a). Additionally, alloy 2219 is also suggested in the project as it is used by Air Liquide in the construction of the LH_2 and LOX tanks for the Ariane 4 launcher. The material is however not accepted by the European pressure vessel codes (Allidieris & Janin, 2002a). However, even though aluminum alloys are in general less susceptible, the proper heat treatment still needs to be applied to the material. The ductility loss is namely most severe for under-aged tempers, intermediate for peak strength tempers and minimal for over-aged tempers (Thompson, 1980).

Hydrogen embrittlement is a reversible process. The absorbed hydrogen can be baked out of the material by the proper heat treatment at the temperature corresponding to the trapping sites of hydrogen in the particular alloy under consideration (Zielinski, 2001).

---

[3] The failure of the X-33 demonstrator was, according to Mital et al. (2006), thought to be initiated by the microcracking of the polymer matrix in the composite inner skin, which resulted from the coefficient of thermal expansion mismatch between the carbon fibre and the polymer matrix.

During the life of the aircraft tanks, possible embrittlement problems might thus be cured at the expense of an increased maintenance cost.

3.2.2 Preliminary material selection

Before down-selecting materials for the insulation and the tank walls, groups of materials are selected based on the required functionality. For both the insulations as well as the tank walls, two groups of materials are chosen to enable a comparison of the final tank designs for each of the groups. Below, the selection procedure as well as the groups of materials picked out is described. First, the insulation materials are reviewed. Then, the tank wall material selection is described.

3.2.2.1 Insulation materials

An efficient and lightweight insulation system is of prime importance for LH_2 storage tanks, especially for long-duration applications, as it will minimize the boiloff of LH_2 while adding minimum mass to the overall tank structure. The insulation system and its key constituents should furthermore possess a low thermal conductivity along with low thermal diffusivity and low mass density (Mital et al., 2006). The conductivity k needs to kept as low as possible to minimize the steady state heat flux into the tank. The thermal diffusivity a , on the other hand, is an indication of the time required to reach this equilibrium condition. The lower the thermal diffusivity, the longer it takes for the thermal energy to reach the cryogenic fluid. After all, the time required to reach steady state t for a given wall thickness t_{wa} and diffusivity a is given by:

$$t = \frac{t_{wa}^2}{2 \cdot a}$$

The thermal conductivity and diffusivity also determine the amount of energy stored in a material for a given temperature rise and time. Minimizing the ratio $k/\sqrt{a}$ namely results in maximizing the energy stored.

Figure 3.1(a) shows the thermal conductivity of various material groups versus their mass density, as the low weight requirement is crucial for an aviation application. The figure indicates that low densiy polymer foams are the most suited candidates from the conductivity and mass point of view. Additionally, so-called multi layer insulations (MLI) combined with a vacuum jacket have a range of densities that is comparable to low density foams and an apparent thermal conductivity that is approximately two orders of magnitude lower than the best low-conductivity foams (beyond the range of Figure3.1(a)).

Figure 3.1(b) shows thermal conductivity versus thermal diffusivity while figure 3.2 gives thermal conductivity versus thermal expansion coefficient α for the different material classes, which is an indication of the degree of thermal distortion of the material. Materials with a high value of k/α namely show small thermal distortions. As insulation materials have a low thermal conductivity by their functionality, they in general show relatively large thermal gradients and consequently high thermal distortions and thermally

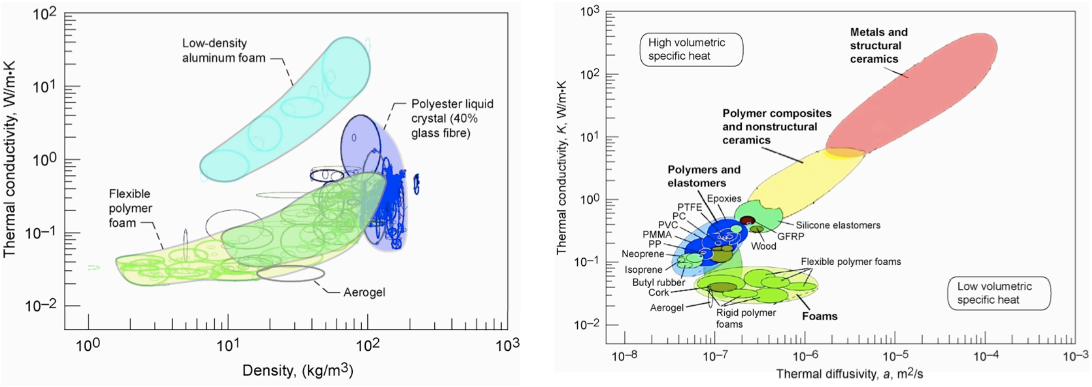

(a) k versus ρ (b) k versus a

Figure 3.1. Thermal properties of various engineering materials, adopted from Mital et al. (2006) based on Ashby (2005).

induced stresses. Once a given class of materials is chosen based on their thermal performance, materials with the lowest value of the thermal expansion coefficient α should thus be used to minimize the thermal distortion.

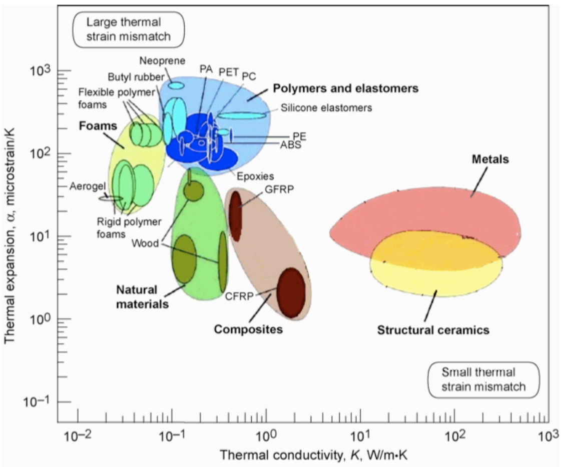

Figure 3.2. Thermal conductivity versus thermal expansion coefficient for various engineering materials, adopted from Mital et al. (2006) based on Ashby (2005).

It can be noted from Figures 3.1 and 3.2 that various foams, aerogels and MLI systems have the most desirable material properties for aerospace applications. This is confirmed by the selection of foams, aerogels, vacuum jackets and MLI systems for cryogenic insulation systems in previous investigations[4] (Allidieris & Janin (2002b), Brewer (1991) and

---

[4] Powders or fibres under vacuum were also considered in the Cryoplane project but they were discarded as being too heavy (Allidieris & Janin, 2002b). Brewer and his team, on the other hand considered micro-spheres as being excellent candidates (Brewer, 1991). As micro-spheres also require a (mild) vacuum but offer a lower thermal performance than MLI, they will not be considered here. After all, Brewer and his team selected micro-spheres because, at the moment of their study, NASA had an interest in acquiring more insight in their functionality and application despite offering a slightly worse performance than MLI (Brewer, 1991).

Brewer et al. (1978). Table 3.2 shows a list of advantages and disadvantages of the various insulation 'methods' in the order of increasing thermal performance.

Table 3.2. Advantages and disadvantages of various insulation methods, adopted from Mital et al. (2006).

Foams	
Advantages	Currently in use, well established
	Low cost, easy to implement
	Light weight and low density
Disadvantages	Relatively high thermal conductivity
	Low resistance to thermal radiation
	Potential damage from environmental hazards
Aerogels	
Advantages	Extremely low thermal conductivity[a]
Disadvantages	New material, not well characterized
	Limited mechanical properties
Vacuum	
Advantages	Near zero thermal conductivity
	Well established
Disadvantages	Heavier tank walls required
	Costly to implement and maintain
	No resistance to radiation heat transfer
	Near catastrophic failure upon loss of vacuum
Multi Layer Insulation	
Advantages	Very low thermal conductivity and radiation heat transfer[b]
	Extremely low density
	Well established
Disadvantages	High vacuum required
	Heavier tank walls required
	Costly to implement and maintain
	Near catastrophic failure upon loss of vacuum

[a] The balance between structural an thermal properties can be altered to optimize for the application.

[b] MLI is available in graded form to improve the thermal properties and to reduce the density, but at a higher cost.

As Table 3.2 shows, low-density polymer foams are amongst the most suited candidates from the conductivity and mass point of view. MLI combined with a vacuum jacket have, on the other hand, a range of densities that is comparable to low density foams and an apparent thermal conductivity that is approximately two orders of magnitude lower than the best low-conductivity foams (Mital et al., 2006). Low-density aerogels in a flexible fibrous matrix offer on their turn a relatively low heat transfer, a great ease of use and maximum longevity (Allidieris & Janin, 2002b). These aerogels are produced by liquid-to-gas drying of wet silica gel (Milliken et al., 2002). Below the different classes of materials are briefly described.

Several families of open and closed-cell foams are suitable insulations for aeronautical applications. Flexible open-cell thermo-formable polyimide foams offer the possibility to insulate more complex shapes easily. They are namely readily adaptable to these complex shapes and can easily be applied as they are thermo-formable. As the foams have open cells, the risk of cryo-pumping however has to be taken into account (Allidieris & Janin, 2002b). Polyurethane and polyisocyanurate foams are rigid and not thermo-formable, which makes their use delicate (Allidieris & Janin, 2002b). Nonetheless, the still are excellent candidates for this application (Brewer, 1991). The Rohacell closed-cell polymethacrylimide foam is on the other hand rigid and thermo-formable, although the thermoforming is delicate (Allidieris & Janin, 2002b).

As shown on Table 3.2, silica aerogels have a slightly better thermal performance than foams. They are high-porosity, very low-density solids that consist of interconnected particles that form an open microstructure. The thermal conductivity of silica aerogels tends to be very low, typically less than 0.040 W/(m·K), due to the very low thermal conductivity of silica as well as the pore sizes that are on the order of nanometres (Mital et al., 2006). However the high porosity and low density, which makes them good insulators, also make the aerogels inherently fragile and brittle. Thus, their use in load-bearing applications as aircraft fuel tanks is far from obvious. Nonetheless, at the moment research is going on to improve the mechanical properties of aerogels without sacrificing their thermal properties (Allidieris & Janin (2002b) and Mital et al. (2006)). In the future, they might thus become interesting for aircraft cryogenic insulations. In this work, they will however not be taken into further consideration.

Multi layer insulation systems use a number of thermal radiation shields perpendicular to the direction of the heat flow. The radiation shields are alternating layers of a low-emissivity metal foil (often aluminized or goldized Mylar (polyester) or Kapton (polyimide)) and a thin insulating spacer (usually polyester, glass fibre paper, silk tissue or Superfloc separators), combined to avoid metal-to-metal contact. To minimize the heat transfer by residual gas conduction, the system has to operate at vacuum levels below 13 mPa (Mital et al., 2006). The metal foils are perforated to allow evacuation of residual gases when setting up the vacuum. Even though MLI insulations offer the potential to obtain a heat flow roughly two orders of magnitudes lower than foams, its performance strongly depends on the pressure and type of residual gas in the insulation. The thermal performance of the MLI degrades quickly for pressures higher than 0.001 mbar (Allidieris & Janin (2002b) and Nast (1998)). MLI insulations are furthermore very sensitive to the layer density (number of layers per unit of thickness) so that local compressions must be avoided during manufacturing. However, some MLI are less sensitive to this compression phenomenon than others. The high thermal conductivity of the reflecting screens makes heat transfer parallel with the layers approximately 1000 times larger than the normal heat transfer.

As illustrated, a low thermal conductivity, low emissivity and a low mass density are the most important parameters for an insulation system used in relatively long-term aeronautical applications. In addition, low thermal diffusivity, a low coefficient of thermal expansion and the ability to accommodate the thermal distortions induced by large thermal gradients are important too. Based on these arguments, the current state of the art suggests that the use of a high vacuum with highly polished wall surfaces with or without an MLI system could provide the required insulation needs for lightweight long-term cryogenic applications. Seen the importance of radiation, only vacuum insulations with MLI will be considered here, despite their slightly higher cost over simple vacuums.

However, this type of system is very sensitive and dependent on maintaining a very high level of vacuum. Any degradation in the vacuum level significantly degrades the insulating properties, which could lead to a mission failure. Allidieris & Janin (2002b) shows that in case of vacuum break venting of boiled-off hydrogen will be necessary after two minutes at a rate around 8-15 times the cruise fuel consumption of the engines. Therefore, foam based systems will also be evaluated for the designs under consideration. After all, the use of closed-cell foams only requires a single tank wall while MLI systems need two relatively thick walls due to the required vacuum. This weight advantage could therefore offset the disadvantage of the thicker insulation due to the relatively high thermal conductivity of foams.

3.2.2.2 Structural tank wall materials

Materials that possess high strength, high fracture toughness, high stiffness as well as low density and low permeation to LH_2 and GH_2 are needed for the tank wall construction. However, no single material provides all these attributes simultaneously. Even though strength and density tend to dominate the design criteria, fracture toughness (K_{Ic}) (and damage tolerant design) becomes an issue especially at cryogenic temperatures, where many materials become brittle. For this application, this is even more critical as any crack that propagates the insulation system can compromise the thermal properties of the insulation system and lead to rapid boil-off of the cryogenic fuel, resulting in the loss of the mission (Mital et al., 2006).

Two fracture toughness related performance indices need to be considered for the tanks, namely yield-before-break, K_{Ic}/σ_f, and leak-before-break, $K_{Ic,2}/\sigma_f$ Mital et al. (2006). The first index ensures that the stress required to propagate a critical flaw is greater than that to yield the material. The vessel would thus deform stably in a way that could be detected. The second criterion, used primarily on larger vessels, ensures that maximum pressure carried would result in the stable growth of a crack just large enough to penetrate both the inner and outer surface so that the leak could be detected prior to catastrophic failure.

Mital et al. (2006) show that the choice of the material to minimize the mass of a spherical tank may be limited by the ability to detect a crack of a given size if both the wall strength and the fracture toughness are not to be exceeded. If only cracks larger than 5 mm can be detected, the material choices will be limited to monolithic metallic alloys, while composites could be viable materials if cracks of 5 μm or larger could be detected (Mital et al., 2006). Polymer matrix composites (PMC) and metal matrix composites (MMCs) are both viable candidates if small cracks can be detected. Metals that have acceptable properties from ambient to cryogenic temperatures on the other hand include austenitic stainless steels, monels and aluminum alloys (Reynolds (1955) and Mital et al. (2006)).

Composite materials offer lower density and higher strength and stiffness than metals used for cryogenic applications and are quite suitable for (short duration) aerospace applications. Mital et al. (2006) indicate that continuous-fibre-reinforced polymers (CFRP) provide the highest strength yet lightest choice. However, the use of CFRP materials will most likely involve higher initial manufacturing costs for the tanks. Discontinuous reinforced metallic composites (DRX), and specifically discontinuous reinforced aluminum (DRA) are identified as lower cost alternatives, as they can be cast. The DRX materials furthermore have the additional benefit of extremely low (if not negligible) hydrogen gas permeability issues (Mital et al., 2006).

Because of their lower density and higher strength, composites offer a potential weight saving. Sharke (2004) reports a 25 % weight saving relative to the latest monolithic aluminium tanks. However, the resins used with PMCs do tend to enable higher hydrogen permeation than metals (Mital et al., 2006). Brewer (1991) notes that filament wound composite structures had not been used for hydrogen tanks due to hydrogen diffusion through the interstices of the bounding material over long durations. Robinson et al. (2002) on the other hand report that, based on results from initial studies, hydrogen permeability was not believed to be a technical barrier to the development of an unlined composite tank[5]. However, the design of unlined composite tank will entail significant non-recurring costs to develop and produce the tank. For space applications, the weight savings resulting from the composite tank will justify extremely high development and production costs (Robinson et al., 2002). It is however not clear whether the same will apply for aircraft applications and a detailed cost study would have to be executed to verify this. Heydenreich (1998) also indicates that the cost of composite tanks will probably lead to Al-Li tanks for aircraft.

The use of monolithic metals, on the other hand, eliminates thermally induced internal stresses due to different coefficients of thermal expansion (CTE) such as the typical constituents of a PMC or MMC materials. Furthermore, as the metallic materials are generally well characterized the safety factors can be smaller than for the newer advanced composite materials. The wide temperature and moisture range in which the composite materials will be used, will even further raise the safety factor Mital et al. (2006)

3.2.3 Properties of the selected materials

In the previous section, foam and MLI insulations were selected as the prime insulation candidates while monolithic metals and composites are chosen for the tank walls. Below, some specific materials will be picked from these groups of materials for further analysis.

---

[5] In the Space Launch Initiative (SLI) a reusable composite tank for the X-33 was designed, built and tested. The tank failed during the high-profile ground test and the failure was at first believed to be material related (permeability issues). Robinson et al. (2002) however report that the problems on the X-33 tank were design and manufacturing flaws and that it is possible to build a good tank with the IM7/977-2 material that was used for the tank that failed the test.

The criteria used in this selection as well as the characteristics of the chosen materials are reported below.

3.2.3.1 Foam Insulations

Within the class of foam insulations, different materials exist that could be suited for the application under consideration. In the Cryoplane project, Air Liquide analyzed and tested 34 foams in several families of polymers, taking density, conductivity, thermal stability as well as mechanical properties into account (Allidieris & Janin, 2002b). Three open-cell polyimide foams, one closed-cell polymethacrylimide foam (Rohacell) and one spray on foam were recommended for aircraft applications in addition to the H920.A foam , the rigid closed-cell PVC foam used on the Ariane 4 and 5 launchers. Lockheed-California conducted a similar study, which was mainly focused on polyurethane foams (Brewer (1991), Brewer et al. (1975a), Brewer et al. (1975b) and Brewer et al. (1978)). Taylor (2003) shows that temperature will not be an issue as polyurethane foams can withstand temperatures up to almost 80°C (175°F). Sharpe & Helenbrook (1978) furthermore indicate that polyurethane foams form excellent candidates for aircraft because of their excellent cyclic behaviour. After submitting several foams to about 4000 thermal cycles (around 14 years), typical for aircraft fuel tanks, the polyurethane foams showed hardly any degradation both mechanically as well as thermally. The Rohacell foam on the other hand failed structurally but showed no significant degradation of its thermal characteristics, even after structural failure.

Based on the available material characteristics, two different foams are selected for further analysis: Rohacell and a polyurethane foam. This namely allows a comparison between two different families of foams. Figure 3.3 shows the variation of the thermal conductivity of the two foams with temperature. The density of the Rohacell foam is taken as 51.1 kg/m^3 (Allidieris & Janin, 2002b) while the polyurethane foam has a density of 32 kg/m^3 (Brewer, 1991).

3.2.3.2 Multi Layer Insulations

As mentioned previously, multi layer insulations consist out of alternating layers of a low-emissivity metal foil and a thin insulating spacer. To minimize the heat transfer by residual gas conduction, the system has to operate at vacuum levels below 13 mPa (Mital et al., 2006). Several materials are available for both the radiation blanket as well as the spacer and the material choice obviously has an important effect on the thermal performance of the MLI.

A big range of thermal properties is reported in literature and, due to a lack of extensive experimental data (available), a selection of the most appropriate correlation is not straightforward. After comparison of the different models available, a general equation that can be tuned to the specific multi layer insulation under investigation was adopted (Johnson et al. (1974), Hastings et al. (2004), Hedayat et al. (2000) and Nast (1998)):

$$q = C_1 \cdot N_t^{C_2} \cdot \frac{(T_H + T_C)\cdot(T_H - T_C)}{2\cdot(N+1)} + C_3 \cdot \epsilon \frac{T_H^{4.67} - T_C^{4.67}}{N} + C_g \frac{P}{N} \cdot \left(T_H^{n_g} - T_C^{n_g}\right) \tag{3.1}$$

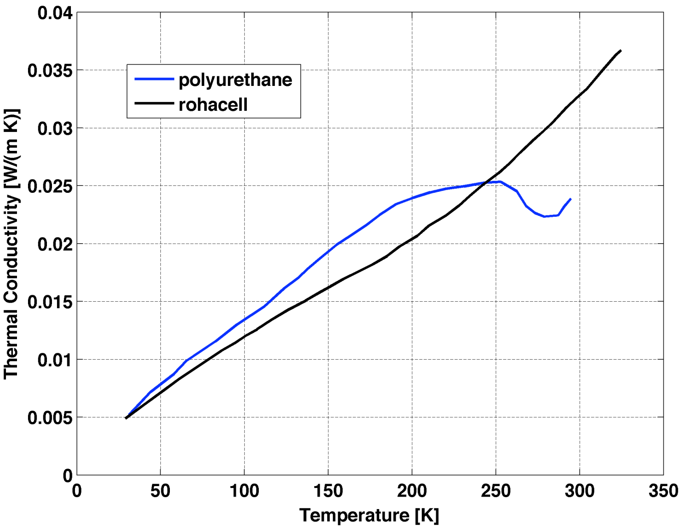

Figure 3.3. Thermal conductivity of the two selected foams, derived from Brewer (1991).

where q is the heat flux through the insulation, C_1, C_2 and C_3 coefficients that are empirically determined for each combination of spacer and insulation blanket material, C_g a coefficient that depends on the interstitial gas in the insulation ($1.46 \cdot 10^4$ for GN_2), n_g an exponent depending on the interstitial gas (0.53 for GN_2) and T_H and T_C the temperatures at the hot respectively cold boundaries of the insulation. N is the total number of layers of the MLI and N_t the layer density of the insulation (in layers/cm). According to Allidieris & Janin (2002b), at least 10 layers should be used in order to obtain an effective insulation and to ensure that the correlations are applicable. The authors therefore selected a 5 mm thick insulation even though the calculated required thicknesses are much smaller. The correlations are valid for layer densities between 2 and 50 layers/cm.

The empirical coefficients C_1, C_2 and C_3 are available for several different spacer materials in Johnson et al. (1974), Nast (1998) and Allidieris & Janin (2002b). All reported MLI combinations only consider double aluminized mylar (DAM) for the radiation shields as the goldized mylar offers no significant performance improvement despite its higher cost Johnson et al. (1974). The three most promising spacer materials as identified in Johnson et al. (1974) were taken into consideration in this work: dacron, tissuglas and double silk net (DSN). Besides the normal DAM blanket, a perforated DAM radiation shield was also considered. Table 3.3 gives the empirical coefficients of the different selected materials.

Figure 3.4 shows the heat flux through the insulation for the different material combinations under vacuum pressure. The figure shows the results for a hot boundary temperature of 225 K and 300 K, as representative for cruise and a hot day takeoff. The heat flux is plotted for a layer density of 37 layers per inch, a typical layer density of an MLI (Nast, 1998).

As can be seen from Figure 3.4, the combinations DAM/DSN and DAM/Tissuglass offer a potential to reduce the heat flux through the insulation for a given number of layers in the MLI, compared to the other investigated MLIs. These two combinations are therefore selected for a more in-depth investigation. Figure 3.5 shows the sensitivity of both MLI to

Table 3.3. Empirical coefficients for different multi layer insulations, adopted from Johnson et al. (1974).

MLI	**C1**	**C2**	**C3**
DAM / Dacron	$8.95 \cdot 10^{-8}$	2.56	$5.39 \cdot 10^{-10}$
DAM / Tissuglas	$4.43 \cdot 10^{-11}$	3.91	$8.03 \cdot 10^{-10}$
DAM / DSN	$2.11 \cdot 10^{-9}$	3.56	$5.39 \cdot 10^{-10}$
Perforated DAM / DSN	$2.98 \cdot 10^{-8}$	2.84	$5.86 \cdot 10^{-10}$

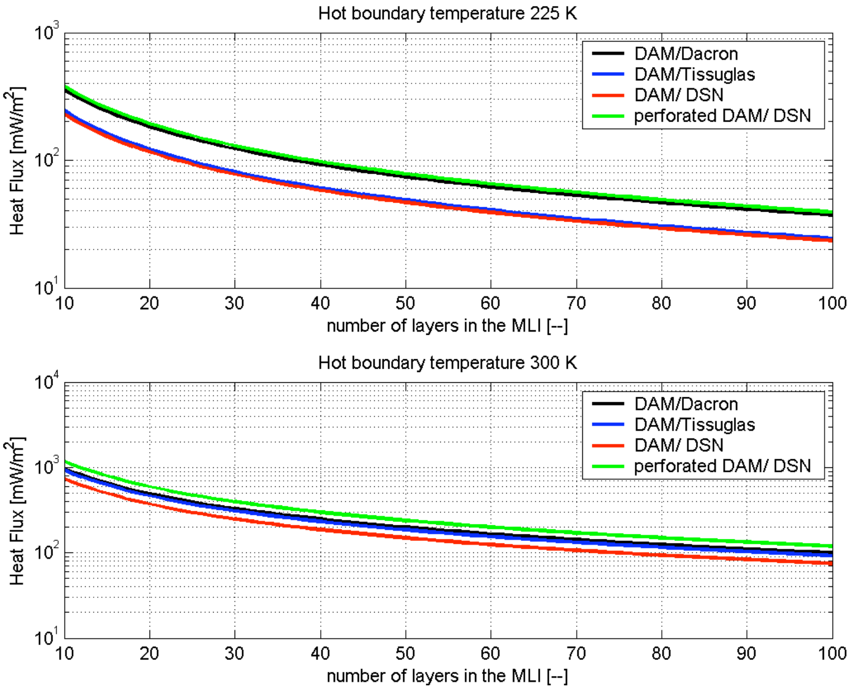

Figure 3.4. Heat flux through 4 different MLI for 2 hot boundary temperature.

local compression. The figure shows the variation of $(k \cdot \rho)$ with layer density. The factor $(k \cdot \rho)$ is used here as it gives an indication of both thermal performance and weight of the MLI. The figure clearly indicates that the DAM/Tissuglas MLI is virtually insensitive to local compression while the DAM/DSN insulation capacity will degrade significantly when local compression occurs. At a layer density of approximately 50 layers/inch, as adopted in the Cryoplane study (10 layers for a thickness of 5 mm[6], Allidieris & Janin (2002b)), the performance of the MLI with tissuglass spacer is much better than that of the MLI with the double silk net.

---

[6] According to Allidieris & Janin (2002b) minimum 10 layers are required for the MLI to be efficient. This minimum value is adopted here too even though it leads to an overly efficient thermal insulation.

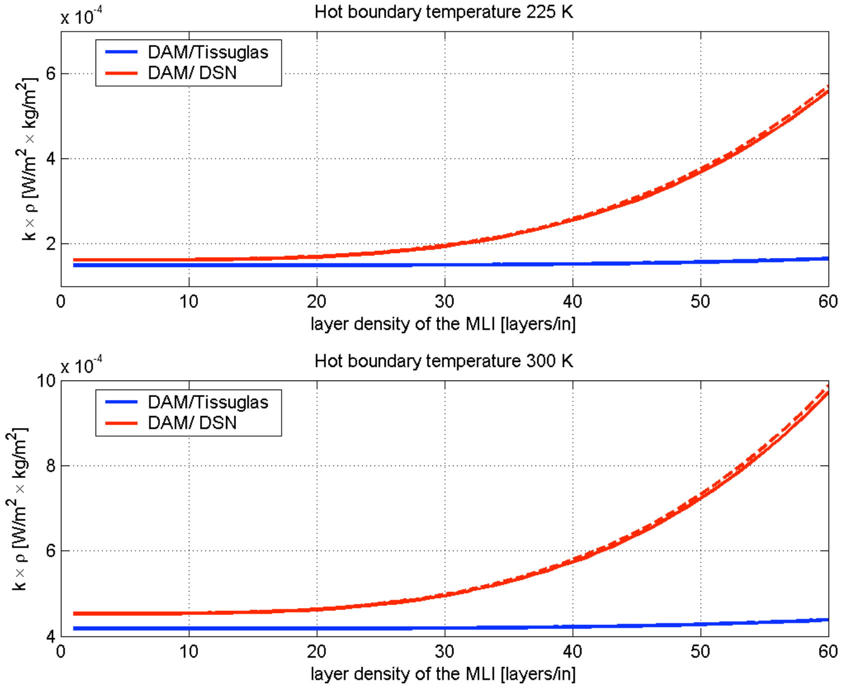

Figure 3.5. Influence of layer density on $k \cdot \rho$ for both selected MLI.

3.2.3.3 Tank wall materials

In the Cryoplane study, stainless steel, aluminium and titanium alloys are considered in the preliminary phase of the design (Allidieris & Janin, 2002b). The final tank weight calculations are however only performed for stainless steel. In the NASA study, on the other hand, Al 2219 was selected for the design of the tank wall (Brewer (1991), Brewer et al. (1975a), Brewer et al. (1975b) and Brewer et al. (1978)) and this alloy is also used for the Ariane 4 and 5 tanks Allidieris & Janin (2002b). As Brewer and his team performed an extensive study of the mechanical design of the tank wall and sufficient data on the used material characteristics is available, Alloy 2219 was selected as the prime material for this study. Aluminum is furthermore one of the few metals known to show only minimal susceptibility to hydrogen embrittlement (Zielinski, 2001).

A density of 2825 $\mathrm{kg/m^3}$ is adopted for the Al 2219 alloy (0.103 $\mathrm{lb/in^3}$ (Brewer et al., 1975b). For ultimate design conditions a stress of 234.4 MPa can be sustained whereas the stress is limited to 172.4 MPa for operating conditions (Brewer et al., 1975b). The allowable stresses are selected using a fatigue quality index (K_t) of 5.0, 50000 hrs of service life (10000 cycles) and a life reduction factor of 4.

As mentioned previously a 25% weight reduction is applied to the tank wall for composite walls. The thickness of the wall itself is however not changed as insufficient data is available to calculate the corresponding thicknesses, which is slightly conservative but only has a small influence on the results.

3.3 Structure of the tank

Until now two alternatives are selected for the insulation material as well as the tank wall material. Both foams and MLI are considered for the insulation, while monolithic metals and composites will be evaluated for the tank wall. As the MLI insulation requires a vacuum and consequently a double wall construction, two different types of tank structures will have to be analyzed. Both are elucidated below.

3.3.1 Single wall construction with foam insulation

The structure of the cryogenic LH_2 tank with foam insulation is shown on Figure 3.6. As can be seen from the figure, the rigid, closed-cell polyurethane foam is applied to the exterior of the tank wall itself, which takes up the mechanical tank loads. A purged layer of compressed open-cell foam is added on top of the insulation to accommodate dimensional changes and to support the exterior composite fairing, which serves as the aircraft skin. As the open-cell foam is purged with gaseous nitrogen, an MAAMF vapor barrier is added on both sides of the open-cell foam layer. The structure was adopted from Brewer et al. (1975b) and Brewer (1991) as an extensive study on different fuel tank architectures was made by Lockheed-California under the auspices of NASA. Brewer adopted the presented structure as it leads to a minimization of the direct operating cost of the aircraft.

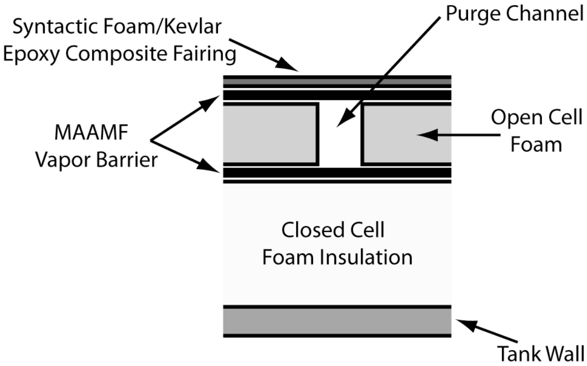

Figure 3.6. The tank structure for the foam based insulation, derived from Brewer (1991).

The MAAMF vapor barrier is a multilayer sandwich that consists out of the following layers Brewer (1991):

1. 0.5 mil Mylar, Type A
2. Adhesive
3. 0.5 mil aluminium foil series 1100.0
4. Adhesive
5. 0.5-1.5 mil aluminium foil series 1100.0
6. Adhesive
7. 0.5 mil Mylar, Type A
8. Dacron or glass net fabric

The total thickness of the MAAMF is 0.0005 to 0.0006 inch and its specific weight is 0.224 kg/m^2 Brewer (1991). The specific weight of the syntactic foam/Kevlar epoxy composite used as the aircraft skin is 1.304 kg/m^2 and its thickness is 1.57 cm. The compressed open-cell foam support has a thickness of 1.78 cm (face sheets included) and a density of 33 kg/m^3 (Brewer, 1991).

3.3.2 Double wall construction with multi layer insulation

As the MLI requires a hard vacuum (10^{-4} to 10^{-5} torr or 13 to 1.3 mPa), a double wall construction is mandatory. As for the single wall construction of the previous paragraph, the double wall construction is derived from Brewer (1991) and is shown on Figure 3.7. As can be seen from the figure, a small layer of closed cell foam insulation is applied to the tank wall to prevent air liquefaction in event of failure of the vacuum. The multi layer insulation is then applied on top of the layer of foam. The aluminum honeycomb core serves on its turn as the external wall to support the loads of the vacuum and to ensure that no mechanical loads are applied on the MLI. Two aluminium face sheets are bonded to the honeycomb core, which is also maintained at vacuum pressure. Finally a fairing is applied to take up the aerodynamic loads.

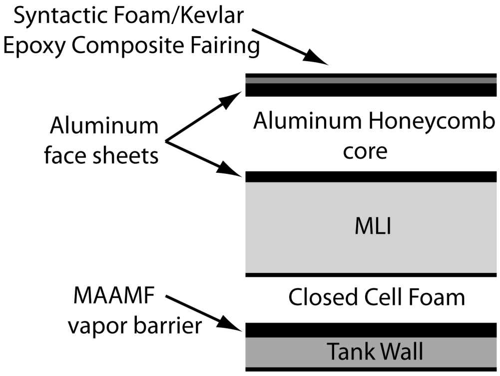

Figure 3.7. The tank structure for the multi layer insulation, derived from Brewer (1991).

The closed-cell foam has a thickness of around 1.27 cm and a density of 35.24 kg/m^3. The aluminium honeycomb core on the other has a thickness of 3 inch (7.62 cm) and a density of 50 kg/m^3. Finally, the aluminium face sheets have a specific weight of 1.36 kg/m^2. For all other components, the values quoted in the previous section are used.

3.4 Sizing of the tank

The design of a cryogenic aircraft tank for LH$_2$ is a compromise between mechanical and thermal requirements. During the flight the pressure will namely rise as a consequence of the heat leaking through the insulation, resulting in the boil-off of some of the liquid. The pressure will on the other hand fall due to the fuel consumption of the engines. So a balance between insulation type, insulation thickness, maximum and minimum allowable pressure inside the tank and total tank volume[7] needs to be found for a particular application.

The model used to calculate the pressure fluctuations in the tank is described in subsection 3.4.1. The mechanical design of the tank is treated next (subsection 3.4.2). Then the thermal design of the tank is discussed (subsection 3.4.3) before the tank volume determination is detailed in subsection 3.4.4.

3.4.1 Pressure fluctuation inside the tank

A general form of the pressure fluctuation model for a homogeneous cryogenic storage tank can be obtained by applying the first law of thermodynamics and conservation of mass to a control volume that contains the tank liquid-vapour contents and is assumed to be in a homogeneous state. The control volume corresponds to the inside surface of the tank wall, not including the internal tank hardware. The model as established here is derived from Allidieris & Janin (2002b) and Lin et al. (1991).

The first law for a variable volume with an inlet and an outlet (neglecting kinetic and potential energy terms) is:

$$\frac{dE}{dt} = Q + W + \dot{m}_{in} \cdot h_{in} - \dot{m}_{out} \cdot h_{out} - p \cdot \frac{dV}{dt} \tag{3.2}$$

where E is the energy of the tank, including fluid and wall, Q the heat input in the tank, W the power input in the tank, $\dot{m}_{in}$ and $\dot{m}_{out}$ the inlet and outlet flow rate , h_{in} and h_{out} the specific enthalpy of incoming and outgoing mass flow rate, V the volume of the tank and p the pressure inside the tank.

At low temperature, the heat capacity of the solid materials is very low and in most cases the thermal inertia of the wall can be neglected Allidieris & Janin (2002b). The energy of the fluid can furthermore be written as:

$$E = \rho \cdot u \cdot V$$

where ρ is the fluid density, V the tank volume and u the the specific internal energy of the fluid, which leads to:

$$\frac{dE}{dt} = \rho \cdot V \cdot \frac{du}{dt} + \rho \cdot u \cdot \frac{dV}{dt} + u \cdot V \cdot \frac{d\rho}{dt} = Q + W + \dot{m}_{in} \cdot h_{in} - \dot{m}_{out} \cdot h_{out} - p \cdot \frac{dV}{dt} \tag{3.3}$$

Conservation of mass for a compression or expansion process is, on the other hand, expressed as:

$$\frac{dm}{dt} = \dot{m}_{in} - \dot{m}_{out} = \rho \cdot \frac{dV}{dT} + V \cdot \frac{d\rho}{dT} \tag{3.4}$$

If the specific internal energy is considered to be a function of pressure and density only (u = u(p,ρ)), then

$$\frac{du}{dt} = \left(\frac{\partial u}{\partial \rho}\right)_p \cdot \frac{d\rho}{dt} + \left(\frac{\partial u}{\partial p}\right)_\rho \cdot \frac{du}{dt} \tag{3.5}$$

---

[7] The total tank volume comprises both the internal volume of the tank as well as the tank wall and insulation.

Combining the above equations and using the definition of enthalpy (h =u + p/ρ, the general-purpose homogeneous equation for pressure change rate is obtained.

$$\frac{dp}{dt} = \frac{\phi}{V}\left\{Q + W + \dot{m}_{in}\left[h_{in} - h - \rho \cdot \left(\frac{\partial h}{\partial \rho}\right)_p\right] - \dot{m}_{out}\left[h_{out} - h - \rho \cdot \left(\frac{\partial h}{\partial \rho}\right)_p\right] + \rho^2 \cdot \left(\frac{\partial h}{\partial \rho}\right)_p \cdot \frac{dV}{dt}\right\} \tag{3.6}$$

where the energy derivative ϕ is defined as[8]

$$\phi = \frac{1}{\rho \cdot \left(\frac{\partial u}{\partial p}\right)_\rho}$$

Values for the (homogeneous) energy derivative have been calculated for para-hydrogen based on thermodynamic data from NIST (2007) using the method proposed in Allidieris & Janin (2002b) which consists of using the expressions from this section for two different conditions in a closed tank. Between the two 'states' a small amount of energy is added and the pressure rise is calculated from the data from NIST (2007). The outcome of this procedure is shown on Figure 3.8 and is compared to data from Allidieris & Janin (2002b) (dots on the right hand side of the figure) and Lin et al. (1991) (dashed lines on the left hand side of the figure). As shown on the figure a good agreement was obtained with the values found in literature. As shown, the pressure will rise faster (higher value of ϕ) near the end of the flight where lower fill levels and higher pressures are obtained.

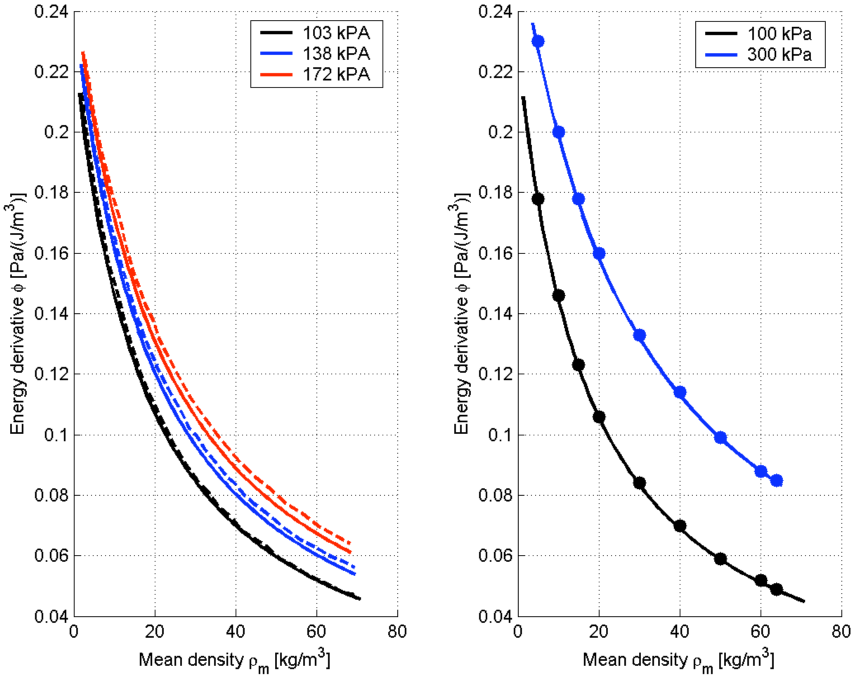

Figure 3.8. The energy derivative in function of pressure and density.

---

[8] ϕ is dimensionless but specifying its dimensions as Pa/(J/m^3) adds to the comprehension of the physical meaning of the derivative. The energy derivative gives the pressure rise per energy input per volume

If the elasticity of the tank wall is neglected (V=constant), there is no incoming mass flow rate and the work input is zero, the expression for the pressure change rate is simplified to:

$$\frac{dp}{dt} = \frac{\phi}{V}\left\{Q - \dot{m}_{out}\left[h_{out} - h - \rho\cdot\left(\frac{\partial h}{\partial \rho}\right)_p\right]\right\} \tag{3.7}$$

This equation can finally be rearranged in the following form (Lin et al., 1991)

$$\frac{dp}{dt} = \frac{\phi}{V}\left\{Q - \dot{m}_{out}\cdot h_{lg}\cdot\left[x\frac{\rho_g}{\rho_l - \rho_g}\right]\right\} \tag{3.8}$$

where x is the quality of the fuel ($x = 0$ for a saturated liquid and 1 for saturated vapor), h_{lg} is the heat of vaporization at the tank pressure and ρ_g and ρ_l are the density of the gas respectively the liquid.

Equation (3.8) gives the pressure rise for a homogeneously mixed tank. However, in reality, some degree of stratification will be present in the tank, which can have a significant influence on the pressure rise. Allidieris & Janin (2002b) show that the pressure rise can be 100 times bigger than the homogeneous pressure rise for a fully stratified tank, if it is assumed that all the heat enters the gas phase. A more realistic heat transfer model, where the heat input into the liquid and the gas is proportional to the tank surface wetted by the liquid respectively gas, shows pressure rise rates in between the homogeneous and the fully stratified model. The real pressure rise rate therefore needs to be determined through full mathematical models or experiments (Allidieris & Janin, 2002b).

Nonetheless, the homogeneous tank model is assumed to be valid for a cryogenic LH_2 aircraft fuel tank in the Cryoplane project. The fluid convection due to the acceleration and vibration levels of the plane and the conductivity of the tank wall will namely result in a more or less homogeneously mixed tank (Allidieris & Janin, 2002b)[9]. Brewer et al. (1975b) show that the temperature difference between the bottom and the top of the tank is smaller than 0.22 K for all considered tank architectures in their work. A considerable degree of stratification was only observed during filling when sub-cooled LH_2 is introduced in the bottom of the tank, but disappeared within 100 minutes. This made the authors conclude that there is little possibility of a sudden pressure reduction due to sudden maneuvers or turbulence (Brewer et al., 1975b).

Lin et al. (1991), on the other hand, adopt a pressure rise rate of 2 times the homogeneous pressure rate as typical for airborne tanks. As this approach is more conservative than the assumption of a fully homogeneous tank, the factor 2 is used in this work too:

$$\frac{dp}{dt} = 2\cdot\frac{\phi}{V}\left\{Q - \dot{m}_{out}\cdot h_{lg}\cdot\left[x\frac{\rho_g}{\rho_l - \rho_g}\right]\right\} \tag{3.9}$$

---

[9] When the plane is parked, only the free convection (due to gravity) and the conductivity of the wall of the tank can prevent thermal stratification to build up. However, in that case, the energy dissipated in the fluid is relatively low (Allidieris & Janin, 2002b). To avoid problems of pressure rise increase due to stratification, a mixer could be added to the tank if necessary. However, its use (even intermittently) will provoke an additional pressure rise due to the dissipated power (heat).

3.4.2 Mechanical design of the tank

The tank needs to resist several types of loads resulting from the difference between the tank pressure and the ambient conditions, the fuel weight, the acceleration of the aircraft (gusts and dynamic loads), sloshing of the fuel due to maneuvers, vibration, aerodynamic loads (pressure distribution), ... As integral tanks have been selected, the tank has to be constructed to sustain all of these. The loads can however not be determined if the tank position inside the fuselage is not known (to know the fuselage bending loads) and a finite element analysis has to be performed in a rigorous analysis as was done in Brewer et al. (1975b) for the aft conical tank. For the design of the cylindrical tank in front of the fuselage, however, the data from the aft tank has been extrapolated (Brewer (1991), Brewer et al. (1975a), Brewer et al. (1975b) and Brewer et al. (1978)). For the Cryoplane study, the tanks are designed for resist only to the pressure loads, as insufficient data was available on the other loads and the time allocated to the tank design was too limited to allow a full finite-element analysis (Allidieris & Janin, 2002a). A minimal change strategy was also adopted for the project (Rostek, 2002).

Here, the latter approach will be adopted, as a full finite element analysis is not feasible within the scope of this work either. The tanks will thus be designed for the pressurization loads and a safety factor is adopted to take the other loads into account. Below, the methodology used in the mechanical design of the tank is described.

To allow an assessment of the optimum tank pressure, the tank design has been made in function of the tank venting pressure. After all, the optimum venting pressure for a specific mission and aircraft size is a trade-off between tank weight and the amount of fuel to be vented or insulation weight. For low venting pressures, a significant amount of hydrogen needs to be vented throughout the flight or a thick insulation is required. High venting pressures lead on the other hand to thick and heavy tank walls. However, some additional margin needs to be added to the maximum sustainable pressure to take the safety valve relief tolerance into account.

As the design loads are known and the allowable stresses have been determined (see section 3.2.3.3), the wall thickness can easily be calculated. Here the method from Barron (1985) has been adopted, which is based on the ASME Boiler and Pressure vessel code:

$$t_{wa} = \frac{p_{des} \cdot d_o}{2 \cdot \sigma_a \cdot e_w + 0.8 \cdot p_{des}} \tag{3.10}$$

where t_{wa} is the tank wall thickness, d_o the outside diameter of the shell, σ_a the allowable tank wall stress and e_w the weld efficiency which is taken here as 80% (Barron, 1985).

The minimum thickness for spherical shells and elliptical or ASME torispherical heads is on the other hand determined from Barron (1985):

$$t_h = \frac{p_{des} \cdot d_o \cdot K}{2 \cdot \sigma_a \cdot e_w + 2 \cdot p_{des} \cdot (K - 0.1)} \tag{3.11}$$

where K is given by the following expression for elliptical heads (Barron, 1985):

$$K = \frac{1}{6}\left[2 + \frac{d}{d_1}\right)\right]$$

with d_1 the minor axis of the elliptical head. In this work, elliptical heads are adopted with a ratio of major to minor axis of 1.6 as this type of bulkheads leads to minimal direct operating costs for subsonic aircraft (Brewer, 1991).

The thickness of both the tank wall and the bulkheads is calculated for limit and ultimate loads and the maximum value of both thicknesses is retained.

3.4.3 Thermal design of the tank

In order to prevent excessive boil-off of the LH_2 inside the aircraft fuel tank, a very good insulation of the tank is needed, as described before. To allow an assessment of the effectiveness of the insulation and the influence of the insulation thickness and type, a complete thermal model has been developed for the tank. The model not only takes the heat flux through the insulation into account but also the convective heat transfer outside and inside the tank.

The model is based on the electrical resistance analogy (amongst others Buchlin (2005) and Lienhard & Lienhard (2004)). The resistance for the external convective heat transfer, the insulation and the internal heat transfer are placed in series. Below all different thermal resistances are treated.

3.4.3.1 Thermal resistance for the convective heat transfer on the external tank surface

During the flight, the external surface of the hydrogen tank is cooled by forced convection due to the forward aircraft velocity. As no correlation was found for forced convection on a cylinder along its axis, the flat plate correlation from Buchlin (2005) is adopted here:

$$Nu_L = 0.03625 \cdot Pr^{0.43} \cdot Re_L^{0.8} \tag{3.12}$$

where Nu_L is the (global) Nusselt number , Pr the Prantl number and Re_L the Reynolds number. The Nusselt number is on its turn defined as:

$$Nu = \frac{h_{ext} \cdot L}{k_{air}}$$

with h_{ext} the external convective heat transfer coefficient, L the characteristic length for the heat transfer phenomenon under investigation (taken here as the length of the cylindrical part of the tank) and k_{air} the thermal conductivity of air. The Prantl number is defined as

$$Pr = \frac{\mu_{air} \cdot c_p}{k_{air}}$$

where μ_{air} is the dynamic viscosity of air and c_p is the specific heat at constant pressure. Finally, the Reynolds number is defined as

$$Re_L = \frac{\rho_{air} \cdot v \cdot L}{k_{air}}$$

where ρ_{air} is the air density and v the flight speed.

Besides heat transfer by convection, heat transfer by radiation also plays a role on the external tank surface. To take the heat transfer by radiation into account, an equivalent convective coefficient h_{rad} is used (Buchlin (2005) and Lienhard & Lienhard (2004)):

$$h_{rad} = \sigma \cdot \epsilon \cdot \left(T_{skin}^2 + T_{atm}^2\right) \cdot (T_{skin} + T_{atm})$$

T_{skin} and T_{atm} are the temperatures of the aircraft skin and the atmosphere. σ is the Stefan-Boltzmann constant and ϵ the emittance of the skin. For the emittance ϵ of the aircraft skin, two different values are adopted: 0.95 is used for an aircraft painted in white, while 0.09 is used for an unpainted aircraft (Lienhard & Lienhard, 2004).

The total external heat transfer coefficient is then simply the sum of both contributions:

$$h_{tot} = h_{ext} + h_{rad}$$

which leads to the following thermal resistance for the external heat transfer:

$$R_{ext} = \frac{1}{2 \cdot \pi \cdot r_{fus} \cdot l_{tank}} \cdot \frac{1}{h_{tot}} \tag{3.13}$$

where r_{fus} is the fuselage radius.

3.4.3.2 Thermal resistance of the insulation

The thermal resistance of both types of insulation is treated below. A similar formulation is used for both types as an equivalent conductivity coefficient is adopted for the MLI.

Foam Insulation

The thermal resistance for a pure conduction heat transfer in cylindrical coordinates is given by Lienhard & Lienhard (2004):

$$R_{ins} = \frac{1}{2 \cdot \pi \cdot r_i \cdot l_{tank}} \cdot \frac{\ln\left(\frac{r_o}{r_i}\right)}{k_{foam}} \tag{3.14}$$

with r_i and r_o the inner and outer radius of the insulation and k_{foam} the thermal conductivity of the foam. However, as the thermal conductivity of the foam strongly depends on its temperature, the foam layer has been divided into a series of 40 sub-layers of equal thickness[10] . For each layer, the thermal resistance is calculated and the total thermal resistance is then given by the sum of the thermal resistances of the sub-layers. An iteration is made until the heat flux through each of the sub-layers is equal.

---

[10] An analysis on the number of sub-layers showed that this was the minimal amount of layers required to obtain a reasonably precise value for the heat flux, despite the significant calculation time this relatively high number entails, it has been chosen here for this study.

Multi Layer Insulation

As the correlation for the multi layer insulation gives a heat flux q instead of a conductivity coefficient, an equivalent conductivity coefficient k_{equiv} is defined for the MLI (Allidieris & Janin, 2002b):

$$k_{equiv} = \frac{q}{\frac{T_H - T_C}{t}}$$

The thermal resistance for the multi layer insulation is then given by replacing k by k_{equiv} in equation (3.14).

3.4.3.3 Thermal resistance of natural convection in the tank

The temperature difference between the inner tank wall and the bulk of the hydrogen fuel will result in natural convection inside the fuel tank. As the natural convection phenomenon will be different for the gas and the liquid, the heat transfer to the two states is independently calculated. Afterwards, the two heat transfer coefficients are combined to yield a single thermal resistance, taking the area wetted by each of the phases into account.

Liquid phase internal convection

For the liquid phase convection, the following correlation is adopted (Hochstein et al., 1986):

$$Nu_h = 0.0605 \cdot Ra_h^{1/3} \tag{3.15}$$

Both the Nusselt and the Rayleigh number are based on the height of the liquid phase. The Rayleigh number is defined as:

$$Ra_h = \frac{g \cdot \beta \cdot \Delta T \cdot h^3 \cdot Pr}{\nu}$$

where g is the gravitational acceleration, β the thermal expansion coefficient of the liquid hydrogen, ΔT the temperature difference between the wall and the bulk of the liquid and ν the kinematic viscosity of the hydrogen. The properties needed are again obtained from NIST (2007).

In Brewer et al. (1975b) a different correlation is proposed for the Nusselt number of the liquid. This correlation however leads to lower heat transfer coefficients for the whole range of Rayleigh numbers considered. The correlation from Hochstein et al. (1986) is thus adopted as it is conservative. All in all, the thermal resistance for the internal heat transfer only takes up a relatively small part of the overall thermal resistance so that the difference between the correlations would only lead to a small difference for the total heat flux. For radiation, again the equivalent convective coefficient is used.

Gas phase internal convection

For the gas phase natural convection, only limited data is available in literature. The only correlation found is therefore adopted Brewer (1991):

$$Nu = 17 \tag{3.16}$$

where the Nusselt number is defined based on the height of the gas phase inside the tank. As gases are transparent for thermal radiation, radiation heat transfer is not added for the gaseous phase.

Total internal convection

As the convective heat transfer coefficients are determined for both phases, the total thermal resistance of the internal heat transfer can be calculated. To do that the area wetted by the liquid and the gas need to be taken into account. This leads to the following expression for the total internal resistance

$$R_{int} = \frac{1}{2 \cdot \pi \cdot r_i \cdot L} \cdot \frac{S_{w,tot}}{h_{LH2} \cdot S_{w,LH2} + h_{GH2} \cdot S_{w,GH2}} \tag{3.17}$$

3.4.3.4 Total thermal resistance

The total thermal resistance for the liquid hydrogen fuel tank is simply the sum of the individual resistances as the internal, insulation and external resistance are placed in series:

$$R_{tot} = R_{int} + R_{ins} + R_{ext} \tag{3.18}$$

However, as the internal heat transfer area is not equal to the external heat transfer area, the different resistances need to be adapted to one common area. Here, the area wetted by the liquid and the gas phase is used, which leads to:

$$R_{tot} = \frac{1}{2 \cdot \pi \cdot r_i \cdot l_{tank}} \cdot \left[\frac{S_{w,tot}}{h_{LH_2} \cdot S_{w,LH_2} + h_{GH_2} \cdot S_{w,GH_2}} + \frac{\ln\left(\frac{r_o}{r_i}\right)}{k_{foam}} + \frac{r_i}{r_{fus}} \cdot \frac{1}{h_{ext}} \right] \tag{3.19}$$

However, until now only the heat transfer through the tank insulation is considered. Some additional heat will flow into the tank through the supports, the connection and the piping. A 30% margin is taken on the calculated heat transfer to take this extra heat input into account (Allidieris & Janin (2002a) and Brewer (1991)):

$$Q = 1.3 \cdot \frac{T_{amb} - T_{H_2}}{R_{tot}} \tag{3.20}$$

where Q is the total heat flux into the tank.

3.5 Volume of the tank

At first sight, the determination of the tank volume is straightforward once the mass to be embarked is known. However, several additional parameters play a role as will be shown below. After all, to allow venting a two-phase mixture needs to be present at all times. The tank filling and venting pressure furthermore plays a significant role as will be shown below.

As indicated before, the pressure rise inside a tank filled with 100% saturated liquid or supersaturated liquid is much higher than for a tank filled with a two-phase mixture (Allidieris & Janin, 2002b). When the tank would be filled with saturated or supersaturated LH_2, a much thicker insulation would thus be required to keep the heat input to the tank to a sufficiently low level so that the tank pressure will not rise drastically during the flight. The vent valve, needed to keep the pressure inside the tank to a reasonably low level, will furthermore be frozen when in contact with the cryogenic liquid hydrogen which will block the valve (Allidieris & Janin, 2002b). Finally, if venting is needed during the flight to keep the pressure inside the tank below a certain level, a much smaller mass of hydrogen needs to be withdrawn when gaseous hydrogen is vented instead of liquid hydrogen. In the Cryoplane study it was therefore assumed that at least 3% of the volume is occupied by gaseous hydrogen at the venting pressure (Allidieris & Janin (2002b), Allidieris & Janin (2002a) and Rostek (2002))[11]. For the NASA study on the other hand, Brewer and his team assumed a 2% ullage allowance for the gas phase Brewer (1991). Here, the 3% allowance from the Cryoplane study is adopted. As this 3% allowance is required at the venting pressure, the mean density of the hydrogen in the tank will depend on the selected vent pressure, as shown on Figure 3.9. The figure shows the variation of the density of the hydrogen inside the tank in function of tank pressure. The black line indicates the density of the saturated liquid (y=1) while the blue line gives the mean density of the two-phase mixture for a vapour volume fraction of 3% (y=0.97).

Figure 3.9 clearly indicates that a higher venting pressure not only increases the tank mass due to the increase in tank wall thickness, but also the tank volume due to a decrease in storage density. At a venting pressure of 3.5 bar (venting pressure selected in the Cryoplane project (Allidieris et al., 2002a)), the mean density is reduced by about 9.7% and therefore the tank volume needs to be increased by the same amount. At 11 bar, the density reduction even rises to 34.7%. The figure also shows that the loss in density due to the 3% gas volume requirement decreases with increasing venting pressure (as the gas density increases with pressure and the liquid density drops). At 1 bar, the 3% gas volume requirement implies a density drop of 2.9% compared to saturated liquid storage, while at 1.5 bar the density drop is reduced to 2.7%.

This density reduction obviously has consequences on the filling of the tank. After all, to minimize the boil-off of LH_2, the pressure at which the tank is filled needs to be significantly lower than the venting pressure in the tank. Like this, the two-phase mixture can absorb some of the heat that enters the tank, which will lead to a pressure rise. Once

---

[11] Two different values are found throughout the different task technical reports of the Cryoplane study. Sometimes a 3% gas volume is assumed while some of the calculations are based on a 5% margin (Allidieris & Janin, 2002b).

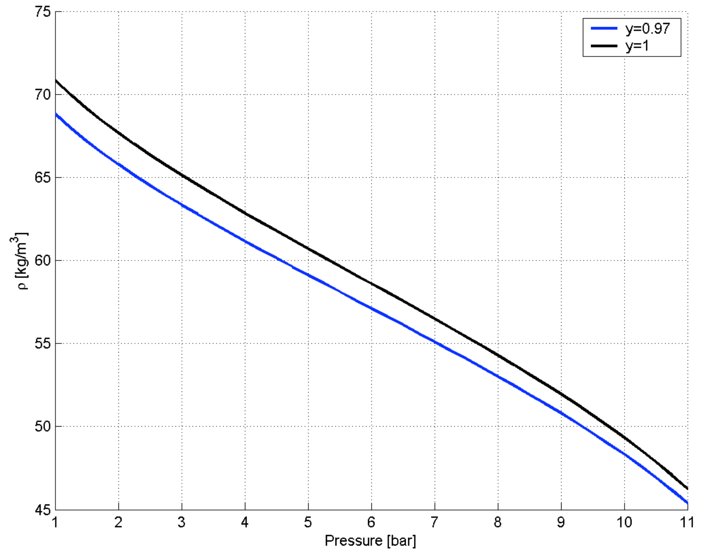

Figure 3.9. The mean density of hydrogen in function of the venting pressure.

the pressure has risen to the vent pressure, venting will be required. In an emergency case due to rupture of thermal degradation of the insulation, the pressure will rise so rapidly that no fuel can be withdrawn. For safety reasons the fill level thus needs to be kept low enough to prohibit an excessive pressure rise in the tank if the vent valve would be blocked as well. The fill level of the tank can thus be determined in function of the fill and venting pressure, as the mean density of the hydrogen does not change during this process. This is graphically represented on Figure 3.10.

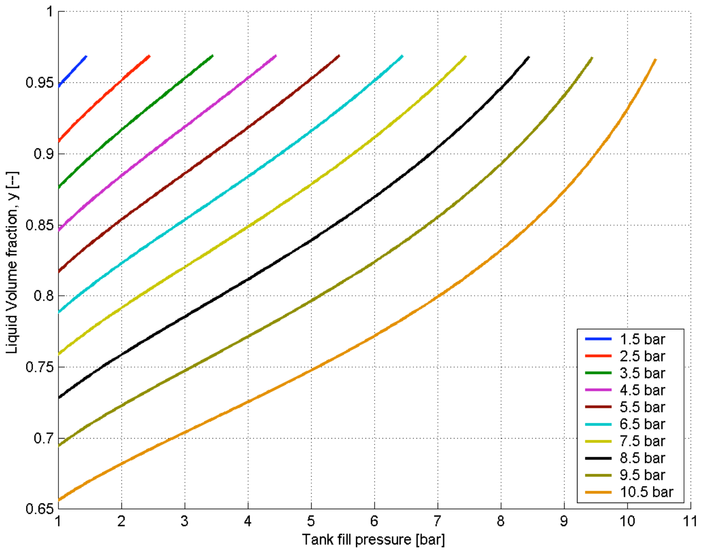

Figure 3.10. Influence of filling and venting pressure on the mean storage density.

The figure shows the liquid volume fraction as a function of filling pressure. Each line on the figure represents a different venting pressure. If the tank is for instance filled at 1.2 bar while the vent pressure is set at 3.5 bar, the tank can only be filled up with liquid to 88.5% of its volume to ensure that 3% of the volume remains gas at the vent pressure. If the tank vent pressure is raised to 10.5 bar, the tank can only be filled to 66.2% of its volume, when filling at 1.2 bar. The tank is filled at 1.2 bar as it needs to be kept at all times at a pressure slightly higher than the atmospheric pressure to prevent air entering the tank, which could lead to an explosive mixture. In the Cryoplane project, a minimum operating pressure of 1.2 bar was selected (Allidieris & Janin, 2002b), while Brewer (1991) selected a pressure of 1.24 bar as minimum operating pressure. Here, 1.2 bar is adopted as the minimum operating pressure.

Besides the previously mentioned pressure effects, some additional allowances must be made for tank contraction due to the cryogenic temperature, expansion due to pressure, internal structure and equipment, trapped and unusable fuel, These allowances are summarized in Table 3.4. Besides the values adopted in this work, the values from the Cryoplane study (Allidieris & Janin, 2002b) and the NASA study (Brewer, 1991) are also given in the table.

Table 3.4. Volume allowances for the fuel tank.

Allowance for [%]	**Brewer**	**Cryoplane**	**here**
Tank contraction and expansion	0.9	-	0.9
Internal structure and equipment	0.6	0.5	0.6
Trapped and unusable fuel	0.3	1.0	0.6
Gas space for exit pipe	1.0	2.0	1.0
Total	1.8	3.5	3.1

Besides these volume allowances, 20 kg needs to be foreseen for engine cool down and pressurant gas is needed to keep the tank at a pressure higher than atmospheric even if empty (Allidieris & Janin, 2002b).

3.6 Influence of the design mission on the tank design

In order to couple both the mechanical and the thermal design of the tanks, a design mission needs to be specified. After all, the pressure fluctuation inside the tank depends on several mission dependent parameters. The heat input through the insulation, the pressure at the beginning of each flight phase, the quantity of fuel left inside the tank as well as the fuel consumption of the engines all play a role on the evolution of the pressure inside the tank.

For a given mission, one therefore tries to find the minimal insulation thickness that would prevent venting of gaseous fuel during the whole flight. After all, if a thinner insulation thickness would be adopted, fuel would have to be vented and the amount to be vented increases rapidly for a relatively small decrease in insulation thickness. This not only results in a loss of fuel (money) but also in an increase in overall system weight (fuel, fuel to be vented, tank and insulation) compared to the optimum thickness. Adopting an insulation that is thicker than strictly needed would obviously also lead to an increase in system mass purely by the addition of insulation. It however also entails a weight penalty for the tank wall itself, as the wall will not be subjected to the maximum pressure for which it is designed and the tank volume will be slightly bigger than strictly needed. If the thickness of the insulation is increased too much it could even become necessary to add heat to the tank in order to ensure that the pressure remains above the minimum specified pressure for the tank (to prevent air leaking in the tank).

The above reasoning clearly depends on the chosen tank venting pressure, which will not only determine the amount of insulation needed but will also influence the tank volume as explained previously. As the optimum tank pressure is not clear beforehand, the tank venting pressure is taken as a variable here and the design is done for different venting pressures. Based on the outcome of the sizing studies the optimum tank pressure will be selected for the tank configuration under analysis.

To show the great importance of the size of the aircraft on the tank design two different applications are selected. First results of a tank sizing for a regional airliner are given as performed under the ENFICA-FC program (FP6) by the author. Then similar results are given for the missions of the case studies in the following chapter.

3.6.1 Regional airliner

For the regional airliner, a simplified mission is used representative of typical operations for this type of aircraft and the profile is split into 7 phases. Details of the mission can be found in Verstraete & Hendrick (2008). The total endurance of the flight is 5 hours including diversion to an alternate airport. In total 3 different options are considered for the tanks. A single tank solution, with an outer diameter of 2.42 m was taken as the reference case even though not practically feasible from a center of gravity point of view. After all this would lead to the highest gravimetric efficiency or lowest tank weight. Where the gravimetric efficiency is defined as:

$$\eta_{grav} = \frac{W_f}{W_f + W_{tank}} \tag{3.21}$$

where W_f is the fuel mass and W_{tank} is the mass of the tank structure. In the second design a twin tank option is chosen, one in front of the cabin and one in the tail cone to optimize the center of gravity position of the fuel. A third design finally consists out of multiple tanks on top of the fuselage and one big tank in the tail cone, as was proposed initially by IAI for this application. Both foam insulation and MLI are considered even though the latter will be much more expensive and more importantly represents an operational danger for the aircraft as noted previously.

The gravimetric efficiency of the single tank solution is given on Figure 3.11 where the blue lines represent the polyurethane foam and the black ones rohacell. The full lines indicate metal tank walls whereas the dashed lines denote a 25% weight reduction for composite materials (Sharke, 2004). The figure clearly shows that the polyurethane foam offers a lighter solution for the tank design. With polyurethane foam the gravimetric efficiency is in the order of 1 to 3% higher than with rohacell foam. It is also obvious from the figure that the weight gain from composite tank walls, even if present, is much smaller than the number from (Sharke, 2004) points out. After all the complete tank weight must be considered not just the tank wall.

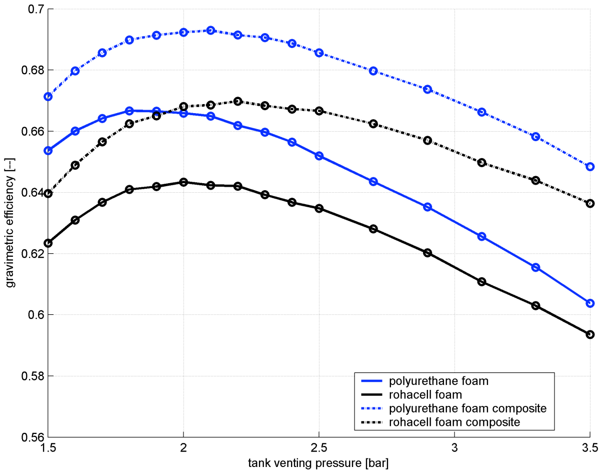

Figure 3.11. Gravimetric efficiency of a single tank option for a regional airliner.

As shown on the figure the the optimal venting pressure lies around two bar and the maximum gravimetric efficiency lies between 62 and 70%. Due to the lower thermal conductivity of the polyurethane foam a slightly longer tank is however obtained for polyurethane as shown on Figure 3.12. Comparing both figures shows that a compromise is needed between minimum tank length (at a higher pressure and higher tank weight) or minimum weight with a slightly longer tank (and fuselage) length.

The figures indicate that for a diameter around 2.4 m and a typical regional jet missions the gravimetric efficiency of foam insulation is limited to 70%. If the two (equal) tanks option is considered this number drops by about 20% due to the decrease in tank length for each individual tank which leads to a higher surface-to-volume ratio and a higher tank wall area and hence weight. Due to the twin tanks the overall tank length increases furthermore with about 1m. When considering multiple small tank on top of the cabin (9 in total) the gravimetric efficiency dropped down to about 35-40% due to the very small diameters of the multiple tanks. As a consequence of this very small diameter and the corresponding significant increase in surface-to-volume ration a higher storage pressure (up to 8 bars for the smallest tanks) is needed which explains the sharp increase in tank weight.

A single tank with MLI insulation did not show a markable improvement in tank gravimetric efficiency compared to the single foam based tanks but the length of the tank was significantly reduced as a lower storage pressure was feasible.

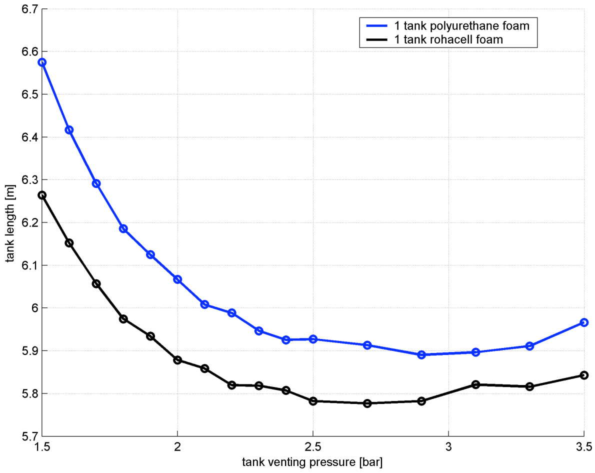

Figure 3.12. Tank length for the single tank option for a regional airliner.

3.6.2 Long range transport aircraft

Figure 3.13 shows a typical gravimetric efficiency curve for the long range transport aircraft as reported in the next chapter. Seen the large diameters for all considered fuselages (compared to the 2.4 m for the regional airliner) a virtually constant gravimetric efficiency of around 79% was found for all designs, regardless of tank diameter and fuel mass to be stored. Even though a more detailed analysis of very large diameter tanks is required to make the conclusion final, this seems to be the upper bound for the gravimetric efficiency of tanks for large long range transport aircraft. The figure also shows that the design venting pressure is close to 1.4 to 1.5 bar whereas a pressure rise up to at least 2 bar had to be sustained for the optimal regional airliner tanks. This lower design pressure entails a significant reduction in weight of the 'pressure vessel'. It has to be verified however whether the additional tank loads do not impose reinforcements leading to extra weight.

Seen the large size of the tanks for this particular application, the design proved to be almost independent of the fuselage diameter. For diameters ranging from about 6.8 to 8.9 diameter the variation in tank gravimetric efficiency is in the order of 2-4%. A similar variation in tank weight is found for a large variety of fuel masses. For fuel masses per tank of 15 to 35 tons the maximum difference in gravimetric efficiency was found to be in the order of 5 %.

Tanks with MLI did not show an improvement over foam tanks for this application either as far as gravimetric efficiency is concerned. They did however result in a slightly smaller tank length. As the rapid boil-off in case of a vacuum loss (Allidieris & Janin, 2002b) presents a critical issue that cannot be accepted for an aircraft application, they are therefore not considered in the remainder of the work.

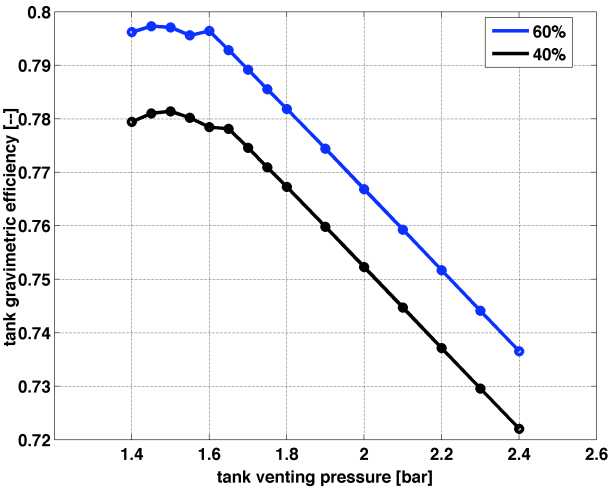

Figure 3.13. Tank gravimetric efficiency for a long range transport aircraft.

3.7 Conclusion

This chapter presents an overview of the tank sizing and design for liquid hydrogen transport aircraft based on an extensive literature review of the subject. The review shows that integral cylindrical tanks with external insulation are the preferred tanks for aviation.

For this type of tank the appropriate material classes for both the tank wall and the insulation system are chosen. The tank structural, load bearing material will most likely be an aluminum alloy to deal with hydrogen permeation and embrittlement issues. Some data is found on composite materials but this was judged to be too limited to be reliable. After all a linerless composite tank will most likely be prone to hydrogen permeation.

Once all the materials are selected, the sizing methods for the tank are described. A model for the pressure fluctuation in the tank is adopted and both the mechanical and the thermal design are accounted for. Finally, it is shown that the tank volume determination is not as straightforward as it seems at first sight. The density at which the hydrogen can be stored is function of both the filling pressure and the venting pressure for which the wall is designed.

In a final section the design method is applied to two different types of aircraft representing a wide range of aircraft sizes and flight conditions. For smaller aircraft, the tank integration is a key issue as shown by the wide variation in gravimetric efficiency between the ideal case of one single tank and the optimal configuration from an integration point of view. If several tanks on top of the fuselage are adopted a drop of around 30% in gravimetric efficiency was found, nearly doubling the tank mass. For the type of aircraft under consideration in the next chapter, the gravimetric efficiency was found to be nearly constant, around 76-80% for a wide range of fuel masses. The large diameter of the fuselage allows the tank to be designed for a relatively low venting pressure in the order of 1.5 bar, which leads to a relatively low specific mass for the tank (compared to the regional airliner).

This page is intentionally left blank

CHAPTER 4

Large long range transport aircraft with hydrogen fuel

As the weight reduction that can be obtained through hydrogen increases with fuel load, large long range transport aircraft seem at first sight a promising aircraft class for conversion. It has however been shown (Astaburuaga et al. (2001) and Westenberger (2003b)) that the main challenge for this category is to meet geometric airport constraints without a performance penalty. As the potential market for this category is likely to increase in time due to airport congestion (Airbus, 2007), large long range type of aircraft are investigated in detail in this chapter.

Designs for two classes of large aircraft are reported for both kerosene and hydrogen fuel. The aircraft performance as well as operating costs are compared. For the operating cost comparison a fuel price per energy content is used to account for the difference in lower heating value. The hydrogen fueled aircraft designs are made for polyurethane foam insulation only as the differences with rohacell were shown to be small for this class of aircraft.

In contrast to the approach adopted in the Cryoplane study, where a common wing size and shape was adopted for both fuels, the wing is optimized for each fuel individually here through a parametric study on wing area and aspect ratio. For all of the designs, the lift-to-drag ratio is increased by 4% and the aircraft structural weight is reduced by 7.5% to account for the time frame in which the aircraft will be adopted. A similar approach was also adopted in the Cryoplane study (see amongst others Astaburuaga et al. (2001) and Astaburuaga & van Holten (2001)). Further projections of these factors for more advanced timeframes can be found in Svensson (2005).

As it is the cornerstone of the design process, the design mission is laid down in section 4.1. As the thermodynamic design of the engine will be common to all aircraft designs, the engine selection is covered next. Using the same specific thrust and fuel consumption the engine is scaled according to the thrust required in each point of the parametric aircraft studies of the wing. Seen the number of design points in the executed parametric studies it was namely not feasible to optimize the engine for each point. Section 4.2 describes the values adopted for the various parameters needed in the engine design point calculations and comments on the trade-studies performed to select the final design point. Once the performance of the engine is established, the conventional long range aircraft designs are reported (section 4.3). Two different categories of aircraft are adopted, a 380 passenger and a 550 passenger aircraft. For each of the categories the results of the wing parametric studies are given for kerosene and hydrogen fuel and a comparison between both is made. Section 4.4 gives the influence of advances in technology and cruise altitude restrictions on the designs for both categories of aircraft. After this, section 4.5 details the twin fuselage design for the very large long range transport aircraft. A description of the concept is given and the results of the executed design are detailed. Before wrapping up this chapter and summarizes the outcome of the investigation in section 4.7, the fuel pre-heat cycle is briefly assessed.

4.1 Design mission

As the design process of an aircraft is centered around its mission specification great care must be taken to ensure the selection of an adequate specification. New transport aircraft design studies are therefore usually preceded by an extensive market and economical analysis before pinning down the final set of requirements the aircraft must comply with. As this falls outside the scope of this work, the mission specifications used here are adopted from Oelkers et al. (2000b) and Oelkers et al. (2000b). Both documents detail the missions requirements laid down by Airbus for the long range transport aircraft design studies performed in the Cryoplane project where a detailed selection of different aircraft classes was made[1]. Two different long range missions are utilized to represent both single and double deck wide body aircraft currently in operation.

The large, long range aircraft category is representative for current single deck wide body aircraft like the Airbus A340 or the Boeing 777. The aircraft of this class typically house between 250 and 500 passengers and have a design range that usually falls between 5000 and 7500 nm. Cruise Mach numbers for this type of aircraft range from 0.82 to 0.85 (Oelkers & Prenzel, 2001). The very large long range aircraft on the other hand is indicative for double deck aircraft that can transport between 400 and 700 passengers over a range higher than 7500 nm[2]. The cruise Mach numbers for this type of aircraft lies between 0.84 and 0.88 (Oelkers & Prenzel, 2001). In this work a capacity of 380 passengers in a 3 class layout is utilized for the large long range category. The very large long range category aircraft is designed for 550 passengers in a 3 class layout. Both aircraft fly at Mach 0.85 and have a design range of 7500 nm. Figure 4.1 shows the destinations that can be reached from various airports with this range. Everything north of the black line is a possible destination when departing from Heathrow airport . The red line shows the limit from New

---

[1] The different classes utilized in the Cryoplane project were chosen so that they encompass all subsonic passenger aircraft (Oelkers & Prenzel, 2001).

[2] As shown in section 4.3 the hydrogen fueled version of the large long range aircraft has a double deck layout whereas the very large long range aircraft with hydrogen requires 3 decks. In the remainder of this work, the aircraft are therefore referred to as large long range and very large long range rather than single and double deck.

York, whereas the blue and green line are located at a great circle distance of 7500 nm from Los Angeles and Sidney respectively.

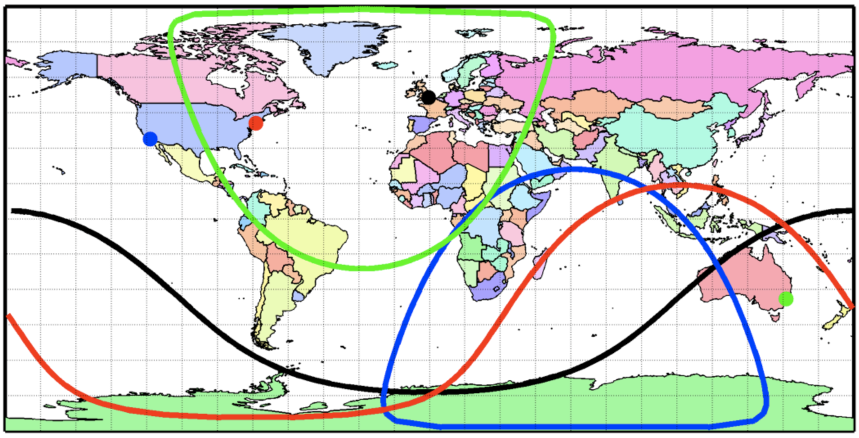

Figure 4.1. Operational capability of the designed aircraft.

To mitigate the financial risks involved with the decision to start a new design project a 'family approach' is usually adopted. Possible future stretch and shrink versions, obtained by plugging in or removing fuselage frames are taken into account in the preliminary phases of the design. For each of the aircraft categories laid down in Oelkers & Prenzel (2001), 3 additional family members are considered besides the baseline. The first family member is obtained by stretching the fuselage to house an additional 20% of passengers. The aircraft should have the same structure as the baseline but has a reduced range. The third third family member is an aircraft designed to cover the range of the baseline aircraft range with the payload of the stretched version. The fourth (and optional) member is the shrink version that is designed for a 20% lower passenger capacity but with an increased range.

To slightly simplify the designs, only two family members are considered in this work: the baseline and the stretch version. The stretch version is taken into account as it will partially determine the geometry of both the wing and the fuselage. The number of passengers abreast for the baseline version will namely depend on the fuselage of the stretch version. The dimensions of the stretch version should after all be compatible with runways and gates of existing airports. As such it should fit in the so-called 80 by 80 by 80 airport gate box. This box of 80 m wide and long and 80 feet high imposes an upper limit on the aircraft size for airports of category 4F. As the stretch version is furthermore designed for a longer range, it must be assured that the fuel storage capacity of the wing is sufficient to fly its mission. As such a costly redesign of the wing in a later stage is avoided.

4.2 Engine Design

As the aircraft of this work are designed for a considerable range, the preferred propulsion system type is a high bypass ratio turbofan. For this type of engine, two layouts are possible: a two spool layout with a booster on the low pressure shaft and a three spool layout. As the three spool layout leads to a significantly shorter engine, which implies a lower aircraft drag, this option has been selected.

Turbofans of long range transport aircraft typically have 3 points that need to be considered in the cycle selection (Saravanamuttoo, 2005). The engine is usually designed for minimum specific fuel consumption (SFC) in cruise. At top of climb however it will operate at its highest non-dimensional rating, leading to the highest relative spool speeds ($N/\sqrt{T_t}$) and pressure ratios for the compressors. The non-dimensional mass flow will also be the highest at this point which implies that the throat of the inlet is sized for mass flow requirements at top of climb. During takeoff on the other hand, the highest temperatures will be reached as well as the highest absolute spool speed. This point therefore determines the amount of turbine cooling air and sets the size of the shaft[3] (Saravanamuttoo, 2005). Following Rollin (2003), the beginning of cruise is set here to a relative corrected fan speed of 95%. Top of climb is fixed at 105% and takeoff is the reference point (100%).

The final design point of the engine will be a compromise that complies with all requirements at all points. It is however not possible to perform the design at all three points at the same time so that one point has to be chosen as the design point and the performance of the engine at the other points is checked to see if the specifications are satisfied. If this is not the case an iteration is made until the design meets all requirements. Seen the great range of the envisaged aircraft, the cruise point is selected as the design point with the objective of minimal SFC. The engine is then sized for each point of the aircraft design studies to ensure the required flow capability at top of climb and it is verified if sufficient thrust is available at takeoff as explained in section B.5. Below the selection of the design point parameters is reviewed in subsection 4.2.1. Then the results of the trade-off studies to fix the final design point are given (subsection 4.2.2).

4.2.1 Selection of the design point parameters

As the cruise rating is chosen for the design of the engine, relatively moderate values need to be chosen for the pressure ratios of the compressors as well as the turbine inlet temperature (TIT). After all, the pressure ratios and the TIT will be higher during both top of climb and takeoff due to the higher non-dimensional spool speed and ambient temperature respectively. The values chosen for the most important design point parameters adopted in this work are described below. An overview of the parameters that need to be specified for design point calculations can be found in Table C.3.

The **ram recovery** of the inlet is set to 0.997. This fairly high value is assumed to reflect the high bypass ratios of the design. After all, only a relatively small fraction of the total airflow rate through the engine will be in contact with the inlet. The value is furthermore consistent with Figure C.3, which is adopted from Jackson (2004).

Seen the high bypass ratio of the designs, the inner and outer part of the fan are considered separately. As explained in section C.3.3 the inner **fan pressure ratio and efficiency**

---

[3] As the ambient pressure is the highest at takeoff conditions this point will usually also set the casing thickness. This will however not be considered here.

are taken as a fraction of the outer fan values. The pressure ratio is set to 80% of the outer fan pressure ratio following Cumpsty (1997). Seen its strong influence on the engine performance, a trade-off study is performed to select the optimum outer fan pressure ratio of the specific designs. After all, the fan pressure ratio affects both the exhaust velocity of both the bypass and the core nozzle. A higher outer fan pressure ratio results in a higher bypass nozzle exhaust velocity but in a lower core nozzle exhaust velocity seen the higher power required from the LP turbine. A careful selection is thus required.

An increase in stage loading of a compressor stage implies a loss in efficiency (Philpot (1995) and Walsh & Fletcher (2004)). The polytropic efficiencies of the fan are therefor varied with the fan pressure ratio even though polytropic efficiency can be judged as a technology factor and can normally be held constant for cycle comparisons with varying pressure ratios (Saravanamuttoo et al., 2001). The variations adopted in this work are derived from Figure 4.2. The higher line of Figure 4.2 is selected for the designs in this work which is in line with values given in Walsh & Fletcher (2004). The outer fan pressure ratio is varied between 1.5 and 1.7 in the trade-off studies. The lower limit is selected to ensure that the fan pressure ratio stays above 1.4 throughout the flight cycle. For lower fan pressure ratios, a variable fan pitch or a variable area nozzle is namely needed to ensure an a satisfactory engine stability and fan surge margin. The fan nozzle will no longer be chocked for lower values which results in large variations in operating line between cruise and takeoff (Zimbrick & Colehour, 1990). Even though the figure indicates values up to about 2 for the single stage fan pressure ratios, the design point value is limited to 1.7 in this work in order to keep the fan pressure ratio at top of climb below 1.9 which is often judged to be the practical limit for single stage fans (Rizvi (2007) and Walsh & Fletcher (2004)).

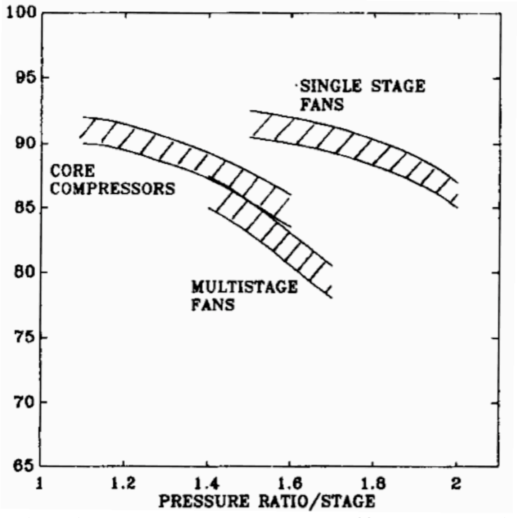

Figure 4.2. Effect of stage loading on compressor efficiency, adopted from Philpot (1995).

The **overall pressure ratio** of the engine is set to 45. This moderate value is adopted for several reasons. First of all, the pressure ratio of all the compressors will be higher at both takeoff and top of climb. Secondly, increasing the overall pressure ratio leads to smaller compressor blades for the last stages. As the bypass ratios under consideration are fairly high, this could lead to problems in the gaspath design of the high pressure compressor despite the high value adopted for the hub to tip ratio of the last HPC stage (0.92 see section C.5.2). A higher bypass ratio will namely lead to a lower mass flow rate through the engine core and thus also to lower blade heights for a given axial velocity in the compressor. As the HPC is furthermore driven by a single stage HP turbine, this would also lead to an unrealistically high RPM of the HP spool. The OPR is finally also limited as it is intended to use the same engine cycle for both fuels to allow a fair ground for comparison between both fuels in a first assessment. As liquid hydrogen fueled aircraft require smaller engines, this also restricts the allowable value for the OPR in the light of the previous reflections.

As a three spool engine is considered the distribution of the core pressure ratio between the intermediate and the high pressure compressor need to be chosen. Values close to unity are often found (for instance in Doulgeris (2008)). Cumpsty (1997) however indicates the use of a slightly higher pressure ratio for the HPC. As the IPC also needs to be driven by a single stage turbine, which will be at a lower rotational speed than the HPT, this practice is adopted here too. The **ratio of the HPC to IPC pressure ratio** is therefore taken as 1.1. As this results in pressure ratios between 5 and 6 for both compressors, variable geometry will not be needed in either of the compressors (Ramsden, 2004a).

The **polytropic efficiency** of both the HPC and IPC are set to 0.905 which is according to Walsh & Fletcher (2004) in line with the stage loading of 0.35 selected for the gas path calculations (see section C.5.2).

The selection of the β parameter (see Appendix C) does not play a role in the design point calculations but it affects the off-design performance of the engine. As it was found that the IPC tended to surge when β was set to its standard value of 0.5 (Kurzke, 2004b) the design point value was set to 0.4 for all of the considered cases.

The **combustion chamber efficiency** is set to 0.995 which is a typical value for modern combustion chambers during cruise operation (Jackson, 2004). The **combustion chamber pressure drop** on the other hand is taken as 5% of the combustor inlet pressure. The turbine inlet temperature is chosen in the next section.

For the **turbine polytropic efficiencies** a value of 0.91 is adopted which is a fairly high value seen the high stage loadings adopted for the design of all turbines (see section C.5.4). However, the turbine efficiency should be regarded as a cold flow efficiency where the losses due to the introduction of the cooling air are not included. They are accounted for by the adopted cooling air model (see section C.3.9). Higher values can furthermore be found in studies on advanced cycles (Doulgeris, 2008). The choice of turbine efficiencies is therefore reasonable but ambitious. For the LPT a slightly lower efficiency (0.89) is adopted to reflect the higher stage loading that was assumed for this turbine.

Finally, as explained in section C.3.9, the amount of cooling air required to keep the metal temperature of the blades and vanes of the HP and IP turbine is varied with the turbine inlet temperature. A metal temperature of 1100 K is imposed for the cycle calculations. This value was adopted after several iterations to obtain a metal temperature at takeoff (the sizing point for the cooling air circuit) below 1300 K which is approximately the highest temperature that current turbine materials can sustain (Kurzke, 2003).

4.2.2 Engine trade-off studies

As explained previously, tradeoff studies are performed to select the final design point for the engine. The turbine inlet temperature and the fan pressure ratio and bypass ratio are the main parameters which are used in the tradeoff studies in this work. Below the choice of the final values for these parameters is elucidated. First however the effect of the overall pressure ratio is indicated. This is shown on Figure 4.3 which gives the engine specific fuel consumption in function of specific thrust for an overall pressure ratio of 35 and 45 for various combinations of outer fan pressure ratio and turbine inlet temperature for kerosene fuel.

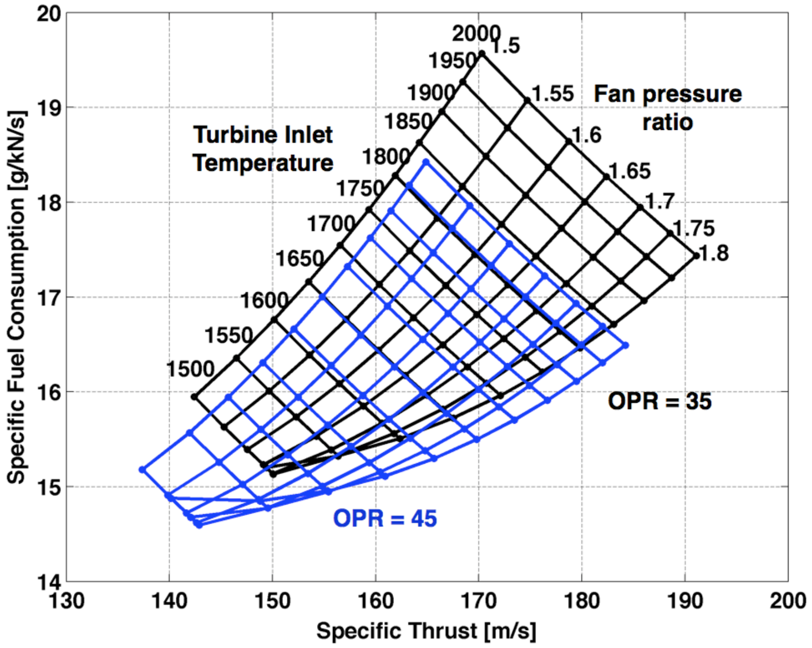

Figure 4.3. The effect of engine overall pressure ratio on performance.

As the figure shows, the turbine inlet temperature (for a given overall and fan pressure ratio) must be selected as a compromise between engine efficiency and engine size (and thus drag). A higher turbine inlet temperature increases the consumption of the engine but leads to a smaller, lighter and less draggy engine. As the cooling air flow is adapted to keep the metal temperature at 1100 K regardless of the turbine inlet temperature, the turbine life is more or less constant over the range of turbine inlet temperature shown on the figure[4]. For a TIT in cruise of 1550 K this leads to slightly less than 10% of the compressor delivery pressure being bled off for cooling air. At 1900 K however over 20% of cooling air is needed. It is assumed here that all cooling air is taken from the HPC exit. In reality the IPT cooling air will be tapped off at lower pressures to reduce the amount of work spent on the cooling air. Bleeding air from an intermediate compressor position

---

[4] The effect of higher temperature gradients and thus thermal stresses on low cycle fatigue is neglected here.

will however require an adaptation of the compressor map for accurate modeling (Kurzke, 2003). As appropriate maps are not available this is not considered here[5]. Seen the small amounts of IPT cooling compared to HPT cooling, omitting this only has a small impact on the cycle results.

Figure 4.3 also indicates that increasing the overall pressure ratio (from black to blue) entails a similar compromise. For a given combination of fan pressure ratio and turbine inlet temperature, the SFC is reduced when increasing the OPR but the specific thrust also falls. For a given turbine inlet temperature, the specific fuel consumption decreases for increasing fan pressure ratios. If the fan pressure ratio is however raised to a too high value, the core nozzle is no longer choked as too much work is extracted by the fan from the LPT. At this point the specific fuel consumption increases again as shown on Figure 4.3 for the lowest turbine inlet temperatures.

Figure 4.4 shows that a similar trade-off is required for the bypass ratio of the engine. The figure shows a similar carpet plot for bypass ratios 8, 10 and 12 for the hydrogen fueled engines. Increasing the bypass ratio leads to a lower specific thrust and thus a bigger engine. The fuel consumption is however reduced.

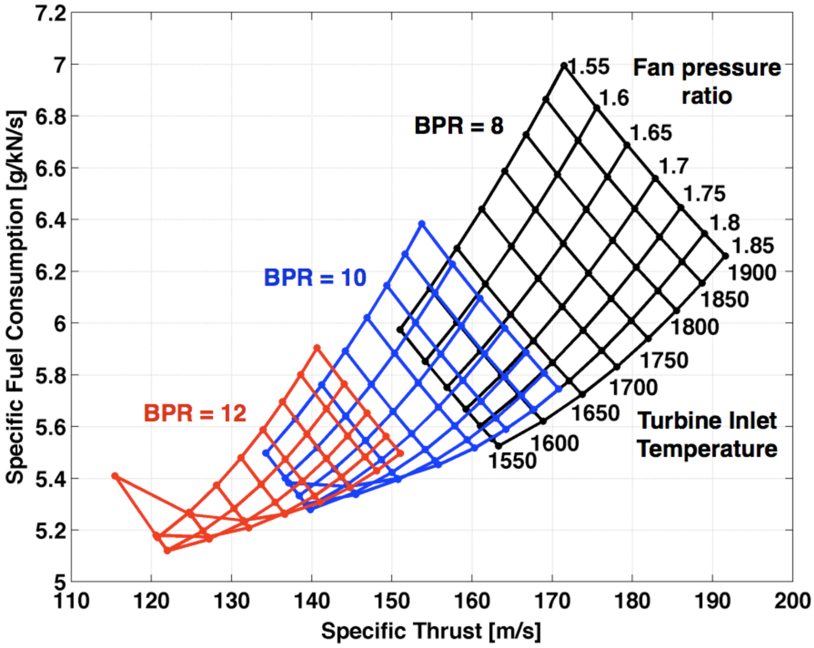

Figure 4.4. The effect of engine bypass ratio on performance.

A comparison between Figures 4.3 and 4.4 indicates the effect of using hydrogen on the engine cycle. For kerosene the core nozzle is already unchoked at a fan pressure ratio of 1.75 to 1.8 for a TIT of 1550 K at an overall pressure ratio of 45 (blue curve on Figure 4.3). When hydrogen is used as a fuel on the other hand the nozzle does not unchoke up to

---

[5] Gasturb allows the specification of an enthalpy fraction for the bleed air without adapting the compressor maps (Kurzke, 2004b). The air is then assumed to have consumed only the imposed fraction of the compressor work.

fan pressure ratios higher than 1.85 at the same BPR, OPR and TIT (black curves on Figure 4.4. This is a direct consequence of the different composition of the combustion gases as explained in section 2.2. The figure also shows that the specific fuel consumption is reduced by about 63.5%. The energy specific fuel consumption increases by about 2 to 3% which is in line with the values found in literature (Boggia (2000), Corchero & Montañés (2003) and Svensson (2005)). Roughly half of that increase could be recuperated by increasing the turbine inlet temperature to 250 K as would be feasible in a conventional cycle by the introduction of a heat exchanger in the exhaust pipe (Corchero & Montañés, 2003). If the engine would be designed for a constant thrust rather than for constant TIT, the energy specific fuel consumption of the engine could even be reduced slightly as the turbine inlet temperature would drop by 30 to 50 K, as shown in Verstraete et al. (2005a).

As the main objective for a turbofan for a long range transport aircraft is minimum SFC during cruise, a relatively low turbine inlet temperature is adopted to keep the fuel consumption within reason. A value of 1550 K is assumed here which leads to the engine performance given in Table 4.1.

Table 4.1. Engine performance for kerosene and hydrogen fuel.

		Kerosene		**Hydrogen**	
		BPR 8	**BPR 10**	**BPR 8**	**BPR 10**
Cruise	TIT [K]	1550	1550	1550	1550
	SFC [g/kN/s]	14.78	14.17	5.41	5.17
	$F_{N,spec}[m/s]$	149.5	127.8	154.1	132.1
Top of Climb	TIT [K]	1750	1780	1760	1780
	BPR	7.6	9.5	7.6	9.4
	OPR	52.2	53.3	54.0	54.1
Takeoff	TIT [K]	1890	1940	1890	1915
	BPR [-]	7.7	9.6	7.9	9.7
	OPR [-]	49.5	50.4	49.1	50.1
	$F_{N,spec}[m/s]$	335.5	311.4	342.6	316.5

4.3 Conventional aircraft

As explained previously two different classes of long range aircraft will be investigated. A 380 passengers and a 550 passenger aircraft will be considered and for each aircraft type a wing parametric study will be performed. As the passenger capacity does not change, a common fuselage cabin is used for each design of the parametric study[6]. The fuselage dimensions are therefore given first. Then the results of the wing parametric studies for the large long range transport aircraft are given. Both kerosene and hydrogen fueled versions are covered before switching to the very large long range aircraft class.

---

[6] For the kerosene fueled aircraft this implies a common fuselage, for the hydrogen fueled aircraft however, the length of the fuselage is adapted to the fuel required for the mission. Hence the fuselage slightly changes.

4.3.1 Fuselage dimensions

A detailed design of the fuselage of large and very large long range transport aircraft was made for both kerosene and hydrogen fuel in the Cryoplane study by the university of Delft (Astaburuaga & van Holten (2001), Krijnen et al. (2001) and Astaburuaga et al. (2001)). As calculations of the fuselage dimensions by the author resulted in values that were very close to the designs of Delft University, the fuselage for the conventional designs is adopted from these references. Figure 4.5 shows the fuselage of the baseline and the stretch kerosene fueled large long range transport aircraft. As can be seen from the figure, the baseline version can transport up to 550 passengers in a high density layout whereas the stretch version carries up to 650 passengers in the same layout. As the length of the stretch hydrogen version would be exceeding the 80 m gatebox constraint due to the location of the fuel tanks inside the fuselage a double deck layout is required for the hydrogen fueled large long range transport aircraft.

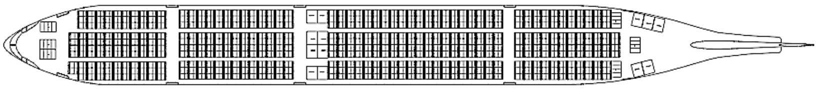

550 seats. High density

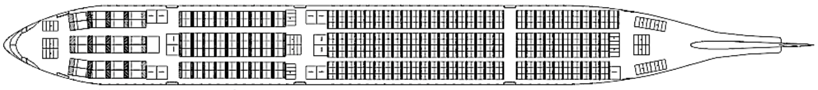

380 seats. 3 Class layout (24 FC, 63 BC, 293 YC)

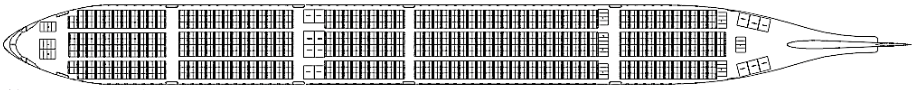

652 seats. High density

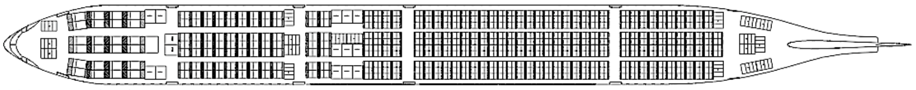

454 seats. 3 Class layout (24 FC, 77 BC, 354 YC)

Figure 4.5. The cabin of the baseline version and stretched version of the large long range transport aircraft with kerosene, adopted from Astaburuaga & van Holten (2001).

Figure 4.6 shows the cross-section of the fuselage of the very large long range transport aircraft for hydrogen (left) and kerosene. The kerosene fueled version has a (conventional) double deck layout whereas the hydrogen fueled version requires a triple deck. Even with this triple deck layout the fuselage length almost exceeds the airport box constraint which makes a future stretch version impossible.

The main characteristics of the fuselages of both classes are indicated in Table 4.2. These characteristics are retained here except for the fuselage length for the hydrogen fueled aircraft. As the engines adopted here differ from the ones used in the Cryoplane study, a different fuel mass will be obtained for a given mission. The fuselage length is therefore adapted keeping the cabin length constant and increasing or reducing the size of the fuel tanks in front and aft of the cabin.

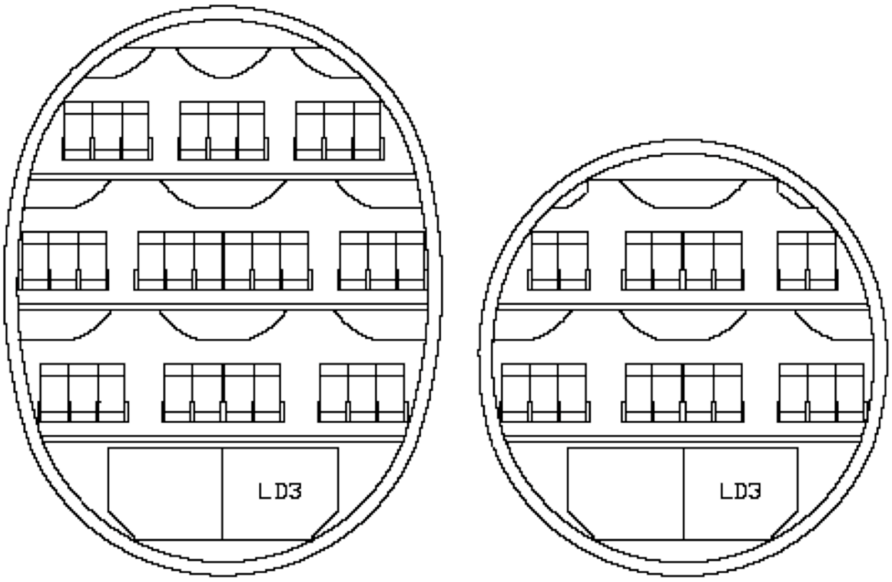

Figure 4.6. Fuselage cross section for the very large long range transport aircraft, adopted from Astaburuaga et al. (2001).

Table 4.2. Fuselage characteristics for the large and very large transport aircraft, derived from Astaburuaga & van Holten (2001) and Astaburuaga et al. (2001).

		380 passengers		**550 passengers**	
		Kerosene	**Hydrogen**	**Kerosene**	**Hydrogen**
Fuselage length [m]		68.5	65.4	63	78
Fuselage width [m]		6.95	7.65	7.20	7.70
Fuselage height [m]		6.95	7.65	7.60	10.00
Seats abreast	First Class	2-2-2	2-2-2 (LD)	2-1-2 (UD)	2-2-2 (MD)
	Business Class	2-3-2	2-2-2 (UD)	2-2-2 (LD)	3-2-3 (MD)
	Tourist Class	3-4-3	2-4-2 (UD)	2-4-2 (UD)	2-4-2 (UD)
			3-4-3 (LD)	3-4-3 (LD)	3-4-3 (LD)

4.3.2 Wing Parametric Study for the large long range transport aircraft

As explained in the introduction of this chapter, the wings of the kerosene and hydrogen fueled aircraft are sized independently of one another, in contrast to the minimal change approach that was adopted for the Cryoplane study where a common wing was utilized for both fuels. For each of the fuels a wing parametric study is thus executed to find the optimum combination of wing area and wing aspect ratio. After all, the fuel consumption of the engines is completely different and the wing of the hydrogen fueled aircraft is not restricted in size by the need to store the mission fuel. The figure of merit used in these studies is the direct operating cost of the aircraft which is determined for a mission with a range of 4000 nm with 550 flights per year (Oelkers et al. (2000b) and Oelkers et al.

(2000a)). As the design point for both fuels is virtually insensitive to the load factor, a load factor of 0.7 is assumed for all direct operating cost calculations. Below, first the results for the kerosene fueled aircraft will be given. The outcome of the parametric study is detailed for hydrogen next, before comparing both fuels.

4.3.2.1 Kerosene fueled aircraft

The direct operating cost for the large long range kerosene aircraft with BPR 8 engines is shown on Figure 4.7. The figure shows contour levels of cost per seat mile for a fuel price of 0.3 $/MJ (approximately 4.0 $/gallon). This high price level is chosen as representative for a timeframe in the future. However, even if both the absolute level of the DOC as well as the share of fuel in the costs obviously change with the assumed fuel price, the design point hardly moves with fuel price for all of the considered cases, except for very low (historical) fuel prices down to 0.8 $/gallon. This is shown for this particular aircraft on Figure 4.8. As similar observations are made for the other cases, the corresponding figures of the later case are not given here. A common design point for all fuel price levels is therefore adopted for each of the case studies.

Besides the DOC levels the figure also shows several restrictions on the design space, as detailed in section B.5.2 of Appendix B. The full thick black line represents the lower limit on the wing size imposed by the need to store the fuel. The line gives the boundary where the wing fuel capacity equals the fuel needed to fly a mission of 110% of the design range with reduced payload (keeping the maximum takeoff mass of the aircraft constant). The dashed black line on the other hand indicates the buffet limit explained in section B.5.3. The white lines on the plot finally indicate levels of approach speeds in knots. After all, the aircraft must not complicate the traffic control near the airport. Its approach speed should therefore be close to the approach speed of other aircraft. As proposed in Oelkers et al. (2000c), a limit of 140 kts is adopted for both aircraft categories. To allow a fair comparison the approach speed is calculated at the weight where half the mission fuel is consumed. The areas of the design space that are restricted by one or more constraints are shaded on Figure 4.7. This practice will be adopted for the remainder of this text. Finally the white dot on the figure indicates the design point for the aircraft which is the point where all boundaries are respected that yields the minimal operating cost. As shown here, this point lies at a wing area of 375 m^2 and an aspect ratio of 11.5.

As the direct operating costs are a function of both the fuel weight (and thus cost) as well as the aircraft initial purchase price (which is mainly function of the takeoff weight), both the fuel weight and the takeoff weight are given on Figure 4.9.

The resulting plots for the parametric study are very similar for engines with a BPR of 10. They are therefore omitted here. The outcome is summarized for both fuels in Table 4.3. The table gives results for both a stepped cruise and a constant altitude cruise option.

As can be seen from the Table, the benefit in specific fuel consumption from the BPR 10 engines is not reflected by a reduction in takeoff weight for either the constant altitude or the stepped cruise climb. This is due to the decrease in lift to drag ratio, resulting from the larger dimensions and thus higher drag of the higher bypass ratio engines. As the weight during the flight is more or less similar for both bypass ratios, the higher bypass ratio

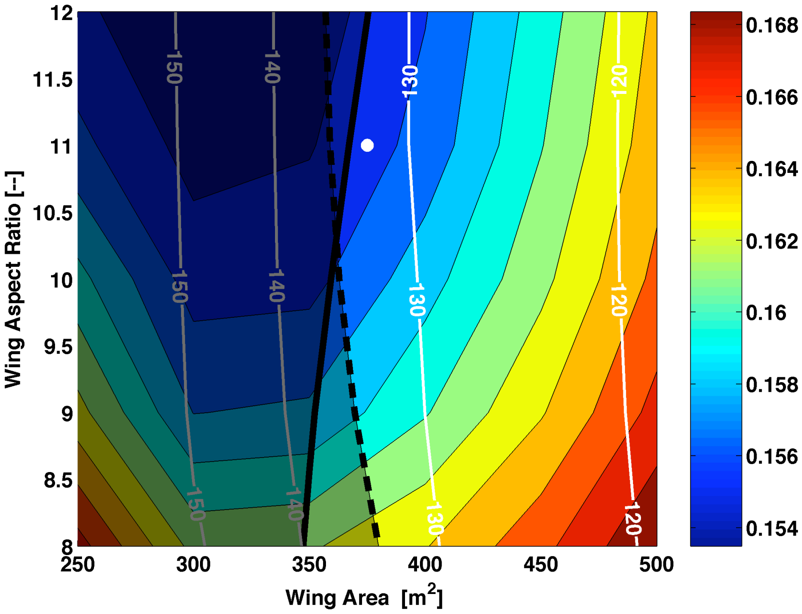

Figure 4.7. Direct operating costs for the kerosene fueled long range transport aircraft equipped with BPR 8 turbofans, for a fuel price of 0.03 \$/MJ.

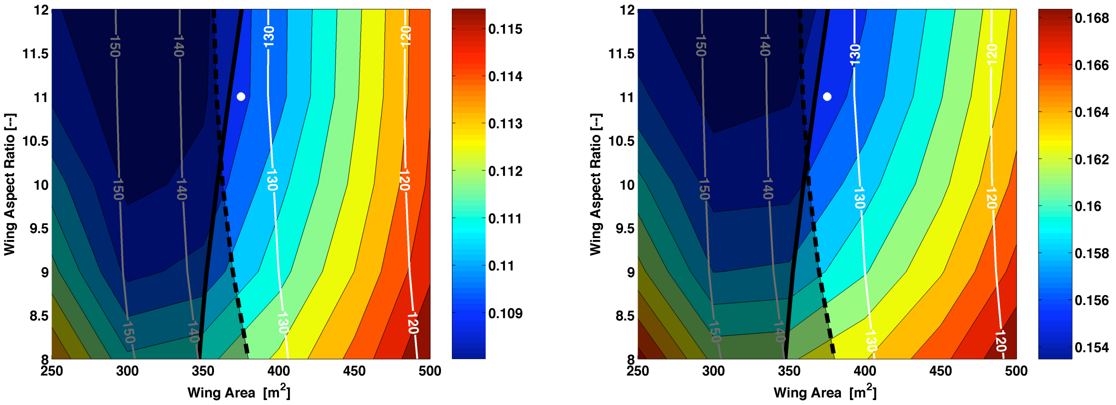

(a) DOC at 0.006 \$/MJ

(b) DOC at 0.03 \$/MJ

Figure 4.8. DOC for low and high fuel price scenario.

engines need to provide a higher thrust throughout the whole flight. The final outcome is that the fuel consumption for the flight increases for the higher bypass ratio, which leads to a higher all up weight. As this is the case for both the constant altitude and stepped cruise flight, it cannot be attributed to a different stepped climb pattern. After all, in the simulations the aircraft is allowed to climb as soon as the specific range is improved at a higher altitude (provided that the engine cruise thrust is sufficient). This entails that the aircraft will climb relatively straightforward to the maximum imposed altitude for some points of the investigated area whereas for other points a relatively long time is spent at low altitudes. This cruise altitude adaptation flexibility is clearly not available in a real flight (unless for very scarcely used routes) where traffic control will give the green light

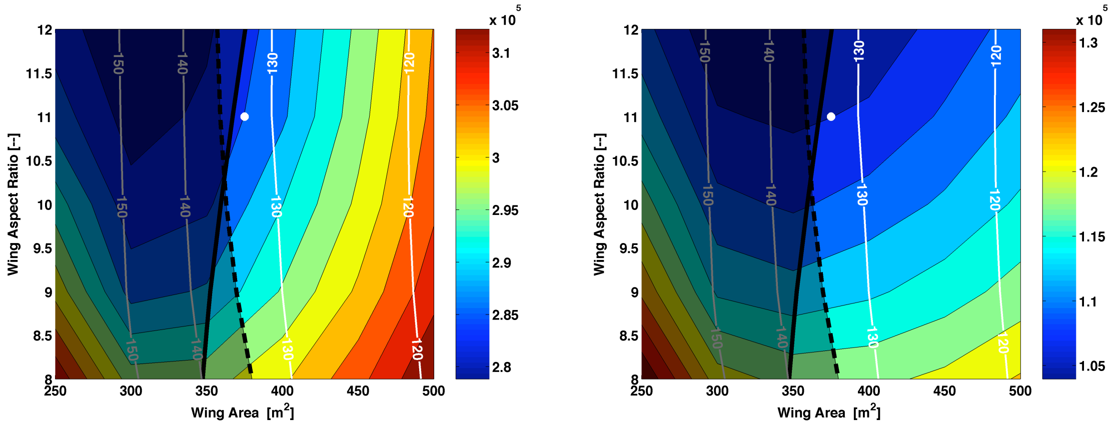

(a) W_{TO} (b) W_F

Figure 4.9. Takeoff and fuel mass for the kerosene fueled large long range transport aircraft with BPR 8 turbofans.

Table 4.3. Design point characteristics for the long range transport aircraft with kerosene fuel.

	Stepped Cruise		**Constant Altitude**	
	BPR 8	**BPR 10**	**BPR 8**	**BPR 10**
Wing Area $[m^2]$	375	385	395	410
Wing Aspect Ratio [–]	11.0	11.0	10.0	11.0
Takeoff Weight $[kg]$	285000	297000	307500	317500
Operating Empty Weight $[kg]$	133250	140000	138000	145250
Fuel Weight $[kg]$	115750	121000	133000	136000
Maximum Fuel Weight $[kg]$	123500	129200	142250	145250
Engine Net Thrust $[kN]$	196.5	232.0	213.4	244.0
Average Lift-to-drag Ratio [–]	17.9	17.7	16.9	17.2
Engine Length $[m]$	3.97	4.59	4.14	4.71
Engine Diameter $[m]$	2.50	2.89	2.60	2.96
Thrust-to-weight ratio [–]	0.281	0.319	0.283	0.314

or not to climb to the optimum altitude. To ensure that it will not bias the results the constant altitude cases are also given.

The higher thrust in Table 4.3 is mainly a consequence of the higher thrust lapse rate with both speed and altitude for the higher bypass ratio engines. The bigger diameter is a direct result of the higher BPR whereas the increase in length is an indirect outcome. As the fan tip speed was limited to a specific speed (see Appendix C), the higher diameter fan will operate at a lower RPM, thus forcing the LPT to turn slower. As a consequence extra LPT stages are required, leading to a (sometimes sharp) increase in length. In general two extra LPT stages were required. Sometimes even three. Although it is realized that this might be cured by changing the details of the gas path calculations in a trade-off study, it falls outside the scope of this work. As the main goal is a comparison between kerosene and hydrogen fueled aircraft, it is believed that this will not change the conclusions. In a more detailed step later on, this could however be adapted.

For the kerosene fueled aircraft, a restriction on its flight level to 35000 ft leads to an increase in takeoff weight in the order of 7 to 8%. As a consequence the empty weight increases by about half that value. The fuel penalty is however significant and falls around 15%. To provide sufficient thrust for the aircraft, the net thrust has to increase by about 8%.

4.3.2.2 Hydrogen fueled aircraft

For the hydrogen fueled large long range transport aircraft a similar study was executed. The DOC results of that study are given on Figure 4.10. The figure clearly looks different as the fuel storage limit on the wing size is no longer present. Instead of one single buffet limit 3 lines are now plotted, representing (from left to right) 100%, 95% and 85% of the lift coefficient to which kerosene fueled aircraft are limited to avoid buffeting of the wing. After all, as indicated in Chapter 2 it is not clear to what extent the presence of fuel acts as a damper. The results for hydrogen fueled aircraft are therefore given here for two buffet limit levels, 95% and 85%. Both design points are indicated on the figure. Table 4.4 summarizes the results for the 95% buffet limit, whereas the 85 % case is given in Table 4.5.

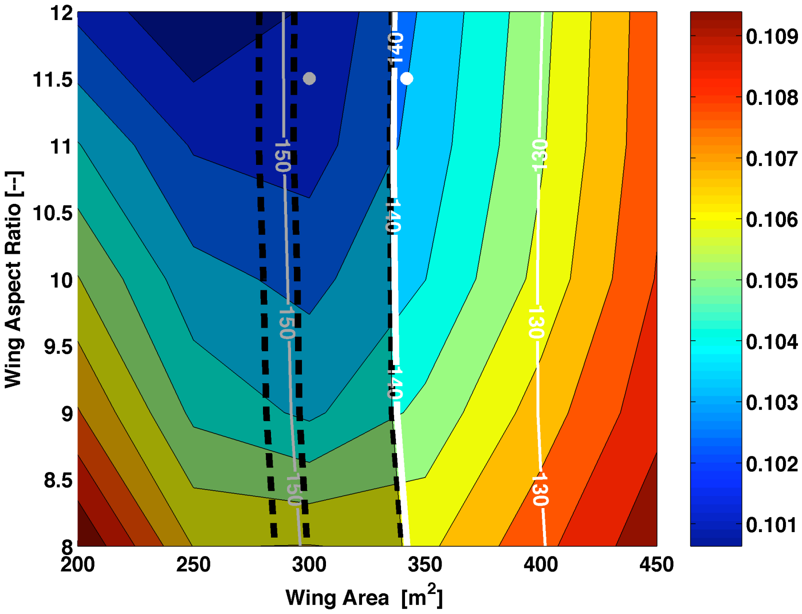

Figure 4.10. Direct operating costs for the hydrogen fueled long range transport aircraft equipped with BPR 8 turbofans, for a fuel price of 0.03 $/MJ.

Despite what the figure might suggest by the reduction in wing area of around 16 to 18 percent, the aircraft characteristics remain very similar. Fuel, takeoff and operating empty weights are virtually identical suggesting that the buffet limit assumption is not as critical as it looks at first sight. If it would prove to be an issue, it can be catered for by an increase in wing area that will not significantly affect the operational characteristics of the aircraft. As an alternative the wing might have to be 'beefed' up to increase the structural rigidity, leading to a small penalty in wing weight, as will be discussed in section 4.5 for the twin fuselage aircraft wing.

Table 4.4. Design point characteristics for the long range transport aircraft with hydrogen fuel at 85% buffet.

	Stepped Cruise		**Constant Altitude**	
	BPR 8	**BPR 10**	**BPR 8**	**BPR 10**
Wing Area [m^2]	340	340	350	345
Wing Aspect Ratio [–]	11.5	11.5	11.0	11.0
Takeoff Weight [kg]	216000	214000	224000	221000
Operating Empty Weight [kg]	141000	140000	145000	143000
Fuel Weight [kg]	38400	37300	43000	41600
Maximum Fuel Weight [kg]	41400	40200	46400	44800
Engine Net Thrust [kN]	168.0	167.9	173.1	172.3
Average Lift-to-drag Ratio [–]	17.0	16.9	16.0	15.9
Engine Length [m]	3.74	3.88	3.80	3.94
Engine Diameter [m]	2.35	2.44	2.39	2.47
Thrust-to-weight ratio [–]	0.317	0.320	0.315	0.318

Table 4.5. Design point characteristics for the long range transport aircraft with hydrogen fuel at 95% buffet.

	Stepped Cruise		**Constant Altitude**	
	BPR 8	**BPR 10**	**BPR 8**	**BPR 10**
Wing Area [m^2]	300	295	305	300
Wing Aspect Ratio [–]	11.5	11.5	11.0	11.0
Takeoff Weight [kg]	211000	208000	218000	215000
Operating Empty Weight [kg]	137000	135000	140000	138000
Fuel Weight [kg]	38000	36900	42000	40700
Maximum Fuel Weight [kg]	41000	39800	45250	43700
Engine Net Thrust [kN]	165.2	164.7	169.9	169.1
Average Lift-to-drag Ratio [–]	16.6	16.4	15.9	15.8
Engine Length [m]	3.71	3.85	3.76	3.90
Engine Diameter [m]	2.33	2.42	2.37	2.45
Thrust-to-weight ratio [–]	0.319	0.322	0.318	0.321

The results for the hydrogen fueled aircraft show that for this mission, the BPR 10 engine proves to be the best choice, despite its slightly bigger dimensions. This is mainly a consequence of the fact that the engines are dimensioned for landing rather than top of climb, as was also discovered by Brewer (1991). This leads to a thrust level that is very similar for both engines. As a consequence, the lower specific fuel consumption of the higher bypass ratio engines pays off and leads to a fuel reduction in the order of 1 ton (3-4%). Consequently the aircraft with the BPR 10 engines has a slightly lower takeoff and operating empty weight.

4.3.2.3 Comparison between both fuels

A comparison between both fuels for the stepped climb case shows that the takeoff weight for the hydrogen fueled aircraft is about 25% lower than when kerosene would be used. The empty weight increases slightly (with maximum around 3%) due to the heavy fuel tanks, but is in the same order of magnitude for both fuels. The most remarkable difference, as expected, lies in the fuel weight which is 67 to 70% lower. Due to the different design point for the engines, the thrust level drops with 16% for the BPR8 engines and even 30% for the BPR 10 engines. Due to the lower fuel weight, wing area can be reduced by about 12% whereas aspect ratios remain more or less the same.

The results differ from what was found in the Cryoplane study. The conclusion of Cryoplane for the long range transport aircraft class were a takeoff weight reduction of 15 percent at an operational empty weight of 27% higher. The fuel weight decreased by about 62% whereas the takeoff thrust remained the same. Even though the difference can be partially attributed to the different models and engine decks (in the Cryoplane study a Trent 884 was used), a significant share comes from the reduction in wing area whereas in the Cryoplane study the wing area was held constant.

As the direct operating costs were used as a figure of merit to select the design point, they are compared for both fuels here too. Figure 4.11 shows the direct operating costs for kerosene and hydrogen in function of the fuel price. For hydrogen 3 levels are given. The first level, named 'H2' in the legend indicates the direct operating costs if no increase in aircraft acquisition and maintenance cost has to be paid due to the hydrogen fuel. The second and third level on the other hand give the direct operating costs for a 10 respectively 50% increase in aircraft acquisition and maintenance costs.

The figure indicates a clear advantage for hydrogen and shows that for all considered prices, hydrogen becomes economically competitive even when a much higher price per energy content is paid. Even if the maintenance and acquisition costs would be 50% higher, the direct operating costs for hydrogen are still competitive for a much higher fuel price. Similar results are obtained with the second method, but they are more obscured by the need to assume a number of aircraft produced as well as a production rate. They are therefore omitted here. A change in BPR from 8 to 10 for the comparison also leads to results that were very alike. The difference is even slightly higher as the BPR 10 version for hydrogen showed better performance whereas the BPR 10 version for kerosene turned out to be worse. The case presented here is therefor judged to be conservative within the validity of the DOC model adopted. As the slope of the DOC for kerosene is higher than that of hydrogen fuel, the figure furthermore indicates that the advantage of hydrogen will become more distinct if fuel prices (of both fuels rise).

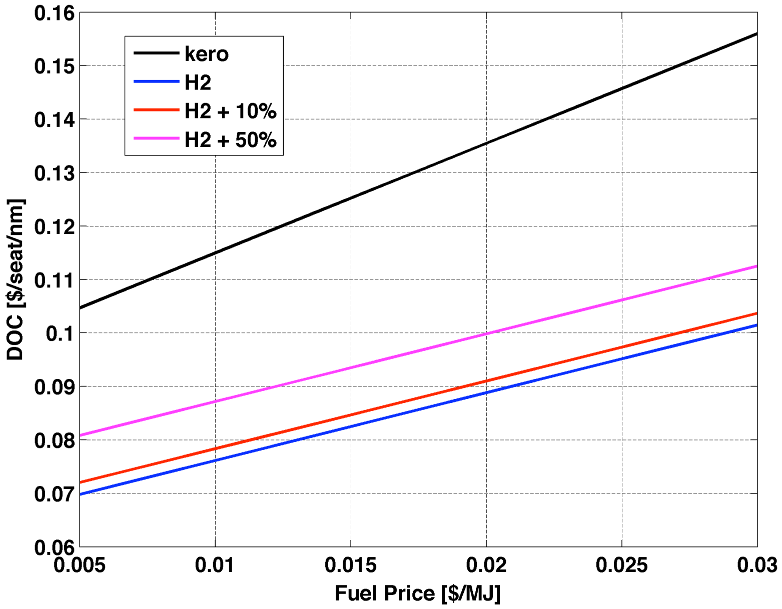

Figure 4.11. Direct operating costs for both fuels for a range of fuel prices.

4.3.3 Wing Parametric Study for the very large long range transport aircraft

A similar study was set up for the very large long range aircraft class. As the buffet limit proved to be less of an issue than could be thought at first sight, results for hydrogen will only be given for the 95% buffet limit case. The differences between both buffet margins namely only amount to about 3% in takeoff and operating empty weight and 1 % in fuel weight. Wing sizes are still significantly different, so both design points will be given on the figures for all considered cases. As similar differences are found between the constant altitude and stepped cruise cases as for the 380 passenger design (percentage wise), only the stepped climb cases are given here.

Figure 4.12 shows the direct operating cost contour plots for both kerosene and hydrogen fuel. As can be seen from the figure, they differ from the 380 passengers case. The main difference is the restriction of a wing span of 80 meters which prohibits the use of the upper right area of the domain. For the hydrogen fueled aircraft, the contour lines also tend to be more wavy, which is partly due to the discretization of the domain but also to a large extent due to the change in fuselage length between the different points of the plot. Seen the higher fuel load bigger adaptations to the fuselage length are needed compared to the 380 pax case presented earlier resulting in a difference of slightly over 5 meter between the point with the lowest fuel weight and the one with the highest one. Table 4.6 summarizes the design point data for both fuels and both bypass ratios. The data for hydrogen represents the 95% buffet limit case as discussed earlier.

As can be seen from the table, the lower fuel consumption of the BPR 10 case now pays off for the kerosene fueled version seen the significantly higher fuel load, resulting in a lower

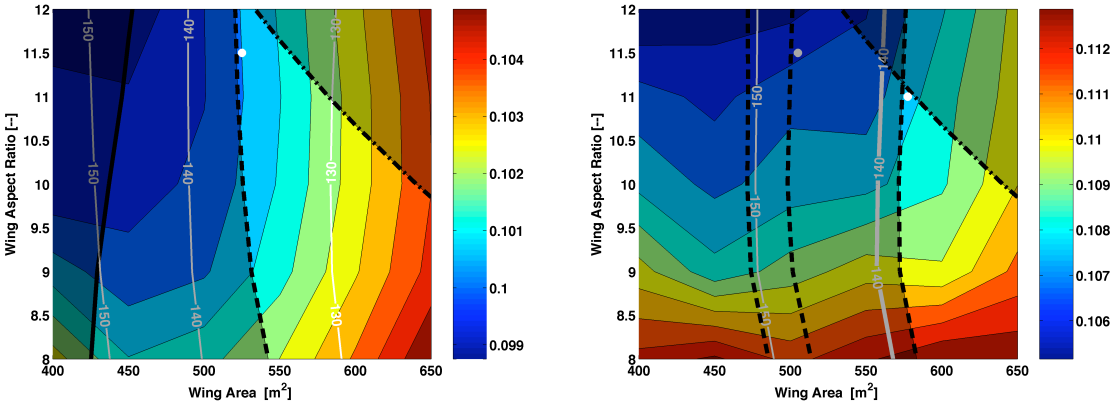

(a) kerosene (b) hydrogen

Figure 4.12. DOC for kerosene and hydrogen fueled very large long range transport aircraft with BPR8 engines.

Table 4.6. Design point characteristics for the very large long range transport aircraft.

	Kerosene		**Hydrogen**	
	BPR 8	**BPR 10**	**BPR 8**	**BPR 10**
Wing Area [m^2]	525	505	505	505
Wing Aspect Ratio [–]	11.5	11.5	11.5	11.5
Takeoff Weight [kg]	413000	398000	360000	358000
Operating Empty Weight [kg]	204000	201000	247000	246000
Fuel Weight [kg]	157000	145000	61300	59700
Maximum Fuel Weight [kg]	168000	153000	66000	64200
Engine Net Thrust [kN]	281.0	289.3	259.1	259.2
Average Lift-to-drag Ratio [–]	19.8	19.4	18.2	18.1
Engine Length [m]	4.75	5.13	4.65	4.83
Engine Diameter [m]	2.98	3.22	2.92	3.03
Thrust-to-weight ratio [–]	0.277	0.296	0.293	0.295

wing area and a reduction in takeoff weight of about 4% and in fuel weight of about 8%. Due to the thrust lapse rate the higher bypass ratio engine still remains bigger and needs to be designed for a higher take-off thrust. For hydrogen, both bypass ratios turn out to be similar as the small gain in fuel weight is compensated by the higher engine weight.

More remarkable are the inter-fuel comparisons. The wing area for both fuels in now almost identical, even for the 'higher' assumption on buffet limit. The takeoff weight is reduced by only about 11-13 % and the empty weight goes up by approximately 23%. The fuel weight is consequently 'only' about 60% smaller compared to almost 70 % for the 380 passenger aircraft. The main difference between the results is related to the high fuel weight, which leads to a significantly higher fuel tank mass than in the large long range case and reduces the benefits from the adoption of hydrogen. This is reflected in Figure 4.13 by the smaller spacing between the kerosene and hydrogen curves. Hydrogen fuel still is competitive at a higher price per energy content, but the price difference is significantly reduced compared to the long range transport aircraft. Whereas for the large long range aircraft a 4 to 6 times higher fuel price per energy content could be afforded, this factor is reduced here to 3 to 5 times.

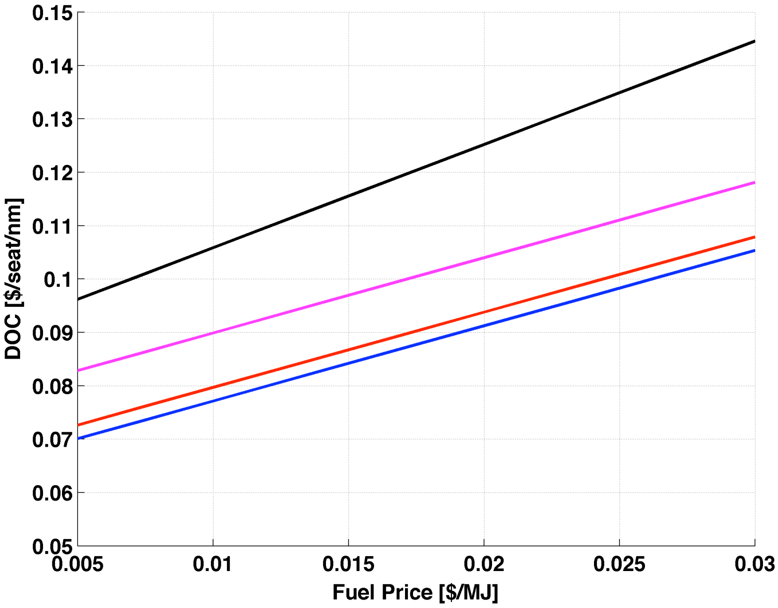

Figure 4.13. Direct operating costs for both fuels for a range of fuel prices.

As the fuselage length is furthermore flirting with the 80 m airport box limit, the potential for this class of aircraft is significantly smaller than for the large long range aircraft. The twin fuselage concept is therefor investigated in the next section.

4.4 Influence of progress in technology and cruise altitude restrictions

To analyze to what extent the results of the design studies are influenced by the assumptions adopted in this work, the influence of technological progress on the characteristics of both kerosene and hydrogen fueled aircraft is looked into. After this, the implications of cruise altitude restrictions to avoid contrails are investigated.

4.4.1 Influence of an advancement in technology

As the timeframe in which hydrogen fueled aircraft could be adopted is still several years or even decades ahead and technology is continuously improving, the influence of technological progress on the design characteristics is assessed in this section. This will not only indicate whether the potential for hydrogen fueled aircraft depends strongly on the assumed level of technology, it will also reveal whether the sensitivity of the design point to an increase in technology is higher for one or the other fuel.

Following Liebeck et al. (1995), Oelkers et al. (2000c) and Oelkers et al. (2000d), three different technology factors are incorporated in the modules of the aircraft design platform. The different factors allow to change the level of technology for aerodynamic properties, mass characteristics and engine specific fuel consumption. The aerodynamic technology factor alters the lift-to-drag ratio of the aircraft to the specified level. The mass technology factor reduces on the other hand the aircraft structural mass whereas the SFC factor lowers the engine fuel consumption by the specified value. For each of the technology factors, a 5% change has been imposed as this allows to identify the area to which the aircraft is most sensitive. The lift-to-drag ratio of the aircraft is increased by 5% whereas the structural weight and the SFC are reduced by 5%. Obviously this change is not as easily obtained for each of the different technologies. Both aerodynamics and engine fuel consumption represent very mature technological fields where a significant improvement is hard to obtain without a change in aircraft of engine configuration. The structural mass of the aircraft can on the other hand be expected to change significantly over the coming decades as a consequence of the adoption of a higher fraction of composite materials for the load bearing primary structure, as indicated by the recent Boeing 787.

Tables 4.7 and 4.8 show the results of this investigation for the kerosene fueled 380 and 550 passengers. Tables 4.9 and 4.10 on the other hand give the outcome for the 380 respectively 550 passengers hydrogen fueled aircraft. For each of the technology factors, the absolute values of the characteristics as well as the difference with the baseline case (in %) are given.

Table 4.7. Influence of progress in technology for the 380 passengers kerosene fueled aircraft with BPR 8 engines.

	Aerodynamic		**Mass**		**SFC**	
Wing Area [m^2]	365	-2.7%	355	-5.3%	355	-5.3%
Wing Aspect Ratio [–]	11.0	–	11.0	–	11.0	–
Takeoff Weight [kg]	275000	-3.5%	270400	-5.1%	274000	-3.9%
Operating Empty Weight [kg]	130600	-2.0%	123300	-7.5%	129200	-3.1%
Fuel Weight [kg]	108050	-6.7%	110900	-4.2%	108600	-6.2%
Maximum Fuel Weight [kg]	115300	-6.7%	118400	-4.1%	115900	-6.2%
Engine Net Thrust [kN]	189.2	-3.7%	187.8	-4.4%	190.5	-3.1%
Average Lift-to-drag Ratio [–]	18.8	+5.0%	17.6	-1.7%	17.6	-1.7%
Thrust-to-weight ratio [–]	0.281	–	0.283	+0.7%	0.284	+1.1%

Table 4.7 shows that both the aerodynamic technology factor as well as the SFC factor have a strong influence on the fuel weight whereas the influence of the mass reduction on the fuel weight is considerably smaller. However, both the takeoff as well as the operating empty weight are reduced much more by a reduction in structural mass. All factors considered, the reduction in structural mass has the highest influence on the overall aircraft design which is reflected by the strongest reduction in wing area and engine net thrust. As

the difference between the direct operating costs per seat mile are very small for the different technology factors, even at high fuel price levels, the direct operating costs are not included in the tables. Similar conclusions can be drawn for the other types of aircraft.

Table 4.8. Influence of progress in technology for the 550 passengers kerosene fueled aircraft with BPR 8 engines.

	Aerodynamic		**Mass**		**SFC**	
Wing Area [m^2]	510	-2.9%	490	-6.7%	500	-4.8%
Wing Aspect Ratio [–]	11.5	–	11,5	–	11.5	–
Takeoff Weight [kg]	397000	-3.9%	386000	-6.5%	395000	-4.4%
Operating Empty Weight [kg]	197200	-3.3%	185400	-9.1%	196000	-3.9%
Fuel Weight [kg]	147500	-6.1%	148500	-5.4%	146700	-6.6%
Maximum Fuel Weight [kg]	157250	-6.4%	158600	-5.6%	156500	-6.8%
Engine Net Thrust [kN]	270.4	-3.8%	264.2	-6.0%	270.5	-3.7%
Average Lift-to-drag Ratio [–]	20.5	+3.5%	19.4	-2.0%	19.5	-1.5%
Thrust-to-weight ratio [–]	0.278	+0.4%	0.279	+0.7%	0.279	+0.7%

A comparison between Tables 4.7 and 4.8 reveals on the other hand that the sensitivity of the very large long range aircraft is higher for all technology factors[7]. This is especially noticeable for the mass technology factor.

Table 4.9. Influence of progress in technology for the 380 passengers hydrogen fueled aircraft with BPR 8 engines.

	Aerodynamic		**Mass**		**SFC**	
Wing Area [m^2]	290	-3.3%	280	-6.7%	290	-3.3%
Wing Aspect Ratio [–]	11.5	–	11.5	–	11.5	–
Takeoff Weight [kg]	204600	-3.0%	199700	-5.4%	205800	-2.5%
Operating Empty Weight [kg]	132500	-3.3%	126800	-7.4%	133550	-2.5%
Fuel Weight [kg]	35900	-5.5%	36650	-3.6%	36050	-5.1%
Maximum Fuel Weight [kg]	38600	-5.9%	39500	-3.7%	38850	-5.2%
Engine Net Thrust [kN]	155.6	-5.8%	159.6	-3.4%	163.3	-1.2%
Average Lift-to-drag Ratio [–]	17.2	+3.6%	16.2	-2.4%	16.4	-1.2%
Thrust-to-weight ratio [–]	0.310	-2.8%	0.326	+2.2%	0.324	+1.6%

Similar conclusions can be made for the hydrogen fueled aircraft. For the 380 passenger aircraft, the influence is of the same order of magnitude as for the kerosene fueled version, except for the reduction in fuel weight, which is slightly smaller than for kerosene. For the 550 passenger aircraft on the other hand, the gain in performance from the progress in technology is smaller than for the kerosene fueled equivalent even for the mass reduction,

---

[7] Except for the lift-to-drag ratio where the variations are smaller due to the higher reduction in wing area on the one hand and the higher relative importance of the fuselage drag on the other hand.

Table 4.10. Influence of progress in technology for the 550 passengers hydrogen fueled aircraft with BPR 8 engines.

	Aerodynamic		**Mass**		**SFC**	
Wing Area [m^2]	495	-2.0%	480	-5.0%	495	-2.0%
Wing Aspect Ratio [–]	11.5	–	11,5	–	11.5	–
Takeoff Weight [kg]	350000	-2.8%	339000	-5.8%	352000	-2.2%
Operating Empty Weight [kg]	239800	-2.9%	228000	-7.7%	241500	-2.2%
Fuel Weight [kg]	57800	-5.7%	58500	-4.6%	58000	-5.4%
Maximum Fuel Weight [kg]	62100	-5.9%	63000	-4.5%	62400	-5.5%
Engine Net Thrust [kN]	244.3	-5.7%	248.3	-4.2%	256.0	-1.2%
Average Lift-to-drag Ratio [–]	18.9	+3.8%	17.8	-2.2%	18.0	-1.1%
Thrust-to-weight ratio [–]	0.285	-2.7%	0.295	+0.7%	0.297	+1.4%

in contrast to what would be expected for this highly constrained design which lead to a relatively heavy aircraft. The gain is however still higher than for the 380 LH_2 passenger aircraft.

4.4.2 Cruise altitude restrictions

As indicated in section 1.1, the utilization of hydrogen would in any case lead to a significantly lower environmental impact compared to kerosene. After all, most of the pollutant emissions are strongly reduced due to the nature of the fuel. Only the emission level of water vapor increases by a factor of approximately 2.6. Even though the water vapor itself only has a small direct contribution to the global warming effect, its indirect contribution through the formation of contrails could significantly reduce the environmental benefits of the adoption of hydrogen.

As the current scientific understanding of contrails and their formation is far from complete, especially for hydrogen fueled aircraft, a thorough assessment of contrail mitigation strategies is not attempted here. However, a reduction in cruise altitude could lead to a considerably lower frequency of appearance of contrails during flight and as such make the environmental impact of hydrogen fueled aircraft almost completely disappear, as is indicated on Figure 4.14. As the figure indicates, the effect of water vapor emissions increases strongly with altitude above nominal flight levels around 10 km.

However, a restriction in cruise altitudes comes at a price of a higher aircraft mass and higher mission fuel burn, as indicated on Figure 4.15. Whereas this higher fuel burn leads to a higher environmental effect for kerosene fueled aircraft, this is not the case for hydrogen fueled aircraft.

As Figure 4.15 does not include the effect of contrails, a reduction in cruise altitudes will have an even stronger effect on the environmental impact than shown here. After all, cruise altitude restrictions have been proposed as contrail mitigation measures, even for

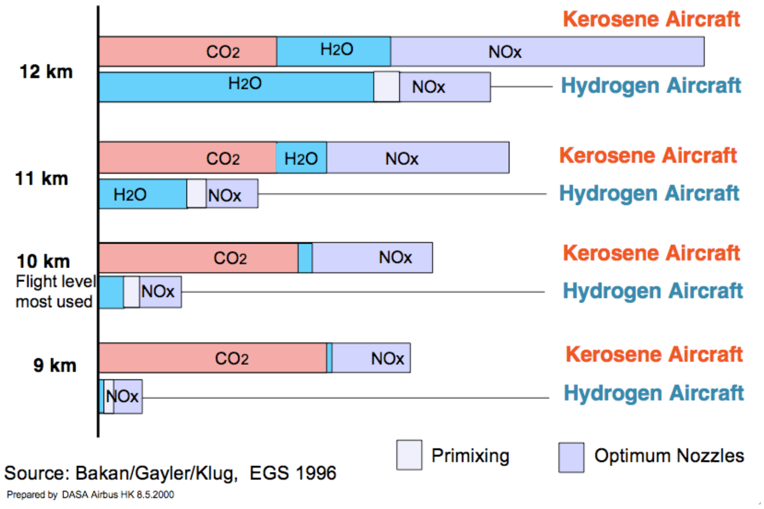

Figure 4.14. Effect of cruise altitude on environmental impact, adopted from Faass (2001).

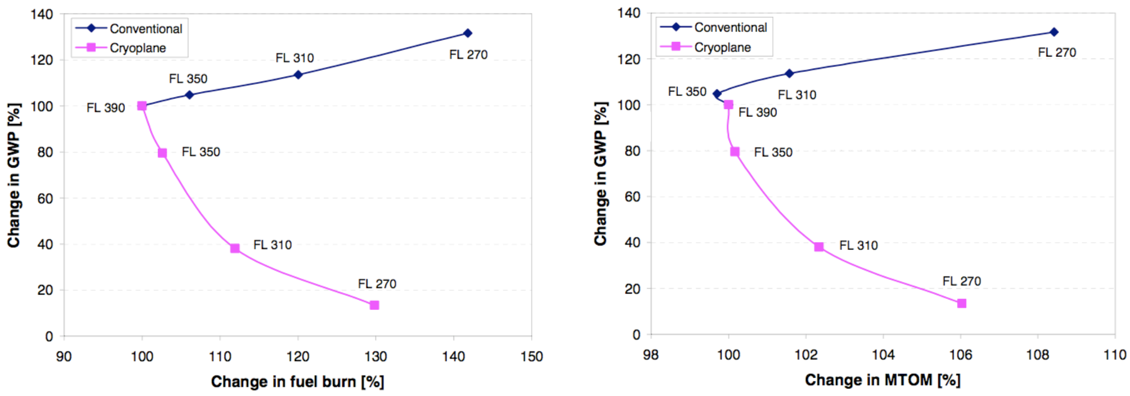

(a) fuel burn

(b) MTOM

Figure 4.15. Influence of change in cruise altitude on fuel burn and maximum take-off mass for medium range hydrogen fueled aircraft, adopted from Svensson (2005).

kerosene fueled aircraft despite the increase in CO_2 emissions (amongst others in Noppel (2007), Williams et al. (2003), Williams & Noland (2005) and Williams et al. (2007)).

A real measure to avoid contrails completely would either entail a very low cruising altitude or require innovative air traffic management (Williams et al. (2003) and Williams et al. (2007)). A strong dependence on seasonal and local variations furthermore exists (Williams & Noland, 2005). A cruise altitude restriction to 29000 ft is therefor arbitrarily selected in this thesis as it entails a significant departure from the previously studied altitudes. A more detailed analysis of the required altitude restriction is however in order before final conclusions on the price of contrail avoidance for hydrogen fueled aircraft can be made. After all, the formation of contrails depends on local weather phenomena as well as engine efficiency and the emission index of the fuel (amongst others (Noppel (2007) and Ponater et al. (2006) and Schumann (2005)).

Figure 4.16 shows the direct operating costs for both the 380 and the 550 passenger hydrogen fueled aircraft with BPR 10 engines. As shown on the figure, the wing area is no longer sized by the buffet limit but by the approach speed. This is a direct consequence of the higher density at the lower cruising altitude. The figure indicates the approach speed for a landing with half of the mission fuel present. The assumption of a landing at mid-fuel mass however yields a strong increase in wing area, compared to the landing mass at the end of the mission, as shown by the two white dots on the figure. As a landing at mid-fuel mass will only occur in an emergency situation, it is believed that this would over-penalize the constant altitude cases. Table 4.11 therefore only gives the results for the actual landing weight at the end of the mission.

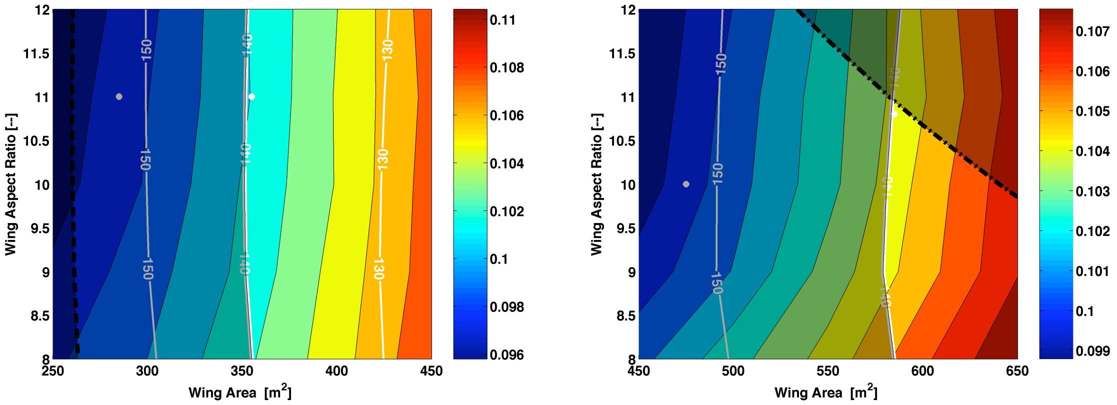

(a) 380 pax

(b) 550 pax

Figure 4.16. DOC for BPR10 engines at a constant cruise altitude of 29000 ft.

Table 4.11. Influence of progress in technology for the 550 passengers hydrogen fueled aircraft with BPR 8 engines.

	380 pax		**550 pax**	
	BPR8	**BPR10**	**BPR8**	**BPR10**
Wing Area [m^2]	285	285	460	475
Wing Aspect Ratio [–]	11.5	11.0	11.5	10.0
Takeoff Weight [kg]	224800	224500	375000	377500
Operating Empty Weight [kg]	142500	141600	252000	251700
Fuel Weight [kg]	46100	46800	70700	73500
Maximum Fuel Weight [kg]	49600	50400	76000	79100
Engine Net Thrust [kN]	183.4	186.0	280.4	291.9

A comparison with the stepped cruise cases shows that the wing area is reduced compared to the original cases as the wing is no longer sized by buffet considerations. A reduction between 4 to 9% in wing area is found. Due to the higher drag at lower altitude the fuel mass however increases between 15 and 23 % for the very large long range aircraft and between 21 to 27% for the large long range aircraft. For both aircraft the higher values are found for the BPR 10 engines. As a consequence of this higher fuel weight, the takeoff mass is between 4 and 8 % higher and the operating empty mass rises with 4 to 5 % despite the reduction in wing area. These values are in line with the results found for the medium range aircraft in Svensson (2005).

4.5 Twin fuselage very large long range transport aircraft

As a stretch version of the very large long range transport aircraft is impossible due to the limits imposed by the airport box, an alternative unconventional configuration is considered here for this particular design. After all, the market potential of the very large long range aircraft would be greatly reduced if a family could not be built around the baseline version.

Several unconventional configurations were however already analyzed in the Cryoplane study (see Sefain (2005)), and the conclusion was that none of them provided a clearly identifiable advantage over the conventional configurations (Westenberger, 2003b). Even so, the unconventional designs were analyzed for medium range aircraft which did not suffer from the geometrical constraints identified earlier for the very large long range aircraft. The unconventional configuration from the Cryoplane study that resembles the twin fuselage configuration selected here the closest is the twin boom configuration that was analyzed in Sefain (2005) which is shown on Figure 4.17.

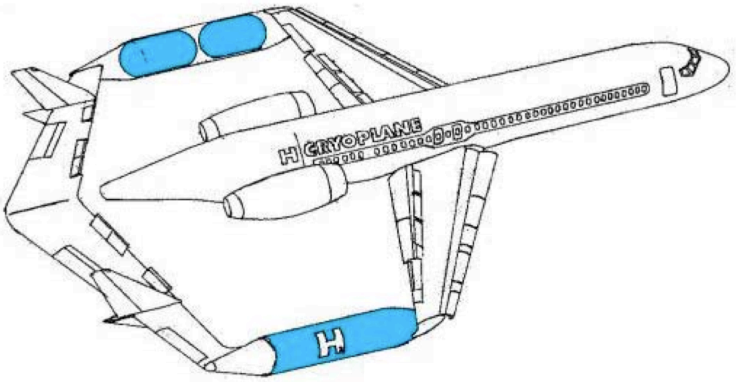

Figure 4.17. Twin boom medium-range liquid hydrogen fueled aircraft, adopted from Sefain & Jones (2002).

In the brainstorm session to select the unconventional configurations to be analyzed in the Cryoplane project, this configuration was considered to be very close to the twin fuselage configuration but with an additional safety advantage of separation between the hydrogen (stored in wing mounted tanks) and the passengers. It was this safety advantage that lead to its selection over the twin fuselage concept (Sefain, 2005). Nonetheless, the extra drag from the external fuel tanks penalized the aerodynamic characteristics of the aircraft which made any potential performance improvement disappear. Additionally, which was not considered in detail in the aircraft designs of the Cryoplane study, the small diameter of the wing tanks would result in strong reduction of the gravimetric efficiency of the tank or a big increase in tank weight, as was the case for the regional jet aircraft analyzed in chapter 3.

The twin fuselage configuration, in the true sense of the word is just the same believed to offer significant benefits for the very large long range transport aircraft if its performance proves to be competitive. Besides enabling the adoption of a family of aircraft, the aircraft would furthermore probably be cheaper to build than the conventional aircraft as a consequence of the learning curve effect on price due to the commonality between the two fuselages as indicated by the cost reduction factors in Moore et al. (1982). Chiesa et al. (2000) uses this as the main argument in favor of this configuration for high-capacity aircraft as the one under consideration.

The concept offers furthermore similar benefits as the spanloader or blending wing body aircraft but retains configurational and operational characteristics that are more like those of conventional aircraft (Moore et al., 1982). Synergies furthermore apply to the twin fuselage concept under consideration that also make it a configuration that is often analyzed for launch vehicles as shown on the figure below and by the configuration of the White Night aircraft from Scaled Composites which is designed to carry SpaceshipOne.

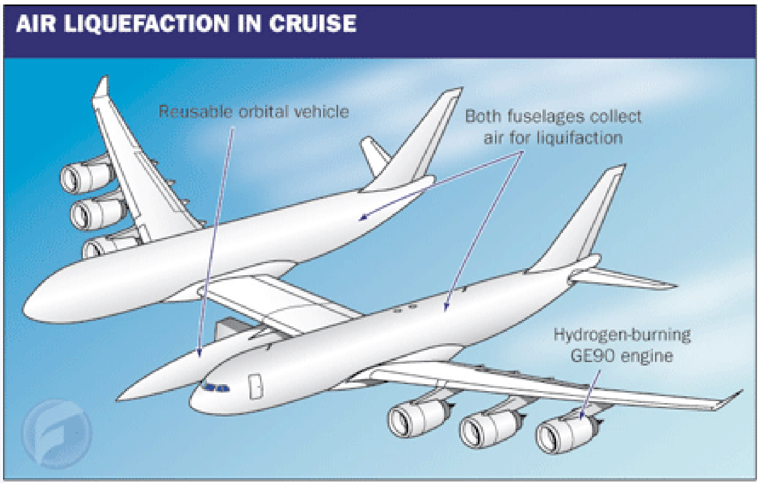

Figure 4.18. Twin fuselage mothership for a two-stage-to-orbit launch vehicle, adopted from Coppinger (2007) after Verstraete et al. (2008).

Below first the possible synergies for this particular application are reviewed. Then the modifications needed to the aircraft design routine to simulate this configuration are covered after which the fuselage design is discussed very concisely. Finally the results of the wing parametric study are given.

4.5.1 Synergies and disadvantages for liquid hydrogen twin fuselage transport aircraft

Two main synergies can be identified for the twin fuselage configuration for the particular aircraft under consideration. The most obvious one is the reduction in fuselage length that can be obtained by dividing the cabin into two cabins of equal size. As mentioned before, this would restore the potential to develop a family of aircraft for the very large long range transport aircraft as both fuselages will remain well within the limits from the airport box.

However, liquid hydrogen fueled aircraft can furthermore also benefit from the reduction in wing root bending moment due to the outboard placement of the two fuselages as shown in Figure 4.19. The separation between the fuselages is extra advantageous for liquid hydrogen fueled aircraft as it will restore the loss of moment alleviation due to the absence of the fuel in the wing. Obviously the reduction in bending moment will also be beneficial for other aircraft, but to a lesser extent as some form of wing root bending moment relief is already present[8].

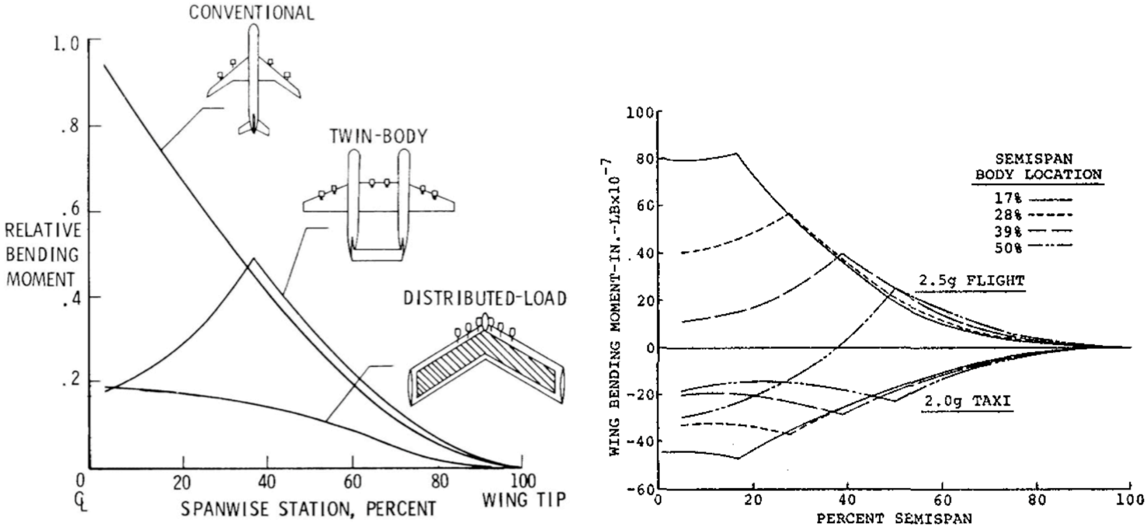

(a) Nagel (1978)

(b) Moore et al. (1982)

Figure 4.19. Wing bending moment for twin fuselage aircraft compared to other configurations and influence of body location, adopted from Nagel (1978) and Moore et al. (1982).

As shown on Figure 4.19(b) there is however an upper limit for the spanwise separation after which the bending moment is no longer decreasing but the structure has to be beefed

---

[8] Torenbeek (2000) argues that the H-cabin derivative where the central section of the wing is increased in chord to obtain a reasonable height to allow passengers to be housed in the wing could be a viable candidate for liquid hydrogen aircraft as fuel could be stored in the wing. Preliminary calculations however show that this configuration suffers from a too far aft cg if no additional tanks are placed in front of the cabin. As these were present in the standard version anyway, this configuration is not further investigated here. After all, increasing the amount of tanks (with a small diameter) leads to a significant increase in overall tank weight as was shown in Chapter 3.

up as the negative moment at the root becomes bigger than the taxi load. This limiting spanwise position is according to Moore et al. (1982) located around 40% of the wing span. Besides this bending moment limit, the spanwise position is also restricted by runway width, which is according to Torenbeek & Jesse (2001) more restricting that the aforementioned weight related limit. For category 4F airports the maximum runway width is limited to 16 m (De Jong & Slingerland, 2003). Both limits are considered in this work.

Obviously the twin fuselage configuration does not only have benefits. The main potential pitfalls for this configuration is related to the lateral stability and flying qualities. In a roll maneuver the passengers will namely be subjected to g-forces. However, both Moore et al. (1982) and Torenbeek (Torenbeek (2000) and Torenbeek & Jesse (2001)) indicate that this might be solved by a proper design of the control system. Moore et al. (1982) indicate that only the sideward acceleration during roll could be an issue whereas it is suggested to move one fuselage up with the other forming the center of roll to alleviate this issue in Torenbeek & Jesse (2001).

Other disadvantages include the increase in wetted area due to the second fuselage, the reduction in Oswald efficiency factor due to the second fuselage and the doubling of some of the structure and systems which will entail a weight increase. The fuselage effect on drag is according to Torenbeek & Jesse (2001) likely to be less than 5% of the drag in the design condition of the aircraft. Houbolt (1982) even shows that two fuselages can reduce the total wetted area for large aircraft. Moore et al. (1982) show on the other hand that the reduction in Oswald factor is only in the order of 2 to 3 % (which has been taken into account here). Fuselage pitch oscillations might also prove to be an issue (Chiesa et al., 2000). Moore et al. (1982) finally indicate that flutter of the outer part of the wing was a problem. It could however be solved by locally beefing up the structure which added about 5% in wing weight.

The main disadvantage specific to this application is the need to store fuel tanks in both fuselages. Not only will there be 4 tanks instead of 2, the diameter of the fuselage is also smaller, which might lead to a reduction in gravimetric efficiency. However, as shown in section 4.5.3 the resulting diameters are still fairly high. Besides this, the need to locate the engines on the wing, rather than aft of the fuselage is also a drawback. Engines aft of the fuselage could lead to a smaller vertical tail as the critical engine out yawing moment will be smaller which makes it the preferred option for engine installation according to Torenbeek & Jesse (2001). This installation could furthermore easily allow the accommodation of very high bypass ratio engines. However as the fuel tanks are located in the tail cone, it is considered that this is not a viable option for the hydrogen twin fuselage aircraft. Engines are therefore located in pairs of 2 at a conventional inboard engine position of 35% of the (outer) span.

4.5.2 Adaptation of the conceptual design routine to the twin fuselage configuration

The main adaptation to the routine obviously was concentrated around the wing mass. As the wing mass correlations that are adopted for this work already were selected to consider wing root bending moment relief, this was not an issue (see section B.2.2). The correlation from Jenkinson et al. (1999) could readily be applied to the wing mass of the twin fuselage aircraft. The correlation from Howe (2000) on the other hand required some modification as the wing root bending relief factor is not detailed enough for this case. The bending relief factors of Table 4.12 were derived from Moore et al. (1982) and Torenbeek & Jesse (2001) to account for this.

Table 4.12. Bending relief factors for the wing mass determination.

Spanwise location of the fuselage	Relief factor
0.17	0.80
0.28	0.55
0.39	0.40
0.50	0.40

Besides adapting the wing weight, the fuselage weight, the nose landing gear and the empennage weight need to be doubled. Following Torenbeek & Jesse (2001), the weight of the flight controls, hydraulics and electrics are assumed to be stored in one fuselage or tailplane and are thus not doubled. Finally, the structural weight is increased by 5% to take more severe airworthiness regulations into account for a new configuration (Torenbeek & Jesse, 2001).

4.5.3 Fuselage design

Each of the fuselages is assumed to house half of the passengers. Therefore only one fuselage is designed, despite the fact that there will be some small differences[9]. As the fuselage holds approximately 300 passengers either an 8 or a 9 abreast configuration could be adopted for the tourist class (Jenkinson et al., 1999). The differences between fuselages with 8 or 9 passengers abreast are fairly small since there is only a difference of 2 rows between both configurations. Either one could thus be adopted. The final design has been made here for the 9 abreast configuration as the slightly higher diameter could (marginally) improve the tank gravimetric efficiency.

To obtain a fair comparison with the fuselage designs from the Cryoplane studies, the overall cabin characteristics (seat pitch and width, aisle size, . . .) were adopted from Oelkers et al. (2000d) which resulted in a fuselage length without front tank of 58.49 m and a fuselage diameter of 6.77 m.

---

[9] There will for instance be only one cockpit. The nose of the other fuselage could for instance have no windshield as it it a source of significant drag (Jenkinson et al., 1999). Alternatively it could be used as part of the first class section of the cabin.

4.5.4 Wing parametric study for the hydrogen fueled twin fuselage aircraft

The results of the wing parametric study for the twin fuselage aircraft can be found on Figure 4.20 and Table 4.13. As shown, the performance of the twin fuselage aircraft is very similar to that of the conventional aircraft with the takeoff weight increasing only about 2 %. This is related to the reduction in wing weight on the one hand and the weight increase of the fuselages that is smaller than could be expected. After all, a significant increase in fuselage weight had to be imposed for the triple deck fuselage due to the large stresses on the vertical sides (see Appendix B). The configuration clearly restores the possibility for a family of aircraft as the fuselage length lies around 64 m.

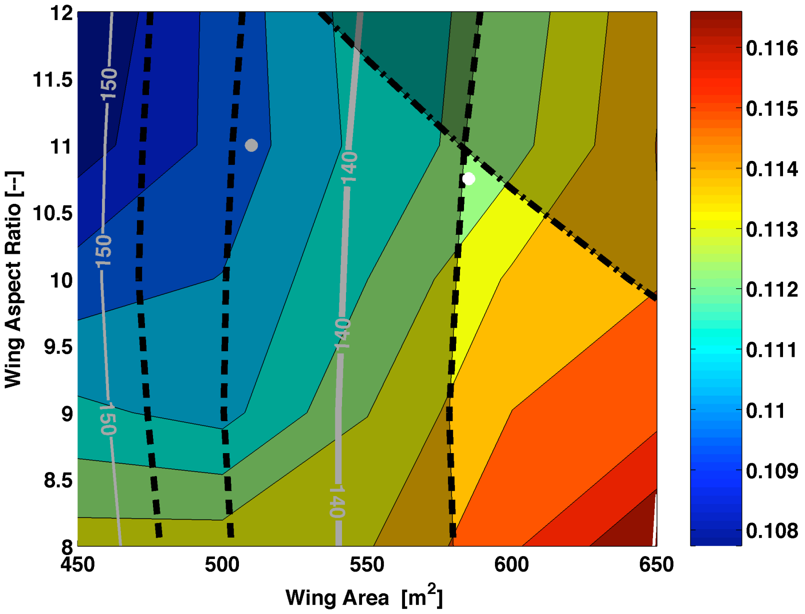

Figure 4.20. Direct operating costs for the twin fuselage aircraft equipped with BPR 8 turbofans, for a fuel price of 0.03 $/MJ.

4.6 Regenerative fuel pre-heating

As indicated in section 2.2, several unconventional cycles that make use of the cooling capacity of hydrogen can be envisaged. Of those cycles, the compressor inter-cooling and the turbine cooling air cooling cycle seem to be the most promising cycles. Here, however only the influence of pre-heating the fuel by the addition of a heat exchanger in the exhaust pipe will be investigated as it is the cycle that requires the smallest changes compared to conventional engine cycle. The heat exchanger could namely be integrated in the exhaust pipe and in the struts present in that exhaust pipe as indicated in Svensson (2005). As the heat exchanger could be made of a simple coil, wrapped around the engine exhaust, it would furthermore not significantly change the core nozzle characteristics.

Table 4.13. Design point characteristics for the conventional and twin fuselage very large long range transport aircraft with hydrogen fuel.

	Conventional		**Twin fuselage**	
	BPR 8	**BPR 10**	**BPR 8**	**BPR 10**
Wing Area [m^2]	505	505	510	495
Wing Aspect Ratio [–]	11.5	11.5	11.0	11.5
Takeoff Weight [kg]	360000	358000	367000	368000
Operating Empty Weight [kg]	247000	246000	246000	249000
Fuel Weight [kg]	61300	59700	68500	66700
Maximum Fuel Weight [kg]	66000	64200	73600	71700
Engine Net Thrust [kN]	259.1	259.2	284.2	283.9
Average Lift-to-drag Ratio [–]	18.2	18.1	16.6	16.6
Engine Length [m]	4.65	4.83	4.86	5.05
Engine Diameter [m]	2.92	3.03	3.06	3.17
Thrust-to-weight ratio [–]	0.293	0.295	0.316	0.315

Figure 4.21 gives a schematic of the engine cycle, as used in Ecosimpro^{TM} to set up the engine design point calculations. The fuel pre-heater is given on the top left hand side of the figure. As shown, heat is exchanged between the fuel coming from the tank and the combustion gases downstream of the low pressure turbine. Following Brewer (1991) where a detailed investigation of the fuel pre-heater performance is made, the heat exchanger effectiveness is taken as 0.8 and the pressure drop on the air side is set to 5%. In off-design calculations the effectiveness of the heat exchanger is kept constant even though this will lead to a small underestimation of the heat exchanger performance for most of the cruise phase. After all, when the flow through the heat exchanger is reduced a slightly higher effectiveness can be expected as the ratio of heat transfer surface area to mass flow is increased (Walsh & Fletcher, 2004). For take-off and during most of the climb phase the reverse will be true, so both effects will compensate partially. Due to the length of the cruise phase, this assumption is nonetheless conservative. To account for the extra component, the turbofan mass is increased by 10%, following Doulgeris (2008).

Figure 4.21 presents the performance of the fuel pre-heating cycle. The pre-heating cycle, indicated in blue is compared with the conventional engine cycle, with a fuel injection temperature of 150 K. For both cycles an overall pressure ratio of 45 is used. As shown on the figure, regenerative fuel heating leads to a reduction in both specific fuel consumption as well as specific thrust. The specific thrust is reduced due to the pressure drop before the nozzle on the one hand and the temperature drop due to the heat exchange with the fuel on the other hand. The reduction in fuel consumption adds to reduction in specific thrust leading to a specific thrust that is about 6-8% smaller.

The specific fuel consumption is reduced due to the higher energy input in the combustion chamber. As the fuel is preheated to temperatures between 550 and 850 K, the amount of fuel required to heat up the air to the specified turbine inlet temperature is lowered. The specific fuel consumption drops by approximately 5 to 7% for the wide range of turbine inlet temperatures of the figure.

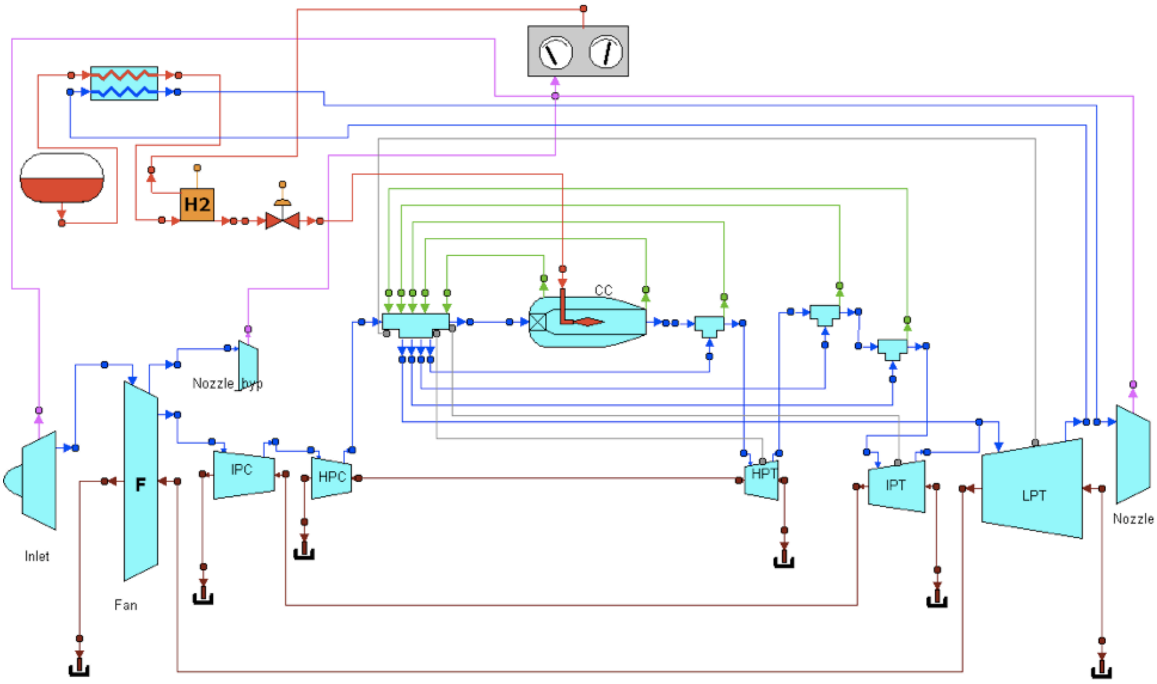

Figure 4.21. Schematic of the fuel pre-heating cycle.

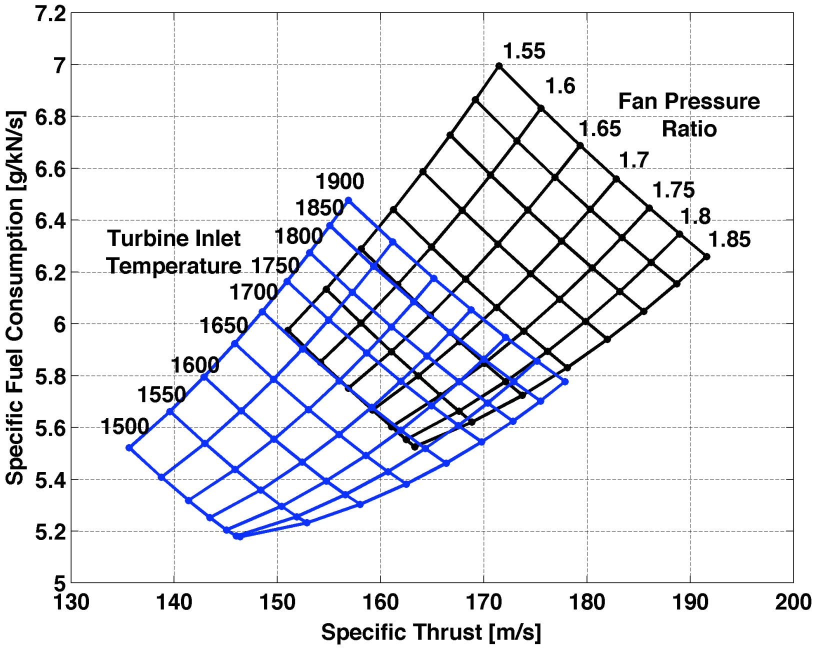

Figure 4.22. Performance of the fuel pre-heating cycle compared to the conventional cycle, for BPR 8.

Tables 4.14 and 4.15 show the results for both the large long range and the very large long range transport aircraft. As the tables indicate, the adoption of the fuel pre-heated cycle does not lead to an increase in performance for the overall aircraft. This is mainly a result of the increased engine mass which leads to a higher empty weight for a given wing size. As a consequence of this higher empty weight, the wing size has to increase which leads to a leverage effect on the overall aircraft mass and as a consequence also to a higher mission fuel mass. Similar performance penalties are found for both aircraft sizes.

Table 4.14. Design point characteristics for the large long range aircraft using the fuel pre-heated unconventional engine cycle.

	Conventional	**Fuel pre-heating**	**Difference [%]**
Wing Area [m^2]	300	310	3.3%
Wing Aspect Ratio [–]	11.5	11.5	–
Takeoff Weight [kg]	211000	219300	3.9%
Operating Empty Weight [kg]	137000	142000	3.6%
Fuel Weight [kg]	38000	41200	8.4%
Maximum Fuel Weight [kg]	41000	44400	8.3%
Engine Net Thrust [kN]	165.2	169.3	2.5%
Average Lift-to-drag Ratio [–]	16.6	16.9	1.8%
Thrust-to-weight ratio [–]	0.319	0.315	-1.3%

Table 4.15. Design point characteristics for the very large long range aircraft using the fuel pre-heated unconventional engine cycle.

	Conventional	**Fuel pre-heating**	**Difference [%]**
Wing Area [m^2]	505	525	4.0%
Wing Aspect Ratio [–]	11.5	11.5	–
Takeoff Weight [kg]	360000	375800	4.4%
Operating Empty Weight [kg]	247000	245800	4.0%
Fuel Weight [kg]	61300	66500	8.5%
Maximum Fuel Weight [kg]	66000	71600	8.5%
Engine Net Thrust [kN]	259.1	266.6	2.9%
Average Lift-to-drag Ratio [–]	18.2	18.5	1.6%
Thrust-to-weight ratio [–]	0.293	0.289	-1.4%

4.7 Conclusions

In this chapter the results of wing parametric studies on two large long range transport aircraft are reported. A 380 passenger and a 550 passenger aircraft are designed for both hydrogen and kerosene fuel. It is shown that the performance characteristics of the hydrogen fueled aircraft strongly depend on the category under investigation. Where for the large long range aircraft a strong reduction in wing area is possible compared to kerosene, this is no longer the case for the very large long range aircraft.

As a consequence, the weight reduction from the adoption of hydrogen is significantly reduced for the 550 passenger aircraft. The takeoff weight reduction drops from 25% for the large long range transport aircraft to between 11 and 13 % for the very large aircraft. Similar weight differences occur for operating empty, which goes from about the same weight for long range aircraft to an increase of 23% for the very large long range aircraft. The reduction in fuel weight on the other changes with about 10% between the two classes.

This drastic change in performance obviously affects the direct operating cost of the aircraft. Whereas for the large long range aircraft a 4 to 6 times higher fuel price per energy content could be afforded to obtain the same direct operating costs, this factor is reduced to about 3 to 5 times for the very large long range transport aircraft.

As the market potential of the very large long range transport aircraft is furthermore limited by the length of the fuselage which prohibits the adoption of a stretch version, an alternative configuration is investigated: the twin fuselage aircraft. It is shown that this configuration restores the capability to a family of aircraft at only a very small penalty. This can mainly be related to the strong increase in fuselage weight of the triple deck design of the conventional configuration. A more detailed investigation of the weight of fuselages and wing of the new configuration is however definitely needed before final conclusions can be made. Nonetheless, the configuration seems promising.

The investigations in this chapter furthermore show that a reduction in structural mass has a stronger influence than an equivalent reduction in SFC or increase in aerodynamic efficiency. Similar values are found for both fuels although the impact on fuel mass of each of the technology factors is slightly lower for hydrogen fuel.

Cruise altitude restrictions to 29000 ft for contrail avoidance on the other hand have a strong impact on the aircraft performance. Even though the wing area can be reduced as it is no longer sized by buffet limitations, the takeoff mass increases by about 4 to 8%. This is mainly a consequence of the strong increase in fuel mass which lies between 15 and 27 % depending on aircraft and engine type. A high price thus has to be paid for contrail avoidance.

This page is intentionally left blank

CHAPTER 5

Conclusions and recommendations for future work

5.1 Conclusions

Aviation faces a rising conflict to sustain growth in a way that meets the needs of society while not harming the environment. The forecasted growth rates in the order of 5% per annum namely outweigh the technological advances leading to an increased amount of greenhouse gas emissions in the atmosphere. This might ultimately limit the expansion of the aeronautical sector or will at least slow it down. As a green energy carrier hydrogen could aid in protecting the aeronautical sector from restrictions imposed by policy makers or the public opinion. After all its use almost completely eliminates emissions of greenhouse gases and at the same time provides energy security.

The adoption of hydrogen in aviation however still faces many technical challenges before it can become reality. One of the main issues, identified from the very first reports on hydrogen is the design of lightweight, highly insulated tanks that can meet lifetimes typical for aviation. The design of the tanks namely requires a complex balance between mechanical and thermal requirements.

Even though at first sight large long range aircraft seem to be an ideal category for the utilization of hydrogen seen their large fuel load, it has been shown by previous studies that geometrical restrictions make it hard to capture the potential hydrogen could have for this type of application.

In light of these two particular issues a set of tools has been developed in this work to enable the design of large long range transport aircraft with hydrogen.

- An aircraft design tool has been set up and adapted to allow trade-off studies to determine the optimum wing size of hydrogen fueled aircraft and to analyze the potential for a twin fuselage configuration for the very large long range transport aircraft category.

- The design of liquid hydrogen aircraft tanks has been investigated by the development of a sizing method that accounts for mechanical thermal as well as operational requirements.
- An engine design and performance assessment tool has been created that allows coupling of engine and aircraft design.

The analysis made in this work using the developed set of tools leads to the following conclusions:

- The design of the liquid hydrogen tanks strongly depends on the category of investigated aircraft. For regional airliners a strong influence of tank diameter and configuration was found. For large long range transport aircraft on the other hand the tanks seem to be almost independent of the size (down to a certain limit). It was found that variations of only a few percent in gravimetric efficiency are obtained for a wide range of fuselage diameters and fuel masses for both rohacell and polyurethane foams. Even though multi layer insulation systems offer some weight reduction, the risk of rapid boil-off upon loss of vacuum will most likely prevent their use for aviation.
- Even though buffeting of the wing might be an issue for hydrogen fueled aircraft due to the absence of the damping effect of the fuel mass in the wing, buffet limits do not influence the performance of the aircraft significantly. They do strongly affect the size of the wing, but only marginally change the fuel and takeoff mass.
- The large long range transport aircraft, with passenger capacities of about 400 passengers hold significant promise for hydrogen. Takeoff weight reductions around 25 % can be obtained with fuel weights of only about 30% of the kerosene fueled equivalent aircraft. As a consequence the wing size can be reduced by about 20%. Operating empty weights are on the other hand similar for both fuels. As a consequence hydrogen leads to similar direct operating costs for a fuel price per energy content of 3 to 6 times higher than the kerosene price.
- For very large long range transport aircraft the adoption of hydrogen is far less promising. The weight reductions are significantly smaller due to geometrical restrictions, leading to wing sizes similar of those of kerosene fueled aircraft of the same class. Despite these limitations a considerably higher fuel price can still be afforded. Depending on the kerosene price, a 2 to 5 times higher price per energy content would yield similar direct operating costs.
- Twin fuselage aircraft restore the potential for a family of very large long range transport aircraft with hydrogen fuel. Even though they are not subjected to the severe geometrical limitations, weights in the same order of magnitude as the conventional aircraft of the same class are found. As the fuselage length is only about 65 m

for the baseline version, the market potential is nonetheless significantly higher as a stretch version is still feasible.

- Contrail avoidance through flight altitude restrictions changes the design space of the wing as buffeting is no longer an issue due to the increased air density at the lower cruising altitude. As a consequence a lower wing area can be adopted. A significant penalty in fuel mass of around 15-27% needs to be paid. In contrast to kerosene fueled aircraft this increase in fuel mass however only implies an increase in direct operating costs and not in environmental impact.

5.2 Recommendations for future work

The analysis revealed several areas that hold promise for improvement of the performance of hydrogen fueled aircraft but also showed some limitations. The main areas for improvement and future work are therefore

- A detailed study of the wing and fuselage weight of hydrogen fueled airplanes is mandatory to confirm the outcomes of this analysis. The fuselage weight could be significantly influenced by tank integration issues and the point loads arising from the integration of the tanks inside them. The wing could on the other hand be prone to buffeting as the fuel normally acts as a damper for aerodynamic vibrations. A detailed study of the buffet characteristics of a wing without fuel and the implications this has on the wing mass seems required for fine-tuning of the results obtained in this work.

- Even though several studies outline the theoretical performance gains of unconventional cycles, most also seem to conclude that the practical application of those cycles onboard of the aircraft is limited. The developed set could be used for an in-depth assessment of this.

- Various trade-off studies should be made to look for an optimized configuration and operation of hydrogen fueled aircraft. Whereas the tendency for kerosene fueled aircraft is to sweep the wing more to allow for a higher fuel storage capacity, the opposite could prove to be the way to go for hydrogen as the wing is not limited by its fuel storage capacity.

- The influence of the design Mach number on the hydrogen fueled aircraft performance should be checked. As the larger fuselages are bulky, flying at a slightly lower Mach number could yield a significant drag reduction leading to a strong improvement of the aircraft performance.

- The performance gains from natural flow through surface cooling require more attention. As shown by previous studies a significant drag reduction is possible. The influence on the overall aircraft performance could be looked into by the developed set of routines.

- Turbine cooling for hydrogen fueled engines should be looked at in detail. The first order calculations performed in this thesis showed that the amount of cooling air is in the same order of magnitude as for kerosene fuel. The changed emissivity and composition of the combustion gases could however have second order effects that would enable an improvement in engine performance without the need for highly complex changes to the engine architecture.
- More detailed design studies around the design points identified by the parametric studies should be made to verify the models and to gain further insight in the trade-offs resulting from the adoption of hydrogen as a fuel.
- Various synergies as fuel cells for APU replacement have to be looked into as they will increase the gain in performance from the use of hydrogen.

References

A.D. Little (1982). *An Assessment of the Crash Fire Hazard of Liquid Hydrogen Fueled Aircraft*. A.D. Little, Inc., National Aeronautics and Space Administration, NASA-CR-165525.

Air Liquide (2009). *Gas Distribution network of Air Liquide in Northern Europe*. `http://www.airliquide.be`: Air Liquide.

Airbus (2004). *A380 airplane characteristics for airport planning AC - Preliminary Issue*. Airbus.

Airbus (2007). *Global Market Forecast 2007-2026*. Airbus.

Alexander, D., Ying-Ming, L., Guynn, M., & Bushnell, D. (2002). Emissionless aircraft study. In *38^{th} AIAA/ASME/SAE/ASEE Joint Propulsion Conference and Exhibit*, AIAA-2002-4056. Indianapolis, Indiana, VS.

Alexiou, A., Baalbergen, E., Kogenhop, G., Mathioudakis, K., & Arendsen, P. (2007). Advanced capabilities for gas turbine engine performance simulations. In *ASME Turbo Expo 2007: Power for Land, Sea and Air*, ASME-GT-2007-27086. Montreal, Canada.

Alexiou, A., & Mathioudakis, K. (2005). Development of a turbofan performance model using a generic simulation tool. In *ASME Turbo Expo 2005: Power for Land, Sea and Air*, ASME-GT-2005-68678. Reno, Nevada, USA.

Allidieris, L., & Janin, F. (2002a). *Fuel system components - mechanical tank design trade-off*. Task Technical Report 3.6.2.2. Cryoplane project.

Allidieris, L., & Janin, F. (2002b). *Tanks (including insulation)*. Task Technical Report 3.6.2.1. Cryoplane project.

Allidieris, L., & Verroust, T. (2002). *Review of liquefaction processes*. Task Technical Report 7.4. Cryoplane project.

Anderson, J. J. (1999). *Aircraft performance and design*. Mc Graw-Hill.

Antoine, N. E., & Kroo, I. M. (2005). Framework for aircraft conceptual design and environmental performance studies. *AIAA Journal*, *43*(10), 2100–2109.

Ardema, M., Chambers, M., Patron, A., Hahn, A., Miura, H., & Moore, M. (1996). *Analytical fuselage and wing weight estimation of transport aircraft*. National Aeronautics and Space Administration, NASA-TM-110392.

Ashby, M. (2005). *Materials selection in mechanical design*. Butterworth-Heinemann, Third ed.

Asselin, M. (1997). *An introduction to aircraft performance.* AIAA Education Series. American Institute for Aeronautics and Astronautics.

Astaburuaga, M., & van Holten, T. (2001). *Conventional aircraft description long range aircraft*. Task Technical Report 2.1.3. Cryoplane project.

Astaburuaga, M., van Holten, T., & Krijnen, J. (2001). *Conventional aircraft description very long range aircraft*. Task Technical Report 2.1.4. Cryoplane project.

BACAS (2006). *Hydrogen as an energy carrier*. Belgian Academy Council of Applied Science.

Baerst, C., & Riple, J. (1979). Preliminary studies of a turbofan engine and fuel system for use with liquid hydrogen. In *International DGLR/DFVLR Symposium on hydrogen in air transportation.* Stuttgart, Germany.

Balat, M. (2008). Potential importance of hydrogen as a future solution to environmental and transportation problems. *International Journal of Hydrogen Energy, 33*(15), 4013–4029.

Balepin, V., Yoshida, M., & Kamijo, K. (1994). Rocket based combined cycles for single stage rocket. In *Aerospace Atlantic Conference & Exposition*, SAE-941166. Dayton, Ohio, USA.

Barbir, F. (2005). *Safety issues of hydrogen in vehicles.* Proton Energy Systems.

Barron, R. (1985). *Cryogenic Systems.* Oxford University Press, Second ed.

Benner, J., & van Geuns, L. (2008). *Zoeken, vinden en ontginnen (Search, find and harvest).* Dossier 16. Vlaams Instituut voor Wetenschappelijk en Technologisch Aspectenonderzoek (ViWTA) (Flemish Insitute for Research on Scientific and Technological Aspects).

Bil, C. (1988). *Development and application of a computer-based system for conceptual aircraft design.* Delft University Press.

Billig, F. (1991). Chapter 1: Propulsion systems from takeoff to high-speed flight. In S. Murthy, & E. Curran (Eds.) *High-Speed Flight Propulsion Systems*, vol. 137 of *Progress in Astronautics and Aeronautics*, (pp. 21–100). American Institute for Aeronautics and Astronautics.

Boeing (1976). *An exploratory study to determine the integrated technological air transportation system ground requirements of liquid-hydrogen fueled subsonic, long-haul civil air transports.* Preliminary design department, The Boeing Commercial Airplane Company, National Aeronautics and Space Administration, NASA-CR-2699.

Boeing (2008). *Current Market Outlook 2008-2027*. Boeing Commercial Airplanes.

Boggia, S. (2000). *Novel concepts for Aero gas turbine engines burning hydrogen - Cryoplane.* Master's thesis, Cranfield University, School of Engineering, Cranfield, England.

Boggia, S., Jackson, A., & Singh, R. (2001). Unconventional cycles for aero gas turbine engines burning hydrogen. In *15^{th} International symposium on airbreathing engines (ISABE)*, ISABE-2001-1245. Chattanooga, Tennessee, USA.

Bovet, L. (2004). *Optimisation conceptuelle de la croisière: Application aux avions de transport civil (Conceptual optimisation of cruise: Application to civil transport aircraft).* Ph.D. thesis, Sup'Aero, Toulouse, France.

Brand, J., Sampath, S., Shum, F., Bayt, R. L., & Cohen, J. (2003). Potential use of hydrogen in air propulsion. In *AIAA/ICAS International Air & Space Symposium and Exposition: The Next 100 Years*, AIAA-2003-2879. Dayton, Ohio, USA.

Brewer, G. (Ed.) (1976). *LH_2 airport requirements study.* Lockheed-California company, National Aeronautics and Space Administration, NASA-CR-2700.

Brewer, G. (1979). Characteristics of liquid hydrogen-fueled aircraft. In *International DGLR/DFVLR Symposium on hydrogen in air transportation.* Stuttgart, Germany.

Brewer, G. (1991). *Hydrogen aircraft technology.* CRC Press.

Brewer, G., Morris, R., Davis, G., Versaw, E., Cunnington, G., Riple, J., Baerst, C., & Garmong, G. (1978). *Study of fuel systems for LH_2-fueled subsonic transport aircraft, Volume I and II.* National Aeronautics and Space Administration, NASA-CR-145369.

Brewer, G., Morris, R., Lange, R., & Moore, J. (1975a). *Study of the application of hydrogen fuel to long-range subsonic transport aircraft, Volume I.* National Aeronautics and Space Administration, NASA-CR-132558-VOL-1.

Brewer, G., Morris, R., Lange, R., & Moore, J. (1975b). *Study of the application of hydrogen fuel to long-range subsonic transport aircraft, Volume II.* National Aeronautics and Space Administration, NASA-CR-132559-VOL-2.

Brewer, G., Wittlin, G., Versaw, E., Parmley, R., Cima, R., & Walther, E. (1981). *Assessment of Crash Fire Hazard of LH_2-Fueled Aircraft.* Lockheed-California company, National Aeronautics and Space Administration, NASA-CR-165525.

Brooks, C., Wang, W., & Eyman, D. (1994). *Supported transition metal catalysts for para to ortho hydrogen conversion.* National Aeronautics and Space Administration, NASA-CR-197007.

Brown, G. (1991). *Preliminary design proposal for a 1500 seat long range passenger aircraft.* Master's thesis, Cranfield Institute of Technology, College of Aeronautics, Aerospace Technology, Cranfield, England.

Buchlin, J. (2005). *Phénomènes de Transport (Transport Phenomena).* Course notes: Université Libre de Bruxelles.

Burns, J. (1994). *Aircraft cost estimation methodology and value of a price per pound derivation for preliminary design development applications.* Society of Allied Weight Engineers, SAWE-2228.

Calli, B. (2005). Biological production of hydrogen. In *Waterstof als energiedrager voor de toekomst? (Hydrogen as energy carrier for the future?)*. Mol, Belgium: Vlaams samenwerkingsverband brandstofcellen (Flemish cooperation for fuel cells).

Chai, S., & Mason, W. (1996). *Landing gear integration in aircraft conceptual design.* MAD 96-09-01. Blacksburg, Virginia, USA: Multidisciplinary analysis and design center for advanced vehicles, Virginia Polytech Institute and State University.

Chiesa, P., Lozza, G., & Mazzocchi, L. (2005). Using hydrogen as gas turbine fuel. *Journal of Engineering for Gas Turbines and Power, 127*(1), 73–80.

Chiesa, S., Di Sciuva, M., & Maggiore, P. (2000). The double-fuselage layout: a preliminary case study of a possible way of reducing the development costs for new high-capacity aircraft. *Proceedings of the Institution of Mechanical Engineers, Part G: Journal of Aerospace Engineering, 214*(2), 85–95.

CoA (2000). *Conceptual Aircraft Design.* Cranfield University, College of Aeronautics.

Conner, M. (2001). *Hans Von Ohain: Elegance in Flight.* General Publication Series. American Institute for Aeronautics and Astronautics.

Conrad, E. (1979). Turbine engine altitude chamber and flight testing with liquid hydrogen. In *International DGLR/DFVLR Symposium on hydrogen in air transportation.* Stuttgart, Germany.

Contreras, A., Yigit, S., Ozay, K., & Vezirogly, T. (1997). Hydrogen as aviation fuel: a comparison with hydrocarbon fuels. *International Journal of Hydrogen Energy, 22*(10/11), 1053–1060.

Coppinger, R. (2007). *ESA study finds in-flight oxidiser collection possible.* `http://www.flightglobal.com/articles/2007/07/10/215340/esa-study-finds-in-flight-oxidiser-collection-possible.html`: Flightglobal.

Corchero, G., & Montañés, J. L. (2003). An approach to the use of hydrogen in actual commercial aircraft engines. In *16th International symposium on airbreathing engines (ISABE)*, ISABE-2003-1187. Cleveland, Ohio, USA.

Cordina, E. (2002). *Aviation and the environment - A study on ways to limit the environmental harm caused by engine emissions and an assessment of future environmentally friendly aircraft technologies.* Master's thesis, London City University, London, England.

Corke, T. (2003). *Design of Aircraft.* Prentice Hall.

Corporan, E., Dagett, D., Hendricks, R., & Walther, R. (2007). Alternate fuels for use in future commercial aircraft. In *18th International symposium on airbreathing engines (ISABE)*, ISABE-2007-1196. Beijing, China.

Cumpsty, N. (1997). *Jet Propulsion: A simple guide to the aerodynamic and thermodynamic design and performance of jet engines.* Cambridge University Press.

Cunnington, G., & Parmley, R. (1980). Aerodynamic surface cooling for laminar flow control for hydrogen-fueled sybsonic aircraft. In *Aerospace Congress & Exposition*, SAE-801155. Los Angeles, California, USA.

Currey, N. (1988). *Aircraft landing gear design: principles and practices*. AIAA Education Series. American Institute for Aeronautics and Astronautics.

Dahl, G., & Suttrop, F. (1998). Engine control and low-no$_x$ combustion for hydrogen fuelled aircraft gas turbines. *International Journal of Hydrogen Energy*, *23*(8), 695–704.

Dahl, G., & Suttrop, F. (2000). *Combustion chamber and emissions, Review of Proposed Hydrogen Combustors, Benefits and Drawbacks*. Task Technical Report 4.4.4. Cryoplane project.

Dalhuijsen, J., & Slingerland, R. (2004). Preliminary wing optimization for very large transport aircraft with wingspan constraints. In *42nd AIAA Aerospace Sciences Meeting and Exhibit*, AIAA-2004-699. Reno, Nevada, USA.

DARCorp (2004). *The Advanced Aircraft Analysis software manual*. DARCorporation.

De Jong, S., & Slingerland, R. (2003). Analysis of the twin-fuselage configuration and its H-cabin derivative. In *AIAA 3rd Annual Aviation Technology, Integration and Operations Conference (ATIO)*, AIAA-2003-6811.

de la Calzada, P. (2003). Low pressure turbines design. In *Von Karman Institute Lecture Series on aero-engine design: a state of the art*. Von Karman Institute, April 7-11.

Dierick, C. (2006). Waterstofproductie via nucleaire energie (Hydrogen production through nuclear energy). In *Brandstofcellen en waterstof in Vlaanderen (Fuel Cells and hydrogen in Flanders)*. Mol, Belgium: Vlaams samenwerkingsverband brandstofcellen (Flemish cooperation for fuel cells).

Dierick, W. (2005). *Voorontwerp van een very high bypass ratio turbofan voor een subsoon lange-afstands transportvliegtuig (Preliminary design of a very high bypass ratio turbofan for a subsonic long range transport aircraft)*. Master's thesis, Vrije Universiteit Brussel, Brussels, Belgium.

Dieters, G. (1986). *Mechanical Metallurgy*. Mc Graw-Hill, Third ed.

DOE/EIA (2008). *Annual Energy Outlook 2008 With Projections to 2030*. US Department of Energy, Energy Information Administration.

Doulgeris, G. (2008). *Modeling & Integration of Advanced Propulsion Systems*. Ph.D. thesis, Cranfield University, School of Engineering, Cranfield, England.

Drnevich, R. (2003). *Hydrogen Delivery Liquefaction & Compression*. Presentation for the Strategic Initiatives for Hydrogen Delivery Workshop, Praxair.

Drolet, B., Gretz, J., Kluyskens, D., Sandmann, F., & Wurster, R. (1996). The Euro-Québec Hydro-Hydrogen Pilot Project (EQHHPP): Demonstration phase. *International Journal of Hydrogen Energy*, *21*(4), 305–316.

Dupont, W. (2000). *Avant projet d'avion de transport commercial (Advanced project of a commercial transport aircraft).* Aérospatiale.

EC (2003). *Hydrogen Energy and Fuel Cells - A vision of our future.* Special Report, European Commision, Directorate General for Energy and Transport.

Edeskuty, F. (1979). Safety of liquid hydrogen in air transportation. In *International DGLR/DFVLR Symposium on hydrogen in air transportation.* Stuttgart, Germany.

EIA (2009). *World Proved Reserves of Oil and Natural Gas, Most Recent Estimates.* `http://www.eia.doe.gov/emeu/international/reserves.html`: Energy Information Agency.

El-Sayed, A. (2008). *Aircraft propulsion and gas turbine engines.* CRC Press.

Empresarios Agrupados (2009). Ecosimpro - modelling and simulation software.
URL `http://www.ecosimpro.com/`

Epstein, A. (2004). Milimeter-scale micro-electro-mechanical systems gas turbine engines. *ASME Journal of Engineering for Gas Turbines and Power, 126*(2), 205–226.

ESDU (1961). *Specific heat capacities and their ratios as function of temperature for several common gases.* Engineering Science Data Unit, ESDU 00.01.08.

ESDU (1976). *Geometryical properties of cranked and straight tapered wing panforms.* Engineering Science Data Unit, ESDU 76003.

Eshelby, M. (2000). *Aircraft Performance - Theory and Practice.* Arnold Publishers.

Eshelby, M. (2007). *Aircraft Performance.* Lecture Notes of the Short Course in Propulsion Systems Performance and Integration: Cranfield University, January 29 - February 2.

Faass, R. (2001). *Cryoplane, Flugzeuge mit wasserstoffantrieb (Cryoplane, aircraft with hydrogen propulsion).* Presentation in Hamburg, Germany.

Fluent (1999). *FLUENT 5 User's Guide.* Fluent, Inc.

Forsberg, C. (2009). Meeting U.S. liquid transport fuel needs with a nuclear hydrogen biomass system. *International Journal of Hydrogen Energy.* Article in Press.

Freeman, C. (1992). Method for the prediction of supersonic compressor blade performance. *Journal of Propulsion and Power, 8*(1), 199–208.

Gauss, M., Isaksen, I., Lee, D. S., & Sovde, O. (2006). Impact of aircraft NO_x emission on the atmosphere - tradeoffs to reduce the impact. *Atmospheric Chemistry and Physics, 6*, 1529–1548.

Gebman, J., & Stanley, W. (1976). *The potential role of technological modifications and alternative fuels in alleviating air force energy problems.* RAND-1829-PR. Santa Monica, California, USA: The Rand Corporation.

Gerend, R., & Roundhill, J. (1970). Correlation of gas turbine engine weights and dimensions. In *AIAA 6^{th} Propulsion Joint Specialist Conference*, AIAA-1970-669. San Diego, California, USA.

Glieb, P., & Janardan, B. (2003). *Ultra-high bypass engine aeroacoustic study*. National Aeronautics and Space Administration, NASA-CR-2003-212525.

Goodyear (2002). *Goodyear Aircraft Tire Data book*. `http://www.goodyearaviation.com/tiredatabook.html`: The Goodyear Tire & Rubber Company.

Gordon, S., & McBride, B. (1994a). *Computer Program for Calculation of Complex Chemical Equilibrium Compositions and Applications - I. Analysis*. National Aeronautics and Space Administration, NASA-RP-1311.

Gordon, S., & McBride, B. (1994b). *Computer Program for Calculation of Complex Chemical Equilibrium Compositions and Applications - II. Users Manual and Program Description*. National Aeronautics and Space Administration, NASA-RP-1311.

Green, J. E. (2003). Civil aviation and the environmental challenge. *The Aeronautical Journal*, *107*(1072), 281–299.

Green, J. E. (2006). Civil aviation and the environment - the next frontier for the aerodynamicist. *Aeronautical Journal*, *110*(1110), 469–486.

Greener by Design (2005). *Air Travel - Greener by Design: Mitigating the Environmental Impact of Aviation: Opportunities and Priorities*. Report of the Science & Technology subgroupThe Royal Aeronautical Society.

Greener by Design (2007). *Air Travel - Greener by Design: Annual Report 2006-2007*. The Royal Aeronautical Society.

Guynn, M., & Olson, E. (2005). *Evaluation of an aircraft concept with over-wing, hydrogen-fueled engines for reduced noise and emissions*. National Aeronautics and Space Administration, NASA-TM-2002-211926.

Hall, C., & Crichton, D. (2005). Engine and installation configurations for a silent aircraft. In *17^{th} International symposium on airbreathing engines (ISABE)*, ISABE-2005-1164. Munich, Germany.

Hapke, J., & Bode, S. (2001). *Review of conventional hydrogen production processes*. Task Technical Report 7.2.1. Cryoplane project.

Harasgama, S. (1995). Heat transfer and cooling in gas turbines. In *Von Karman Institute Lecture Series on aero-thermal aspects of gas turbine flows*. Von Karman Institute, May 8-12.

Hasan, B. (1995). *Design of derivative two spool high bypass Turbofan for commercial aircraft*. Master's thesis, Cranfield University, School of Engineering, Cranfield, England.

Hastings, L., Hedayat, A., & Brown, T. (2004). *Analytical modelling and test correlation of variable density multilayer insulation for cryogenic storage.* National Aeronautics and Space Administration, NASA-TM-2004-213175.

Hedayat, A., Brown, T., Hastings, L., & Martin, J. (2000). Variable density multilayer insulation for cryogenic storage. In *36^{th} AIAA/SAE/ASME/ASEE Joint Propulsion Conference,* AIAA-2000-3790.

Hendrick, P. (2006). *Aircraft Propulsion.* Course notes of Université Libre de Bruxelles: Université Libre de Bruxelles and Royal Military Academy of Belgium.

Hendrick, P., Heintz, N., & Romera, J. (2008a). Development and testing of air - hydrogen heat exchangers for advanced space launchers. In *ESA Space Propulsion Conference.* Heraklion, Greece.

Hendrick, P., Heintz, N., Romera, J., Murray, J., & Ngendajumana, P. (2008b). Experimental study of air-hydrogen heat exchangers. In *15^{th} AIAA International Space Planes and Hypersonic Systems and Technologies Conference,* AIAA-2008-2502. Dayton, Ohio, USA.

Heydenreich, R. (1998). Cryotanks in future vehicles. *Cryogenics, 38*(1), 125–130.

Hochstein, J., Ji, H., & Aydelott, J. (1986). Effect of subcooling on the on-orbit pressurization rate of cryogenic propellant tankage. In *4^{th} AIAA/ASME Joint Thermophysics and Heat Transfer Conference,* AIAA-1986-1253. Boston, Massachussets, USA.

Horlock, J., Watson, D., & Jones, T. (2001). Limitations on gas turbine performance imposed by large turbine cooling flows. *Transactions of the ASME Journal of Engineering for Gas Turbines and Power, 123*(3), 487–494.

Houbolt, H. (1982). Why twin-fuselage aircraft? *Astronautics and Aeronautics,* (pp. 26–36).

Houghton, E. (2003). *Aerodynamics for Engineering Students.* Butterworth-Heinemann.

Howe, D. (2000). *Aircraft conceptual design synthesis.* Professional Engineering Publishing Limited.

Hoyt, J. (1979). Design concept for LH_2 airport facilities. In *International DGLR/DFVLR Symposium on hydrogen in air transportation.* Stuttgart, Germany.

Hutchinson, H., Barrick, P., & Brown, L. (1965). Experiment study of reaction kinetics for para-ortho hydrogen at 20 to 80 k. In *Advances in Cryogenic Engineering,* vol. 10. Plenum Press.

IEA (2008). *World Energy Outlook - 2008: Executive Summary.* International Energy Agency.

Ishutkina, M., & Hansman, R. (2008). Analysis of interactions between air transportation and economic activity. In *26^{th} Congress of the International Council of Aeronautical Sciences Including the 8^{th} AIAA Aircraft Technology, Integration, and Operations Conference,* AIAA-2008-8888. Anchorage, Alaska, 2008.

Isikveren, A. (2002). *Quasi-analytical modelling and optimisation techniques for transport aircraft design.* Ph.D. thesis, Royal Institute of Technology (KTH), Stockholm, Sweden.

Isikveren, A. (2005). Section 8: Introduction to systems integration. In *Industrial transport aircraft design - a compendium of principles, practises and techniques*, Issue MMV. Montreal, Canada.

Jackson, A. (2004). *Gas Turbine Performance - Chapter 2: Component Modelling*. Lecture Notes of the Short Course in Gas Turbine Performance: Cranfield University, May, 24-28.

Jenkinson, L., Simpkin, P., & Rhodes, D. (1999). *Civil Jet aircraft design.* AIAA Education Series. American Institute for Aeronautics and Astronautics.

Joesbury, A. (2005). *Design study of reduced environmental impact transport aircraft*. Master's thesis, Cranfield University, School of Engineering, Cranfield, England.

Johnson, W., Keller, C., Cunningtion, G., & Glassford, A. (1974). *Thermal performance of multilayer insulation.* National Aeronautics and Space Administration, NASA-CR-134477.

Kaminski-Morrow, D. (2009). *Tupolev's cryogenic Tu-155- 20 years on!*. `http://www.flightglobal.com/blogs/flight-international/2008/04/tupolevs-cryogenic-tupolev-tu1.html`: Flightglobal.

Kanoglu, M., Dincer, I., & Rosen, M. (2007). Meeting U.S. liquid transport fuel needs with a nuclear hydrogen biomass system. *International Journal of Hydrogen Energy*, *32*(17), 4250–4257.

Kawaike, K., Kobayashi, N., & Ikeguchi, T. (1984). Effect of new blade cooling system with minimized gas temperature dilution on gas turbine performance. *Journal of Engineering for Gas Turbines and Power*, *106*(4), 756–764.

Klug, H. (1997). Cryoplane - liquid hydrogen propulsion for aircraft. In *Aerospace Propulsion Conference*. London, England.

Klug, H., & Grassl, H. (1993). The Cryoplane project, aircraft using cryogenic fuel and their impact on the atmosphere. In *Europen Geophysical Society XVIII General Assembly*. Wiesbaden, Germany.

Koroneos, C., Dompros, A., Roumbas, G., & Moussiopoulos, N. (2004). Life cycle assessment of hydrogen fuel production processes. *International Journal of Hydrogen Energy*, *29*(14), 1443–1450.

Koroneos, C., Dompros, A., Roumbas, G., & Moussiopoulos, N. (2005). Advantages of the use of hydrogen fuel compared to kerosene. *Resources, Conservation and Recycling*, *44*, 99–113.

Kowe, D., & Wynosky, T. (1985). *Energy Efficient Engine Program - Advanced turbofan nacelle definition study.* National Aeronautics and Space Administration, NASA-CR-174942.

Krijnen, J., van Holten, T., & Astaburuaga, M. (2001). *Conventional aircraft description long range aircraft - partial report*. Task Technical Report 2.1.4 (D9). Cryoplane project.

Kroo, I. (2006). *Aircraft Design: Synthesis and Analysis*. Desktop Aeronautics, Inc. URL `http://adg.stanford.edu/aa241/AircraftDesign.html`

Kurzke, J. (1992). Calculation of installation effects within performance computer programs. In *Steady and Transient Performance of Gas Turbines*, AGARD Lecture Series 183. North Atlantic Treaty Organization, Adivsory Group for Aerospace Research and Development.

Kurzke, J. (2003). Preliminary design. In *Von Karman Institute Lecture Series on aeroengine design: a state of the art*. Von Karman Institute, April 7-11.

Kurzke, J. (2004a). *Component Map Collection - Issue 2*. `http://www.gasturb.de`.

Kurzke, J. (2004b). *GasTurb 10 User's Manual*. `http://www.gasturb.de`.

Kurzke, J. (2008). Preliminary design. In *Von Karman Institute Lecture Series on aeroengine design: from state of the art turbofans towards innovative architectures*. Von Karman Institute, March 3-7.

Lange, R., Sturgeon, R., Adams, W., Bradley, E., Cahill, J., Eudaily, R., Hancock, J., & Moore, J. (1972). *Study of the application of advanced technologies to long-range transport aircraft - Volume 1: Analysis and Design*. National Aeronautics and Space Administration, NASA-CR-112088.

Laskaridis, P. (2004). *Performance investigations and systems architectures for the more electric aircraft*. Ph.D. thesis, Cranfield University, School of Engineering, Cranfield, England.

Lefebvre, A. (1999). *Gas Turbine Combustion*. Taylor and Francis, Second ed.

Lewis, R. (1996). *Turbomachinery Performance Analysis*. Elsevier Ltd.

Liebeck, R., Andrastek, D., Chau, J., Girvin, R., Lyon, R., Rawdon, B., Scott, P., & Wright, R. (1995). *Advanced subsonic Airplane Design & Economic Studies*. National Aeronautics and Space Administration, NASA-CR-195443.

Lienhard, J., & Lienhard, J. (2004). *A heat transfer textbook*. Phlogiston Press, Third ed.

Lin, C.-S., Van Dresar, N., & Hasan, M. (1991). A pressure control analysis of cryogenic storage systems. In *AIAA/SAE/ASME/ASEE 27th Propulsion Joint Specialist Conference*, AIAA-1991-2405. Sacramento, California, USA.

LLNL (2008). *Lawrence Livermore National Laboratory - Science in the National Interest*. `http://www.llnl.gov`: Lawrence Livermore National Laboratory.

Louis, J. (1978). Systematic studies of heat transfer and film cooling effectiveness. In *High temperature problems in gas turbine engines*, North Atlantic Treaty Organization, Advisory Group for Aerospace Research and Development. AGARD Conference Proceedings 229.

Marek, J., Smith, T., & Kundu, K. (2005). Low emission hydrogen combustors for gas turbines using lean direct injection. In *41st AIAA/ASME/SAE/ASEE Joint Propulsion Conference and Exhibit*, AIAA-2005-3776. Tucson, Arizona, USA.

Marquart, S., Ponater, M., Mager, F., & Sausen, R. (2003). Future development of contrail cover, optical depth, and radiative forcing: Impacts of increasing air traffic and climate change. *Journal of Climate*, *16*(17), 2890–2904.

Marquart, S., Sausen, R., Ponater, M., & Grewe, V. (2001). Estimate of the climate impact of cryoplanes. *Aerospace Science and Technology*, *5*(1), 73–84.

McCormick, B. (1995). *Aerodynamics, Aeronautics and Flight Mechanics*. John Wiley & Sons, Second ed.

Meerkötter, R., Schumann, U., Doelling, D., Minnis, P., Nakajima, T., & Tsushima, Y. (1999). Radiative forcing by contrails. *Annales Geophysicae*, *17*, 1080–1094.

Menard, E. (2006). *Design study of a fuel cell powered aircraft*. Master's thesis, Cranfield University, College of Aeronautics, Cranfield, England.

Meyer, P. (1923). *Is there any available source of heat lighter than gasoline?*. National Aeronautics and Space Administration, Technical Note 136.

Mikolowsky, W., & Noggle, L. (1976). *An evaluation of very large airplanes and alternative fuels*. R-1889-AF. Santa Monica, California, USA: The Rand Corporation.

Milliken, J., Petrovic, J., & Podolski, W. (2002). Hydrogen storage issues for automotive fuel cells. In *International Workshop on hydrogen in materials and vacuum systems*. Newport News, Virginia, USA.

Mital, S., Gyekenyesi, J., Arnold, S., Sullivan, R., J., M., & Murthy, P. (2006). *Review of current state of the art and key design issues with potential solutions for liquid hydrogen cryogenic storage tank structures for aircraft applications*. National Aeronautics and Space Administration, NASA-TM-2006-214346.

Moore, J., Craven, E., Farmer, B., Honrath, J., Stephens, R., & Meyer, R. (1982). *Multibody Aircraft Study Volume 1*. National Aeronautics and Space Administration, NASA-CR-165289.

Muehlbauer, J. (1982). Very large aircraft with alternate fuels -LH2 most promising. In *AIAA 2nd International Very Large Vehicles Conference*, AIAA-82-0813. Washington D.C.

Nagel, A. (1978). *Studies of advanced transport aircraft*. National Aeronautics and Space Administration, NASA-TM-78697.

NASA (1997). *Safety standards for hydrogen and hydrogen systems: Guidelines for hydrogen system design, materials selection, operation, storage and transportation*. National Aeronautics and Space Administration, NASA Technical Report NSS 1740.16.

Nast, T. (1998). Multilayer insulation systems. In J. Weisend (Ed.) *Handbook of Cryogenic Engineering*, (pp. 186–201). Taylor and Francis.

Nicolai, L. (1984). *Fundamentals of aircraft design.* Mets, Inc.

NIST (2007). *Thermophysical Properties of Fluid Systems.* `http://webbook.nist.gov/chemistry/fluid/`: National Institute of Standards and Technology.

Noppel, F. (2007). *Contrail and cirrus cloud avoidance technology.* Ph.D. thesis, Cranfield University, School of Engineering, Cranfield, England.

Oelkers, W., & Prenzel, E. (2001). *Aircraft Configuration - Short/Medium Range Aircraft.* Task Final Report 2.3.4. Cryoplane project.

Oelkers, W., Schulz, H., & Prenzel, E. (2000a). *Design requirements for long range commercial transports.* Task Technical Report 2.2.5R. Cryoplane project.

Oelkers, W., Schulz, H., & Prenzel, E. (2000b). *Design requirements for very long range commercial transports.* Task Technical Report 2.2.4R. Cryoplane project.

Oelkers, W., Schulz, H., & Prenzel, E. (2000c). *Design standards for long range commercial transports.* Task Technical Report 2.2.5S. Cryoplane project.

Oelkers, W., Schulz, H., & Prenzel, E. (2000d). *Design standards for very long range commercial transports.* Task Technical Report 2.2.4S. Cryoplane project.

Onat, E., & Klees, G. (1979). *A method to estimate weight and dimensions of large and small gas turbine engines.* National Aeronautics and Space Administration, NASA-CR-189481.

Payzer, R., & Renninger, S. (1979). Hydrogen fueled high bypass turbofans in subsonic aircraft. In *International DGLR/DFVLR Symposium on hydrogen in air transportation.* Stuttgart, Germany.

Penner, J., Lister, D., Griggs, D., Dokken, D., & McFarland, M. (1999). *Aviation and the global atmosphere: A special report of IPCC Working Groups I and III.* Cambridge University Press.

Philpot, M. (1995). Practical consideration in designing the engine cycle. In *Advanced Aero-Engine Concepts and Controls,* AGARD Conference Proceedings 572. North Atlantic Treaty Organization, Advisory Group for Aerospace Research and Development.

Plencner, R. (1989). *Plotting Component Maps in the NAVY/NASA Engine Program (NNEP) - A method and Its Usage.* National Aeronautics and Space Administration, NASA-TM-101433.

Ponater, M., Marquart, S., & Sausen, R. (2002). Contrails in a comprehensive global climate model: Parametrisation and radiative forcing results. *J. Geophys. Res., 107*(D13), 4164.

Ponater, M., Pechtl, S., Sausen, R., Schumann, U., & Hüttig, G. (2006). Potential of the cryoplane technology to reduce aircraft climate impact: A state-of-the-art assessment. *Atmospheric Environment, 40*(36), 6928–6944.

Ramsden, K. (2004a). *Axial Compressor Design and Performance.* Lecture Notes of the Short Course in Gas Turbine Performance: Cranfield University, May, 24-28.

Ramsden, K. (2004b). *Axial Turbine Design and Performance.* Lecture Notes of the Short Course in Gas Turbine Performance: Cranfield University, May, 24-28.

Ramsden, K. (2005a). *Axial Compressor Design Manual.* Lecture Notes of the Short Course in Gas Turbine Design and Performance: Cranfield University, April 18-29.

Ramsden, K. (2005b). *Axial Turbine Design Manual.* Lecture Notes of the Short Course in Gas Turbine Design and Performance: Cranfield University, April 18-29.

Rayee, T., Verstraete, D., & Hendrick, P. (2008). Development of a mixer model to compare mixed and unmixed HBPR turbofans. In *44^{th} AIAA/ASME/SAE/ASEE Joint Propulsion Conference and Exhibit*, AIAA-2008-4963. Hartford, Conneticut.

Raymer, D. (1989). *Aircraft Design: A conceptual Approach.* AIAA Education Series. American Institute for Aeronautics and Astronautics, Third ed.

Reynolds, T. (1955). *Aircraft Fuel Tank Design For Liquid Hydrogen.* National Aeronautics and Space Administration, NACA-RM-E55F22.

Rizvi, S. (2007). *Design of high bypass ratio turbofan for a civil aircraft.* Master's thesis, Cranfield University, School of Engineering, Cranfield, England.

Robinson, M. (1994). Composite cryogenic propellant tank development. In *35^{th} AIAA/ASME/ASCE/AHS/ASC Structures, Structural Dynamics and Materials Conference*, AIAA-1994-1375. Washington D.C., USA.

Robinson, M., Eichinger, J., & Johnson, S. (2002). Hydrogen permeability requirements and testing for reusable launch vehicle tanks. In *43^{th} AIAA/ASME/ASCE/AHS/ASC Structures, Structural Dynamics and Materials Conference*, AIAA-2002-1418. Denver, Colorado, USA.

Rollin, G. (2003). Combustion chamber. In *Von Karman Institute Lecture Series on aero-engine design: a state of the art*. Von Karman Institute, April 7-11.

Rolls-Royce (2005). *The Jet Engine.* Rolls-Royce plc.

Rolls-Royce (2007). *Market Outlook 2007 - Forecast 2007-2026.* Rolls-Royce plc.

Romeo, G., Moraglio, I., & Novarese, C. (2007). ENFICA-FC: Preliminary survey & design of 2-seat aircraft powered by fuel cells electric propulsion. In *7^{th}AIAA Aviation Technology, Integration and Operations Conference (ATIO)*, AIAA-2007-7754.

Roskam, J. (1989a). *Airplane Design Part IV: Layout of Landing Gear and Systems.* DARCorporation.

Roskam, J. (1989b). *Airplane Design Part V: Component Weight Estimation.* DARCorporation.

Roskam, J. (1989c). *Airplane Design Part VIII: Airplane Cost Estimation: Design, Development, Manufacturing and Operating*. DARCorporation.

Roskam, J. (1997a). *Airplane Design Part I: Preliminary Sizing of Airplanes.* DARCorporation.

Roskam, J. (1997b). *Airplane Design Part II: Preliminary Configuration Design and Integration of the Propulsion System.* DARCorporation.

Roskam, J. (1997c). *Airplane Design Part VI: Preliminary Calculation of Aerodynamic, Thrust and Power Characteristics.* DARCorporation.

Roskam, J. (2002). *Airplane Design.* Lecture Notes of the Aerospace Short Course in Aircraft design: The University of Kansas.

Rostek, N. (2002). *Mini Requirement Spec. Tank.* Task Technical Report 3.6.2. Cryoplane project.

RTO-AVT (2007). *Performance Prediction and Simulation of Gas Turbine Engine Operation for Aircraft, Marine, Vehicular and Power Generation.* Final Report, RTO-TR-AVT-036. North Atlantic Treaty Organization, Research and Technology Organisation.

Rubini, P. (2005). *Turbine Blade Cooling*. Lecture Notes of the Short Course in Gas Turbine Design and Performance: Cranfield University, April 18-29.

Sanghi, V., Kishore Kumar, S., Sundararajan, V., & Sane, S. (1998). Preliminary estimation of engine gas-flow-path size and weight. *Journal of Propulsion and Power*, *14*(2), 208–214.

Saravanamuttoo, H. (2005). *Gas Turbine Design Process.* Lecture Notes of the Short Course in Gas Turbine Design and Performance: Cranfield University, April 18-29.

Saravanamuttoo, H., Rogers, G., & Cohen, H. (2001). *Gas Turbine Theory.* Pearson Education, Fifth ed.

Sarigiannis, D., & Kronberger, B. (2001). *D22 Emissions inventory and comparative assessment of emissions from alternatives in hydrogen production from renewables.* Task Technical Report 7.3.1. Cryoplane project.

Sausen, R., Isaksen, I., Grewe, V., Hauglustaine, D., Lee, D. S., Myhre, G., Köhler, M. O., Pitari, G., Schumann, U., Stordal, F., & Zerefos, C. (2005). Aviation radiative forcing in 2000: An update on IPCC (1999). *Meteorologische Zeitschrift*, *14*(4), 555–561.

Sausen, R., & Schumann, U. (2000). Estimates of the climate response to aircraft CO_2 and NO_x emissions scenarios. *Climatic Change*, *44*, 27–58.

Schaufele, R. (2000). *The Elements of Aircraft Preliminary Design.* Aries Publications.

Schmidtchen, U., Behrend, E., Pohl, H. ., & Rostek, N. (1997). Hydrogen aircraft and airport safety. *Renewable and Sustainable Energy Reviews*, *1*(4), 239–269.

Schnieder, H., & McKay, D. (2001). *Global energy resources and hydrogen supply costs.* Task Final Report 8.4-1. Cryoplane project.

Schumann, U. (2005). Formation, properties and climatic effects of contrails. *Comptes Rendus Physique, 6*(4-5 SPEC. ISS.), 549–565.

Schwartz, J. (2008). *Advanced Hydrogen Liquefaction Process.* Presentation for the DOE Annual Merit Review Meeting, Praxair.

Seddon, J., & Goldsmith, E. (1999). *Intake Aerodynamics.* AIAA Education Series. American Institute for Aeronautics and Astronautics.

Sefain, M. (2005). *Hydrogen aircraft concepts & ground support*. Ph.D. thesis, Cranfield University, School of Engineering, Cranfield, England.

Sefain, M., & Jones, R. (2002). *Unconventional Aircraft Configurations.* Task Final Report 2.4-4. Cryoplane project.

Sergeant, N., Matheys, J., & Van Mierlo, J. (2008). *Waterstof - motor van de toekomst? (Hydrogen - engine of the future?).* Dossier 17. Vlaams Instituut voor Wetenschappelijk en Technologisch Aspectenonderzoek (ViWTA) (Flemish Insitute for Research on Scientific and Technological Aspects).

Serovy, G. (1976). Compressor and turbine prediction system development - lessons from thirty years of history. In *Modern prediction methods for turbomachinery performance,* AGARD Lecture Series 83. North Atlantic Treaty Organization, Adivsory Group for Aerospace Research and Development.

Sharke, P. (2004). H_2 tank testing. *Mechanical Engineering -CIME, 126*(4).

Sharpe, E., & Helenbrook, R. (1978). Cryogenic foam insulation for LH_2 fueled subsonic transports. In *2^{nd} AIAA/ASME Thermophysics and heat transfer conference,* AIAA-1978-0875. Palo Alto, USA.

Sherif, S., Barbir, F., & Vezirogly, T. (2003a). Principles of hydrogen energy production, storage and utilization. *Journal of Scientific & Industrial Research, 62,* 46–63.

Sherif, S., Barbir, F., & Vezirogly, T. (2003b). Wind energy and the hydrogen economy. In *41^{st} AIAA Aerospace Sciences Meeting and Exhibit,* AIAA-2003-691. Reno, Nevada, USA.

Shimko, M. (2008). *Innovative Hydrogen Liquefaction Cycle.* FY 2008 Annual Progress Report, DOE Hydrogen Program.

Silverstein, A., & Hall, E. (1955). *Liquid hydrogen as a jet fuel for high-altitude aircraft.* National Aeronautics and Space Administration, NASA-RM-E55C28a.

Simon, B., Brines, G., & Orlov, V. (1994). Joint cryogenic engine study. *International Journal of Hydrogen Energy, 19*(7), 617–623.

Singh, R. (2004). *An Overview: Gas Turbine Combustion Generated Pollutants and the Emerging Technology Solutions.* Lecture Notes of the Short Course in Gas Turbine Performance: Cranfield University, May, 24-28.

Singleton, A., Lapin, A., & Wenzel, L. (1965). Rate model for ortho-parahydrogen reaction on a highly active catalyst. In *Advances in Cryogenic Engineering*, vol. 10. Plenum Press.

Sloop, J. (1978). *Liquid hydrogen as a propulsion fuel, 1945-1959*. National Aeronautics and Space Administration, NASA-SP-4404.

Smith, C. (2005). The environmental challenge - bringing technology to market. In *17^{th} International symposium on airbreathing engines (ISABE)*, ISABE-2005-1008. Munich, Germany.

Sosounov, V., & Orlov, V. (1990). Experimental turbofan using liquid hydrogen and liquid natural gas as fuel. In *AIAA/SAE/ASME/ASEE 26^{th} Propulsion Joint Specialist Conference*, AIAA-1990-2421. Orlando, Florida, USA.

Stabe, R., Whitney, W., & Moffitt, T. (1984). Performance of a high-work low aspect ratio turbine tested with a realistic inlet radial temperature profile. In *20^{th} Joint Propulsion Concerence*, AIAA-1984-1161 & NASA-TM-83655. Cincinnati, Ohio, USA.

Stordal, F., Myhre, G., Stordal, E., Rossow, W., Lee, D. S., Arlander, D., & Svendby, T. (2005). Is there a trend in cirrus cloud cover due to aircraft traffic. *Atmospheric Chemistry and Physics*, *5*, 2155–2162.

Stroe, M. (2005). *Hydrogen embrittlement of ferrous materials*. Ph.D. thesis, Université Libre de Bruxelles, Brussels, Belgium.

Svensson, F. (2005). *Potential of reducing the environmental impact of civil subsonic aviation by using liquid hydrogen*. Ph.D. thesis, Cranfield University, School of Engineering, Cranfield, England.

Svensson, F., Hasselrot, A., & Moldanova, J. (2004). Reduced environmental impact by lowered cruise altitute for liquid hydrogen-fuelled aircraft. *Aerospace Science and Technology*, *8*(4), 307–320.

Svensson, F., & Singh, R. (2004). Effects of using hydrogen on aero gas turbine pollutant emissions, performance and design. In *ASME Turbo Expo 2004*, ASME-GT2004-53349. Vienna, Austria.

Svoboda, C. (2000). Turbofan engine database as a preliminary design tool. *Aircraft Design*, *3*, 17–31.

Syed, M., Sherif, S., Vezirogly, T., & Sheffield, J. (1998). An economic analysis of three hydrogen liquefaction systems. *International Journal of Hydrogen Energy*, *23*(7), 565–576.

Taylor, M. (2003). HP axial flow turbine aerodynamic design. In *Von Karman Institute Lecture Series on aero-engine design: a state of the art*. Von Karman Institute, April 7-11.

Theisen, J., & Brewer, G. (1979). Laminar flow stabilization by surface cooling on hydrogen fueled aircraft. In *AIAA Aircraft Systems and Technology Meeting*, AIAA-1979-1863. New York, New York, USA.

Thibault, J. (1979). Hydrogen liquefaction, storage and transfer on an airport site. In *International DGLR/DFVLR Symposium on hydrogen in air transportation*. Stuttgart, Germany.

Thompson, A. (1980). Current status of the role of hydrogen in stress corrosion cracking. *Materials Science and Engineering*, *43*, 41–46.

Tong, M., Halliwell, I., & Ghosn, L. (2004). A computer code for gas turbine engine weight and disk life estimation. *ASME Journal of Engineering for Gas Turbines and Power*, *126*(2), 265–270.

Torenbeek, E. (1973). *The computation of characteristic areas and volumes of major aircraft components in project design*. Delft University of Technology, Report M-189.

Torenbeek, E. (1980). *Fundamentals of conceptual design optimization of subsonic transport aircraft*. Delft University of Technology, Report LR-292.

Torenbeek, E. (1982). *Synthesis of subsonic airplane design*. Delft University Press.

Torenbeek, E. (2000). *The case for twin-fuselage configurations and the H-cabin*. National Aerospace Laboratorium (NLR), NLR-TR-2000-095.

Torenbeek, E., & Jesse, E. (2001). *Exploratory design study of a transonic airliner with twin fuselage configuration*. National Aerospace Laboratorium (NLR), NLR-TR-2001-309.

Trilla, J., Grossen, J., Robinson, A., Funke, H., Bosschaerts, W., & Hendrick, P. (2008). Development of a hydrogen combustion chamber for an ultra micro gas turbine. In *Powermems 2008 Conference*. Sendai, Japan.

USBoLS (2009). *Economic News Release, Consumer Price Index*. `http://www.bls.gov/news.release/cpi.toc.htm`: US Bureau of Labor statistics.

Verstraete, D., Bizzarri, D., & Hendrick, P. (2008). In-flight oxygen collection for a two-stage air-launch vehicle: integration of vehicle and separation cycle design. In L. DeLuca, C. Bonnal, O. Haidn, & S. Frolov (Eds.) *Progress in propulsion physics, Chapter 6: Air-Breathing Turbomachinery and LAPCAT*, vol. 1, (pp. 551–568). Toruss Press & EDP Sciences.

Verstraete, D., & Hendrick, P. (2006). Gasturb 10 - usage and capabilities. Presentation to the students of Université Libre de Bruxelles and Royal Military Academy of Belgium.

Verstraete, D., & Hendrick, P. (2008). *Parametric Sizing of More-Electric regional jet aircraft with hydrogen fuel - Addendum A: Sizing of the tanks*. Deliverable D2/6 Add. A. ENFICA-FC (Environmentally Friendly Inter City Aircraft with Fuel Cell propulsion).

Verstraete, D., Hendrick, P., Pilidis, P., & Ramsden, K. (2005a). Hydrogen as an (aero) engine fuel. In 17^{th} *International symposium on airbreathing engines (ISABE)*, ISABE-2005-1212. Munich, Germany.

Verstraete, D., Hendrick, P., Pilidis, P., & Ramsden, K. (2007). Development and validation of a modular gas turbine engine performance model. In *18th International symposium on airbreathing engines (ISABE)*, ISABE-2007-1330. Beijing, China.

Verstraete, D., Trilla, J., De Bruyn, N., & Hendrick, P. (2005b). Numerical simulations in the design of an ultra micro gas turbine combustion chamber. In *17th International symposium on airbreathing engines (ISABE)*, ISABE-2005-1271. Munich, Germany.

Verstraete, W. (2006). Microbiële brandstofcellen: van afval naar electriciteit (microbiological fuel cells from waste to electricity). In *Brandstofcellen en waterstof in Vlaanderen (Fuel Cells and hydrogen in Flanders)*. Mol, Belgium: Vlaams samenwerkingsverband brandstofcellen (Flemish cooperation for fuel cells).

Vicente, E. (1994). *Effect of bypass ratio on long range subsonic engines*. Master's thesis, Cranfield University, School of Engineering, Cranfield, England.

Villarino, M. (2005). Ramanujan's perimeter of an ellipse.
URL `http://www.citebase.org/abstract?id=oai:arXiv.org:math/0506384`

Volders, M., & Slingerland, R. (2003). Environmental harm minimization during cruise-flight for long-range preliminary aircraft design. In *AIAA 3rd Annual Aviation Technology, Integration and Operations Conference (ATIO)*, AIAA-2003-6803.

Walsh, P., & Fletcher, P. (2004). *Gas Turbine Performance*. Blackwell Publishing, Second ed.

Waters, M., & Schairer, E. (1977). *Analysis of turbofan propulsion system weight*. National Aeronautics and Space Administration, NASA-TM-73199.

Wentz, W., Myose, R., & A.S., M. (2005). Hydrogen-fueled general aviation airplanes. In *5thAIAA Aviation Technology, Integration and Operations Conference (ATIO)*, AIAA-2005-7324.

Westenberger, A. (2003a). Hydrogen fuelled aircraft. In *AIAA/ICAS International Air & Space Symposium and Exposition: The Next 100 Years*, AIAA-2003-2880. Dayton, Ohio, USA.

Westenberger, A. (2003b). *Liquid Hydrogen fuelled aircraft - System Analysis, Final Technical Report (Publishable version)*. Cryoplane project.

Wilcock, R., Young, J., & Horlock, J. (2005). The effect of turbine blade cooling on the cycle efficiency of gas turbine power cycles. *Journal of Engineering for Gas Turbines and Power*, *127*(1), 109–120.

Williams, D. (2007). *Airframe Engine Integration*. Lecture Notes of the Short Course in Propulsion Systems Performance and Integration: Cranfield University, January 29 - February 2.

Williams, V., & Noland, R. (2005). Variability of contrail formation conditions and the implications for policies to reduce the climate impacts of aviations. *Transportation Research Part D: Transport and Environment*, *10*(4), 269–280.

Williams, V., Noland, R., Majumdar, A., Toumi, R., Ochieng, W., & Molloy, J. (2007). Reducing environmental impacts of aviation with innovative air traffic management technologies. *The Aeronautical Journal*, *111*(1125), 741–749.

Williams, V., Noland, R., & Toumi, R. (2003). Air transport cruise altitude restrictions to minimize contrail formations. *Climate Policy*, *3*(3), 207–219.

Wilson, D., & Korakianitis, T. (1998). *The Design of High-Efficiency Turbomachinery and Gas Turbines*. Prentice Hall, Second ed.

Witcofski, R. (1981a). *Alternate aircraft fuels - prospects and operational implications*. National Aeronautics and Space Administration, NASA-TM-X-74030.

Witcofski, R. (1981b). *Dispersion of Flammable Vapor Clouds Resulting from Large Spills of Liquid Hydrogen*. National Aeronautics and Space Administration, NASA-TM-83131.

Young, J., & Wilcock, R. (2002a). Modeling the air-cooled gas turbine: Part 1 - general thermodynamics. *Journal of Turbomachinery*, *124*(2), 207–213.

Young, J., & Wilcock, R. (2002b). Modeling the air-cooled gas turbine: Part 2 - coolant flows and losses. *Journal of Turbomachinery*, *124*(2), 214–222.

Younghans, J., & Paul, D. (1989). Chapter 4: Inlets and engine/inlet integration. In G. Oates (Ed.) *Aircraft propulsion systems technology and design*, AIAA Education Series. American Institute for Aeronautics and Astronautics.

Yuasa, S., Oshimi, K., & Wong, S. (2005). Specified problems and development of prototypes of ultra-micro combustor. In *17th International symposium on airbreathing engines (ISABE)*, ISABE-2005-1272. Munich, Germany.

Zielinski, A. (2001). Hydrogen-assisted degradation of some non-ferrous metals and alloys. *Journal of Materials Processing Technology*, *109*, 206–214.

Ziemann, J., Shum, F., Moore, M., Kluyskens, D., Thomaier, D., Zarzalis, N., & Eberius, H. (1998). Low-NO_X combustors for hydrogen fueled aero engine. *International Journal of Hydrogen Energy*, *23*(4), 281–288.

Zimbrick, R., & Colehour, J. (1990). Investigation of very high bypass ratio engines for subsonic transports. *Journal of Propulsion*, *6*(4), 490–496.

This page is intentionally left blank

APPENDIX A

Some aspects of hydrogen in aviation

Hydrogen is an efficient, versatile and potentially very clean energy carrier that together with electricity could enable a permanent, sustainable energy system independent from energy sources. It however has several unique characteristics that might warrant its applicability for aviation. A review of the characteristics of hydrogen and their compatibility with aeronautical applications is thus in order. This appendix therefore comments on several aspects of the utilization of hydrogen in aviation.

In section A.1 some properties of hydrogen are reviewed. Particular attention is paid to specificities of liquid hydrogen as it is the preferred form of storage of hydrogen for long range transport aircraft. Production methods of hydrogen are given next in section A.2. Hydrogen is namely an energy carrier and not a fuel and thus has to be produced. As environmental compatibility is one argument in favor of hydrogen the environmental impact of the production method is included in this section. As liquid hydrogen will be used, liquefaction methods are subsequently described (section A.3). After this some aspects of distributing the hydrogen to and in the airport as well as storing it on site are covered in section A.4. Finally the impact of hydrogen on aircraft handling and safety are dealt with. The goal of this appendix is not to be exhaustive nor complete but rather to touch upon some of the aspects that are important in aviation. Extensive reference is made in all sections to the sources of the information. These should be consulted for a more complete view.

A.1 Properties of hydrogen

Hydrogen is the most abundant element of the universe and could as such provide an omnipresent energy carrier for transportation provided it has the right properties as a fuel. The most important properties of hydrogen are therefore compiled in Table A.1. Characteristics of other alternative fuel candidates are also given in the table to allow a comparison. As can been seen from the table, hydrogen has a very high lower heating value (on a mass basis), which makes it a prime candidate for weight limited applications such as aviation and aerospace. Due to its low density as both a liquid but especially as a gas, the energy density per volume of hydrogen is however rather low compared to the alternatives. Under normal temperature and pressure (NTP) conditions, gaseous hydrogen for instance has a density 14 times less than air. Even when compressed, the density remains fairly low which makes liquid hydrogen the only viable option for long range transport aircraft[1] (Barbir (2005), Brewer (1991), Westenberger (2003a) and Westenberger (2003b)). Gaseous storage under high pressure seems on the other hand the most reasonable alternative for ground storage (Barbir, 2005).

The boiling point of hydrogen at atmospheric pressure is -252.7°C. Cryogenic liquid hydrogen can thus only exist at very low temperatures. The critical point of hydrogen is namely at a temperature of 32.94 K and a pressure of 12.84 bar at which the liquid density is reduced to 31.40 kg/m^3. A careful design of the insulation system of the tanks is hence primordial as described in Chapter 3.

Table A.1. Properties of hydrogen, methane and) synthetic kerosene (synjet, adopted from Contreras et al. (1997).

Property	**Synjet**	**Methane**	**Hydrogen**
Average formula	$C_{12.5}H_{24.4}$	CH_4	H_2
Boiling point [°C]	167.0-266.0	-161.3	-252.7
Melting point [°C]	-50.0	-182.0	-259.2
Density at boiling point [g/cm^3]	0.8	0.423	0.071
Lower heating value [kJ/kg]	42906	48139	119970
Flame temperature [°C]	2022	1973	2158
Heat of combustion [kJ/g]	42.8	50	120
Heat of vaporization [J/g]	360	510	446
Standard heat of formation [kJ/mol]	-208.4	-74.8	0
Stoichiometric FAR	14.7	17.2	34.2
kg fuel/ GJ	233	208	83.3
m^3 fuel/ GJ	0.032	0.048	0.12
Flammability limits in air [vol%]	0.8-6.0	5.3-15.0	4.0-75.0
Detonation limits in air [vol%]	1.1-3.3	6.3-13.5	13.0-65.0
Minimum ignition energy in air [mJ]	0.25	0.29	0.02
Laminar burning velocity in air [cm/s]	43	40	265
Auto-ignition temperature [°C]	440	40	585
Thermal energy radiated by surroundings [%]	33-43	23-33	17-25
Theoretical explosion energy [kg TNT/m^3 gas]	44.42	7.03	2.02
Diffusion coefficient in air [cm^2/s]	0.05	0.16	0.61
Buoyancy in air [m/s]	none	0.8-6.0	1.2-9.0

---

[1] Allidieris & Janin (2002a) also considered storage as a supersaturated liquid. This was however abandoned as the pressure rise in a supersaturated liquid is about 10 times higher than for a saturared liquid for the same heat input. Slush hydrogen, a mixture of liquid and solid hydrogen, was also considered in the Cryoplane study. It was not adopted as the additional energy required to solidify a part of the fuel mass resulted in an increase of the aircraft direct operating costs despite the gain in density (Westenberger, 2003b).

Despite its low density, hydrogen is an attractive candidate as alternative fuel as it allows a very stable combustion over a wide range of operating conditions. This is reflected in Table A.1 by the wide flammability limits, the high flame velocity and the low ignition energy. Its favorable combustion characteristics make hydrogen also the main fuel for ultra micro gas turbine engines (amongst others Epstein (2004), Trilla et al. (2008), Verstraete et al. (2005a), Verstraete et al. (2005b) and Yuasa et al. (2005)).

In spite of its simple molecular structure, ordinary molecular hydrogen can exist in two distinct isomers which differ in nuclear spin[2]. Ortho-$\mathrm{H_2}$ has the nuclear spins of the two protons aligned in the same direction, or spin unpaired, whereas para-H_2 has opposite spins of the protons, or spin paired. At temperatures higher than -50 °C, the equilibrium composition of the two forms is approximately 75 vol% ortho- and 25 vol% para-hydrogen, which is called normal hydrogen. At the normal boiling point the equilibrium composition is however 0.20 vol% ortho and 99.80 vol% para-hydrogen, which shows the strong dependency of the equilibrium composition on temperature. As the different nuclear spins of the two forms entails a different energy level, the heat of conversion from ortho to para-hydrogen is also a strong function of temperature (and independent of pressure), as shown on Figure A.1. The dotted lines on the figure represent an analytical approximation to the curves, derived by Balepin et al.. Since para-hydrogen cannot be converted to normal hydrogen at low temperatures but only to equilibrium hydrogen, the heat of conversion to equilibrium hydrogen is shown on the right-hand side of the figure.

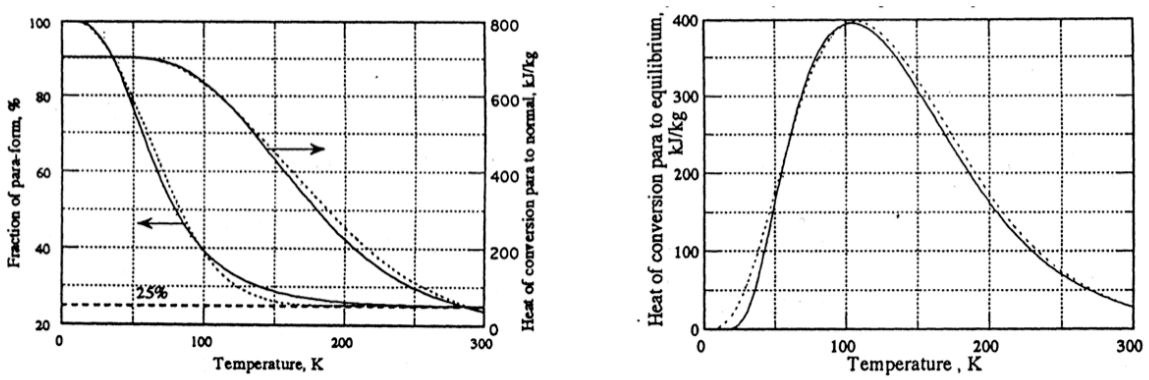

Figure A.1. Hydrogen equilibrium composition and heat of conversion, adopted from Balepin et al. (1994).

An important aspect of this conversion is the region between roughly 50 and 200 K, where a significant amount of heat can be tied up in the para- to equilibrium transition. If a pinch point in the heat exchanger system occurs in the region of this 'peak', the rate of conversion becomes an important consideration in the system design and performance (Balepin et al., 1994). The conversion from para to equilibrium hydrogen is however typically significantly slower than the the residence time in a non-catalytic heat exchanger (Billig, 1991). On top of that, the initial composition is very stable and spontaneous conversion only occurs at 1000-1100 K (Balepin et al., 1994). If there is no pinch point in the

---

[2] Both forms are however ordinary hydrogen and should thus not be confused with the isotopes deuterium and the unstable and very rare tritium.

heat exchanger system and the final temperature of the hydrogen is in excess of about 280 to 330 K then this heat lost issue does not arise (Billig, 1991).

The effect of the para to equilibrium conversion can be expressed as an increase in specific heat capacity in the equilibrium state, as shown on Figure A.2. As can be seen from the figure, the enthalpy difference peaks at about 60-80 K. The figure shows that the total heat capacity for equilibrium hydrogen exceeds the heat capacity of para-hydrogen by about 36 % at 80 K. At this temperature the heat lost in the conversion from para-H_2 to equilibrium-H_2 thus amounts to about 36 % of the cooling capacity available in bringing para-hydrogen from its storage conditions to 80 K. Even though a reduction of this loss in cooling capacity is possible by using a catalytic bed to accelerate the conversion, some loss is nevertheless inherent. This implies that if the para-hydrogen is passed through a catalytic bed the mass of the heat exchanger could be reduced by up to 30 % if the enthalpy difference is completely recovered (Balepin et al., 1994). Metal catalysts such as Pt, Ni and W could be applicable but with current technology of conversion by catalysts their mass and size make them most unlikely for flight applications. According to Billig (1991) approximately 70% of the loss in refrigerative efficiency can nonetheless be recuperated without an excessive mass penalty. Some older studies however show promising results for nickel oxide silica gel catalyst where a reaction rate increase of 100 to 1000 compared to 'conventional' metal catalysts is reported (Hutchinson et al. (1965) and Singleton et al. (1965)). This might be a promising path to pursue to reduce the heat exchanger mass.

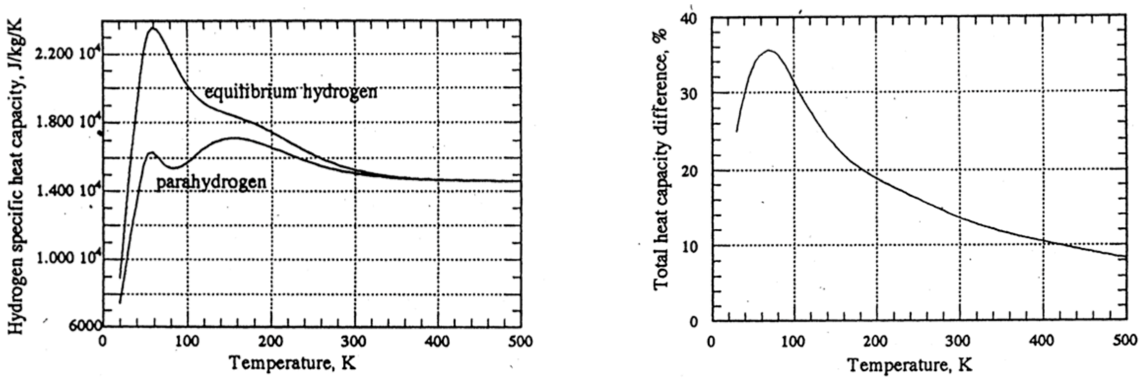

Figure A.2. Specific heat capacity and enthalpy difference between equilibrium and para hydrogen, adopted from Balepin et al. (1994).

The para to ortho conversion furthermore requires that a non-equilibrium hydrogen composition needs to be considered in precise calculations of the flow path. As only normal hydrogen is available in the software used to generate the thermodynamic properties of the combustion gases (see section C.1), this was however not possible for this work. It is nevertheless very unlikely that this will significantly change the trends analyzed in this work. Verification is nonetheless required, preferably by tests.

According to (Billig, 1991), the curve of para-to-ortho conversion only serves as a reference in regard to the design and performance of the propulsion system. The ortho-to-para conversion on the other hand has significant importance in the preparation of the liquid hydrogen and in filling and maintaining the liquid hydrogen tanks. After all, when cooling down the hydrogen, the original ortho-hydrogen molecules drop to a lower molecular-energy level and this changeover involves a release of a quantity of energy. This energy released in the exothermic reaction would namely lead to vaporization of the liquid hydrogen. For instance, at 20 K the heat of conversion from ortho to para-H_2 is 520.0 kJ/kg while the latent heat of vaporization is 452 kJ/kg (Allidieris & Verroust, 2002). More information on the rate of the ortho to para-H_2 transformation can be found in Barron (1985), Brooks et al. (1994), Hutchinson et al. (1965) and Singleton et al. (1965).

Because of the different weighing of the energy levels of the two forms of hydrogen, the specific heats for ortho- and para-hydrogen are different as indicated previously. Because of this difference in specific heats, other thermal and transport properties, related to the specific heat, are also affected. For instance, the enthalpy, the entropy, the velocity of sound as well as the thermal conductivity vary strongly with the composition of the mixture while the effect on density and viscosity is very small (Barron, 1985). In general, the thermal properties of the above-mentioned compositions differ only at low temperatures up to the Boyle temperature of 110 K where they become practically identical. However, the caloric properties (heat capacity, enthalpy, entropy) differ up to 500 K (Barron, 1985). As the influence of these differences on the combustion gases cannot be included in the cycle calculations, they are neglected here. Figure A.3 shows the temperature enthalpy diagram of para and equilibrium hydrogen

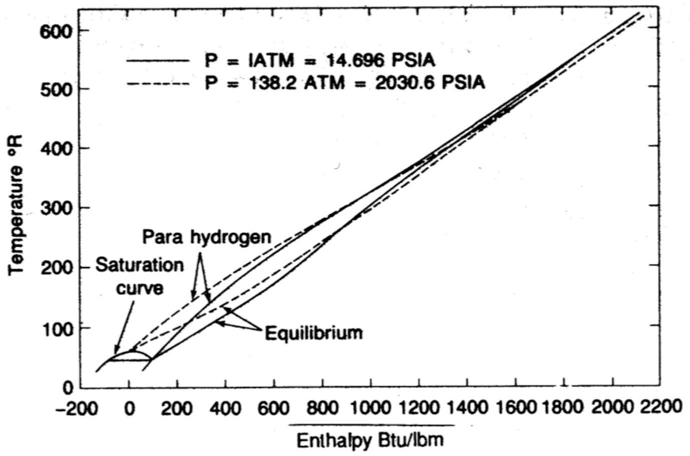

Figure A.3. Temperature enthalpy diagram of para and equilibrium hydrogen, adopted from Barron (1985).

A.2 Hydrogen production

As hydrogen cannot be found in nature in its pure form, but only in combination with other elements (mainly with oxygen, carbon and nitrogen), it needs to be produced. It is therefore not an energy source as conventional hydrocarbon fuels but an energy carrier. As an energy carrier hydrogen can however be produced in many different ways, from many 'raw materials' and with a wide range of technologies, as shown on Figure A.4. As indicated on the figure, the production methods can basically be split into processes using only water as raw material and processes using other raw materials (in addition to water or not). The latter group produces other byproducts besides hydrogen as well. Below, a brief description is given of hydrogen production processes. The overview is far from complete but focusses on the main production methods. As the adoption of hydrogen is partially motivated by its cleanness, the emissions of greenhouse gases during production are also accounted for.

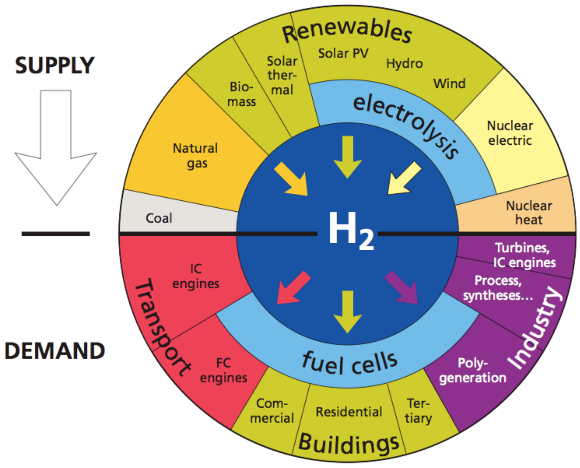

Figure A.4. Primary energy sources, energy converters and applications for hydrogen, adopted from EC (2003).

The bulk of the hydrogen is produced today from fossil fuels, through steam reforming of methane or natural gas or through partial oxidation of hydrocarbon fuels. At present, almost 48% of the world's hydrogen is produced from **steam reforming** of methane, which is the most common and least expensive method of producing hydrogen (Balat, 2008). Steam reforming furthermore produces the smallest amount of emissions of current mass production processes (Hapke & Bode, 2001). Often natural gas is used as feed but heavier hydrocarbons up to naphtha can also be processed (Koroneos et al. (2004) and Koroneos et al. (2005)). As shown on Figure A.5, steam reforming basically involves three main steps. In a first steps the natural gas is catalytically split in the presence of steam at temperatures around 800-900°C. Normally, nickel catalysts are used in a gas-fired oven (Hapke & Bode (2001) and Koroneos et al. (2004)). During this split the so-called syngas is produced, which is a hydrogen rich gas with on the order of 70-75% of hydrogen on a dry basis, along with smaller amounts of CH_4, CO and CO_2 (Balat, 2008). The basic equation for the split is

$$C_nH_m + n\,H_2O \rightarrow n\,CO + (n + m/2)\,H_2$$

In the following step, the shift-reaction, the carbon monoxide from the syngas is converted into carbon dioxide and hydrogen according to the following reaction

$$CO + H_2O \rightarrow CO_2 + H_2$$

The shift reaction is often catalyzed using iron oxide. In the final purification step, the hydrogen is separated from the product gas. Pressure swing adsorption is mostly used for

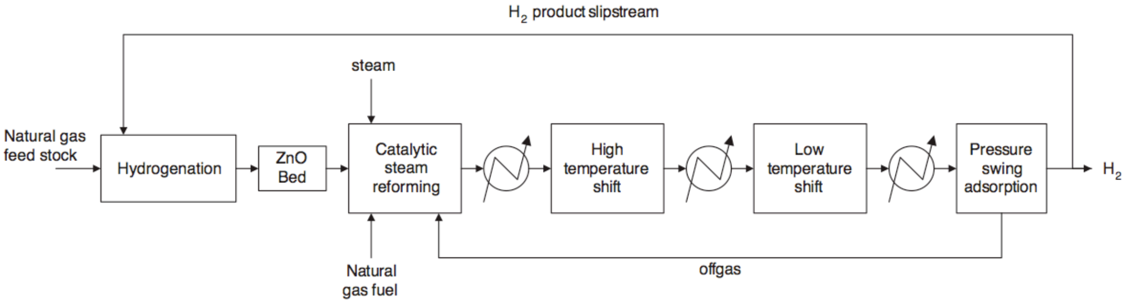

Figure A.5. Block flow diagram of steam reforming, adopted from Koroneos et al. (2004).

this step nowadays (Koroneos et al., 2004). The remaining product gas is used to fire the reactor and is released into the atmosphere after passing several heat exchangers.

Partial oxidation is an exothermic reaction involving oxygen and steam. The need for external energy can be eliminated by controlling the amounts of oxygen and water vapor (Balat (2008) and Sergeant et al. (2008)). Natural gas (or other hydrocarbons) react in the partial oxidation process under high pressure with the oxygen to hydrogen and CO, which consequently reacts with the steam to form CO_2. Partial oxidation is less energy-efficient than steam reforming but it is one of the cheapest methods to produce hydrogen if the oxygen is freely available (Sergeant et al., 2008). The high carbon content of the feed stock however results in significant CO_2 emissions. **Coal gasification** also suffers from this drawback. In this process, coal reacts with water vapor to yield a mixture of hydrogen and carbon monoxide. Both technologies can only be used on a large scale in an environmentally friendly way if the generated CO_2 is sequestered. Sequestration is however not a mature technology. It is very expensive and entails the risk of release of the stored gas after some time which would annul the environmental benefits (Sergeant et al., 2008).

Hydrogen can also be produced from **biomass**, a potential competitor as alternative fuel for aviation[3] (Corporan et al., 2007). Biomass however suffers from several drawbacks that could be avoided by the utilization of hydrogen. First of all, it is not completely carbon neutral as the crops need to be transported from the harvesting fields to the factories which would use a CO_2 releasing fuel (Ishutkina & Hansman, 2008). For aviation the carbon neutrality is even less the case since the greenhouse gases are emitted at altitude where their radiative forcing is bigger. The main drawback from large-scale biomass fuel production is however the pressure it exerts on natural resources and on the available farmland for food production (Ishutkina & Hansman (2008) and Sergeant et al. (2008)). Additionally, all arable land in the European Union could for instance provide only 20% of the currently required energy (Sergeant et al., 2008) and the current annual fuel consumption of aviation alone would require the coverage of the entire surface area of Europe (Corporan et al., 2007). New biomass fuel production technologies such as algae that would significantly increase the productivity of biomass fuel generation are however

---

[3] Ironically, hydrogen can also be used to increase the liquid fuel production per unit of biomass (Forsberg, 2009).

currently available at lab scale. Using algae, aviation fuel would for instance 'only' require the coverage of an area the size of Belgium (Corporan et al., 2007).

Electrolysis is to date the only available method to generate hydrogen at a large scale in the post fossil fuel era (Sherif et al., 2003a). Electrolysis is furthermore a mature technology and is very efficient due to the absence of moving parts (Sherif et al., 2003a). Currently electrolysis is used to generate about 4% of the total amount of hydrogen produced worldwide (Sergeant et al., 2008).

When applying a potential to an electrolysis cell filled with a suitable electrolyte[4], the following overall cell reaction takes place (Sherif et al., 2003a):

$$H_2O\,(l) \rightarrow H_2\,(g) + O_2\,(g)$$

which is the result of the reaction at the cathode and the anode. The cathode reaction is:

$$2\,H_2O\,(l) + 2\,e^- \rightarrow H_2\,(g) + 2\,OH^-\,(aq)$$

whereas at the cathode the following reaction occurs:

$$2\,OH^-\,(aq) \rightarrow 1/2\,0_2\,(g) + H_2O\,(l)$$

The efficiency of electrolysis currently lies around 72-82% depending on the operating conditions and the capacity of the plant with more advanced alkaline electrolytes being developed at the moment that allow the efficiency to be improved to around 90% (Sherif et al., 2003a). Various technologies exist for electrolytic production of hydrogen: conventional electrolysis, (high pressure) alkaline electrolysis, membrane electrolysis, ...High-pressure electrolysis is the most appealing form as it provides high pressure hydrogen which is favorable for transportation through pipelines (Sarigiannis & Kronberger, 2001).

As electrolysis plants can operate over a wide range of operating capacities, electrolysis is appealing for coupling with renewable energy sources, especially with photovoltaics and wind energy. Photovoltaics namely generate low voltage-direct current, which is exactly what is needed for electrolysis (Sherif et al., 2003a). There is furthermore a good match between the polarization curves of PV cells and electrolyzers which allows them to be matched directly without power tracking electronics and with a coupling efficiency higher than 93 % (Sherif et al., 2003b). The main drawback of this production method is the cost of the photovoltaic cells which leads to a relatively high hydrogen price. Wind energy on the other hand could lead to a fairly cheap production of hydrogen as it does not suffer from such huge capital investment costs (Sherif et al., 2003b). Some matching difficulties however arise mainly related to the big variability in power generated by wind and the intermittent nature of the renewable energy source.

These difficulties however also offer potential benefits. Hydrogen generation could namely be used as peak shaving method whereby a base load is provided to the electricity grid and the additional power generated by the wind turbine is used to produce hydrogen which allows recovering energy that otherwise is waisted[5]. The produced hydrogen can then be

---

[4] A suitable electrolyte is for instance an aqueous solution of KOH or NaOH or NaCl (Sherif et al., 2003a).

[5] The efficiency of the electrolysis plant is then however lower than the aforementioned values (Sherif et al., 2003b).

used to generate extra power when the demand for electricity peaks. Hydrogen production through (off-shore) wind turbines could furthermore result in an increased 'recovery' of the available wind energy. To ensure the availability of electricity whenever needed, a backup unit is namely needed for every wind turbine. The backup unit is then used when there is no wind available. Economically and practically, only about 20% of the nominal power of the grid can therefore be generated through wind turbines and a huge amount of freely available wind energy cannot be utilized.

For both solar and wind power hydrogen production could thus help with load leveling and balancing the intermittent nature of the renewable source. After all, hydrogen is stored more easily than electricity. Similar arguments can also be raised for hydropower and nuclear plants, when the excess power during off-peak hours is used to generate hydrogen (Sherif et al., 2003b).

Besides the aforementioned methods, several 'more exotic' production techniques are currently investigated such as thermolysis or direct thermal decomposition of water using high temperature nuclear technology, photolysis or direct hydrogen extraction from water using sunlight (rather than heat), photo-electrochemical and photo-biological production, … (Calli (2005), Dierick (2006), Sergeant et al. (2008), Sherif et al. (2003a) and Verstraete (2006)). Most of these technologies are far from mature and suffer from various drawbacks.

As hydrogen is an energy carrier and needs to be produced, the production method however needs to be considered when claming the environmentally friendly nature of the fuel. Figure A.6 shows the total impact of the different production methods for hydrogen. Besides production and liquefaction of hydrogen, the emissions generated during the manufacturing of the 'equipment' are also considered. The figure shows the effect of greenhouse gas emissions, acidification emissions (measured by the amount of protons released in the atmosphere), eutrophication air emissions (enrichment of water and soil with nitrogen and phosphorus) and winter smog emissions (chemical emissions of dust and SO_2). As indicated in Koroneos et al. (2004), the absolute values of the evaluation scores on the figure do not matter, but the relative classification is important. It is clearly shown that renewable sources lead to a much lower environmental impact. There is however a big difference within the renewables due to the production methods for the equipment and wind energy has the lowest life cycle impact.

With current technology there is however a trade between environmental impact and cost of hydrogen production, as shown on Figure A.7. The figure however assumes that the European mix including fossil fuels is used for the electricity generation necessary for the construction of the equipment and is therefore not applicable for future scenarios. The figure nonetheless confirms that wind energy seems to be preferable over solar energy for the production of hydrogen for both costs and emissions.

A.3 Hydrogen liquefaction

As the hydrogen needs to be stored as a liquid onboard the aircraft, its temperature must be brought down to roughly 20 K. Before cooling the hydrogen down it has to be puri-

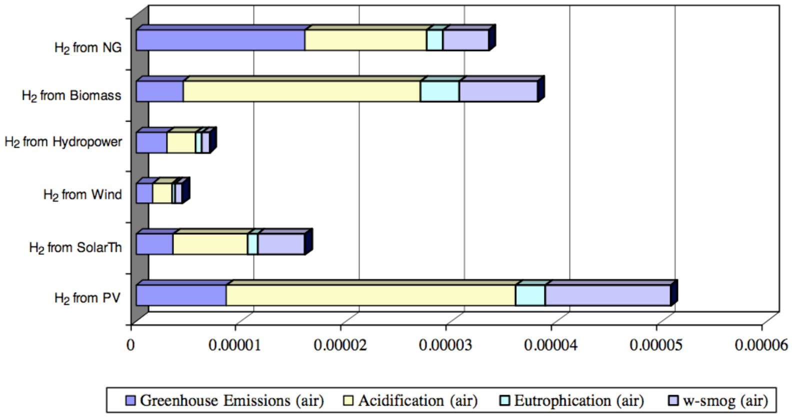

Figure A.6. Total impact scores of different hydrogen production paths, adopted from Koroneos et al. (2004).

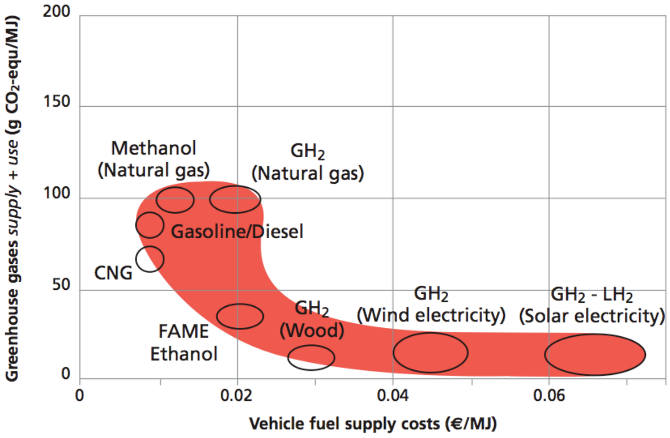

Figure A.7. Specific greenhouse gas emissions as a function of cost, adopted from EC (2003).

fied though. All potential impurities will namely solidify at temperatures higher than the liquefaction temperature of hydrogen and would therefore potentially block the heat exchanger passages of the liquefaction plant. According to Allidieris & Verroust (2002), this purification process typically involves two steps. The warm purification is a classical step and consists out of the removal of vapor and carbon dioxide by adsorption. If electrolysis is used oxygen can be suppressed in a 'deoxo', a catalytic reactor operated at high temperature. The second step, or cold purification, is specific to hydrogen liquefaction and consists of suppressing all gases (CH_4, N_2, Ar) that would become solid during the final cool down. Typically these gases are adsorbed on an activated charcoal bed at cryogenic temperatures around 80 K (Allidieris & Verroust, 2002).

As mentioned previously, a conversion from normal to para-hydrogen is also mandatory during the liquefaction or a significant amount of the stored liquid will be boiled-off. As the conversion is slow a catalyst will be used in the liquefier to speed up the process. According to Allidieris & Verroust (2002), only two catalysts are commercially used. Aluminum with 19% chrome oxide has a weak activity and hence needs long contact times. It is therefore replaced nowadays with iron oxide which is more active.

The conversion needs to be carried out at the highest possible temperature to decrease the consumed power as much as possible. It is usually carried out from 80 K down to 20 K (Allidieris & Verroust, 2002). Either an adiabatic, an isothermal or a continuous conversion are possible. As the gas is heated up by the heat of conversion, an adiabatic conversion decreases the efficiency of the liquefier. Isothermal conversion, takes place in small tubes which are cooled by liquid nitrogen or hydrogen. For continuous conversion on the other hand the catalyst is positioned in the inner circuits of the heat exchanger and the heat of conversion is evacuated by the refrigerant. As hydrogen is close to the ortho-para equilibrium at all temperatures, continuous conversion has the best thermodynamic efficiency (Allidieris & Verroust, 2002). Both adiabatic and isothermal conversions occur at the liquid nitrogen temperature (77 K) whereas the continuous conversion is used between 80 and 20 K.

A considerable amount of energy needs to be spent to bring the temperature of the hydrogen down to below the critical point. Cooling down gaseous hydrogen at 20 bar[6], 300 K, converting it into para hydrogen and liquefying it consumes 4468 kJ/kg (Allidieris & Verroust, 2002). Bringing it down to 80 K in the pre-cooling zone requires 2923 kJ/kg, Reducing the temperature from 80 K further to 20 K and liquifying the hydrogen necessitates 1025 kJ/kg and a final 520 kJ/kg is needed for the conversion to para hydrogen (Allidieris & Verroust, 2002).

All liquefier cycles use a combination of expansions in turbines and through valves (Joule-Thomson expansion). As the inversion temperature of hydrogen (for pressure below 50 MPa) is around 190 K (Allidieris & Verroust, 2002), turbines need to be used for the expansions down to this temperature. Using a constant enthalpy expansion in a throttling or flashing process at temperatures higher than 190 K would namely result in heating up the gas rather than cooling it.

Besides the expansion devices obviously several heat exchangers and compressors are needed in a liquefaction cycle. Several cycles are possible, ranging from a simple, not so efficient Joule-Thompson expansion cycle, over various forms of the Brayton and Claude cycle to combinations of the Reverse-Brayton expansion cycle (or a modified Claude cycle) with the Joule-Thompson expansion cycle (amongst others Allidieris & Verroust (2002), Drnevich (2003), Shimko (2008), Schwartz (2008) and Syed et al. (1998)). As several heat exchangers and turbomachinery components are needed the optimum cycle for a specific plant strongly depends on the plant production capacity and requires a careful balance between plant capital investment costs and operating costs (Syed et al., 1998).

Figure A.8 shows two possible liquefaction cycles. Figure A.8(a) shows the Claude cycle which is the current standard cycle for larger production units (Allidieris & Verroust, 2002). The plants are very capital intensive with capital costs representing over half of the total costs (Schwartz, 2008). Despite the plant efficiency of over 80% (with projections to almost 90% for the near future), the process is also very energy intensive, resulting in an energy consumption of about 12.5 to 15 kWh$_e$/kg, or around 40% of the lower heating value of hydrogen (Drnevich (2003), Sherif et al. (2003a) and Schwartz (2008)). In the

---

[6] According to Allidieris & Verroust (2002), the optimal pressure for liquefaction is around 15 to 25 bar.

Kourou plant of Air Liquide this cycle is used and the hydrogen is cooled down in 3 steps. From 300 K to 230 K a mechanical refrigerant group is used. From 230 K to 80 K nitrogen is used. Finally, the temperature is brought down to 20 K using liquid hydrogen (Allidieris & Verroust, 2002).

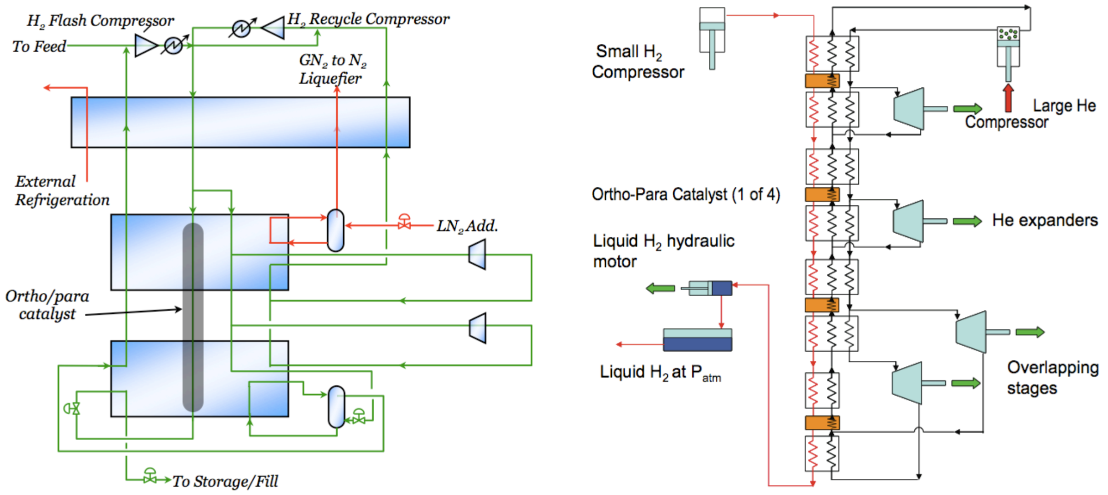

(a) Claude cycle, modified from Drnevich (2003) (b) Modified cycle, adopted from Shimko (2008)

Figure A.8. Hydrogen liquefaction cycles.

Figure A.8(b) shows a modified once-through cycle, currently under investigation at the Gas Equipment Engineering Corporation for the DOE Hydrogen Program in the US. It uses a helium based refrigeration cycle with Reverse-Brayton turbomachinery and standard two- and three-channel heat exchangers for heat removal. The cycle currently has been modified from isothermal catalytic conversion (as shown on the figure) to continuous conversion to obtain a further gain in efficiency (Shimko, 2008). An increase in efficiency of 30% over present state-of-the-art is claimed with energy requirements reduced down to between 9.7 and 7.4 kWh/kg, or 22 to 29% of the lower heating value (Shimko, 2008). Kanoglu et al. (2007) claim additional reductions in the amount of energy required in the liquefaction process by pre-cooling the gas in a geothermal absorption cooling system.

Besides these cycles, Brayton cycles with Neon are looked at seen the very interesting thermodynamic behavior of the Neon. The huge capital costs of the Neon and the consequences of potential leaks nonetheless have a too significant impact on the economy of the cycle to make it practical, according to Air Liquide (Allidieris & Verroust, 2002). Magnetocalorific liquefaction is also investigated but is not considered as an industrial process (Allidieris & Verroust, 2002).

A.4 Distribution and airport storage

Ideally, hydrogen would be produced and liquefied at the airport. However, implementation of this ideal scenario on existing airports will most likely be limited due to space restrictions. Several airport requirement studies therefore assume that gaseous hydrogen will be delivered to the airport which will be liquefied on site (Brewer (1976) for Chicago O'Hare International Airport and Boeing (1976) for San Francisco International Airport). Others however stress the desire to deliver liquid hydrogen on site (Schmidtchen et al., 1997). The latter option will however make the delivery to the airport much harder since vacuum-jacketed lines would be required which is only viable for distances up to approximately 70 km. For larger distances railroad supertankers are more cost efficient (Brewer, 1991). Seen the considerable amount of hydrogen required for daily airport usage this would entail a too high traffic density and might jeopardize airport safety (Schmidtchen et al., 1997). According to Hoyt (1979) and Thibault (1979), delivery of liquid hydrogen will furthermore raise the costs.

If gaseous hydrogen is delivered to the airport, underground pipelines are the preferred means of transportation seen the large volume required. It would be possible to use the natural gas pipelines with some minor modification to the existing infrastructure (Sherif et al., 2003a). For hydrogen pipelines steel less prone to embrittlement[7] by hydrogen under pressure is namely required. Reciprocating compressors used for natural gas can be used for hydrogen without major design modifications[8]. Special attention must be given to sealing and to materials selection for parts subjected to fatigue stress (Sherif et al., 2003a). Several extensive hydrogen pipelines network exist throughout the world. In the US a network of over 700 km is used whereas a network of over 1500 km is operated by Air Liquide in Northern Europe to connect various ports and important users of hydrogen from the chemical industry (Sergeant et al., 2008). Around 800 km is located in the Benelux as shown on Figure A.9 where the hydrogen pipelines are indicated in red. The network is in use for several decades without any significant accident.

On the airport site, liquid hydrogen is thus either delivered or generated. In either case a significant amount of liquid hydrogen needs to be stored as a buffer to deal with fluctuations in demand from the aircraft. A buffer of approximately 24 hours is proposed in Brewer (1976), Boeing (1976) and Thibault (1979). In all studies spherical vessels located above the surface are proposed to store the liquid hydrogen (Brewer (1976), Boeing (1976), Sefain (2005) and Schmidtchen et al. (1997)). Brewer (1976) for instance indicates that soil conditions at San Francisco International Airport are inappropriate for underground installation of the tanks as the water level is too close to the ground level, resulting in the tanks to be submerged in water. To minimize boil-off losses large tanks are required and redundancy is needed even for smaller airports (Schmidtchen et al., 1997).

The liquid hydrogen is delivered from the buffer tanks through insulated pipelines located either under the ground in positively ventilated tunnels or in open trenches. Both

---

[7] Due to its small size, hydrogen molecules penetrate into the material structure weakening the bonds and making a ductile material brittle. Due to the more compact molecular structure face-centered materials like Aluminum are less prone to this phenomenon. High strength steel on the other hand is known to be very susceptible to hydrogen embrittlement (Stroe, 2005). Once embrittled, the material can be cured by a proper heat treatment, which could be used during the main overhaul services of the aircraft tank to ensure a longer utilization of the tanks.

[8] Due to its very low molecular mass, centrifugal compressors cannot be used for hydrogen. After all, their functionality depends on the conversion of kinetic energy to pressure. As a consequence of the low molecular mass of hydrogen, the kinetic energy is too low to obtain a reasonable pressure with realistic rotational speeds and a limited number of stages (Allidieris & Verroust, 2002).

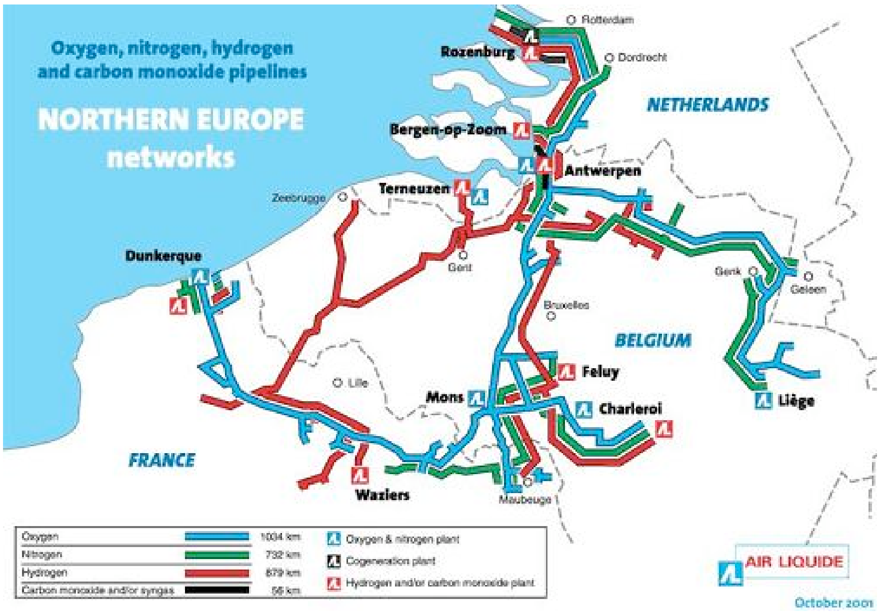

Figure A.9. Gas distribution network of Air Liquide, adopted from Air Liquide (2009).

methods are compatible with airport requirements (Brewer, 1976). The fueling of the plane itself then takes place either using hydrant refueling points fixed around the gates (Brewer, 1976) or using a fueling tanker/hydrant service vehicle (Boeing, 1976). Both options are shown on Figure A.10. The fuel tanker option would require a smaller capital cost investment but will lead to more ground traffic congestion near the gate and results in higher operating costs (Sefain, 2005).

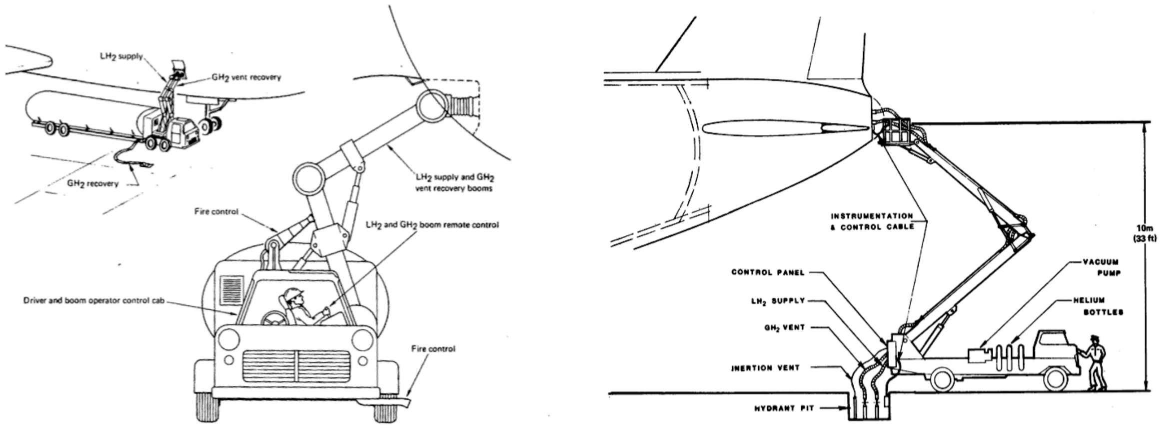

(a) Fueling tanker, adopted from Boeing (1976)
(b) Hydrant fueling, adopted from Brewer (1976)

Figure A.10. Hydrogen aircraft refueling options.

As the liquid temperature will rise due to heat transfer to the pipelines on the airport grounds, it needs to be assured that LH_2 flash vaporization will not occur during loading of the aircraft. Flash vaporization of the liquid immediately upstream of the ground to aircraft connection is the preferred means of doing this as it leads to the lowest delivery pressure for a given size, the smallest amount of lines and the lowest overall losses (Boeing, 1976). Sub-cooled hydrogen needs to be delivered to the aircraft tank to minimize fuel losses after introduction of the hydrogen to the tanks (Brewer, 1991). Sub-cooled liquid furthermore allows more rapid fueling of the aircraft due to its higher density and reduces the return vent line size and cost. As some boil-off will nonetheless occur during both fueling of the aircraft as well as flight a vapor return line namely needs to be provided to recover the boiled off hydrogen. This leads to a reduction in hydrogen cost. The recuperated gaseous hydrogen is then re-liquified and reintroduced in the buffer tank (Boeing (1976), Brewer (1976) and Sefain (2005)). Finally the lines must be pump-fed as pressure-fed systems lead to boil-off losses that are several times higher Brewer (1991).

A.5 Impact on aircraft handling and safety

In order for hydrogen to be a viable candidate aircraft fuel both the aircraft handling as well as safety of aircraft and airport need to be compliant with current levels. Minimum changes to current practices are preferable even though the distinct features of hydrogen make this very unlikely.

Boeing (1976), Brewer (1976) and Sefain (2005) all show that LH_2 aircraft can be handled exactly like conventional fueled aircraft. The aircraft can be fueled at the gate while housekeeping operations are performed, passengers board and cargo is loaded. Figure A.11 shows a typical aircraft servicing schedule for liquid hydrogen fueled aircraft. Turnaround times are furthermore likely to be the similar to kerosene fueled aircraft (Brewer, 1991). To minimize fueling times and boil-off losses, as well as fatigue due to thermal cycling of the tank, the hydrogen tanks should remain at cryogenic temperatures at all times. The tank temperature should be allowed to rise only when the aircraft is expected to be out of service for an extended period or if entering the tanks for inspection or maintenance is required. The tank must then first be de-fueled, subsequently purged with inert gas while carefully warming up the tank after which the inert gas is replaced with air. Refueling must on its turn be preceded with purging, replacing of the inert gas with gaseous hydrogen and a gradual chill-down before filling the tank with liquid hydrogen again. This is expected to take up to several hours, mainly depending on the size of the tank (Brewer (1991) and Sefain (2005)).

Since the accident with the Hindenburg airship, it is commonly believed that hydrogen is a very dangerous fuel. Several safety studies, conducted for industry branches ranging from aircraft over cars to nuclear utilization of hydrogen have however shown that hydrogen provides excellent safety features due to its inherent properties and as such does not deserve its reputation. The common misbelief concerning hydrogen safety is thus a psychological rather than physical problem. Obviously each specific design must be made with the characteristics of hydrogen in mind from the start. Key issues in hydrogen safety are ensuring that hydrogen cannot accumulate in certain areas by proper venting and allocation of sensors to detect the presence of hydrogen. Below some features of hydrogen safety will be commented upon. The properties of hydrogen to which reference is made in this section are compiled in Table A.1.

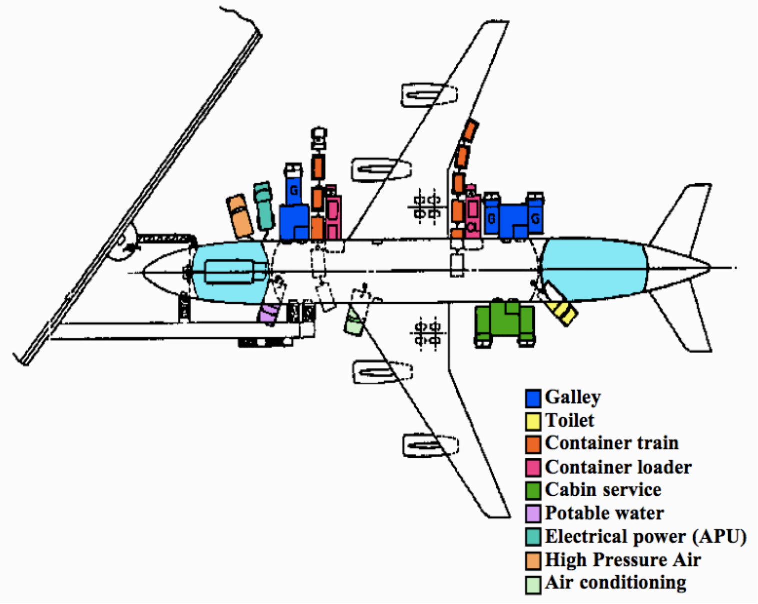

Figure A.11. Typical liquid hydrogen fueled aircraft servicing, adopted from Sefain (2005).

Since hydrogen is the smallest molecule it has a greater tendency to escape through small openings than any other liquid or gaseous fuel. Based on properties such as density, viscosity and diffusion coefficient in air, (subsonic) hydrogen leaks through holes or joints of low pressure fuel lines occur at a rate 1.3 to 2.8 times faster than a natural gas leak from the same size of hole (Barbir, 2005). As hydrogen has a very low energy density per unit volume, its leak will nonetheless result in a much smaller energy release than most other fuels (Barbir, 2005). If the leak would occur in a high pressure line on the other hand, the flow will be sonic at the hole and the higher speed of sound in hydrogen (1308 m/s (Barbir, 2005)) would lead to a much higher leak rate compared to other fuels. The lower energy density argument however also applies here leading to similar conclusions as for the laminar leak (Barbir, 2005).

If a leak should occur for whatever reason, hydrogen will disperse more rapidly than any other fuel due to the combination of its high diffusivity in air and its buoyancy (Barbir (2005) and Faass (2001)). This is reflected by the danger zones from Figure A.12. The figure shows the danger zones for a 3.3 cubic meter liquid gas spill with 4 m/s wind. The hydrogen will evaporate in a very short time and rise and dissipate into the atmosphere so rapidly that the hazardous area remains very small (Brewer, 1991).

If the spill would be ignited, as will be the case with most aircraft accidents for most fuels, the duration of the LH_2 fire will be very short so that the fuselage will not be heated to the point of collapsing (Brewer (1991), Brewer et al. (1981), Faass (2001), A.D. Little (1982) and Witcofski (1981b)). For a 400 passenger aircraft, the fuel-fed burn would for instance only last for 15 s (Brewer, 1991). The low radiative heat transfer further aids in keeping the fuselage temperature low.

As the tanks are mounted inside the fuselage and are designed for a higher pressure than the fuselage itself, they will most likely not rupture during a crash. They furthermore present much smaller dimensions for frontal impact and are protected by a significant

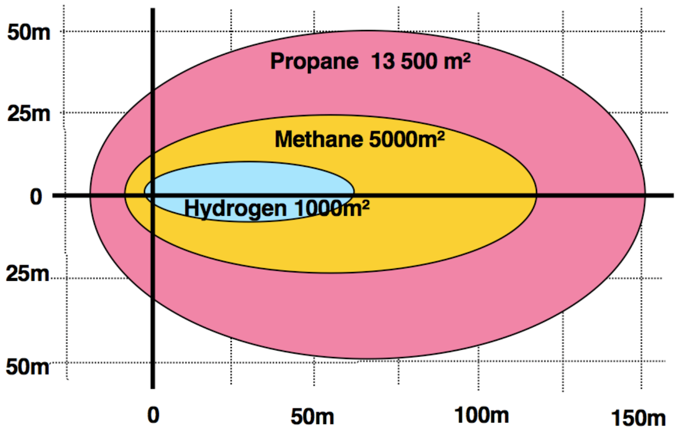

Figure A.12. Danger zones of spilled liquid gases, adopted from Faass (2001).

amount of structure, both ahead and beneath them which must be penetrated before they are exposed (Brewer (1991) and Brewer et al. (1981)).

The separation between the lower flammability limit and the lower detonation limit furthermore prohibits detonation in the free atmosphere. Detonations are only possible when the hydrogen is confined on at least 3 sides (A.D. Little, 1982). As the tanks contain no air or oxygen a detonation inside the tanks is also impossible. The crash fire study performed by A.D. Little (1982) even showed that hydrogen would not ignite from impact, either from smashing the container or firing bullets through it.

The cryogenic liquid hydrogen however poses a unique potential problem as passengers could be exposed to the cryogenic fuel after a crash or a leak of the fuel tanks or fuel delivery lines. This would result in significant frostbite. However, both the design of the tanks as well as their installation arrangement makes this very unlikely (Brewer, 1991). Fuel tanks will nevertheless have to pass rigorous leak testing upon entry into service and throughout their useful life (Edeskuty, 1979). Brewer (1979) therefore recommends routine visual inspection of the tank structure from inside the tank at least every 8000 hours, consistent with airline practice for all primary structure.

This page is intentionally left blank

APPENDIX B

Conceptual Aircraft Design Tool

The conceptual design of an aircraft is a highly iterative process by nature due to the high level of interaction between the involved disciplines. In order to model this process in a flexible way, a modular conceptual design tool was developed in Matlab®. The incorporation of modularity makes the routine easier to use and allows a quick adaptation of the various modules to the diverse design studies carried out. After all, several modifications are needed to various modules to allow for the designs of both hydrogen-fueled as well as unconventional aircraft.

The adopted structure for the preliminary aircraft design tool is schematically represented on Figure B.1. On that figure, the most important interactions between the different modules are indicated with arrows. As can be seen from the figure, input is required for the design mission as well as the aircraft geometry, the engines and the wing position before the calculations can be started. The aerodynamic characteristics, the performance and the mass of the aircraft are consequently calculated as well as the position of the center of gravity of the aircraft at its operating empty weight. The wing position along the fuselage is then iterated upon until the desired center of gravity position is obtained. Finally, the c.g. excursion and the direct operating costs are determined.

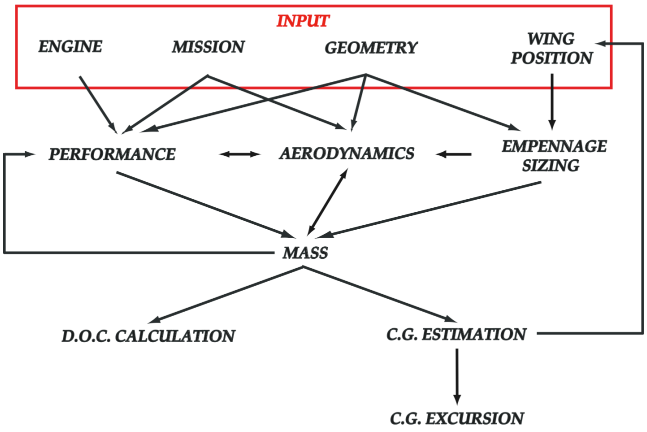

Figure B.1. The structure of the developed tool.

The different modules and the correlations used in them are described in this appendix. Section B.1 discloses the way in which the aircraft geometry is defined. Then the mass and aerodynamic calculations are discussed in sections B.2 and B.3 respectively. After this, the computation of the position of the center of gravity and its excursion when loading the aircraft is tackled before the imposed performance constraints are dealt with. A final section reviews the calculation of the direct operating costs. When applicable, the input required to set up the calculations is detailed for each section.

B.1 Aircraft Geometry

The geometry of the aircraft is divided into five main components which are described in the following subsections. The aircraft fuselage, wing, tail and nacelle geometry are detailed consecutively, after which the determination of the landing gear length is discussed. In order to allow tailoring of the shape of the aircraft to the different designs in this work, several geometrical characteristics are left as input parameters to the routine. To set up calculations for a given design, the following geometrical parameters need to be defined:

- the fuselage width
- the fuselage height
- the fuselage length
- the number of decks and the number of seats abreast for each deck
- the longitudinal position of each row of seats
- the wing area
- the wing aspect ratio
- the wing taper ratio

The values adopted for these parameters are specified for each of the designs in the different chapters of this work.

B.1.1 Fuselage

Two different shapes are considered for the geometry of the fuselage to reflect the differences between the single and multiple deck layouts of typical large transport aircraft. After all the single deck designs usually feature a fuselage with a circular cross-section while multiple deck designs often have a "double-bubble" type cross-section in the central part of the fuselage, which will be approximated here by an elliptical shape.

First the additional parameters needed to determine the complete shape of the fuselage are described and the numerical values adopted are given. Then the calculation of the wetted area of the fuselage is set out.

B.1.1.1 Shape

As the central part of both types of fuselages has a constant cross-section and the width and height of this central part are input parameters for the different designs, only the length and the shape of the forward and the aft section need to be determined to unambiguously lay down the fuselage geometry for conceptual design type calculations (see Figure B.2). The shape of these sections is in this phase of the design usually set by its length-to-diameter ratio l/d_{fus} (see amongst others Jenkinson et al. (1999), Kroo (2006), Raymer (1989), Roskam (1997a) and Torenbeek (1982)) where the diameter is taken here as the actual diameter for a cylindrical fuselage or the height of the fuselage for the multiple deck fuselages.

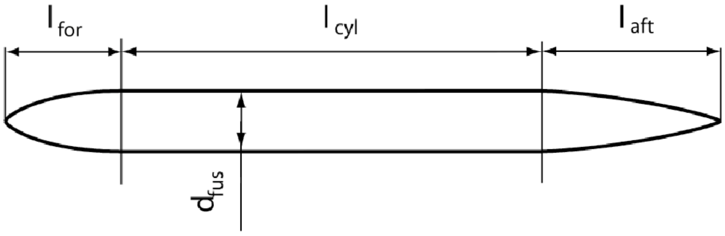

Figure B.2. The different sections of the fuselage and their length (top view).

The length-to-diameter ratio of the forward section of the fuselage will usually determine the drag divergence Mach number of the fuselage, especially for the multiple deck designs. The profile of the aft section of the fuselage is on the other hand chosen to provide a smooth, low drag shape which supports the tail surfaces. Besides that, the lower side of the aft fuselage must also provide adequate clearance for the aircraft to rotate at the minimum unstick speed. The actual shape of both parts of the fuselage will generally be determined through an extensive CFD simulation in a later stage of the design. In conceptual or preliminary design, however, some general rules based on both statistical data and basic aerodynamic calculations are used. In literature a wide range is found for both length-to-diameter ratios. For the nose cone a range from 1.5 to 2.5 in found, whereas the tail cone ratios vary between 2.5 and 3.6 ((Bovet, 2004), Kroo (2006) and Torenbeek (1982)). After comparison with existing large transport aircraft the following values are adopted:

$$l_{for}/h_{fus} = 1.7 \qquad l_{aft}/h_{fus} = 2.5 \tag{B.1}$$

B.1.1.2 Wetted area

Correlations for the wetted area of the fuselage can be found in Bovet (2004), Kroo (2006), Roskam (1997b), Torenbeek (1973), and Torenbeek (1982). A comparison between these correlations, shows a close resemblance between the methods laid down in Bovet (2004), Kroo (2006) and Roskam (1997b). The equations given in these references for the forward and aft section namely all have the following shape:

$$S_{wet} = k \cdot d_{fus} \cdot l$$

where S_{wet} denotes the wetted area of the considered section, k is an empirical coefficient, d_{fus} stands for the diameter of the fuselage and l indicates the length of the fuselage section under consideration. The values for k_{for} found in literature vary from 2.34 to 2.54 while k_{aft} ranges between 2.10 and 2.30. The highest values are withheld here in order to be conservative in the fuselage drag estimations.

$$S_{wet,for} = 2.54 \cdot d_{fus} \cdot l_{for} \qquad \& \qquad S_{wet,aft} = 2.30 \cdot d_{fus} \cdot l_{aft} \tag{B.2}$$

The wetted area of the cylindrical mid-section is on its turn calculated as:

$$S_{wet,cyl} = \pi \cdot d_{equiv} \cdot l_{cyl} \tag{B.3}$$

where the equivalent diameter for the mid-section wetted area of the double and triple deck fuselages is derived from the perimeter of the ellipse[1]:

$$d_{equiv} = \left(\frac{w_{fus} + h_{fus}}{2}\right) \cdot \left[1 + \frac{3 \cdot z}{10 + \sqrt{4 - 3 \cdot z}}\right]$$

where z is given by:

$$z = \frac{\left(h_{fus} - w_{fus}\right)^2}{\left(h_{fus} + w_{fus}\right)^2}$$

and w_{fus} is the fuselage width and h_{fus} the height.

The total wetted area of the fuselage $S_{wet,fus}$ is found by summing up the individual contributions.

B.1.2 Wing

The gross wing area of the aircraft is left as an input parameter to the routine, so that only the airfoil section profile and the wing planform shape need to be known to fix the overall wing geometry for conceptual design work where usually only equivalent straight tapered wings are considered[2] (Roskam, 1997b). Besides the gross wing area S_w, three geometric parameters are needed to define the planform shape. In this work the wing aspect ratio AR_w, taper ratio λ_w and quarter-chord sweep angle $\Lambda_{c/4,w}$ are chosen, since they all are important design variables. As indicated previously, the aspect ratio and taper ratio are also retained as input to the routine to allow an adaptation of the wing planform to the specific design attempted. The wing sweep on the other hand will be fixed as a function of the design cruise Mach number.

Below, the formulae used to obtain the main wing planform characteristics are given first. After this, the quarter chord sweep angle and the thickness to chord ratio are fixed as a function of the design cruise Mach number. The wetted area calculations are disclosed in a fourth subsection while the dimensioning of the high-lift devices and the ailerons is reported next. Finally, the calculation of the volume inside the wing fuel tanks is discussed.

---

[1] For the calculation of this perimeter Ramanujan's second equation is chosen for the approximation because of its high accuracy despite the simplicity of the equation (Villarino, 2005).

[2] In the plots of the geometry and in the positioning of main landing gear legs, however, a so-called yehudi, or cranked trailing edge is used. The determination of the 'real' wing geometry with yehudi from the equivalent straight tapered wing is done based on ESDU (1976).

B.1.2.1 Planform

From the definitions of S_w, AR_w and λ_w all other geometric characteristics of the wing can be determined:

$$S_w = \frac{b_w \cdot (c_{r,\,w} + c_{t,\,w})}{2} \qquad AR_w = \frac{b_w^2}{S_w} \qquad \lambda_w = \frac{c_{t,\,w}}{c_{r,\,w}} \tag{B.4}$$

where $c_{r,\,w}$ and $c_{t,\,w}$ are the wing root respectively tip chord and b_w is the wing span . The sweep angles Λ can be found from equation (B.5):

$$\tan\Lambda_{y\cdot c} = \tan\Lambda_{x\cdot c} - \frac{4 \cdot (1-\lambda_w)}{AR_w \cdot (1+\lambda_w)} \cdot (y-x) \tag{B.5}$$

where x and y indicate the location with reference to the chord. For instance, for the quarter-chord the parameter x equals 0.25 while the leading edge is indicated by 0 and the trailing edge by 1. The mean aerodynamic chord (MAC or $\overline{c}_w$) of the straight-tapered wing and its spanwise position $y_{\overline{c},\,w}$ can be found from:

$$\overline{c}_w = \frac{2 \cdot c_{r,\,w}}{3} \cdot \frac{1+\lambda_w+\lambda_w^2}{1+\lambda_w} \qquad y_{\overline{c},\,w} = \frac{b_w}{6} \cdot \frac{1+2\cdot\lambda_w}{1+\lambda_w} \tag{B.6}$$

Finally, the wing dihedral angle needs to be set. The wing geometry is given a certain dihedral to increase the lateral yaw stability, especially in cross-wind conditions for low wing aircraft. According to Jenkinson et al. (1999), the dihedral angle for a conventional unswept trapezoidal low wing typically lies between 3 and 6°. Even though sweep back increases the aircraft yaw stability and would thus require a lower dihedral angle for the same stability 'margin', low swept back wings will often have a slightly higher dihedral angle than necessary for stability reasons to ensure adequate ground clearance for wing mounted engines (see section B.1.5). Based on these arguments and on a survey of existing low wing transport aircraft, the minimum wing dihedral is simply fixed as 5 degrees. After all, the final dihedral angle is usually set after careful analysis of wind tunnel test data (Nicolai, 1984, p. 21-14).

If needed by the required power-plant clearance requirements, the inboard dihedral angle is however increased by the adoption of a so-called "gull wing", as is found on the Airbus A380 and was adopted in Joesbury (2005) (see Figure B.3). Based on the A380 wing (Airbus, 2004), the inboard wing dihedral angle is increased to 12° for the inner 22% of the wing span and to 9.7° up to 43% of the wing span. The remainder of the wing is then set to a dihedral angle of 5°, resulting in an overall dihedral of about 7.5°. If the adoption of the gull wing is insufficient to provide the necessary ground clearance for the high bypass ratio engines, the landing gear height is finally increased as explained in section B.1.5.

B.1.2.2 Wing quarter chord sweep angle

Whereas the wing area, aspect ratio and taper ratio are kept as design variables for the different designs, the quarter chord sweep angle $\Lambda_{c/4}$ is determined as a function of the design cruise Mach number as given in Table B.1. The range of subsonic design cruise Mach numbers is chosen to encompass most civil airliners operations but can easily be expanded to allow designs at other cruise Mach numbers.

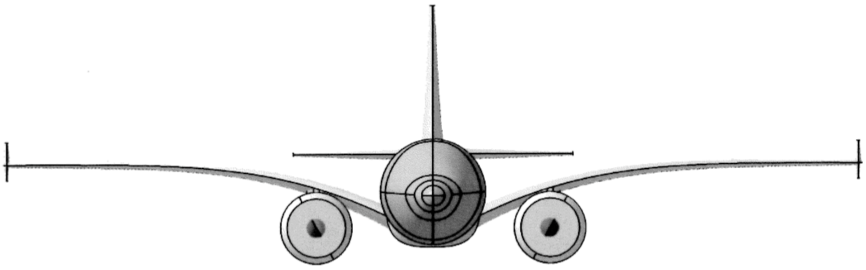

Figure B.3. *The gull wing geometry (adopted from Joesbury (2005, p. D-5)) .*

Table B.1. Wing sweep in function of M_{cr} (adopted from Jenkinson et al. (1999, pp. 115-116)).

M_{cr}	**0.80**	**0.81**	**0.82**	**0.83**	**0.84**	**0.85**
$\Lambda_{c/4}$	26.1	27.3	28.4	29.8	30.7	32.0

B.1.2.3 Spanwise thickness distribution

The thickness of the wing is a compromise between aerodynamic, structural and volumetric requirements. The thickness distribution will determine the wetted area and the aerodynamic characteristics of the wing. A spanwise variation in thickness is furthermore needed to provide appropriate local flow condition (Jenkinson et al., 1999). Fuel storage and structural criteria oppose the aerodynamic need to minimize the thickness of the wing and force the design towards the highest (aerodynamically) acceptable thickness. Since the bending moment due to lift increases from the wing tip to the root, the wing thickness of a transport aircraft is often chosen to be smaller at the tip and is gradually increased along the span to the fuselage connection at the root of the exposed wing. All these criteria lead to a wing thickness distribution as shown on Figure B.4.

In Jenkinson et al. (1999), the authors indicate that the wing thickness at the root is almost constant, regardless of the subsonic cruise Mach number. Following the reference, a value of 14 % is taken for the designs of this work which is in line with the 13.44% of the Boeing 747 as quoted in Brown (1991). The outer thickness of the wing is however not constant to reflect the influence of M_{cr} on the wing design. The thickness of the outer wing is therefore calculated with the following equation (Jenkinson et al., 1999, p. 116):

$$M_{cr} = 0.877 - 1.387 \cdot \left(\frac{t}{c}\right)_t + 0.431 \cdot \Lambda_{c/4}^2 \cdot 10^{-4} + 0.1195 - 0.18 \cdot C_{L,des} \qquad \text{(B.7)}$$

where $(t/c)_t$ is the thickness over chord ratio of the outer wing and $C_{L,des}$ the design lift coefficient which is given by the following relationship, derived from the same reference:

$$C_{L,des} = \frac{\left(\frac{1.6}{8.41} \cdot (AR_w - 5.36) + 1\right) \cdot c_a}{\sqrt{AR_w}} \cdot \cos\Lambda_{c/4} \qquad \text{(B.8)}$$

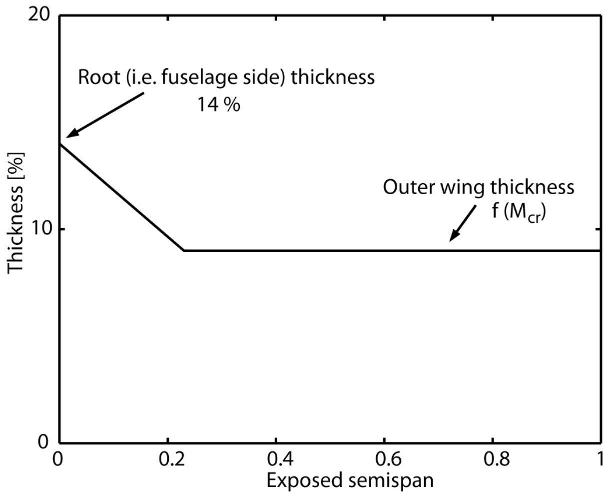

Figure B.4. Typical wing thickness spanwise distribution (Jenkinson et al., 1999, pp. 115-116).

The factor c_a in this equation reflects the influence of wing camber on the design lift coefficient. For conventional sections values from 1.02 to 1.05 are suggested while for supercritical sections a value of 1.00 is recommended. As the $(t/c)_t$ values obtained with eq. (B.8) are low compared to the actual values found in literature, a value of 1.05 is employed for c_a despite the implicit adoption of supercritical airfoils. The average thickness is then determined as:

$$(t/c)_{avg} = \frac{3 \cdot (t/c)_t + (t/c)_r}{4}$$

B.1.2.4 Wetted area

After a comparison of the wing wetted area formulae available in literature[3] an average between $S_{wet,w1}$, the wetted area obtained with the method given in Roskam (1997b, p. 284) and (Torenbeek, 1982, p. 448) and $S_{wet,w2}$, derived from Raymer (1989, p. 167) and Corke (2003, p. 76), is selected in this work.

$$S_{wet,w1} = 2 \cdot S_{w,exp} \cdot \left[1 + 0.25 \cdot \left(\frac{t}{c}\right)_r \cdot \frac{1+\tau \cdot \lambda_w}{1+\lambda_w}\right] \quad \text{(B.9)}$$

$$S_{wet,w2} = S_{w,exp} \cdot \left(1.977 + 0.52 \cdot \left(\frac{t}{c}\right)_{avg}\right) \quad \text{(B.10)}$$

where $S_{w,exp}$ denotes the exposed wing area and τ is defined as

$$\tau = \frac{(t/c)_t}{(t/c)_r}$$

---

[3] Among others Corke (2003), Kroo (2006), Roskam (1997b), Raymer (1989) and Torenbeek (1982), contain equations for the wetted area of the wing.

B.1.2.5 High-lift devices

The chordwise size of the high-lift devices is closely coupled to the location of the two wing spars which is a compromise between slat and flap size, weight, structural design and fuel tank volume. Typically, a clearance 2 % of the chord is available between the nested flaps and the rear spar for control system elements (Roskam, 1997b). Typical values for large long range transport aircraft, derived from Roskam (1997b, pp. 153,197-198) and Torenbeek (1982, p. 261) are used in this work, as shown on Figure B.5.

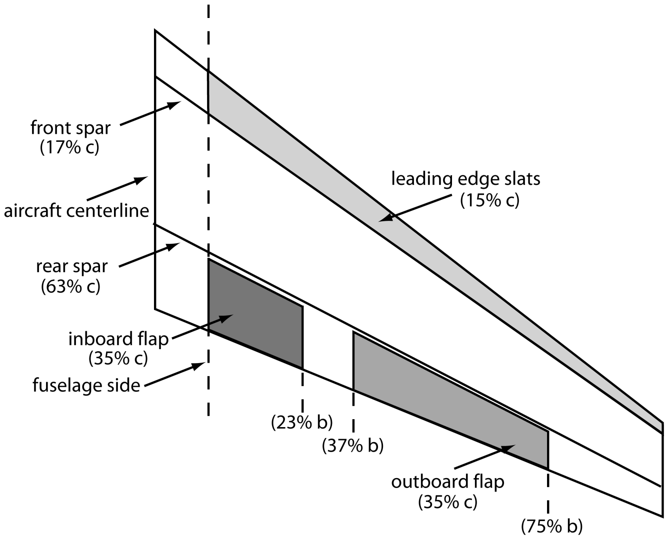

Figure B.5. The dimensions of the high-lift devices and the location of the spars.

The chordwise positions are indicated on the figure in percentage of the local chord length while the spanwise dimensions are given as a percentage of the wing semi-span. The inboard aileron is located between the in- and the outboard flap, while the outer part of the wing is covered by the outboard aileron.

B.1.2.6 Fuel volume

As the gross of the fuel for kerosene fueled transport aircraft is housed in integral tanks[4] inside the wing, the wing size (volume) will to a big extent determine the aircraft fuel capacity and as a consequence its range (for a given payload). As such, for a given range, a lower limit is imposed on the wing size especially for the long range aircraft under consideration in this work. This limit can somewhat be shifted to lower wing sizes by the adoption of tanks inside the horizontal tail[5]. The horizontal tail tanks can additionally be

---

[4] Integral tanks are created by sealing the wing torque box that is made of the fore and aft spars. They are mainly adopted as they allow to maximize the wing volume utilized to store the fuel (Isikveren (2002) and Roskam (1997b)).

[5] The wing fuel capacity could also be increased by carrying fuel beyond the 85% span point, which is the usual limit for the fuel tanks to prevent lightning strikes from starting an in-flight fire. Fuel could be stored in the wing tips if the skin is locally "beefed up" to ensure that enough metal is present to disperse the lightning strikes. This would however increase the wing weight significantly (Roskam, 1997b).

used to keep the c.g. at the aft-most limit during flight by pumping fuel into the tail tank, thereby reducing the trim drag as is e.g. done on the MD-11 (Raymer, 1989). Seen the considerable range of the different design studies carried out in this work and the possible trim drag reduction, a tail tank is assumed for all kerosene fueled aircraft. A similar practice was also adopted in the Cryoplane project (Astaburuaga et al. (2001), Astaburuaga & van Holten (2001) and Krijnen et al. (2001)).

Two different statistical correlations were found that yield the determination of the wing fuel volume. Torenbeek (1982, pp. 448-449) and Roskam (1997b, p. 153) suggest the following correlation:

$$V_f = 0.54 \cdot \frac{S_w^2}{b_w} \cdot \left(\frac{t}{c}\right)_r \cdot \frac{1 + \lambda_w \cdot \sqrt{\tau} + \lambda_w^2 \cdot \tau}{(1 + \lambda_w)^2} \tag{B.11}$$

whereas Howe (2000, p. 132) proposes the following equation to determine the fuel mass that can be stored in the wing:

$$W_f = 420 \cdot S_w \cdot b_w \cdot \left(\frac{t}{c}\right) \frac{1 - 0.89 \cdot \lambda_w + 0.49 \cdot \lambda_w^2}{AR_w} \tag{B.12}$$

Using a fuel density of 0.803 kg/m^3, both equations lead to very similar results over a wide range of wing areas. Despite the inaccuracies of about 10% (Roskam, 1997b, p. 154), the equations are adopted here as more precise information is absent in this stage of the design and the result correlates well with the wing size of the long range Cryoplane design (Krijnen et al., 2001). An average of both results is used to determine the limit of the available wing and tail tank fuel volume.

The wing fuel volume is divided into 3 tanks on each side of the fuselage. The first tank is the center tank inside the fuselage and the wing fillet. The second tank runs from the fuselage side to 23% of the semi-span, whereas the third tank covers the rest of the wing up to the 85% spanwise limit suggested by Roskam. The division into tanks is made to allow for a more precise center of gravity calculation of the fuel. After all, FAR 25 regulations require all engines to be fed from a separate tank at takeoff. For the 4-engined versions at least 4 tanks would thus be required.

B.1.3 Empennage

In this section, the geometry of the horizontal and vertical tail is defined. As both tailplanes basically are wing sections, the equations of section B.1.2 can be used with the right definition of the different tailplane characteristics. This is done here to keep the calculations as simple as possible. This section thus basically only discloses the choice of the values for the empennage parameters.

The thickness over chord ratio and the sweep angle of the tailplanes are usually chosen so that the tail surfaces will not stall before the wing does to keep the control surfaces stall free throughout the entire flight envelope of the aircraft. This practise is adopted here too based on the data from Howe (2000), Kroo (2006), Raymer (1989), Roskam (1997b) and Schaufele (2000). The values adopted for the horizontal and vertical tail are given first. The method used to size the tail is laid down in a third paragraph.

B.1.3.1 Horizontal and vertical tail planform

The aspect ratio of the horizontal tail is related to the aspect ratio of the wing as proposed in Howe (2000):

$$AR_{ht} = 0.5 \cdot AR_w$$

The lower value from the range suggested by Howe is adopted as it is more in line with the range of values found in literature. Howe suggests a range from 0.5-0.6 for the proportionality factor whereas aspect ratio ranges between 3.0 and 6.5 are suggested in the other references. For the vertical tail, a fixed value of 1.6 is adopted after Schaufele (2000). The average value derived by Schaufele for transport aircraft lies well within the range found in the other references (0.7-2.0).

$$AR_{vt} = 1.6$$

Following Howe (2000), the taper ratios of both horizontal and vertical tail are related to the taper ratio of the wing:

$$\lambda_{ht} = 1.2 \cdot \lambda_w \qquad \lambda_{vt} = 0.5 \cdot \lambda_w$$

The sweep and thickness-to-chord ratio's of the tailplanes are, as indicated earlier, chosen to ensure that the wing will stall first. Therefore the quarter chord sweep of the horizontal tail is set 3.0° higher than the sweep of the wing, whereas for the vertical tail an increase of 7.0° is adopted. The thickness-to-chord ratio of the tailplanes are taken as 95% of the average wing thickness-to-chord.

B.1.3.2 Size of the tailplanes

The tail surfaces are predominantly sized to provide adequate stability and control for the aircraft, which boils down to generating sufficiently large moments about the center of gravity to counteract any destabilizing forces. Other requirements may have to be met by the tail (e.g. fuel tankage, structural support,...) but these are regarded as secondary to the stability and control criteria (Jenkinson et al., 1999). A full stability and control analysis is thus normally required to size the tailplanes. However, in the initial project phases insufficient information is known about the aircraft to carry out such an analysis and the so-called volume coefficient method is usually used (see a. o. Jenkinson et al. (1999), Roskam (1997b), Raymer (1989) and Schaufele (2000)).

In this volume coefficient or $\overline{V}$-method, the tail volume coefficients are defined as follows:

$$\overline{V}_{ht} = \frac{x_{ht} \cdot S_{ht}}{S_w \cdot \overline{c}_w} \qquad \overline{V}_{vt} = \frac{x_{vt} \cdot S_{vt}}{S_w \cdot b_w} \tag{B.13}$$

where S_{ht} and S_{vt} are the areas of the horizontal respectively vertical tail. The horizontal and vertical tail arms x_{ht} and x_{vt} are on the other hand defined as the distances between the quarter chord point at the wing MAC and the quarter chord point at the MAC of the horizontal respectively vertical tail. For $\overline{V}_{ht}$ a range of 0.54-1.48 is found for transport aircraft in the aforementioned references while the values for the $\overline{V}_{vt}$ range from 0.055 to

0.120. A value of 0.80 is utilized here for the horizontal tail, which reflects a jet transport aircraft with 'relaxed' static stability combined with a digital 'fly-by-wire' flight control system (Roskam, 1997b).

For the vertical tail, the method laid down in Schaufele (2000) is used as it allows to take the presence of the second fuselage for the twin-fuselage configurations into account without resulting in an increased complexity. Schaufele namely uses a non-dimensional directional fuselage volume parameter which is defined as

$$\overline{V}_{fus} = \frac{h_{fus}^2 \cdot l_{fus}}{S_w \cdot b_w}$$

Schaufele relates this directional fuselage volume coefficient to $\overline{V}_{vt}$. The following expression, derived from Figure 6.15 of Schaufele (2000) is used:

$$\overline{V}_{vt} = 0.03 + 0.34 \cdot \overline{V}_{fus} \tag{B.14}$$

By doubling $\overline{V}_{fus}$ in the case of a twin-fuselage aircraft, the vertical tail area is slightly increased. It is namely indicated in Torenbeek & Jesse (2001, p. 23) that the stability calculations showed that "it is likely that the vertical tails must be increased in size to ensure adequate control during crosswind landings" after the authors sized the tails using a conventional vertical tail volume coefficient. Moore et al. (1982) however also adopted a conventional vertical tail volume coefficient for their designs and their lateral stability analysis did not reveal that issue. In a later stage of the design, a full stability and control analysis would anyway be required to ensure that the vertical tail area resulting from this approach is large enough. However this falls outside the scope of this work and does not significantly influence the results seen the relatively low weights of the vertical tails[6].

As the vertical tail volume coefficients derived from this method are slightly below the values found on recent 4-engined transport aircraft, an increase of 10% is taken for the aircraft having 4 engines on the wing. After all, the most critical (outboard) engine out condition is most likely the sizing criterion for the vertical tail of such a configuration.

B.1.4 Nacelle

As the majority of new transport aircraft have a podded under-wing installation of the engines, this configuration is adopted as the baseline for this work[7]. Only for some of the twin-fuselage configurations, an installation at the rear-fuselage is considered. Below, first the geometry of the nacelle is described, then some installation issues are reviewed before finally the nacelle wetted area is commented upon.

---

[6] It might however change the position of the wing on the fuselage to obtain a proper c.g. excursion throughout the whole loading envelope.

[7] Installations of the engines over the aircraft wing to shield the engine noise are sometimes also proposed, especially for advanced configurations (a.o. Guynn & Olson (2005), Hall & Crichton (2005), Rizvi (2007) and Smith (2005)). Besides offering a noise reduction benefit, this type of installation furthermore allows a higher vertical separation between the nacelle and the wing without influencing the landing gear height. It is not considered here however due to the increased maintenance costs that this type of installation entails.

B.1.4.1 Geometry

The nacelle consists out of 3 distinct parts: the forebody, the cylindrical midbody and the afterbody. Depending on the engine length and the type of nacelle chosen, the midbody is sometimes omitted, as shown on Figure B.6[8]. Here, only so-called short cowl fan nacelles are adopted as the long cowl nacelle, often found for smaller engines and mixed flow turbofans, would lead to excessive nacelle drag for the high bypass ratio turbofans under consideration.

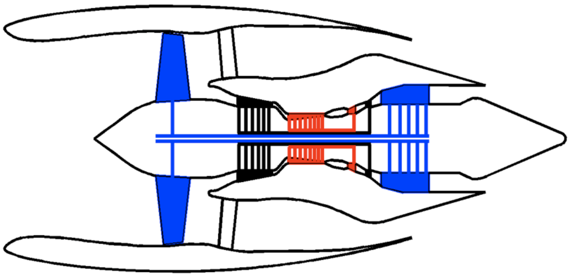

Figure B.6. Short cowl nacelle geometry.

In preliminary calculations, a NACA 1-Series cowl shape is often adopted for the design of the forebody of the fan cowling. These cowls have gained wide acceptance for practical use as they closely approximate constant velocity profiles which give a uniform pressure distribution (Seddon & Goldsmith, 1999). Non-dimensional ordinates for the external profile of these intake cowls can be found in Seddon & Goldsmith (1999) and Williams (2007). The length of the forebody cowl l_{fore} as well as its maximum diameter d_{max} are set by the drag divergence Mach number M_D and the critical mass flow ratio for which the cowl is designed MFR_{crit}, by the following equations (Williams, 2007):

$$MFR_{crit} = \left(1 - \frac{4 \cdot \left(1 - \frac{d_{hl}}{d_{max}}\right)^2}{l_{fore}/d_{max}}\right)^{5/2} \tag{B.15}$$

$$M_D = 1 - \frac{1}{8} \cdot \frac{\sqrt{1 - \left(\frac{d_{hl}}{d_{max}}\right)^2}}{l_{fore}/d_{max}} \tag{B.16}$$

where d_{hl} is the highlight diameter of the nacelle.

The influence of the drag rise Mach number and the critical mass flow ratio on the maximum diameter and the forebody length of the nacelle are shown on Figure B.7. In this work, the drag rise Mach number of the forebody is set to the drag divergence Mach number of the aircraft and the critical mass flow ratio is chosen in function of the mass flow ratio at the end of cruise to avoid significant spillage drag in cruise.

---

[8] The external shape of the nacelle and its length are calculated throughout this work whereas the internal shape is adopted from similar nacelles to give a reasonable representation of the overall engine cross-section.

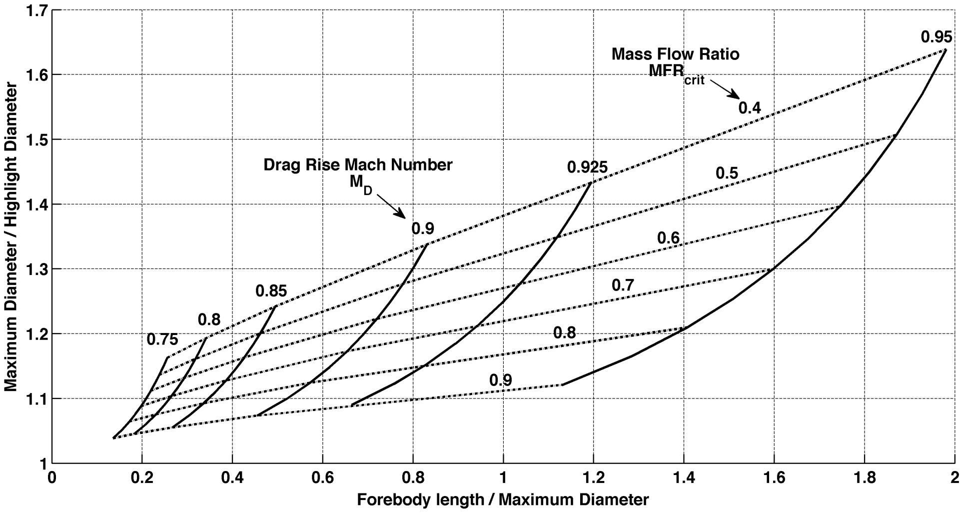

Figure B.7. Influence of M_D and MFR_{crit} on nacelle forebody geometry.

The forebody geometry furthermore depends on the contraction ratio CR, which is defined as the ratio between the highlight and the throat area of the nacelle:

$$CR = \frac{A_{hl}}{A_{thr}}$$

and is set in this work to 1.25 based on data for advanced current technology nacelles from Glieb & Janardan (2003) and Kowe & Wynosky (1985). This value is furthermore on the lower side of the range of 1.20 to 1.35 proposed in Williams (2007). Specifying the throat Mach number then completely fixes all geometrical characteristics of the nacelle forebody. Here, a value of 0.75 is adopted. This is the maximum value suggested in Younghans & Paul (1989) and Williams (2007) and accounts for flow path curvature and boundary layer growth as well as a choke margin to avoid an excessive drop in the pressure recovery of the inlet and to allow some future engine thrust growth.

The afterbody of the nacelle is usually a circular arc (Williams, 2007) and its length is set by the drag divergence Mach number of the afterbody and the maximum accepted boattail chord angle. As suggested in Williams (2007), the boattail chord angle is limited to 16° to avoid separation of the flow over the nacelle. This boattail angle β_f, together with the drag rise Mach number of the afterbody (and the maximum diameter) determine the length of the nacelle afterbody (Williams, 2007):

$$l_{aft} = \frac{0.04}{(1 - M_D)^2} \cdot d_{max} \cdot \sin\beta_f \tag{B.17}$$

As for the forebody, the drag rise Mach number of the afterbody is set to the drag divergence Mach number of the aircraft.

If the gas generator cowl protrudes from the bypass nacelle, its boattail angle is set to the value adopted for the bypass nacelle afterbody. A similar practice is used for the engine plug.

B.1.4.2 Installation

The installation of the engine nacelle or pod needs to ensure both a low nacelle drag and efficient wing aerodynamics by minimizing the interference between the pod and the wing as well as the reduction of wing maximum lift coefficient due to the presence of the pod. The horizontal and vertical separation distances between pod and wing as well as the free-stream Mach number and the aircraft incidence set the level of interference drag (Williams, 2007). From a drag perspective, the best position of the pods is in front and below the leading edge of the wing, as shown on Figure B.8. As the separations also affect the design of the pylon, the torsional loads on the wing box and the ground clearances, a compromise is needed between aerodynamic and structural drivers.

The gulley depth or vertical separation H can be expressed as a spacing ratio in terms of the nacelle diameter. Williams (2007, p. 51) indicates the following range for under-wing installations:

$$0.70 < \frac{H}{d_{max}} < 1.1$$

Williams however uses a smaller value of 0.61 in the examples to represent a vertically close-coupled pod installation, which is more in line with the installations of several modern transport aircraft given in El-Sayed (2008, p. 411) where a range between 60 and 63 % is shown. In this work, a value of 0.615 is therefore adopted.

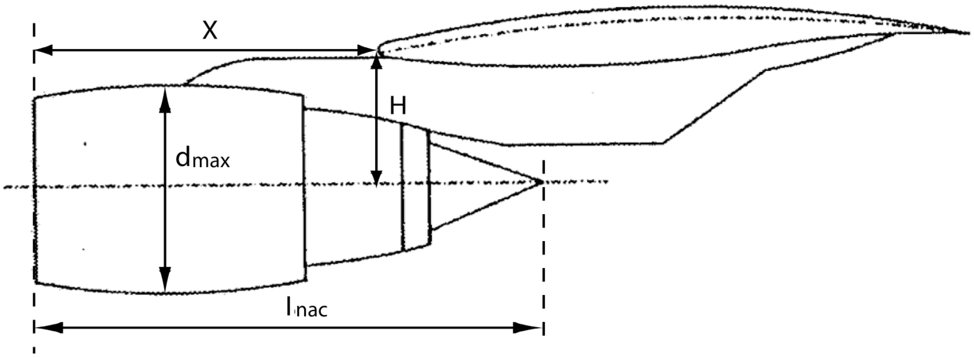

Figure B.8. Under-wing pod installation, modified from El-Sayed (2008, p. 411).

The horizontal separation distance is set by thrust reverser efflux and rotor disk burst considerations. In Williams (2007), X is normalized with the total nacelle length l_{nac} and the following typical values are indicated:

$$0.6 < \frac{X}{l_{nac}} < 0.8$$

A value of 0.64 is adopted in this work as it is in line with the installations presented in El-Sayed (2008).

B.1.4.3 Wetted area

As the empirical correlations used in the nacelle drag calculations are derived based on the wetted area of a cylindrical section for each of the parts of the nacelle (Williams, 2007), the wetted area of the fore- and afterbody as well as the gas generator cowl and the plug are determined in this work as the wetted area of a cylinder. The length of the cylinder is taken as the actual length of the considered part whereas the diameter is taken as the maximum diameter of the considered part. When the exact wetted area of the nacelle is needed, Torenbeek (1982, p. 449) gives more detailed correlations.

B.1.5 Landing gear

The length of the landing is set by several requirements, that are either related to the fuselage shape or the engine installation. The landing gear must first of all be sufficiently large to avoid the tail from scraping on the ground during the takeoff rotation. For this, an angle of 15° between the fully extended aft landing gear and the bottom of the fuselage tailcone is usually provided in preliminary design (Roskam, 1997b). The landing gear must furthermore be long enough to avoid touching of the ground by the nacelles or the wing tip in a cross-wind or engine-out landing (a.o. Currey (1988), Roskam (1997b), Roskam (1989b), Schaufele (2000) and Torenbeek (1982)). Usually a roll angle of about 5° is assumed for this requirement as it is the roll angle used to size the rudder at the minimum unstick speed in an engine-out case. The main gear length must additionally be set so that there is sufficient clearance for the nacelle in case of a nose gear collapse during landing (Currey (1988), Isikveren (2005) and Jenkinson et al. (1999)). Finally, the nacelle must be placed sufficiently far from the ground to avoid foreign-object-damage. According to Isikveren (2005), the engine to ground distance must be bigger than 23% of the fan diameter to ensure this.

Obviously, the landing gear length obtained from several of these requirements depends on the landing gear disposition, which is detailed in section B.4.3. As the length of the landing gear will strongly influence its mass, a 'correction' for the landing gear length is added to the mass determination when the length is set by the engine-related requirements of the very high bypass ratio engines. If the gear length is on the other hand determined by the tail scrape requirement, no correction is used, as described in section B.2.5.

As in some cases, the length of the fully extended gear must be used whereas for others the gear is supposed to be in fully compressed position, the stroke of the oleo shock absorber needs to be determined. The stroke can be determined from the following equation (amongst others found in Currey (1988), Isikveren (2005), Raymer (1989), Roskam (1989a) and Torenbeek (1982)) where it is assumed that each gear takes the same load:

$$\frac{n_g \cdot v_v^2}{2 \cdot g} = \left(\eta_{sa} \cdot N_g \cdot s_{sa}\right) + \left(\eta_{ty} \cdot N_g \cdot s_{ty}\right) \tag{B.18}$$

where v_v is the vertical speed of the aircraft at landing for which a value of 12 ft/s is adopted following Roskam (1989a). N_g is the number of landing gear, n_g a gear load factor which is 1.25 for FAR 25 aircraft, according to Roskam. η_{sa} and η_{ty} are the efficiency of the shock absorber respectively tyre. A value of 0.85 is adopted as typical for oleo struts for a transport aircraft, whereas a value of 0.47 is adopted for the tyres based on the previously mentioned references. s_{sa} and s_{ty} are the stroke of the shock absorber and tyre respectively. For the tyre, it is taken from manufacturers data based on the loaded radius from the catalogue (Goodyear, 2002). The stroke of the landing gear is determined from equation (B.18).

As suggested in Raymer (1989, p. 287), a one inch safety margin is added to the calculated stroke. The height is assumed to be 2.5 times the stroke unless dictated by other requirements. The static to fully open strut travel is assumed to be 80% of the stroke (Isikveren, 2005).

B.2 Aircraft Mass

In the conceptual or preliminary design phase, the aircraft mass is normally determined by dividing the aircraft into a limited number of components or groups and the mass of each component (group) is determined from an empirical or statistical correlation. This section discloses the mass breakdown used in this work and the formulae used to determine the mass of the different components. To avoid double- or mis-accounting of masses resulting from different component definitions in various references, the mass breakdown is based on the breakdown from Jenkinson et al. (1999) as most of the component mass correlations used in this work are adopted from that same reference. Only for the fuselage, the wing and the landing gear other references are considered because they either showed a considerably higher accuracy when applied to the limited amount of component mass data available (Bovet (2004, pp. 345-348) and Roskam (1989b, pp. 150-159)) or were better suited to draw a comparison between the different configurations from this work. As the accuracy for both the fuselage and the wing mass remained relatively low despite the adoption of "more accurate" correlations, two different methods are used for both components and their results are averaged. The following mass breakdown is used:

1. Fuselage: W_{fus}
2. Wing group: W_w
3. Empennage: W_{emp}
4. Nacelle: W_{nac}
5. Landing gear: W_{lg}
6. Surface controls: W_{sc}

   Total Structure Mass: $W_{str} = W_{fus} + W_w + W_{emp} + W_{nac} + W_{lg} + W_{sc}$

7. Propulsion group: W_{prop}
8. Fixed Equipment: $W_{fix\,eq}$

   Basic Empty Mass: $W_e = 1.01 \cdot \left(W_{str} + W_{prop} + W_{fix\,eq}\right)$

9. Operational Items: $W_{oper\,it}$
10. Crew: W_{crew}

Operational Empty Mass: $W_{oe} = W_e + W_{oper\,it} + W_{crew}$

11. Payload: W_{pl}

    Maximum Zero Fuel Mass: $W_{mzf} = W_{oe} + W_{pl}$

12. Fuel: W_f

    Maximum Take-Off Mass: $W_{TO} = W_{mzf} + W_{fuel}$

The factor 1.01 is included in the empty mass to make the mass estimation slightly more conservative. The wing group mass includes the ailerons, the high-lift devices and the spoilers. The empennage mass on the other hand comprises both the horizontal and the vertical tail, including the elevator and the rudder while the landing gear mass is made up of the nose and all main gear legs (Jenkinson et al., 1999). The correlations utilized for the different component masses will be reviewed below.

B.2.1 The fuselage mass

As the accuracy of the correlations for the fuselage mass was relatively low[9], two correlations are applied and the final component mass is taken as the average of both results. The correlations from Dupont (2000) (as cited in Bovet (2004, p. 69)) and Howe (2000, pp. 154-155) have the additional benefit that they both use the width and the height of the fuselage and are for that reason considered to be more adequate to compare single and double deck fuselages. Despite these benefits, a fudge factor of 50% is used for the double and triple deck layouts in this work as suggested by Prof. Slingerland from Delft University (personal communication). Both methods are reported below.

B.2.1.1 The method from Dupont (2000)

The correlation for W_{fus} from Dupont (2000) (as cited in Bovet (2004, p. 69)) is selected as it is by far the most accurate for the available fuselage mass data:

$$W_{fus} = S_{wet,fus} \cdot \left(10 + 1.2 \cdot w_{fus} + 1.9 \cdot 10^{-4} \cdot \frac{n_{ult} \cdot W_{dim}}{(h_{fus})^{1.7}}\right) \cdot K_{eng} \cdot K_{lg} \tag{B.19}$$

where n_{ult} is the ultimate load factor , W_{dim} the fuselage dimensioning mass and K_{eng} and K_{lg} correction factors for the engine respectively main landing gear location . In the case of passenger transport aircraft the ultimate load factor is 3.75 $(1.5 \cdot 2.5)$ while the dimensioning mass is taken as 1.05 the maximum zero-fuel mass.

$$W_{dim} = 1.05 \cdot W_{MZF}$$

The values for the correction factors K_e and K_{lg} are adopted as recommended in Bovet (2004). The value for K_{lg} is 1.05 when the main landing gear is retracted in the wing, while 1.10 is used for a landing gear that retracts into the fuselage. When the engines are installed under the wing, a value of 1.00 is adopted for K_e. For engines installed at the rear fuselage on the other hand, a value of 1.02 must be used.

---

[9] Correlations from Ardema et al. (1996), Bil (1988), Dupont (2000) (as cited in Bovet (2004)), Jenkinson et al. (1999), Roskam (1989b), Torenbeek (1980) and Torenbeek (1982) were compared with the available data.

B.2.1.2 The method from Howe (2000)

The second method that allows to account for the differences between single and multipl deck fuselages is found in Howe (2000, pp. 154-155) where the following correlation is proposed for pressurized fuselages:

$$W_{fus} = K_p \cdot \Delta p_{fus} \cdot \left(9.75 + 5.84 \cdot w_{fus}\right) \cdot \left(\frac{2 \cdot l_{fus}}{w_{fus} + h_{fus}} - 1.5\right) \cdot \left(w_{fus} + h_{fus}\right)^2 \qquad \text{(B.20)}$$

where Δp_{fus} is the maximum working pressure differential and l_{fus}, w_{fus} and h_{fus} denote the fuselage length, width and height respectively. K_p is a correction coefficient which depends on the actual type of pressurized fuselage. For airliners with four or more abreast seating a value of 0.79 is proposed by Howe for wing-mounted landing gear, whereas 0.81 should be used for fuselage-mounted landing gear.

B.2.2 The wing group mass

As for the fuselage mass, two different correlations are selected for the wing group mass calculation[10]. Both correlations use a form of wing bending moment relief to account for the reduction in wing root bending moment due to the off-center placement of the fuselages of the twin fuselage versions.

B.2.2.1 The method from Jenkinson et al.

The correlation from Jenkinson et al. (1999) only accounts for the basic wing structure mass, without the mass of the high lift devices or the spoilers. For those, the method from Torenbeek (1982) is used. Both methods are described below.

The basic wing structure mass

Jenkinson et al. (1999, pp. 134-135) give the following equation for the basic wing structure mass:

$$W_{w,str} = 0.021265 \cdot \left(W_{TO} \cdot n_{ult}\right)^{0.4843} \cdot S_w^{0.7819} \cdot AR_w^{0.993} \cdot \left(1 + \lambda_w\right)^{0.4} \cdot \frac{\left(1 - \frac{R_i}{W_{TO}}\right)^{0.4}}{\cos \Lambda_{c/4} \cdot \left(\frac{t}{c}\right)_{avg}^{0.4}} \qquad \text{(B.21)}$$

where the factor R_i represents the effect of inertial relief on the wing root bending moment and is given by:

$$R_i = W_{w,str} + W_f + 2 \cdot W_{eng} \cdot \frac{b_{ieng}}{0.4 \cdot b_w} + 2 \cdot W_{eng} \cdot \frac{b_{oeng}}{0.4 \cdot b_w}$$

---

[10] Several extra methods were found in literature (a.o. in Ardema et al. (1996), Bil (1988), Kroo (2006), Raymer (1989), Roskam (1989b) and Torenbeek (1982)). They however did not allow to account for the effect of the off-center disposition of the fuselages for the twin fuselage layouts.

W_{eng} is the individual engine plus nacelle mass and b_{ieng} and b_{oeng} represent the distance between the inboard respectively outboard engines.

The mass of the high-lift devices

The mass of the high-lift devices W_{hld} is calculated based on the figures from Torenbeek (1982, p. 454) which are reproduced in Figure B.9. As the data from Torenbeek (1982) gives specific masses for the slats and flaps, the values obtained from Figure B.9 are multiplied by the area of the devices. An additional 20% is added in the calculation of the final wing mass as recommended by Torenbeek.

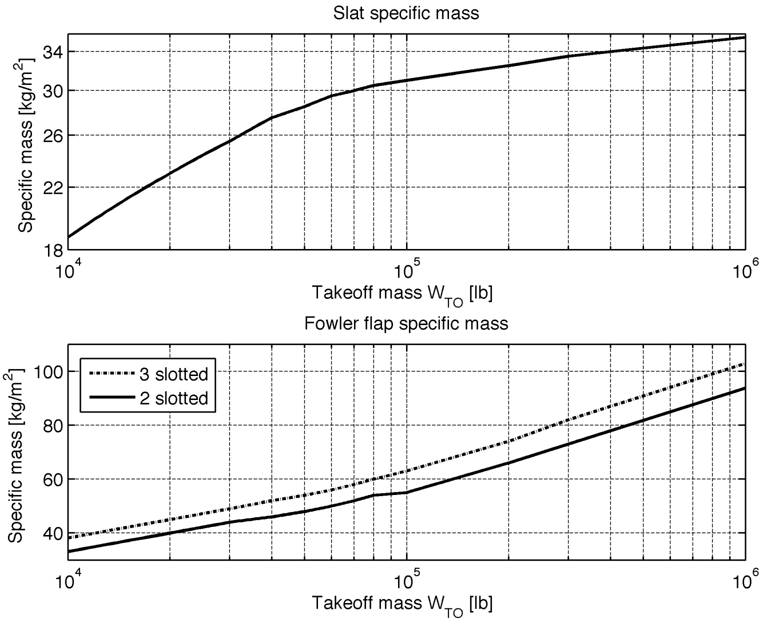

Figure B.9. The specific mass of the high lift devices.

The total wing group mass

To calculate the total wing group mass only the mass of the spoilers must still be known. According to Torenbeek (1982), a good first estimate for the spoiler mass is approximately 1.5% of the wing mass, which leads to:

$$W_w = 1.015 \cdot \left(W_{w,basic} + 1.2 \cdot W_{hld}\right)$$

B.2.2.2 The method from Howe

The correlations for the wing group mass from Howe (2000, pp. 342-346) are to some extent based on a theoretical approach that gives the "ideal" mass of the primary wing structure. Allowances are then made "for departure of the structural concept from ideal" and finally simplified statistical data is used to estimate the mass of high lift devices and controls. The final result comprises the complete wing group. The different steps needed to calculate the wing group mass with this method are detailed below.

Ideal primary wing structure mass

The ideal primary structure mass W_{ips} is calculated based on the theoretically required bending strength and is the sum of two terms. The first term, W_{cov} gives the contribution of the structural box covers and spanwise shear webs whereas W_{rib} represents the mass of the ribs required to support them.

$$\frac{W_{ips}}{W_{TO}} = W_{cov} + W_{rib} \tag{B.22}$$

where:

$$W_{cov} = 1920 \cdot \frac{AR_w^{1.5} \cdot S_w^{0.5} \cdot \overline{N} \cdot R \cdot (1 + \lambda_w) \cdot \sec^2 \Lambda_{c/4} \cdot \sigma_a}{(t/c)_r} \tag{B.23}$$

and

$$W_{rib} = \frac{3 \cdot S_w^{1.25} \cdot (t/c)_r}{W_{TO} \cdot AR_w^{0.25}} \cdot \left[\left(1 - 0.34 \cdot \lambda_w + 0.44 \cdot \lambda_w^2\right) + 2.2 \cdot (t/c)_r \cdot \sqrt{\frac{S_w}{AR_w}} \cdot \left(1 - \lambda_w + 0.72 \cdot \lambda_w^2\right) \right] \tag{B.24}$$

In these equations σ_a is the allowable working stress of the airframe material and is, according to Howe, for a light alloy given by:

$$\sigma_a = 1.12 \cdot 10^5 \cdot \sqrt{\frac{\overline{N} \cdot R \cdot AR_w^{1.75} \cdot W_{TO}}{S_w^{0.75} \cdot (t/c)_r 1.5} \cdot (1 + \lambda_w)^{2.5} \cdot \sec^2 \Lambda_{c/4}}$$

$\overline{N}$ is the effective ultimate design factor, which is either 1.65 times the limit manoeuvre factor, $n_{l,man}$ or, where it is greater, the comparable ultimate discrete gust factor:

$$1.65 + \frac{6.45 \cdot v_D \cdot S_w}{W_{TO} \cdot \left(\frac{2}{AR_w} + \sec \Lambda_{c/4}\right)}$$

where v_D is the design dive speed of the aircraft. R_i is the inertial relief factor for which Howe presents the following expressions:

2 wing-mounted powerplants: $R_i = 1 - \left(0.2 + \left(1 - W_{mzf}/W_{TO}\right)\right)$

4 wing-mounted powerplants: $R_i = 1 - \left(0.22 + \left(1 - W_{mzf}/W_{TO}\right)\right)$

If no wing-mounted powerplants are present, the factor 0.2 (or 0.22) becomes 0.12.

Allowance for departure from the structural ideal

Attachments for powerplants, landing gear, wing folding and others represent penalties to the ideal structural mass derived above. Allowances suggested by Howe as a fraction of the maximum take-off mass are as follows:

- Attachments for powerplants (2/4) : 0.001/0.0015
- Attachment for landing gear: 0.004
- Cutout in the primary structure for landing gear: 0.01

Allowance for secondary structure

As for the previous allowances, values suggested by Howe as a fraction of maximum take-off mass are adopted throughout the work:

- Ailerons: 0.02
- Slotted trailing edge flaps (double/triple): 0.006/0.012
- Leading edge slats: 0.007
- Spoilers/air brakes: 0.0015
- Tips, fairing, etc.: 0.002

As the mass prediction equations were derived for a typical fuselage width to wing span ratio β of 0.1, a correction for a different β finally needs to be applied. Howe suggests the following factor for this correction when β is not equal to 0.1 and λ_w departs from 0.45:

$$1.13 \cdot \left[\left(1 - 5 \cdot \beta^2\right) - 0.0027 \cdot \left(1 + 43 \cdot \beta\right) \cdot \lambda_w \right]$$

B.2.3 The empennage mass

Even though the tail mass represents only a small fraction of the maximum take-off mass, it is necessary to evaluate it accurately because the tail is positioned well aft of the center of gravity. The tail mass will therefore affect the overall balance of the aircraft. In this work the method from Jenkinson et al. (1999, p. 135) is used[11].

$$W_{emp} = W_{ht} + W_{vt} = K_{ht} \cdot S_{ht} + K_{vt} \cdot S_{vt} \tag{B.25}$$

where W_{ht} and W_{vt} are the masss of the horizontal respectively vertical tail. The coefficients K_{ht} and K_{vt} are determined statistically with values ranging from 22 to 32 kg/m^2. The following typical values are suggested in Jenkinson et al. (1999):

$$K_{ht} = 25 \qquad K_{vt} = 28 \tag{B.26}$$

The values suggested in Jenkinson et al. (1999) are used throughout this work.

---

[11] Several other correlations were amongst others found in Kroo (2006), Raymer (1989), Roskam (1989b) and Torenbeek (1982). As none of them showed a significantly higher resemblance with the available data than the selected one, the correlation from Jenkinson et al. (1999) is adopted in this work for reasons of consistency.

B.2.4 The nacelle mass

In determining the nacelle mass, it is very difficult to specify which items must be attributed to the nacelle group. Some of the structure can namely be considered as a part of the wing, the body or the propulsion or undercarriage group. Care must thus be taken to avoid double accounting of mass items with other component mass groups. In order to be consistent with the other mass component definitions, the correlation from Jenkinson et al. (1999, pp. 136-137) is used in this work. The author furthermore indicates a very good resemblance with nacelle mass data from existing aircraft.

$$\begin{aligned} W_{nac} &= 6.8 \cdot T_{TO,SLS} \qquad (T_{TO,SLS} < 600\,kN) \qquad \text{(B.27)} \\ &= 2760 + 2.2 \cdot T_{TO,SLS} \qquad (T_{TO,SLS} > 600\,kN) \qquad \text{(B.28)} \end{aligned}$$

where $T_{TO,SLS}$ is the total installed sea-level static take-off thrust (in kN).

B.2.5 The landing gear mass

The mass of the landing gear will depend on the specified maximum landing mass and the rough field landing capability of the aircraft. To avoid the need of fuel jettisoning in case of an emergency landing shortly after take-off, aircraft are now often designed for a landing mass close to the maximum take-off mass (Jenkinson et al., 1999). As most airlines are operated from good quality paved runways, the biggest difference in the landing gear mass of aircraft lies in the degree of complication and the type of retraction mechanism which is set by the necessary compactness (Currey (1988) and Jenkinson et al. (1999)). Again, several references contain data on the landing gear mass. The correlation from Torenbeek (1982, pp. 282-283) is selected as it is a detailed correlation without requiring excessive data.

$$W_{lg} = K_{lg} \cdot \left(A + B \cdot W_{TO}^{3/4} + C \cdot W_{TO} + D \cdot W_{TO}^{3/2}\right) \qquad \text{(B.29)}$$

where K_{lg} is 1.00 for low-wing airplanes and 1.08 for high-wing aircraft. The coefficients A, B, C and D are determined based on a statistical evaluation of data on landing gear mass of existing aircraft. Torenbeek suggests the values from Table B.2 for the nose respectively main landing gear.

Table B.2. Coefficients for the calculation of the landing gear mass (Torenbeek, 1982, pp. 282-283).

	A	B	C	D
Nose gear	9.1	0.080	0.000	$2.97 \cdot 10^{-6}$
Main gear	18.1	0.131	0.018	$2.23 \cdot 10^{-5}$

As explained in section B.1.5, a correction on the obtained mass is made if the landing gear length is set by engine-related criteria instead of the conventional tailscrape limit. As such, the penalty on the landing gear mass by the adoption of very high bypass ratio turbofans is to some extent accounted for. The dependency of the landing gear mass on its length is derived from Raymer (1989, p. 475):

$$W_{lg,m} \propto l_{lg,m}^{0.4} \qquad W_{lg,n} \propto l_{lg,n}^{0.5} \tag{B.30}$$

If the length of the landing gear needs to be increased to allow a proper installation of the very high bypass ratio turbofans, the mass obtained from equation (B.29) is factored by the ratio of the final landing gear length to the length determined from the tailscrape requirement raised to the exponents obtained from Raymer.

B.2.6 The surface controls mass

The surface controls include all movable surfaces on the wing that have not been included in the flap mass calculation. The group includes all the internal wing controls and the controls for the external leading edge devices and lift dumpers/air brakes. Jenkinson et al. (1999, p. 138) suggest the following correlation for the surface controls mass. According to the authors, this equation shows a 90 % correlation with existing aircraft data.

$$W_{sc} = 0.4 \cdot W_{TO}^{0.684} \tag{B.31}$$

B.2.7 The propulsion group mass

The propulsion group mass comprises the dry mass of the engines, the mass of the accessory gearbox, the induction and exhaust system, the engine controls and starting system, the thrust reversers,... As in the early design phases details of all the components in this mass group are unavailable, mass estimates must be based on the bare engine mass (Jenkinson et al., 1999). The bare engine mass is thus determined first. Then the total propulsion group mass is tackled.

B.2.7.1 The bare engine mass

Various bypass ratio turbofans as well as advanced cycles are investigated for the different aircraft studies. A relatively detailed yet general method to assess the bare engine mass is thus required in order to provide the proper engine mass trends for the different cycles without resorting into too detailed correlations that require information that is not available in this stage of the design. Most models found in literature are however either too simplistic or too detailed. The simplistic methods generally rely only on take-off thrust (e.g. Jenkinson et al. (1999) and Svoboda (2000)). They are therefor not able to provide the necessary trade-off between propulsion system mass and size with varying bypass ratio. Other methods often require a significant amount of data to assess the engine mass, as they consist out of a build up of masses of individual components such as rotor disks, blades, casings,... (e.g. Onat & Klees (1979), Sanghi et al. (1998) and Tong et al. (2004)) and are as such outside the scope of this work. The only methods applicable for the desired type of investigations are found in Gerend & Roundhill (1970) and Waters & Schairer

(1977). The method of Gerend & Roundhill (1970) is more detailed without requiring extensive information. With the proper tuning it can be extended to modern high-bypass ratio turbofans yielding reasonable accuracy[12] (Dierick (2005), Doulgeris (2008), Hasan (1995) and Vicente (1994)). This method is therefor retained here.

The method from Gerend & Roundhill (1970) allows to determine the engine bare mass based on the engine bypass ratio BPR, the turbine inlet temperature TIT, the engine overall pressure ratio OPR and the total fan face air flow rate $\dot{m}_{tot}$. All cycle variables apply at sea level static, standard day takeoff conditions. From these input values the engine mass is determined as:

$$W_{eng} = \left(\frac{W_{eng}}{\dot{m}_{tot}}\right)_{corr} \cdot \dot{m}_{tot} \cdot K_{eng} \cdot \left(K_{gg} \cdot K_{HP} + \left(1 - K_{gg}\right) \cdot K_{LP}\right) \tag{B.32}$$

where

$$\left(W_{eng} / \dot{m}_{tot}\right)_{corr} = 14$$

K_{eng} is a correction factor applied to the complete engine, K_{gg} the ratio of gas generator mass to total engine mass, K_{HP} is the correction factor applied to the high pressure (HP) section and K_{LP} is the correction factor applied to the low pressure (LP) section. These correction factors are on their turn composed out of several contributions:

$$\begin{aligned} K_{eng} &= K_{BPR} \cdot K_y \cdot K_{life} \cdot K_M \cdot K_{duct} \\ K_{HP} &= K_{TIT} \cdot K_{OPR} \cdot K_{\dot{m}_{gg}} \end{aligned}$$

The correction factors are specified on figures or in tables in Gerend & Roundhill (1970). As some had to be extended outside the original range of application, they are detailed below.

- K_{BPR} is the correction factor for BPR and represents the relative engine weight per total airflow. K_{BPR} decreases with increasing BPR as more air bypasses the relatively heavy gas generator. This can be seen on Figure B.10(a).

- K_y is the correction factor for the year of the first flight and reflects the advance in technology over the years due to lighter and stronger materials as well as higher aerodynamic loading of turbomachinery (Gerend & Roundhill, 1970). Following Vicente (1994), a value of 0.357 is adopted to represent 1990 as the year of first flight. Progress in technology from that year onwards is integrated in the overall mass reduction factor.

- K_{life} represents the type of engine design. Engines are either classified as lift engines, short, medium or long life engines. Here a value of 1.07 is adopted for K_{life} to represent long life cruise engines.

- K_M is a correction for Mach number which is 1.0 below a Mach number of 2.

---

[12] Due to the high dependency on numerous details, engine mass prediction in the conceptual stage is very hard and even the detailed correlations are restricted to an accuracy in the order of 10% (Onat & Klees, 1979).

- K_{duct} is used to distinguish between short and long duct nacelles. For short ducts a value of 1.0 needs to be used.

- K_{TIT} depicts the trend of increasing turbine inlet temperature over the years. As this leads to higher thermal stresses and lower allowable stresses, an increase in engine mass would be expected with increasing TIT. However, this trend is not observed, partially due to advances in cooling technology and materials and partially due to the usage of the K_y correction factor (Gerend & Roundhill, 1970). The authors therefore derived a representative line of TIT in function of year and use this as a reference value for which no penalty on engine mass is needed. They then used a statistical regression and found a rate of change of gas generator specific mass of 3% per 100° F (55.56 K). This method is adopted here too, taking the lowest BPR kerosene engine as the baseline and adjusting the mass of other BPR engines and hydrogen fueled engines accordingly.

- K_{OPR} denotes the overall pressure ratio correction factor. Smaller engines tend to have a higher rate of change of engine mass with pressure ratio than larger engine due to minimum gage effects (Gerend & Roundhill, 1970). The correlation is therefore given for different mass flow rates, as shown on Figure B.10(b).

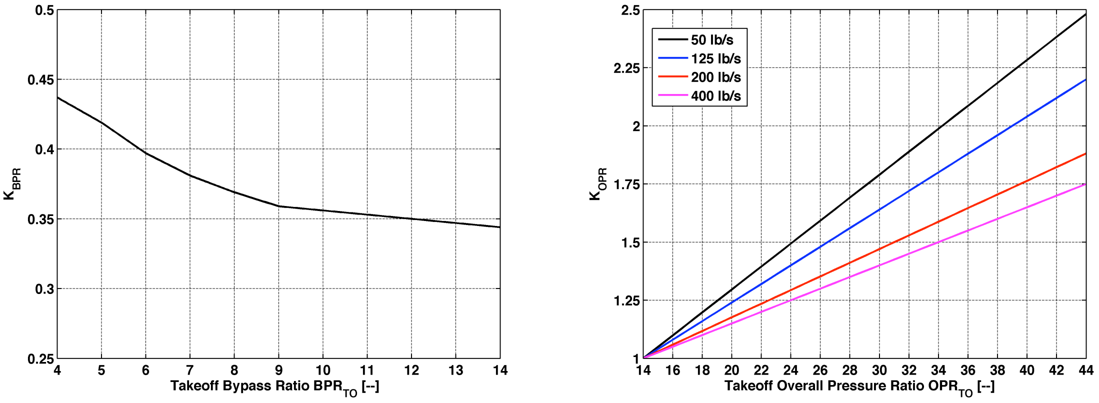

(a) Correction factor K_{BPR}

(b) Correction factor K_{OPR}

Figure B.10. Engine mass correction factors K_{BPR} and K_{OPR}.

- $K_{\dot{m}_{gg}}$ represents the scaling effect of engine mass with gas generator (core) engine mass flow rate. As some auxiliaries and fixed weight components do not scale with engine size, this scaling factor depends on air flow rate. Additionally, minimum gage effects also play a role through minimum standard material sizes, ability to manufacture, ... (Gerend & Roundhill, 1970). Figure B.11(a) depicts the combinatorial effect of all factors on engine gas generator scaling.

- K_{LP} is the correction factor for the low pressure section of the engine. As this scaling is already to some extent given through the K_{BPR} factor, Gerend & Roundhill scale all engines to a reference primary (core) air flow rate of 150 lb/s and use the following relationship afterwards:

$$K_{LP} = \left(\frac{\dot{m}_{gg}}{\dot{m}_{gg,\,ref}} \right)^{0.3}$$

This practice is adopted here too

- K_{gg} finally represents the ratio of gas generator mass to total engine mass and depends on the BPR of the engine. Its trend is given on Figure B.11(b).

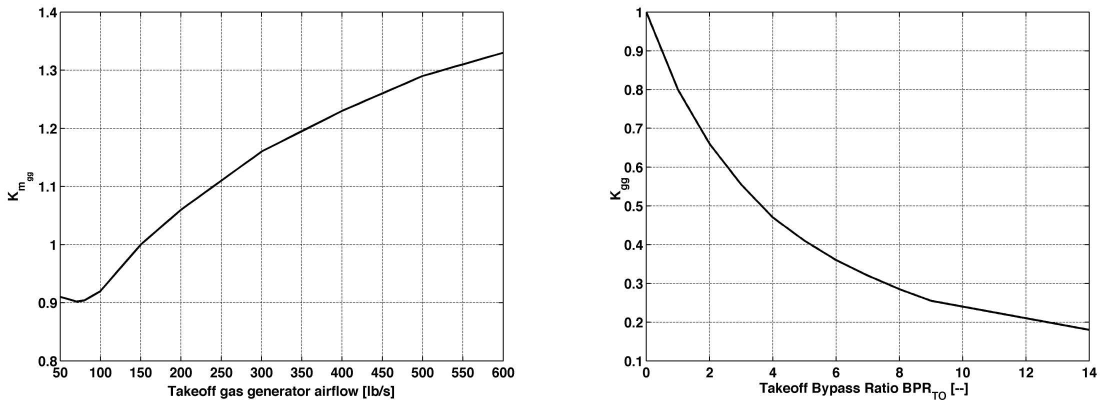

(a) Correction factor $K_{\dot{m}_{gg}}$ (b) Correction factor K_{gg}

Figure B.11. Engine mass correction factors $K_{\dot{m}_{gg}}$ and K_{gg}.

As the correlations from Gerend & Roundhill (1970) date from several years ago, some tuning is required to adapt the engine mass to new technology engine data, as is done in Dierick (2005), Hasan (1995) and Vicente (1994). Based on engine mass data from relatively new engines, the correction factor $\left(W_{eng}/\dot{m}_{tot}\right)_{corr}$ is updated. However, a significant spread is found for this factor even for the relatively small amount of available data. Vicente (1994) for instance reports that the correction factor should be multiplied by 1.25 for three spool engines and 1.16 for 2 spool engines, whereas Hasan (1995) indicates multiplication factors in the order of 1.40 for two spool engines. Based on data on three spool engines and adding a small amount of conservatism, a multiplication factor of 1.35 is adopted here.

$$\left(W_{eng}/\dot{m}_{tot}\right)_{corr} = 1.35 \cdot 14$$

Despite the extrapolations required for the correlations from Gerend & Roundhill (1970) for higher bypass ratios and the significant multiplication factor needed to tune the engine mass to new designs, it is believed that the trends in engine mass will be represented correctly when using this method.

B.2.7.2 The propulsion group mass

Once the bare engine mass is known, the propulsion group mass can be determined. Here, the correlation from reference Jenkinson et al. (1999, p. 139) is used:

$$\begin{aligned} W_{prop} &= 1.43 \cdot W_{eng} & W_{eng} < 10000\,kg \\ W_{prop} &= 1.16 \cdot W_{eng} + 2700 & W_{eng} > 10000\,kg \end{aligned}$$

where W_{eng} is the bare engine mass. The values from the above expressions assume a conventional installation with thrust reversers and normal engine accessories.

B.2.8 The fixed equipment mass

The fixed equipment mass group covers a wide variety of aircraft systems. Amongst others the instruments and navigation systems, the hydraulic, electrical and avionics systems, the furnishings and the auxiliary power unit are comprised in this group. The mass of a lot of these subcomponents is highly dependent on the type of aircraft under consideration and the items to be included furthermore depend on operational practices and aircraft specification (Jenkinson et al., 1999). The correlations from CoA (2000) (as cited in Sefain (2005)) are retained as some guidelines on adaptations to hydrogen fueled aircraft are found in Sefain (2005). They are summarized in Table B.3.

Table B.3. Correlations for the components of the fixed equipment mass (Sefain, 2005, p. 115).

Component	Mass correlation
Hydraulics and pneumatics	$W_{hyd} = 3.2 \cdot W_{TO}^{0.5}$
Electrics	$W_{elec} = 0.75 \cdot W_{TO}^{0.67}$
Accessory drives & APU	$W_{APU} = 300$ kg
Air conditioning	$W_{airco} = 0.035 \cdot W_{TO}^{0.88}$
De-icing	$W_{deice} = 0.16 \cdot W_{TO}^{0.7}$
Avionics	$W_{av} = 1250$ kg

where W_{airco} is the mass of the complete air conditioning, pressurization and oxygen supply system and all masses except for the APU and the avionics are given in lbs. The mass of the avionics is taken from Howe (2000) where a range between 1000 and 1500 kg is suggested. The furnishing mass is finally derived from Oelkers et al. (2000a) and Oelkers et al. (2000b), following the guidelines given in Table B.4 where FC stands for first class, BC for business class, YC for economy class and HD indicates the single class high density layout of the cabin. It is assumed here that each galley can store 2 trolleys that each hold 28 meals (Oelkers et al., 2000b). The galleys weigh 113.4 kg (Torenbeek, 1982, p. 191), which only includes the galleys themselves not the trolleys or the meals. These are namely accounted for in the operational items mass. The lavatories on the other hand weigh 136.0 kg.

Table B.4. Furnishing mass requirements (Oelkers et al., 2000a).

Component	**FC**	**BC**	**YC**	**HD**
Lavatories [pax/lav]	10	25	45	60
Meals [meals/pax]	14	7	2.8	1.6

B.2.9 The operational items mass

Some of the operational items are specific to the type of aircraft and other operational practices and must be assessed individually. The data proposed in Oelkers et al. (2000c) and Oelkers et al. (2000d) is utilized for all designs and is summarized in Table B.5. Following those references, each LD3 container can store the luggage of 33 passengers. For the emergency equipment, the mass of the slides, which depends on the door type and the door sill height, needs to be added to the mass specified in Table B.5.

Table B.5. The operational items mass (Oelkers et al., 2000c).

Fluids			
Oil for engines	F_N [lbs]/1000		
Unusable fuel	0.3 %		
Water for galleys and lavatories	3 kg/pax		
Galley			
Structure	30 kg/trolley		
	FC	**BC**	**YC**
Fixed Equipment [kg/pax]	4	2	1
Catering [kg/pax]	35	23	14
Seats [kg/seat]	32	25	14
Loading devices	75 kg/LD3		
Aircraft Documents	46 kg		
Emergency equipment			
Aircraft dependent	18 kg/ac		
Passenger dependent	0.3 kg/pax		

B.2.10 The crew mass

The crew mass mainly depends on the number of passengers given in the mission specification. As for the operational items and the fixed equipment mass, the guidelines from Oelkers et al. (2000a), Oelkers et al. (2000b), Oelkers et al. (2000c) and Oelkers et al.

(2000d) are followed. A flight crew of 2 pilots and 1 observer is proposed in those references, whereas the cabin crew number is selected from Table B.6. A weight of 90.7 kg per crew member (including baggage) is utilized which is in line with values found in literature (Jenkinson et al. (1999), Roskam (1997b), Schaufele (2000) and Roskam (1997a)).

Table B.6. Passengers per cabin attendant (Oelkers et al., 2000c).

	FC	BC	YC	HD
Pax/attendant	8	25	35	50

B.2.11 The payload mass

The payload of passenger aircraft naturally mainly consists out of the passengers and their luggage. In preliminary design, standard masses are therefore used for both the passenger and his luggage. Following Oelkers et al. (2000a) and Oelkers et al. (2000b), a value of 95.25 kg/pax is adopted, which accounts for a passenger mass of 75 kg and 20.25 kg of luggage. For the standard design payload, the 3 class configuration is used to determine the overall payload mass. The maximum payload is on the other hand determined from the single class HD configuration with the cargo bays filled with additional cargo in LD3 containers. A density of 160 kg/m^3 is used and it is assumed that the containers are 85% full (Oelkers et al., 2000b). Two cargo bays are accounted for. The front bay starts aft of the cockpit and runs up to the wing fuselage intersection. The aft bay begins aft of the wing and ends at the end of the cylindrical fuselage section.

B.2.12 The fuel mass

The fuel mass is determined from the design mission. The design mission used in this work can be found in Figure B.12 and is based on guidelines for long range international flights from Jenkinson et al. (1999), Oelkers et al. (2000a), Oelkers et al. (2000b), Schaufele (2000), Roskam (1997a) and Torenbeek (1982). As can be seen from the figure, the complete mission is split into two legs, the main mission and the fuel reserves mission leg. Each leg is further split into several phases and the required fuel is determined for each of the phases. The range of the design mission takes the distance flown during climb and descent into account. The distance flown in the climb phase is calculated, whereas for the distance travelled during descent an allowance of 30 nautical miles for every 10000 ft of descent is utilized (Eshelby, 2007).

Based on this mission profile, the fuel mass is calculated using the so-called fuel fraction method (Roskam, 1997a), where the fuel fraction for each phase of the complete mission is determined. The fuel fractions of the different phases, defined as the ratio of the mass at that end of the phase W_i to the mass at the beginning of the phase, W_{i-1}, are then simply

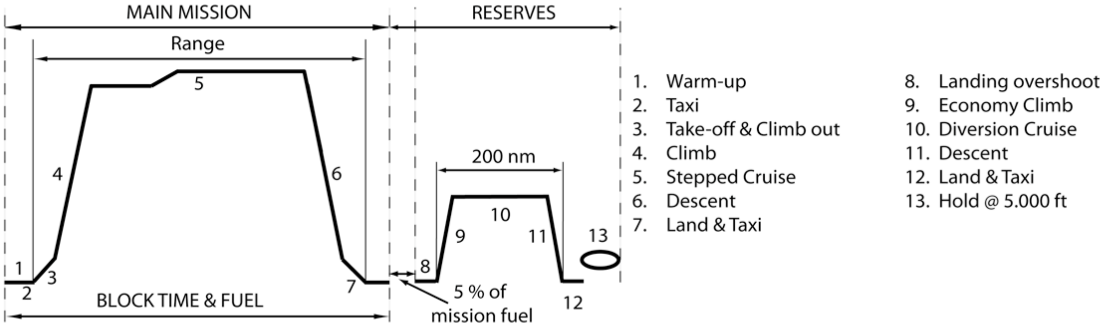

Figure B.12. The mission profile for the design mission.

multiplied to yield the overall mission fuel fraction:

$$M_{ff} = \prod_{i=1}^{z} \frac{W_i}{W_{i-1}} \tag{B.33}$$

where z is the total number of mission phases for the whole mission. W_1 is the takeoff mass and W_z is the landing mass of the aircraft.

The fuel fractions of each phase are on their turn found from a simple calculation or estimated based on statistical data or experience. For the fuel un-intensive phases[13], statistical data is used. Data for the different flight phases is amongst others found in Asselin (1997), Raymer (1989) and Roskam (1997a). A comparison of the data from these references shows a very good agreement between the three sources. Therefore, the data from Roskam is used, which is summarized in Table B.7. As shown in the table, a fixed fuel fraction is used for both climb phases as they only form a small fraction of the total mission seen the considerable range envisaged. The values are adopted from Roskam (1997a) and are determined based on the cruise Mach number. The distance and time required to climb are estimated from Brewer (1991, pp. 411-414).

Table B.7. Fuel fractions for the fuel un-intensive phases, adopted from Roskam (1997a, p. 12).

Flight phase	M_{ff}
Warmup	0.995
Taxi	0.990
Takeoff	0.995
Climb	0.96
Descent	0.990
Land & Taxi	0.992
Landing overshoot	0.992
Reserve climb	0.98

---

[13] The fuel un-intensive phases are flight phases during which a relatively small amount of fuel is used. Examples are: warm-up, taxi, take-off,...

For the fuel intensive phases, on the other hand, the Breguet equations for range and endurance are used to calculate the fuel fractions:

$$\ln M_{ff} = \frac{-R_{cr} \cdot SFC_{cr} \cdot g}{v_{cr} \cdot (L/D)_{cr}} \tag{B.34}$$

where R_{cr} is the range of the cruise phase, SFC_{cr} the specific fuel consumption in cruise, v_{cr} the cruise speed and $(L/D)_{cr}$ the lift-to-drag ratio in cruise. To increase the accuracy of the calculations the cruise phase is split into several segments and the fuel fraction of each mission is determined. A segment length of 150 km is utilized as a compromise between increased accuracy and calculation time.

For the missions where a stepped cruise is used, at each cruise segment, a check is made to see if the specific range[14] of the aircraft can be increased by climbing to a higher cruise flight level. If this is the case, a climb phase is started to the higher cruising altitude. Steps of 2000 ft are adopted here, which is in line with current practice.

As shown on Figure B.12, the reserve mission fuel incorporates an allowance of 5% of the main mission fuel mass, as specified in Penner et al. (1999). Similar allowances are found in Jenkinson et al. (1999), Roskam (1997a) and Schaufele (2000). After this, a "classical" reserves mission profile is used to account for a divergence to an alternate airport. The total reserve mission range is set to 200 nm and the cruise segment of the reserves is flown at Mach 0.6 at 20000 ft (Oelkers et al., 2000c). The reserve mission ends with a hold phase of 30 minutes at 1500 ft.

B.3 Aircraft aerodynamics

A relatively accurate estimation of the drag of the aircraft and its lift capability is necessary to be able to model aircraft performance with a reasonable accuracy. As detailed data is not available in the conceptual or preliminary design phase, generalized methods are normally used to determine both the drag as well as the maximum lift capability. Below, first the determination of the aircraft drag is elucidated. Then the lift calculation and the maximum lift capability are set forth.

B.3.1 The aircraft drag

Most drag estimation methods found in literature[15] rely on the so-called flat plate analogy with small differences in definitions. As the method from Jenkinson et al. (1999) has been applied to a set of three Airbus aircraft with an accuracy of 1% for the payload-range diagrams of all three aircraft (Laskaridis, 2004), this method has been retained in this work. The nomenclature used here is adopted from the same reference.

---

[14] The specific range is defined as the distance flown per kg of fuel used.

[15] among others in Bovet (2004), Jenkinson et al. (1999), Raymer (1989), Roskam (1997c) and Torenbeek (1982).

To use the flat plate analogy, the aircraft is split into components and each component is separately assessed to determine its contribution to the overall drag of the aircraft. Jenkinson et al. (1999, p. 170) divides the overall drag of subsonic civil aircraft into three categories, as shown by equation (B.35). The profile drag results from the pressure field around the shape and from the skin friction effects in the boundary layer while the wave drag comes from shock waves as part of the accelerated flow over the surfaces becomes supersonic. The lift induced drag finally results from the changes in pressure due to attitude variations resulting from the generation of lift.

$$C_D = C_{D,0} + \Delta C_{D,W} + C_{D,i} \tag{B.35}$$

where $C_{D,0}$ is the total profile drag coefficient, $\Delta C_{D,W}$ the additional drag resulting from shock waves, and $C_{D,i}$ is the total effect of all lift dependent components.

Using $C_{D,W}$ as the sum of the profile and the wave drag yields

$$C_D = C_{D,W} + k_{D,i} \cdot C_L^2 = C_{D,W} + \frac{C_L^2}{\pi \cdot e \cdot AR_w} \tag{B.36}$$

where e is the Oswald efficiency factor of the aircraft. The three different drag contributions of equation (B.35) are treated in more detail below.

B.3.1.1 Profile drag

The profile drag of each component is calculated with

$$C_{D0,comp} = C_f \cdot F \cdot Q \cdot \frac{S_{wet}}{S_{ref}} \tag{B.37}$$

where C_f is the skin friction coefficient of the component, F the component form (shape) factor, Q an interference factor, S_{wet} is the wetted area of the component as given in section B.1[16] and S_{ref} the reference area used for the calculation of the drag coefficient. As is usually done, this reference area is taken here as the gross wing planform area without slats and flaps deployed. The total profile drag coefficient is then given by the sum of the profile drag of the different drag components. The different contributions to equation (B.37) are discussed next.

The skin friction coefficient

The skin friction coefficient of a component depends on whether the flow over this component is laminar or turbulent and thus on the Reynolds number of the flow over the component Re_c. The transition from laminar to turbulent is generally taken at a Reynolds number of 300.000 (McCormick, 1995, p. 152).

$$Re_c = \frac{\rho \cdot v \cdot l}{\mu}$$

---

[16] The overlapping areas of the different components should be subtracted from the equations given (reference Roskam (1997b, pp. 281-287)). As suggested in Laskaridis (2004) this is not done here as this leads to more conservative results.

where ρ is the air density , v is the aircraft flight speed, l is the component characteristic length, and μ is the kinematic viscosity of air, which is calculated by Suterlands law with T the air static temperature (Fluent, 1999).

$$\mu = 1.4568 \cdot 10^{-6} \cdot \frac{T^{1,5}}{T + 110.4}$$

For the turbulent boundary layer the Prantl-Schlichting formula must be used to calculate the skin friction coefficient of the component while for any component or area with laminar flow the second correlation of equation (B.38) must be used (Jenkinson et al., 1999, p. 172).

$$C_{f,turb} = \frac{0.455}{\left(\log Re_c\right)^{2.58} \cdot \left(1 + 0.144 \cdot M^2\right)^{0.65}} \qquad C_{f,lam} = \frac{1.328}{\sqrt{Re_c}} \tag{B.38}$$

where M is the Mach number at the operational conditions under investigation.

For components with both laminar and turbulent flows the value of C_f should be an area weighted average of the two results (Jenkinson et al., 1999, p. 172). However, as the areas with laminar flow will only be very small for most flight conditions for the type of aircraft under investigation, the assumption will be made here that the whole flow is turbulent. Not only is it shown in Laskaridis (2004) that this leads to accurate results, it is conservative too.

The form and interference factors for the different components

The form factors are calculated from the component geometry using a component-specific formula[17]. For most components, the correlations from Jenkinson et al. (1999, pp. 170-180) have been applied in order to be consistent. The different components are treated consecutively in what follows.

Fuselage

$$F_{fus} = 1.1 + \frac{2.2}{f_{fus}^{1.5}} - \frac{0.9}{f_{fus}^{3.0}} \qquad Q_{fus} = 1.00$$

where f_{fus} is the fuselage fineness ratio ($f_{fus} = l_{fus}/d_{fus}$).

Wing

$$F_w = \left(3.3 \cdot \left(\frac{t}{c}\right)_{avg} - 0.008 \cdot \left(\frac{t}{c}\right)_{avg}^2 + 27.0 \cdot \left(\frac{t}{c}\right)_{avg}^3\right) \cdot \cos^2 \Lambda_{0.5c} + 1 \qquad Q_w = 1.10$$

For the wing interference factor Q_w, Jenkinson et al. (1999) recommend a value between 1.0 and 1.2 for conventional designs. A value of 1.1 is taken here as reported in Laskaridis (2004).

---

[17] Amongst others Bovet (2004), Jenkinson et al. (1999), Kroo (2006), Raymer (1989), Roskam (1997c) and Torenbeek (1982) give correlations.

Empennage

$$F_{tail} = \left(3.52 \cdot \left(\frac{t}{c}\right)\right) \cdot \cos^2 \Lambda_{0.5c} + 1 \qquad Q_{tail} = 1.20$$

Nacelle

$$F_{nac} \cdot Q_{nac} = 1.25$$

For initial estimates, Jenkinson et al. (1999) state that a value of $(F_{nac} \cdot Q_{nac})$ of 1.25 must be used. For rear-fuselage installations this value is increased to 1.50 as suggested in Williams (2007).

Landing gear

Jenkinson et al. (1999) suggest the following formula for the landing gear drag as insufficient data is known in this design stage for more detailed calculations:

$$C_{D,0} = 0.00157 \cdot \frac{W_{lg}^{0.73}}{S_w}$$

Flaps

The method from Jenkinson et al. (1999, pp.166-180) is adopted for both double as well as triple slotted Fowler flaps as it allows to investigate the effect of the flap angle on the performance of the aircraft. The objective of the method is to produce a quick yet reasonably accurate estimate of the flap drag at take-off, second-segment climb and landing approach conditions. The method is built around two figures which give the flap drag increment as a function of the number of slots, the wing area extension ratio, the flap deflection angle and the quarter chord sweep of the wing. Details of the flap drag calculation, can be found in Jenkinson et al. (1999).

Secondary items

The extra drag from secondary items is typically due to excrescences, surface imperfections and system installations and can be considerable[18]. Jenkinson et al. (1999) suggest the estimates given in Table B.8 for initial project design work. In addition to the above items, the cockpit windshield will increase the fuselage drag by 2 to 3% while the trim drag is typically taken as 5 drag counts[19] (Jenkinson et al., 1999, p. 176). Despite the adoption of tail fuel tanks, which could be used to position the center of gravity at the position that yields minimum trim drag, this value is retained here.

B.3.1.2 Wave drag

As civil aircraft are designed to be operated away from the worse effects of the wave drag rise, it is according to Jenkinson et al. (1999) acceptable to use a simple addition to the

---

[18] According to Jenkinson et al. (1999), the drag of secondary items can be up to 10 % of the profile drag calculated using the above method.

[19] One drag count equals a drag coefficient of 0.0001

Table B.8. The drag of the secondary items.

Item	Drag
Wing	$0.06 \cdot C_{D0,\,w}$
Fuselage and empennage	$0.07 \cdot C_{D0,\,fus}$
Engine installation	$0.15 \cdot C_{D0,\,nac}$
Systems	$0.03 \cdot C_{D0}$

aircraft drag when operating at speeds greater than Mach 0.7 (e.g. in cruise). Jenkinson et al. state that the additional drag due to compressibility will lie between 5 and 20 drag counts.

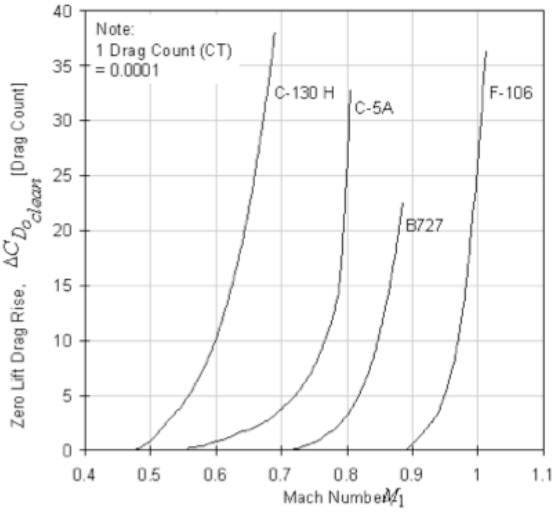

Figure B.13. Wave drag rise estimate for some aircraft (DARCorp, 2004).

As can be seen from Figure B.13 this agrees very well with the data from Roskam (1997b, p. 286) and DARCorp (2004). Therefore, the drag rise at the design cruise Mach number is taken here as 7 drag counts for all the designs under consideration regardless of the value of the design cruise Mach number. After all, the influence of the design cruise Mach number is already incorporated in both the wing sweep and the thickness to chord ratio of the wing tip, as explained in section B.1.2.

B.3.1.3 Lift induced drag

According to Jenkinson et al. (1999), the lift dependent drag mainly arises from three principal effects, which are associated with the distribution of lift along the wing span. There is a component from the wing planform geometry $\left(k_{D,\,i}\right)_1$, a contribution from the non-optimum wing twist $\left(k_{D,\,i}\right)_2$, and a component due to viscous flow forces $\left(k_{D,\,i}\right)_3$. These three contributions will now be reported consecutively.

The wing planform component $\left(k_{D,i}\right)_1$

The component of the induced drag coefficient that stems from the wing planform geometry, is estimated by the following equation (Jenkinson et al., 1999, pp. 178-179).

$$\left(k_{D,i}\right)_1 = \frac{C_1/C_2}{\pi \cdot AR_w}$$

where the coefficient C_1, given in Table B.9, represents the component arising from the planform geometry and is derived from the classical lifting line theory in function of AR_w and λ_w[20]. The values given by the lifting line theory are corrected by a factor C_2, empirically derived from previous aircraft designs (see Figure B.14). Depending on the wing aspect ratio, the correlation leading to the lowest drag is used in every design.

Table B.9. The uncorrected planform factor C_1, derived from (Jenkinson et al., 1999, p. 176).

λ_w \ AR_w	6	8	10	12
0.25	1.014	1.019	1.023	1.028
0.30	1.011	1.015	1.018	1.022
0.40	1.006	1.009	1.013	1.017
0.50	1.005	1.009	1.013	1.017
0.60	1.008	1.013	1.018	1.024

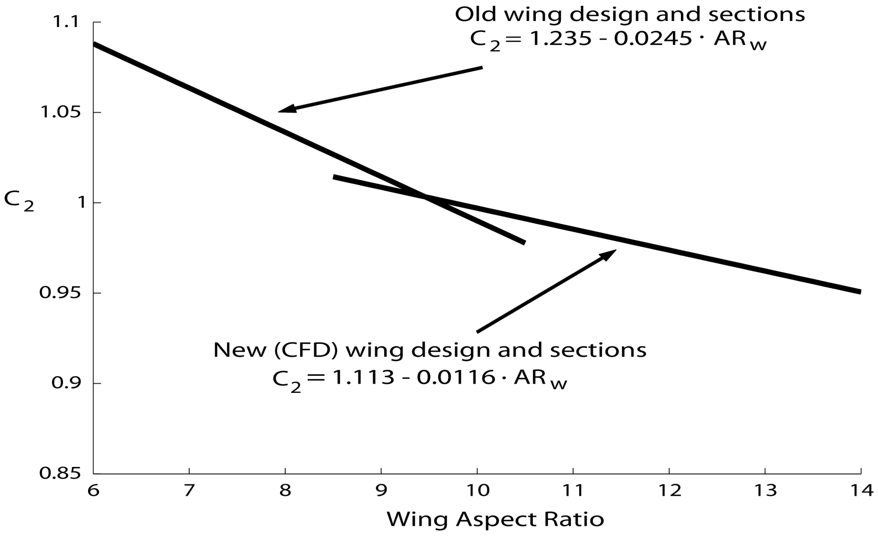

Figure B.14. Empirical correction factor C_2, adopted from (Jenkinson et al., 1999, p. 179).

---

[20] For aspect and taper ratio's not explicitly given in the table, a cubic interpolation between the values from the table is used.

The non-optimum twist contribution $\left(\mathbf{k_{D,i}}\right)_2$

The contribution from the effect of non-optimum wing twist requires a knowledge of the distribution of the airfoil section twist and of the changes in the sectional lift curve shape along the span. In the preliminary design stage such details are however not yet fixed. According to Jenkinson et al. (1999, p. 179) a correction of 0.0003 to 0.0005 must therefore be applied to the lift curve slope, with a value of 0.0004 being suitable for conventional civil turbofan layouts. In order to be conservative and to account for the high bypass ratio of the turbofans, the high-end value is nevertheless applied here:

$$\left(k_{D,i}\right)_2 = 0.0005$$

The viscous flow forces component $\left(\mathbf{k_{D,i}}\right)_3$

The third and final contribution to the lift-induced drag originates from the viscous flow forces. The viscous flow effects on the lift-induced drag are significant and exhibit themselves in the boundary layer growth arising from changes in wing incidence. Jenkinson et al. (1999) state that an empirical analysis of conventional civil aircraft geometries and operating conditions shows that this contribution to $dC_{D,i}/dC_L^2$ is proportional to the aircraft profile drag. For advanced technology designs (as the A330/340 and the B777) a value of 0.15 is suggested for the proportionality factor, while for older technology designs (as the B737-300, the B757 and the B767) a value of 0.35 is recommended in Jenkinson et al. (1999, p. 179). The suggested value of 0.15 for advanced technology aircraft is retained here.

$$\left(k_{D,i}\right)_3 = 0.15 \cdot C_{D,0}$$

Hence the total lift dependent drag coefficient for the aircraft is the sum of that three effects:

$$C_{D,i} = \left[\frac{C_1/C_2}{\pi \cdot AR_w} + 0.0005 + 0.15 \cdot C_{D,0}\right] \cdot C_L^2 \tag{B.39}$$

The effect of high-lift devices on the lift-induced drag

The deployment of the high lift devices changes the spanwise distribution of the lift and as such also the lift-induced drag. As the method from Jenkinson et al. (1999) does not consider this effect, the corrections suggested in Roskam (1997b) are added here when the slats and flaps are put into service. Roskam suggests a reduction in Oswald efficiency factor of 0.05 in the takeoff configuration and 0.1 for landing. These values are applied here.

B.3.2 The aircraft lift

In order to evaluate the drag of the aircraft, the lift coefficient must be known (see equation B.36). A first paragraph of this section reports the methods used in this work to determine the lift coefficient of the aircraft in both the cruise and the climb segment of the mission profile. A second paragraph then reports how the maximum lift capabilities of the aircraft are determined.

B.3.2.1 The lift coefficient in cruise and in climb

The cruise and climb lift coefficient are given in equation (B.40):

$$C_{L,cr} = \frac{W \cdot g}{\frac{\rho \cdot V^2}{2} \cdot S} \qquad C_{L,cl} = \frac{W \cdot g}{\frac{\rho \cdot V^2}{2} \cdot S} + \frac{dC_L}{d\alpha} \cdot \Delta\alpha \tag{B.40}$$

where the additional term for $C_{L,cl}$ is added to account for the climb angle and the rate of climb. In this equation, $\Delta\alpha$ stands for the increase in angle of attack due to the climb rate:

$$\tan \Delta\alpha = \left(\frac{RoC}{v_{cl}} \right)$$

The lift curve slope a on the other hand is calculated with the following equation from Anderson (1999, p. 92):

$$a = \frac{dC_L}{d\alpha} = \frac{a_0 \cdot \cos \Lambda_{LE}}{\sqrt{1 - M^2 \cdot \cos^2 \Lambda_{LE} + \left(\frac{a_0 \cdot \cos \Lambda_{LE}}{\pi \cdot AR_w} \right)^2} + \frac{a_0 \cdot \cos \Lambda_{LE}}{\pi \cdot AR_w}} \tag{B.41}$$

where a_0 is the lift curve slope for the incompressible 2D case is calculated as (Houghton, 2003).

$$a_0 = \left(\frac{dC_L}{d\alpha} \right)_0 = 1.8 \cdot \pi \cdot \left(1 + 0.8 \cdot \left(\frac{t}{c} \right)_{avg} \right)$$

As suggested in Schaufele (2000, p. 217), the lift curve slope a is increased by 8% to account for the lift contribution of the rest of the airplane.

B.3.2.2 The maximum lift capabilities

The maximum lift capability of the aircraft depends on the settings of the high-lift devices. First, the clean airplane, with neither slats nor flaps deployed, is discussed. Then the increments stemming from the high-lift devices are addressed. Finally, the limitations in $C_{L,max}$ to avoid buffet at high Mach numbers are treated.

The clean airplane

The maximum lift coefficient for the clean airplane mainly depends upon the choice of the section profile as this determines the section maximum lift coefficient. However as the spanwise wing loading is not constant from root to tip, the wing lift coefficient will always be smaller than the section maximum value[21]. Including the wing sweep effect, the following correlation is thus used for the maximum lift coefficient of the wing (Jenkinson et al. (1999, p. 164) and Raymer (1989, p. 328)):

$$\left(C_{L,max} \right)_{3D} = 0.9 \cdot \left(C_{L,max} \right)_{2D} \cdot \cos \Lambda_{c/4}$$

---

[21] After all, the wing will normally be twisted (geometrically or aerodynamically) to assure that stall will occur at a spanwise position where no control surfaces are present and the wing will thus stall at one particular spanwise position before complete wing has attained the maximum lift coefficient. Besides this there is a Reynolds number effect leading to a (slightly) lower $C_{L,max}$ at the tips

For the 2D maximum lift coefficient a value of 1.8 is taken following Schaufele (2000, p. 94) and Roskam (1997a, p. 91). The maximum of the range suggested for transport aircraft in both references is adopted.

The maximum lift increments from the high-lift devices

The lift increment for a wing with leading or trailing edge devices may according to Jenkinson et al. (1999, p. 167) and Raymer (1989, p. 339) be estimated from two-dimensional section data as follows:

$$\left(\Delta C_{L,max}\right)_{3D} = \left(\Delta C_{L,max}\right)_{2D} \cdot \frac{S_{fl}}{S_W} \cdot \cos \Lambda_{HL}$$

where $\left(\Delta C_{L,max}\right)_{2D}$ is the sectional lift coefficient increment of the high-lift device (see Table B.10), S_{fl} the wing area in the flowpath of the device and Λ_{HL} the sweepback angle of the hinge line of the device under consideration. As suggested in Jenkinson et al. (1999) the hinge line angles are approximated here by the sweep angle of the leading respectively trailing edge for the different devices. For take-off Jenkinson et al. (1999, p. 168) suggests to use 60 to 80 % of the values of the Table. Here, 60 % is used as this results in values that are more in line with the ball-park estimates from Roskam (1997a, p. 91).

Table B.10. The sectional lift increment from high-lift devices for the landing configuration.

Device	$\left(\Delta \mathbf{C}_{\mathbf{L,max}}\right)_{\mathbf{2D}}$
LE slat	$0.4 \cdot c^{'}/c$
Single slotted TE Fowler flap	$1.3 \cdot c^{'}/c$
Double slotted TE Fowler flap	$1.6 \cdot c^{'}/c$
Triple slotted TE Fowler flap	$1.9 \cdot c^{'}/c$

Mach number effect on maximum lift coefficient

As the Mach number increases to high subsonic values, the local velocities on the wing near the leading edge will become supersonic at high angles of attack (near the maximum lift coefficient). This leads to local shock waves and separation, limiting the attainable maximum lift coefficient. As buffet onset occurs prior to reaching $C_{L,max}$ (see section B.5) it is necessary to estimate the variation of airplane $C_{L,max}$ with Mach number. A trend curve which correlates the $C_{L,max}$ characteristics of a number of aircraft versus Mach number has been developed in Schaufele (2000, pp. 262-263). Schaufele (2000) gives the ratio of $C_{L,max}$ at high Mach number to $C_{L,max}$ at low speed with no Mach number effects. This ratio is plotted versus Mach number as shown in Figure B.15.

B.4 Aircraft load and balance diagram

Obviously, the designed aircraft will not only be flown at the maximum takeoff weight. For full confidence in the design, it is therefore necessary to consider all possible varia-

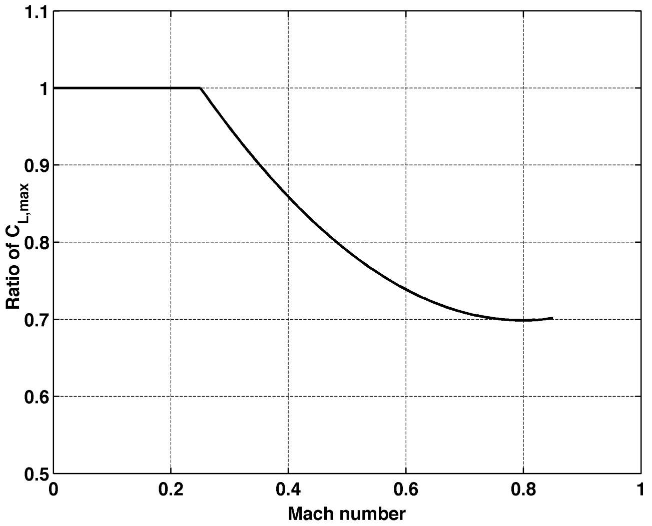

Figure B.15. Typical $C_{L,max}$ ratios for transonic aircraft, derived from Schaufele (2000).

tions in the load and payload distributions to establish the most forward and rearward (acceptable) center of gravity positions. These positions will namely not only dictate the critical loads on the tail surfaces and the landing gear, they will also affect the stability and control characteristics of the aircraft. In order to check whether the aircraft is stable at all possible 'flight conditions'[22] an aircraft balance diagram where the most forward and the most aft c.g. position are indicated, is drawn.

This section describes the determination of the most forward and rearward c.g. positions for the designs in this work. First, the adopted positions of the centers of gravity of the different components are given. Then, the so-called aircraft balance diagram (or c.g. excursion diagram) is briefly discussed. The method used to draw up this diagram is explained and an example is given. Finally, the landing gear disposition is tackled.

B.4.1 The component centers of gravity

The longitudinal location of the center of gravity of the different components can among others be found in Jenkinson et al. (1999, p. 148), Roskam (1989b, pp. 113-116) and Torenbeek (1982, pp. 294-302). For most components all the references use the same formula or position. Here and there the different references however differ slightly. The c.g.'s of the components as used in this work are summarized in Table B.11. The position in the Table is shown relative to the component location for both the longitudinal and vertical position, except for the height of the horizontal tail.

For the wing, the longitudinal position is taken as 70% of the distance between the front and the rear spar at 35% of the semi-span from the aircraft centerline.The vertical position of the wing center of gravity is calculated from the wing dihedral for the same spanwise

---

[22] Flight conditions alludes here to combinations of weight, center of gravity conditions and flight Mach numbers.

Table B.11. The c.g. position of the components.

Component	Longitudinal	Vertical
Fuselage	$0.42 \cdot l_{fus}$	$0.55 \cdot h_{fus}$
Wing	$0.492 \cdot c_{0.175 b_w}$	
Horizontal Tail	$0.42 \cdot c_{0.17 b_{ht}}$	$0.95 \cdot h_{fus}$
Vertical Tail	$0.42 \cdot c_{0.38 h_{vt}}$	$0.38 \cdot h_{vt}$
Nacelle	$0.4 \cdot l_{nac}$	engine centerline
Surface Controls	trailing edge of MAC_w	c.g._w
Propulsion Group	$0.5 \cdot l_{nac}$	$1/12 \cdot d_{nac}$ below centerline
Fixed Equipment	$0.42 \cdot l_{fus}$	$0.55 \cdot h_{fus}$
Operational Items	$0.42 \cdot l_{fus}$	$h_{deck} + 0.70$
Crew	$0.42 \cdot l_{fus}$	$h_{deck} + 0.70$

position. The longitudinal position of the landing gear c.g. is taken as the mass weighted average of the nose and main gear. The vertical position is fixed at 85% of the gear height for the main gear and 50% of the nose gear height. When the engines are installed at the aft fuselage, the fuselage c.g. is shifted to 47% of the fuselage length. As the payload center of gravity position depends strongly on the specific fuselage design, it is calculated based on the seat positions and the positions of the front and aft cargo bay for each specific design. Finally, the fuel center of gravity is determined for each fuel tank following Jenkinson et al. (1999, p. 148). The center of gravity of a single prismoid tank with a length l between parallel end faces with areas S_1 and S_2 is determined as:

$$\frac{l}{4} \cdot \left(\frac{S_1 + 3 \cdot S_2 + 2 \cdot \sqrt{S_1 \cdot S_2}}{S_1 + S_2 + \sqrt{S_1 \cdot S_2}} \right)$$

B.4.2 The balance diagram

This section describes the construction of the aircraft balance diagram, and the steps used to construct it (as derived from Jenkinson et al. (1999, p. 149) and Torenbeek (1982, pp.295-302). A typical balance diagram with the different loading loops is shown on Figure B.16.

B.4.2.1 Step 1: The c.g. at the operational empty weight

As the c.g.'s of all the components are known, the c.g. of the aircraft at its operational empty weight is simply calculated as:

$$x_{oe} = \frac{\sum x_i \cdot W_i}{\sum W_i}$$

However, the longitudinal location of the wing on the fuselage has not been fixed so far. According to Torenbeek (1982, pp. 299-300) and Jenkinson et al. (1999, pp. 153-155), the

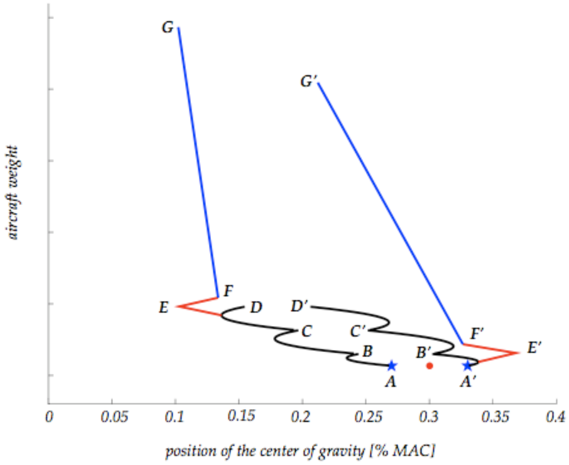

Figure B.16. An example of the aircraft loading loops.

wing position should be chosen so that the c.g. at the operational empty mass is conveniently located. For an aircraft with four wing-mounted engines, Torenbeek suggests an overall empty c.g. that is located between 25 and 30% of the MAC. For an airplane with two wing-mounted engines, the c.g. should according to Torenbeek (1982) lie somewhere between 20 and 25% of the MAC. Potential balance problems are identified for this type of configuration, which could be solved by the provision of a cargo compartment in the fuselage nose in front of the cockpit. If necessary, this strategy will be applied here. When the engines are installed aft of the fuselage, Torenbeek finally indicares a range between 35 and 40% of the MAC as a convenient location for the aircraft operational empty center of gravity.

In this work, the c.g. of the operational empty aircraft is positioned as follows. For a twin-engine aircraft, the c.g. is located at 20 % of the MAC, while for a four-engine aircraft, a c.g. location of 25 % is envisaged. For fuselage mounted engines, 35% of the MAC is chosen.

$$x_{oe,2\,eng} = 20\,\%\,MAC \qquad x_{oe,4\,eng} = 25\,\%\,MAC \qquad x_{oe,fus} = 35\,\%\,MAC$$

The location of the main landing gear relative to the most aft c.g. position is however also subjected to some requirements, amongst others to assure that the airplane will not cant (see section B.4.3). For some designs the wing might therefore be slightly shifted to guarantee a proper landing gear disposition.

As recommended in Jenkinson et al. (1999, p. 149), a 3% variation is taken around the nominal position of the center of gravity at the operational empty mass to account for variations of operational items (passenger movement, undercarriage retraction,...). This results in points A and A' on Figure B.16.

B.4.2.2 Step 2: The loading of the passengers

The loading of the passengers is assumed to take place seat-by-seat according to the so-called window seat rule. Line A to B assumes that the window seats are occupied from front to back. Line A' to B' considers the window seats from the back to the front to be chosen first. Then, the passenger loading is considered to continue with the seats that are not-adjacent to the aisles. (BC from front to back, B'C' from back to front). Finally the remaining (aisles) seats are filled in the same way (CD and C'D'). For the multiple deck layouts, it is assumed that all decks are loaded simultaneously as this leads to a wider range in center of gravity positions and is thus conservative[23].

B.4.2.3 Step 3: The loading of the cargo

To determine the most forward center of gravity position, the cargo in the front bay is added to the most forward position of the passenger loops (point E). However, this case might be considered as too critical and the aircraft load master can in this case decide to load the rear cargo first. If the total c.g. excursion of the designed aircraft is too big, this option is assumed to be adopted. In a next step, the rear cargo is added (point F). This procedure is done similarly for the most rearward c.g. position (E' and F'). Again, the load master option can be used if necessary.

B.4.2.4 Step 4: The loading of the fuel

The fuel is loaded at the most critical point on both the rear and the front loading position to indicate the widest c.g. range possible. As shown on Figure B.16, this leads to points G and G'. The Figure shows that for this particular design the load master must assure that the cargo is loaded in the proper order.

B.4.2.5 The center of gravity range

Now that the full balance diagram is constructed, the c.g. range of the aircraft can be evaluated. According to Torenbeek (1982, p. 299) and Jenkinson et al. (1999, p. 151), the most aft c.g. location for a large passenger transport aircraft is typically 35 to 40 % of the wing mean aerodynamic chord while the most forward position lies around 8% of the MAC. Jenkinson et al. (1999) indicates for instance a typical range of 11-31% for the A300. Similar values can also be found in Roskam (1997b, pp. 237-245). For all the designs of this work, the center of gravity range is checked and measures are taken if it does not comply with the "rules" indicated in this section.

B.4.3 The landing gear disposition

Before the actual disposition of the landing gear legs is tackled, the number of legs to be used, is fixed first. Both items are treated consecutively below.

---

[23] When determining the height of the c.g. however the upper deck is assumed to be loaded first as this yields the (conservative) highest c.g. position.

B.4.3.1 The number of main landing gear bogeys and tyres

The maximum loading per landing gear wheel is limited through the so-called load classification number (LCN) of the runway so that bigger (and thus heavier) aircraft need to have more wheels. The number of wheels per bogey is limited by both structural (retraction) and strut-weight limitations. For takeoff masses higher than a certain value, a landing gear configuration with four main landing gear bogeys must be used as can be noticed on both the Airbus A380 and the Boeing 747.

To determine the number of wheels and the number of bogeys for a given aircraft takeoff weight, an approach similar to the one outlined in Chai & Mason (1996) is adopted. A datalist of tyres and wheels is selected from manufacturers data (Goodyear, 2002) and based on the maximum load per tyre, the number of tyres is determined for a given takeoff mass. To determine the maximum tyre load, the mass is factored by 1.01 to consider the maximum ramp mass to takeoff mass ratio, by 1.07 as specified in the FAR 25 regulations and by 1.25 to take future growth versions into account (Roskam, 1989a, pp. 26-44). For the main gear tyres it is assumed that the complete takeoff mass acts upon the main gear tyres. For the nose gear, the static load is considered to be 15% of the takeoff mass, as detailed in the next section. Besides the static load, a dynamic load is also considered:

$$P_{dyn} = W_{TO} \cdot \frac{l_m + (a_x/g) \cdot h_{cg}}{n_t \cdot (l_m + l_n)} \tag{B.42}$$

where l_m is the distance between the main gear and the most aft c.g. position and l_n is the distance between the nose gear and the most aft center of gravity. a_x/g is the deceleration of the aircraft and is taken as 0.45 which represents a dry concrete runway and anti-skid brakes (Roskam, 1989a, p. 28). The maximum of the static and dynamic load is used to determine the number of nose gear tyres. These considerations lead to the number of tyres indicated in Table B.12 where n_n is the number of nose gear tyres and n_m is the number of main gear tyres. For the nose gear struts it is assumed that maximum 2 tyres can be placed on a single strut. Main gear struts hold either 4 or 6 tyres. As can be seen from the Table, this boils down to a maximum static load of almost 65000 lb/tyre for the nose gear and 78400 lb/tyre for the main gear tyres.

Table B.12. The number of nose and main gear tyres for different W_{TO}.

W_{TO} [kg]	$N_{ty,n}$	$N_{ty,m}$
up to 193000	2	8
up to 290000	2	12
up to 386800	4	16
from 386800	4	24

Besides the load on the tyre, the maximum speed capability and the minimum diameter of the wheel rim to ensure that the brakes can absorb the kinetic energy at landing are also considered in the tyre selection(Raymer, 1989, pp. 281-282). Figure B.17 gives a statistical estimate of the required wheel rim diameter to provide a brake that can absorb a given amount of energy. It is assumed that only the main wheel are provided with brakes (Raymer, 1989).

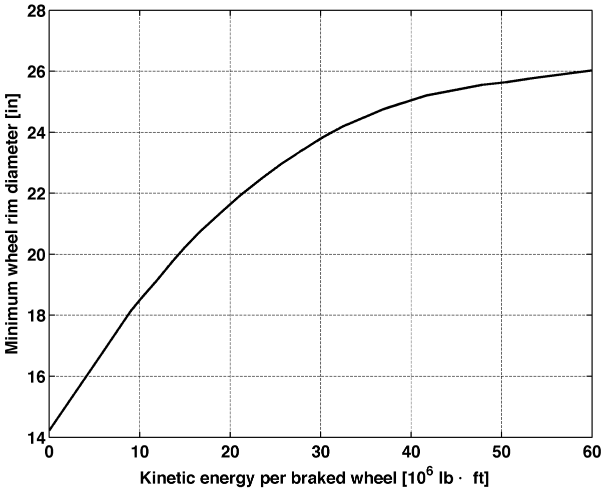

Figure B.17. Minimum wheel rim diameter for braking, derived from Raymer (1989).

B.4.3.2 The landing gear disposition

Now that the number of main landing gear legs is determined, their longitudinal location can be fixed. This so-called landing gear disposition is subjected to several (often conflicting) requirements. The following general guidelines, derived from Jenkinson et al. (1999, pp. 46-47), Roskam (1997b, pp. 217-225) and Torenbeek (1982, pp. 349-356), are followed in this work.

The longitudinal position of the nose-wheel attachment to the fuselage must be consistent with the structural framework in the front fuselage. The designer must assure that the flight deck floor line and the pressure bulkhead positions are not unduly compromised. As this work only consists out of preliminary designs, details of the fuselage framework are not available. Therefore, the nose landing gear position for the kerosene fueled aircraft is simply taken here 6 meter behind the front of the fuselage nose, based on the positions of the nose landing gear of both the Airbus A380 and the Boeing 747. For the hydrogen fueled aircraft, the nose gear is positioned at the front end of the fuel tank in the front of the fuselage. The gear is assumed to be attached to the pressure bulkhead between the tank and the cockpit. Astaburuaga & van Holten (2001) and Astaburuaga et al. (2001) also identify that a more detailed landing gear attachment and load calculation will be required in subsequent design stages due to the restricted nose gear position.

The position of the main landing gear is subjected to even more stringent requirements. The gear must for starters provide an adequate reverse stabilizing moment for the backward towing. It must furthermore also provide a rigid moment when the fuselage is pulled down onto its tail stop (Jenkinson et al., 1999, p. 47). To ensure the aircraft will not tip over laterally, the main landing gear should be sufficiently aft of the most aft center of gravity position. As is common practice, a minimum angle of 15° between the highest and most aft c.g. and the point where the main tyres touch the ground is adopted here (amongst others Currey (1988), Roskam (1997b) and Torenbeek (1982)).

However, the position of the main landing gear will furthermore usually be chosen so that the minimum static load on the nose wheel is at least 8% of the aircraft mass, which is necessary to give reasonable steering forces. Meanwhile it should also be assured that the maximum static load on the nose-wheel does not exceed 15%, as a bigger load would lead to an excessive tail horizontal load to rotate the aircraft at take-off[24]. Besides these requirements , however, structural integration requirements will also play an important role. The designer must namely assure that the landing gear can be efficiently integrated into the aircraft structure without an excessive weight penalty. In order to do this, the gear will usually be attached to the rear wing spar. In some designs, this entails a cranked trailing edge, sometimes called yehudi, in order to be able to store the gear in its retracted position.

In this work the first set of main landing gear is attached to the wing spar. The actual longitudinal position of the gear is then determined by its track width, which is on its term determined by two requirements. A sufficient track width is namely not only needed to assure that the aircraft will not tip over laterally during turns, it must provide sufficient engine-ground clearance too. To ensure this, Currey (1988), Roskam (1997b) and Torenbeek (1982) suggest a maximum overturn angle of 55°[25]. Based on modern transport aircraft data and to add a small margin seen the considerable uncertainty in the determination of the c.g. position, the overturn angle is taken here as approximately 40°. When 4 landing gear struts are needed, the second set of struts is assumed to be positioned at the wing fuselage intersection and its longitudinal position is chosen to yield a proper nose gear load for the complete c.g. range.

B.5 Aircraft performance

All civil aircraft must meet specified airworthiness regulations with regard to flying qualities and performance. Obviously, aircraft are also designed to meet the operational requirements from the mission specification such as speed, range, payload,…Therefore, aircraft performance is a fundamental part of the design process in that it will determine the minimum engine thrust and wing area. As the wing area is one of the design variables chosen for the parametric studies of this work, the different performance requirements described below are used to size the engines (for a given wing geometry). However, as the requirements stipulate different engine ratings and different points in the flight envelope of the aircraft[26], the thrusts obtained by the different requirements need to be brought

---

[24] As Currey (1988) indicates, this range is indicative for current practice rather than an absolute limit. A slight departure from these values is therefore possible. As the nose gear position for the hydrogen fueled aircraft is very restricted, action is not undertaken unless the loads depart significantly from the aforementioned range.

[25] The definition of the overturn angle can amongst others be found in Roskam (1997b, p. 219).

[26] A point in the flight envelope is determined by the speed and the altitude at which the aircraft is flying.

back to a common base. Here, the trust in the take-off rating at sea-level static (SLS) ISA conditions will be used.

Two different performance requirements are used to size the engine: the thrust required at top of climb and the FAR OEI climb rate requirements. After all, the top of climb requirement, also called the initial cruise altitude capability, will usually determine the required engine thrust for a large, long range aircraft (Jenkinson et al. (1999, p. 281) and Dalhuijsen & Slingerland (2004)) due to the fairly relaxed take-off field length requirement. For most of the designs in the work the engine will thus be sized by this requirement. For the twin engine designs, however, the FAR second segment climb requirement is most likely to be the most stringent requirement (Cumpsty, 1997, p. 84). Both requirements are reported in the first paragraph of this chapter.

As the engines are sized only by the two previous requirements, additional performance constraints are imposed on the design space during the parametric studies of this work. Even if the take-off and landing field length requirements appear to be relaxed, a check is needed to ensure that the field lengths are within the limits of the mission specification. Constraints are also added for the approach speed and to prevent buffeting of the wing[27]. These constraints are elucidated in the second paragraph of this section.

B.5.1 Performance requirements

The two conditions used to determine the minimum thrust required by the engines are reported below. First, the top of climb requirement is described. Then the FAR climb gradient requirements are explained.

B.5.1.1 Top Of Climb

At the beginning of cruise some margin over the maximum cruise thrust is required to maintain height and speed under gusty conditions. Usually a rate of climb of 300 ft/min is required as a margin although airlines may sometimes specify 500 ft/min (Jenkinson et al. (1999, p. 268) and Dalhuijsen & Slingerland (2004)). The latter requirement is used here to provide a small additional margin over the regulations. With this rate of climb (RoC) the required thrust can be determined as follows:

$$F_{N\,toc} = W_{toc} \cdot g \cdot \left(\frac{1}{L/D} + \frac{RoC}{v_{cr}} \right) \cdot \frac{1}{N_{eng}} \tag{B.43}$$

where $F_{N\,toc}$ is the required net thrust per engine at the top of climb, W_{toc} the mass of the aircraft at the beginning of the cruise phase, g the gravitational acceleration, L/D the lift to drag ratio of the aircraft at the considered point, v_{cr} the cruise speed and N_{eng} the number of engines of the aircraft under consideration.

---

[27] An additional constraint is imposed to ensure that the mission fuel can be stored in the wing for kerosene-fuelled aircraft as explained in section B.1.2.6. Even though the buffet constraint is strictly speaking not a performance constraint, but can rather be classified as a geometric limit on wing size, it is nevertheless included in this section because it significantly impacts aircraft performance and wing sizing.

B.5.1.2 FAR climb gradients

Airworthiness requirements demand that certain climb gradients are met with one engine failed in the so-called take-off climb. The same type of requirements is also used to assure that a safe climb out is possible after a balked landing. The requirements that apply for the aircraft under consideration are the FAR 25 climb gradient requirements (FAR 25.111, 25.119 and 25.121). First the requirements for the take-off climb are discussed, then the applicable landing requirements are reported.

Take-off climb

The take-off climb phase begins at lift-off and finishes at 1.500 ft above the runway. For the take-off climb gradient analysis, this phase is split into four segments. However, the FAR regulations do not explicitly require a positive climb rate for the third segment. Below, only segments 1, 2 and 4 will thus be given. For all requirements, the aircraft is assumed to be at its maximum take-off weight as stipulated by the regulations.

The settings used for the different requirements of FAR 25.121 can be found in Table B.13 (from Jenkinson et al. (1999, pp. 234-237) and Roskam (1997a, pp. 140-143)). Even though not explicitly mentioned in the table, the stall speed obviously depends upon the aircraft configuration. A different stall speed thus applies for the different segments. Besides the FAR 25.121 requirements, FAR Part 25 section 111 stipulates one additional take-off climb requirement. This time the aircraft is assumed to be at a height of 200 ft above the runway, at 1.2 times the stall speed. The landing gear is retracted and take-off flaps are assumed (Roskam, 1997a, p. 140).

Table B.13. The definition of the different take-off climb segments.

Segment	Altitude [ft]	Flap setting	Landing gear	Engine rating	Speed	Climb gradient [-] 2 engines	4 engines
1	0-35	TO	down	TO	$1.15 \cdot V_s$	0.000	0.005
2	400	TO	up	TO	$1.2 \cdot V_s$	0.024	0.030
4	1500	cruise	up	Max Cont	$1.25 \cdot V_s$	0.012	0.017

For all requirements mentioned above, the most critical engine is assumed to be inoperative. The required thrust can then be determined as follows:

$$F_N = W_{TO} \cdot g \cdot \left(CGR + \frac{1}{L/D} \right) \cdot \left(\frac{N_{eng}}{N_{eng} - 1} \right) \tag{B.44}$$

where CGR is the required climb gradient as stipulated in the airworthiness requirements, The required minimum CGR is given in Table B.13 for each of the considered segments.

Balked landing

Two additional climb rate requirements (FAR 119) are specified to assure a safe climb out after a balked landing; one with all engines operating (AOE) and one with one engine inoperative (OEI). For those cases, a formula similar to equation (B.44) is applicable[28]. This time, the maximum landing weight of the aircraft however needs to be used. The required climb gradients and the settings used to calculate the required thrust are given in Table B.14 (Roskam (1997a, p. 142) and Torenbeek (1982, p. 379)).

Table B.14. The definitions for the balked landing.

	Altitude [ft]	**Flap setting**	**Landing gear**	**Engine rating**	**Speed**	**Climb gradient [-]**	
						2 engines	**4 engines**
AEO	0	land	down	8s	$1.3 \cdot V_s$	0.032	0.032
OEI	0	approach	up	TO	$\leq 1.5 \cdot V_s$	0.021	0.027

The engine thrust used for the AEO landing requirement is the thrust obtained 8 seconds after moving the throttle from minimum flight idle to the take-off position. As a full transient engine analysis is outside the scope of this work it is assumed that the engines are capable of reaching their maximum continuous thrust at that point.

As all other parameters are known, only the landing mass still needs to be determined. Even though the actual landing weight for the mission is known, it will not be used here to allow a comparison in all fairness and to enable landing without excessive fuel jettisoning when engine problems occur immediately after take-off. The landing mass is therefor assumed to be 95% of the takeoff mass.

B.5.2 Performance constraints

Besides the two requirements used to size the engines of the different designs, several additional performance constraints are considered for the parametric studies of this work. Below these constraints are elucidated. First, the method used to calculate the take-off distance is explained. Then, the landing distance constraint and the approach speed of the aircraft are determined.

B.5.2.1 Take-off field length

As stipulated in FAR 25.113, the take-off field length for jet transport is the greater of the all engines operative take-off distance and the balanced field for a one engine inoperative take-off. In case of an engine failure during take-off, there namely is a most critical point (speed) which defines the so-called balanced field length. If the engine fails at this most critical point, called the decision speed v_1, the distance to brake to a halt after the

---

[28] For the AEO case obviously the last term between brackets disappears from the equation.

engine failure equals the distance to continue take-off to an obstacle height h_{obs} of 35 ft on the remaining engines. If the engine fails before the decision speed is reached, the pilot can easily stop the take-off. If failure occurs after the decision speed, the take-off must be continued. The balanced field length is the maximum take-off distance with one engine inoperative. Here only the balanced field length will be used as an indication for the takeoff distance, as it is the metric utilized in Oelkers et al. (2000a) and Oelkers et al. (2000b).

As described previously, the takeoff distance is usually not critical for long range aircraft. A simplified expression is thus used to check the takeoff balanced field length requirement. The method adopted here is derived from (Corke, 2003, p. 167) and Raymer (1989, pp. 566-567) as it allows to take the engine bypass ratio into account.

$$BFL = \frac{0.863}{1+2.3\cdot G}\cdot\left[\frac{\frac{W_{TO}}{S_w}}{\rho\cdot 0.8\cdot C_{L,max}}+h_{obs}\right]\cdot\left[\frac{1}{\frac{F_{N,avg}}{W_{TO}}-U}+2.7\right]+\frac{200}{\sqrt{\frac{\rho}{\rho_{SL}}}} \tag{B.45}$$

where the average takeoff thrust $F_{N,avg}$ for jet engines is given by:

$$F_{N\,avg} = 0.75\cdot F_{N,stat}\frac{5+BPR}{4+BPR}$$

and $F_{N\,stat}$ is the net static thrust at the take-off altitude. U on the other hand represents the drag produced by extended flaps and is according to Corke (2003) and Raymer (1989) given by the following expression for flaps in the take-off position:

$$U = 0.01\cdot C_{L,max}+0.02$$

Finally, G is defined as:

$$G = CGR_{cl}-CGR_{min}$$

with CGR_{min} equal to 0.024 for two-engine aircraft and 0.030 for a four-engine aircraft. Torenbeek (1982, p. 169) recommends to take G equal to zero as it leads to the maximum balanced field length. This practice is adopted here. The obtained BFL is given in meters.

B.5.2.2 The landing distance

For the landing distance, two methods are utilized and the maximum of both calculated distances is taken as the landing distance.

Raymer (1989, p. 102) gives the following expression for the landing distance:

$$s_{land} = 5\cdot\frac{W_l}{S_w}\cdot\frac{1}{\frac{\rho}{\rho_{SL}}\cdot C_{L,max}}+s_a \tag{B.46}$$

where s_a is equal to 304.8 m for an airliner type aircraft.

In Torenbeek (1982, p. 180), the following expression is proposed:

$$s_{land} = \frac{5}{3}\cdot\left(10\cdot h_{obs}+\frac{W_l}{S_w}\cdot\frac{\left(\frac{1.52}{a_x/g}+1.69\right)}{\rho\cdot g\cdot C_{L,max}}\right) \tag{B.47}$$

The landing distance is calculated for an obstacle height h_{obs} if 50 ft and a_x/g is taken as 0.45 as was done in equation (B.42).

B.5.2.3 Approach speed

The approach speed of the designed aircraft must be similar to the speed used by existing aircraft to minimize traffic control problems. Furthermore, as the landing distance is related to the approach speed, this speed should be kept to a reasonable value to limit the required landing distance. Based on both considerations, a limit of 140 kts is put on the aircraft approach speed in the mission specification (following Oelkers et al. (2000a) and Oelkers et al. (2000b)).

For every point of the parametric studies, the approach speed V_{app} is calculated as 1.3 times the stall speed of the aircraft in its approach configuration, as required by FAR25.

$$V_{app} = \sqrt{\frac{2 \cdot W_{app} \cdot g}{S_W} \cdot \frac{1.3^2}{1.13 \cdot \rho \cdot C_{L,\,max}}} \tag{B.48}$$

where W_{app} the mass of the aircraft at approach, ρ is the density of the air, and $C_{L,\,max}$ is the maximum lift coefficient of the aircraft in its approach configuration. The factor 1.13 is a statistical factor that takes the speed loss during the FAR stall maneuver into account (Torenbeek, 1982, p. 577). The mass of the aircraft at approach is determined by the maximum landing mass which is on its term given in section B.5.1.2.

B.5.3 Buffet boundary

For transonic cruise aircraft such as the jet transports under consideration, an additional performance limit called the "buffet boundary" must also be considered during the design to assure a smooth operation for all speed and altitude conditions of the flight envelope. Outside the buffet boundary, the aircraft will namely be subjected to significant separated flow, which results in noticeable shaking or "buffeting" of the structure and flight controls. According to Schaufele (2000, p. 260), this buffeting can be severe enough to cause minor structural damage and can be associated with abnormal aerodynamic stability and control characteristics.

For transonic cruise aircraft, the buffet boundary shape is related to two similar, but actually different airflow conditions (Schaufele, 2000, p. 262). They are:

1. wing upper surface flow separation associated with the approach to the airplane maximum lift coefficient,
2. wing upper surface flow separation associated with operation beyond the drag divergence Mach number and the unsteady flow caused by strong shock waves on the wing.

As the second type of buffet problems is already addressed by the selection of the wing sweep (see section B.1.2.2), only the limit on the available lift coefficient will be considered here. Two different correlations that yield a limit on the lift coefficient to avoid buffeting are found in literature. First the limit as given in Schaufele (2000, p. 262-264) is described. Then, the version found in Howe (2000, p. 142-143) is detailed

The first limit on the usable lift coefficient is taken from Schaufele (2000). According to that reference, a margin of 1.3 g to buffet onset during maneuvering needs to be assured in the design phase through a proper selection of wing area. As the buffet onset occurs at a lift coefficient of about 90 % of the airplane maximum lift coefficient, the following criterion is proposed to avoid buffet problems:

$$\frac{2.3 \cdot g \cdot W_{cr}}{\frac{\rho \cdot V^2}{2} \cdot S_w} \leq 0.9 \cdot C_{L,\,max}$$

Howe (2000) states on the other that the cruise lift coefficient is limited as follows to avoid buffet problems:

$$C_{L,\,cr} \leq 0.65 \cdot \cos \Lambda_{c/4}$$

and comments that this is derived for a typical clean maximum lift coefficient of about 1.5. Comparing both limits shows that the difference between both expressions is less than 2% despite the higher maximum lift coefficient adopted here. The average of buffet limits is thus taken as the limit in this work.

B.6 Aircraft Direct Operating Costs

Decisions that will strongly influence the cost of both acquisition as well as operation of the aircraft are made in the conceptual and preliminary design phase. To make sensible design choices it is therefore important to take the cost implications of manufacturing and operation of the aircraft into account when deciding the configuration and performance. Aircraft operating costs are usually split into direct and indirect operating costs, where the indirect operating costs are the costs that are not directly related to the aircraft parameters, e.g. the costs associated with marketing and sales expenses, administration, headquarters, overheads, ticket sale, training,.... As indirect operating costs are to a big extent determined by airline management and operational aspects, they are largely outside the control of the aircraft designer. Accordingly, the effects of indirect costs on the selection of aircraft design parameters is usually ignored (Jenkinson et al., 1999, p. 305).

Only direct operating costs will thus be considered here to select the optimum wing planform of the aircraft under consideration. As the interest rates are included in the direct operating cost calculations, the method is sometimes called DOC+I instead of simply DOC. Here the latter is employed throughout the text though. Sometimes, so called cash DOC values are quoted, where aircraft standing charges are omitted from the DOC. According to Jenkinson et al. (1999), this is often done when an aircraft has a fuel efficiency advantage over its competitors but is sold at a slightly higher price or when the bulk of the produced aircraft are leased rather than bought. To allow a comparison between all different aircraft, only complete DOC costs are quoted here. After all, the acquisition price of hydrogen fueled and unconventional aircraft will be higher than that of conventional kerosene fueled aircraft which could play a role in the selection of the final aircraft design point.

First, it is explained in detail which cost contributors are considered in this work and how they are divided into different cost components. Once these are defined, the correlations used to calculate the actual value of the different components are given. Then, the method used to bring the different components back to a common base is explained. After all, some of the components are calculated per flight hour while others are determined on a mission basis.

B.6.1 Direct Operating Costs (DOC)

The direct operating costs cover all the costs associated with flying and direct maintenance. These costs are divided here into three broad headings: standing charges, flight costs and maintenance costs. Below, a brief description of each of these headings is given and for every cost item, the assumptions made throughout this work are stated. A more detailed elaboration of the different components is given in (Jenkinson et al., 1999, p. 306-316) and Roskam (1989c, pp. 80-110).

B.6.1.1 Standing Charges

The standing charges are the proportion of the costs that are not directly linked to the aircraft flight but may be regarded as the 'overhead' on the flight (Jenkinson et al., 1999). Such costs include the depreciation of the capital investment, interest charges and aircraft insurance. Even though the last two items are sometimes ignored in cost methods[29], they are included here and they will be discussed first. After all, not considering these cost contributors would shift the minimum direct operating cost point in the parametric studies of this work, putting less emphasis on the initial aircraft purchase price, which can be a decisive factor.

Insurance Cost

The insurance cost is directly related to the risks involved and the potential for claims following loss. As a lot of factors play a role in the final insurance premium, the insurance cost is hard to estimate. As suggested in Jenkinson et al. (1999) the insurance annual premium is taken as 0.5 % of the aircraft initial price.

Interest Charges

Interest charges are if possible even harder to estimate than insurance cost as they depend on many variables. Additionally, they are often subjected to 'off-set' agreements (Jenkinson et al., 1999). Even though sometimes a part of the previous company profits is invested when financing a new project, it is assumed here that interest accounts for a complete financing of the initial aircraft price. For a 100 % financing, Jenkinson et al. (1999, p. 320) indicates an annual percentage rate of 11 % while in Liebeck et al. (1995) a value of 8 % is used for a 100 % financing. The latter value is retained in this work.

---

[29] They are small compared to the cost of depreciation.

Depreciation

As the aircraft is always maintained to a fully airworthy condition throughout its life, it will have a residual value when sold. As with any capital item, the residual value will reduce as the aircraft ages. The depreciation period depends on the accountancy policy of the airline and the expected evolution of the routes the aircraft will serve. Typically, an aircraft may be considered to be at the end of its useful life after 20-30 years with only a small residual value (Jenkinson et al., 1999). Following Jenkinson et al. (1999, p. 320) a useful life of 20 years is used with a 10 % residual value.

B.6.1.2 Flying costs

This cost element encompasses all the costs which are directly associated with the flight. The crew cost, the fuel and oil usage and the landing and navitational charges are summed to give the total flying costs per hour.

Crew costs

The crew costs include the salaries for the flight and cabin staff. The number of cabin crew members and pilots is determined in section B.2.10, so only the hourly salary needs to be determined to allow the calculation of the crew costs. Two different values were found in the literature for the crew salaries. In this work, the average of both values is used.

Jenkinson et al. (1999) propose 360 USD per (block) hour as a typical cost of a pilot while for the cabin crew a value of 90 USD per hour is recommended. The dollars used are 1989 USD[30]. Liebeck et al. (1995), on the other hand, indicates a value of 78 USD per hour for the cabin crew. The pilot salary however depends on the maximum take-off gross weight [lb] of the aircraft as follows:

$$\frac{USD}{BH} = \left(482 + 0.590 \cdot \frac{W_{TO}}{1000}\right)$$

where BH stands for block hour (see section B.6.3.1).

Fuel and Oil cost

Next to depreciation, fuel costs represent the most significant cost parameter in the design. As this work looks into the future and predictions of fuel costs are hard to make, a wide range of prices is adopted for both fuels. After all, the kerosene price is likely to increase in the future seen the depletion of its resources. The hydrogen price is on the other hand likely to drop as new techniques are developed and as the quantity of hydrogen produced would significantly increase if it were adopted as an aviation fuel. The prices range

---

[30] The different works from which DOC data is used, adopt a different time frame. Whenever data from Jenkinson et al. (1999) is used, the values are given in 1989 dollars, except for maintenance on airframe and engine where 1994 is used as the year of reference. Data from Liebeck et al. (1995) are in 1993 dollars and data from Roskam (1989c) have 1989 as basis. Finally, costs from Lange et al. (1972) a,d Liebeck et al. (1995) are given in 1970 respectively 1993 dollars.

from low values around 0.70 USD per gallon (Jenkinson et al. (1999, p. 320) and Liebeck et al. (1995)) for kerosene up to several dollars. Prices are converted to a price per quantity of energy ([\$/MJ]) to allow a comparison between the different fuels. The lower heating value of the fuel is used in this conversion.

Only the mission fuel is used to determine the fuel cost. The reserve fuel is not included in the calculation. The reserve fuel is assumed to be present after landing the aircraft.

Landing and navigational charges

The landing and navigational charges include the so-called landing fee for the aircraft as well as the fee for traffic control services and ground handling of the baggages and cargo. In this work, the method from Jenkinson et al. (1999) is adopted and a value of 6 USD per metric ton of maximum takeoff gross weight per flight is used as the landing fee. The navigation cost per flight depends on both the range and the takeoff gross weight:

$$\frac{USD}{trip} = \frac{\left(l_{stage}\right)}{5} \cdot \left(\frac{W_{TO}}{50}\right)^{0.5}$$

where the maximum take-off gross weight is in metric tonnes and the stage length l_{stage} in km. Finally, a price of 110 USD per metric ton of payload is used for the ground handling charges for the baggage and payload of the aircraft.

B.6.1.3 Maintenance Costs

Prediction of maintenance costs is complicated by the lack of definition for items to be included under this heading. The attribution of the maintenance overhead burden forms as such the biggest variability in the different standard methods for estimating DOC (Jenkinson et al., 1999, p. 312). Jenkinson et al. recommend therefor to use standardized methods for calculating the maintenance costs as soon as sufficient data is availab.

Maintenance charges include labor and material costs associated with routine inspections, servicing and overhaul (for airframe, engines, avionics, ...) as well as the applied maintenance burden. The maintenance tasks are divided into airframe and engine components. The airframe and engine direct maintenance labor and maintenance material costs are based on equations from Liebeck et al. (1995), which were developed by the Boeing Commercial Airplane Group. The maintenance labor, materials and the applied burden for airframe and engines will be treated consecutively.

Airframe Maintenance Cost

The **airframe maintenance labor cost** is based on the airframe mass W_{af}[31] and has both a flight-cycle (FC) and a flight-hour (FH) component. The equation produces either maintenance - man - hour - per - flight - cycle (MMH/FC) or maintenance - man - hour - per

---

[31] the airframe mass is defined as the manufacturer's empty weight less the dry weight of the engines.

- flight - hour (MMH/FH). Each trip consists of one flight cycle and a variable number of flight hours.

$$\frac{MMH}{FH} = 1.260 + 1.774 \cdot \frac{W_{af}}{10^5} - 0.1071 \cdot \left(\frac{W_{af}}{10^5}\right)^2$$
$$\frac{MMH}{FC} = 1.614 + 0.7227 \cdot \frac{W_{af}}{10^5} + 0.1024 \cdot \left(\frac{W_{af}}{10^5}\right)^2$$

The total maintenance man hours per trip are thus given by:

$$\frac{MMH}{trip} = \frac{MMH}{FH} \cdot \frac{FH}{trip} + \frac{MMH}{FC}$$

These hours are converted to direct labor dollars per trip by multiplying by the direct maintenance labor rate of 25 USD per hour (Liebeck et al., 1995).

The **airframe materials cost** also has a cyclic (MAT/FC) and a flight-hour (MAT/FH) component. Liebeck et al. (1995) gives the following correlations for these components:

$$\frac{MAT}{FH} = 12.39 + 29.80 \cdot \frac{W_{af}}{10^5} + 0.1806 \cdot \left(\frac{W_{af}}{10^5}\right)^2$$
$$\frac{MAT}{FC} = 15.20 + 97.33 \cdot \frac{W_{af}}{10^5} - 2.862 \cdot \left(\frac{W_{af}}{10^5}\right)^2$$

The total material cost per trip is then obtained as follows:

$$\frac{MAT}{trip} = \frac{MAT}{FH} \cdot \frac{FH}{trip} + \frac{MAT}{FC}$$

Following Liebeck et al. (1995), the **Airframe Applied Maintenance Burden (AAMB)** is calculated as a function of the airframe direct maintenance labor cost:

$$\text{AAMB} = 2.0 \cdot \text{Airframe Direct Labor Cost}$$

Engine Maintenance Cost

The scaling equation for the **engine direct maintenance labor** is based on the maximum rated uninstalled sea-level static thrust per engine ($F_{N,SLS}$), in pounds force, the flight hours per trip and the number of engines per aircraft (N_{eng}). In contrast to the airframe, the engine maintenance labor cost is not separated into flight-cycle and flight-hour components.

$$\frac{MMH}{trip} = \left(0.645 + 0.05 \cdot \frac{F_{N,SLS}}{10^4}\right) \cdot \left(0.566 + \frac{0.434}{FH}\right) \cdot FH \cdot N_{eng}$$

The engine direct maintenance labor cost is then calculated by multiplying the MMH/trip by the direct maintenance labor rate which is again taken as 25 USD.

The scaling factor for **engine maintenance material cost** is based on these same parameters:

$$\frac{MAT}{trip} = \left(25 + 18 \cdot \frac{F_N}{10^4}\right) \cdot \left(0.62 + \frac{0.38}{FH}\right) \cdot FH \cdot N_{eng}$$

As for the airframe, the **engine applied maintenance burden** is calculated as a function of the engine direct maintenance cost:

$$\text{EAMB} = 2.0 \cdot \text{Engine Direct Maintenance Labor Cost}$$

All three engine maintenance cost elements are calculated on a per-trip basis and summed to get the total engine maintenance cost.

B.6.2 Aircraft price

The standing charges depend on the price of the total airplane (airframe + engines) and its associated spares. However, commercial aircraft are often not sold on a price-per-pound basis, but rather have a selling price that in essence represents a market-based price (without a real relationship to cost). This makes it very hard to get a good estimate of the aircraft price based on weight considerations (Jenkinson et al., 1999, p. 308-309). To account for this, following Liebeck et al. (1995), the airframe and engine prices quoted below are called study prices. They should be regarded as a 'ball-park' estimate rather than a real price.

Two different methods are utilized to determine the study prices. First, mass-based correlations are adopted as they are easily factored to determine the sensitivity of the DOC to aircraft price. As the hydrogen fuel tanks represent new systems inside the aircraft, the purchase price will namely likely be higher. The study prices obtained from the mass-based correlations are therefor factored for liquid hydrogen fueled aircraft. The factor used is varied over a wide range to analyze its influence on the direct operating cost. In a second step, a more detailed method from Burns (1994) is adopted. This method allows a more detailed investigation of the different contributors to the purchase price and recommendations on how to adapt this method to hydrogen fueled unconventional aircraft are found in Sefain (2005). The main drawback of the method from Burns (1994) is that it requires an estimate of the quantity of aircraft produced and the production rate.

B.6.2.1 Study Prices from correlations

First the different correlations for the airframe study price are detailed. The determination of the engine study price is reported next.

Airframe Study Price

Two different correlations are used to determine the airframe study price (Liebeck et al. (1995) and Roskam (1989c, p. 303). The first airframe price correlation was developed from McDonnell Douglas Corporations commercial transport databases through a power curve fit of airframe study prices (ASP) versus airframe weight (W_{af} $[lb]$):

$$ASP = 0.7822 \cdot \left(\frac{W_{af}}{1000}\right)^{0.8937}$$

The ASP is given in millions of US dollars.

The ASP from Roskam (1989c) on the other hand depends on the takeoff weight instead of the airframe weight. The correlation is based on a regression analysis which yielded the following trendline:

$$\log_{10} ASP = 3.3191 + 0.8043 \cdot \log_{10} W_{TO}$$

Engine Study Price

Estimating the price of the engine is always regarded as a difficult issue because of the many variables involved. This will especially be true for the ultra high bypass ratio and intercooled turbofans under consideration. Volders & Slingerland (2003) give the following correlation for the engine study price ESP:

$$ESP = 25482 \cdot F_N + 276334$$

where the net thrust is given in kN and the price in 2004 dollars. In Lange et al. (1972), on the other hand, a distinction is made between engines with a takeoff net thrust less than 55 klb for which:

$$ESP = 1357 \cdot F_N^{0.62}$$

if the thrust is more than 55 klb however, the following relation needs to be applied:

$$ESP = 222 \cdot F_N^{0.79}$$

The net thrust is in both equations given in klb and the prices are in 1970 dollars.

B.6.2.2 Study Price from Burns

In Burns (1994), the total aircraft unit cost and direct operating costs for new development aircraft are estimated by summing all costs associated with purchasing, operating and supporting the aircraft throughout development and production. Costs are calculated based on a fixed production quantity and production rate as well as on an average utilization per year. The method results in a value for the life cycle costs (LCC) for the aircraft, that is subsequently converted into an aircraft unit acquisition cost from which the equivalent airframe and engine study price are subsequently determined.

The life cycle cost includes all costs starting with research and development, over testing and evaluation, acquisition, operation and support down to retirement and decommissioning (Burns, 1994).

$$LCC = C_{DDTE} + C_{acq} + C_{oper} + C_{disp}$$

where C_{DDTE} is the price of design, development, test and evaluation, C_{acq} is the acquisition cost, C_{oper} the operations and support cost and C_{disp} the disposal cost. The different contributions to the LCC are detailed below. All correlations given are derived from Burns (1994), unless otherwise stated.

Engineering hours

The total airframe engineering hours for development E_{HD} and production E_{HP} can be estimated as:

$$EH_D = 0.066 \cdot W_{af}^{0.796} \cdot v_{max}^{1.538} \cdot N_{ac,D}^{0.183} \cdot CF_{TF} \cdot CF_{AMC} \quad \text{(B.49)}$$

$$EH_P = 0.066 \cdot W_{af}^{0.796} \cdot v_{max}^{1.538} \cdot \left(N_{ac,D} + N_{ac,P}\right)^{0.183} \cdot CF_{TF} \cdot CF_{AMC} - EH_D \quad \text{(B.50)}$$

where $N_{ac,D}$ is the number of prototypes used in the development phase, $N_{ac,P}$ is the number of production aircraft. v_{max} is the maximum speed at the best altitude. CF_{TF} is a judgement factor to account for advance technology features. CF_{AMC} is a similar factor for cost of advanced materials relative to conventional metal designs. Both factors are given in Table B.15 for the different types of aircraft designed in this work. Their values were either derived from Burns (1994) or from Sefain (2005, pp. 199-218) where suggestions are made for values adapted to different technology levels and unconventional as well as hydrogen-fueled aircraft. W_{af} is the airframe unit mass (in lbs). It can be estimated from the empty weight as:

$$W_{af} = 0.431 \cdot W_e^{1.05375}$$

To convert the engineering hours to cost, a rate E_{rate} of \$95 per hour is used:

$$C_{AE,D} = EH_D \cdot E_{rate} \cdot CF_s \qquad C_{AE,P} = EH_P \cdot E_{rate} \cdot CF_s$$

where CF_s is a judgement factor for the cost of security. Burns (1994) recommends a value of 1 for commercial aircraft.

Development support

The development support cost C_{DSC} consists out of all the non-recurring manufacturing related engineering design costs during the development, test and evaluation phase. It includes the manufacturing and materials costs to support mock ups, test components, …

$$C_{DSC} = 0.0356 \cdot W_{af}^{0.903} \cdot v_{max}^{1.93} \cdot N_{ac,D}^{0.346} \cdot CF_{TF} \cdot CF_s$$

Flight test operations

Flight test activity costs C_{FT} include all costs incurred to complete the flight test, except the cost of the actual flight test aircraft itself. C_{FT} can be estimated from

$$C_{FT} = 0.00558 \cdot W_{af}^{1.19} \cdot v_{max}^{1.401} \cdot CF_{TT} \cdot CF_s$$

where CF_{TT} is a judgement factor for advanced technology testing. Its value can be found in Table B.15.

Tooling

The tooling cost for development and production includes the hours required for tool design, fabrication, ... The hours depend on production rate and materials used. According to Burns (1994), they are determined as:

$$\begin{aligned} TH_D &= 5.083 \cdot W_{af}^{0.768} \cdot v_{max}^{0.899} \cdot N_{ac,D}^{0.18} \cdot PR^{0.068} \cdot CF_{AMC} && \text{(B.51)} \\ TH_P &= 5.083 \cdot W_{af}^{0.768} \cdot v_{max}^{0.899} \cdot \left(N_{ac,D} + N_{ac,P}\right)^{0.18} \cdot PR^{0.068} \cdot CF_{AMC} - TH_D && \text{(B.52)} \end{aligned}$$

where TH_D are the tooling hours for development, TH_P the tooling hours for production and PR the production rate in aircraft per month.

The tooling cost is then determined from:

$$\begin{aligned} C_{T,D} &= TH_D \cdot T_{rate} \cdot CF_s \\ C_{T,P} &= TH_P \cdot T_{rate} \cdot CF_s \end{aligned}$$

where T_{rate} is the tooling hourly rate and is taken as 80$ per hour.

Manufacturing labour

Manufacturing labour encompasses the cost for machining, fabrication and assembly of the major structures and is given by the following equations

$$\begin{aligned} MH_D &= 43.61 \cdot W_{af}^{0.76} \cdot v_{max}^{0.549} \cdot N_{ac,D}^{0.554} \cdot CF_{AMC} && \text{(B.53)} \\ MH_P &= 43.61 \cdot W_{af}^{0.76} \cdot v_{max}^{0.549} \cdot \left(N_{ac,D} + N_{ac,P}\right)^{0.554} \cdot CF_{AMC} - MH_D && \text{(B.54)} \end{aligned}$$

where MH_D are the manufacturing labour hours for development and MH_P the hours for production. The manufacturing labour cost is then determined using an hourly rate:

$$\begin{aligned} C_{M,D} &= MH_D \cdot M_{rate} \cdot CF_s \\ C_{M,P} &= MH_P \cdot M_{rate} \cdot CF_s \end{aligned}$$

where M_{rate} is the manufacturing hourly labour rate and is taken as 70$ per hour.

Quality control

Quality control involves the inspection of fabricated and purchased parts, subassemblies and assembled components. The quality control cost needed for development C_{QD} and production C_{QP} can be estimated with:

$$\begin{aligned} C_{Q,D} &= 0.13 \cdot MH_D \cdot Q_{rate} \\ C_{Q,P} &= 0.13 \cdot MH_P \cdot Q_{rate} \end{aligned}$$

where Q_{rate} is the hourly rate for quality control (80$).

Manufacturing material and equipment

The manufacturing material and equipment cost covers all the raw material and hardware needed for constructing and assembling the airframe. As both engines and avionics costs are covered elsewhere, they are not comprised in this cost item. As for several of the previously covered cost items, a distinction is made between the cost of manufacturing material and equipment for the development program $C_{MM,D}$ and the production phase $C_{MM,P}$.

$$C_{MM,D} = 96.667 \cdot W_{af}^{0.692} \cdot v_{max}^{0.639} \cdot N_{ac,D}^{0.803} \cdot CF_{AMC} \cdot CF_{LO} \tag{B.55}$$

$$C_{MM,P} = 96.667 \cdot W_{af}^{0.692} \cdot v_{max}^{0.639} \cdot \left(N_{ac,D} + N_{ac,P}\right)^{0.803} \cdot CF_{AMC} \cdot CF_{LO} - C_{MM,D} \tag{B.56}$$

where CF_{LO} is a factor to account for low observable materials. For conventional aircraft the factor is set to 1.0 (Burns, 1994).

Engine

The engine costs C_{eng}, including initial engine development costs can be estimated as:

$$C_{eng} = 121.5 \cdot F_N^{1.00161} \cdot N_{eng} \cdot CF_{adv}$$

where F_N is the sea level maximum thrust (lbs), N_{eng} the number of engines and CF_{adv} a factor to account for a higher engine cost for advanced engine concepts. It is introduced following Sefain (2005, p. 204), where a factor of 1.10 is introduced for hydrogen fueled engines. The factor is judged to account for the increased research and development and is based on past trends of engine cost increases (Sefain, 2005).

Avionics

Avionics cost C_{av} depends on the type of equipment used. Uninstalled avionics are estimated as:

$$C_{av} = 3950 \cdot W_{av} \cdot CF_{unc}$$

where W_{av} is the avionics mass in lbs and CF_{unc} is a judgement factor to account for the increased cost in avionics for the unconventional aircraft configuration, as introduced in Sefain (2005). As a more sophisticated avionics system will most likely be required for the twin fuselage configuration it is set to 1.10, as suggested for unconventional configurations in Sefain (2005).

Interior

Interior costs C_{int} includes seats, ceiling and flooring material, lavatories, ...For commercial production jet transport aircraftis the interior cost given by the following equation:

$$C_{int} = 2000 \cdot N_{pax} \cdot N_{ac,P}$$

where N_{pax} is the number of passengers per aircraft.

Total development and production cost

The total development and production costs are given by summation of the previous items.

$$C_{DDTE} = C_{AE,D} + C_{DSC} + C_{FT} + C_{T,D} + C_{M,D} + C_{Q,D} + C_{MM,D} + C_{eng} + C_{av} \quad \text{(B.57)}$$

$$C_{prod} = C_{AE,P} + C_{T,P} + C_{M,P} + C_{Q,P} + C_{MM,P} + C_{eng} + C_{av} + C_{int} \quad \text{(B.58)}$$

Acquisition unit cost

Finally, the acquisition unit cost can be estimated as:

$$C_{UA} = \left(\frac{C_{DDTE} + C_{prod}}{N_{ac,D} + N_{ac,P}} \right) \quad \text{(B.59)}$$

Here the acquisition unit cost is converted into the airframe and engine study prices for estimating the total DOC in the following way:

$$\begin{aligned} ASP &= C_{UA} - C_{eng} \\ ESP &= C_{eng} / N_{eng} \end{aligned}$$

Judgement factors

For the calculation of many cost items, judgement factors were introduced to account for advanced materials, unconventional configurations, ...The values adopted in this work for these variables are given in Table B.15. They are derived following guidelines from both Burns (1994) and Sefain (2005). The latter work was mainly used for the unconventional configurations. When two values are given in a single cell of the table, the value on the left stands for the current timeframe, whereas the value on the right is used for projections into the future.

As shown by the table, the advanced materials cost factor goes up when switching to hydrogen fuel to account for the tanks and hydrogen compatibility of materials. It also goes up over time, as it is foreseen that more advanced material will be used as time progresses. The unconventional configurations are also subjected to a higher fraction of advanced materials. Similar trends apply for the advanced technology features (CF_{TF}) and the testing of advanced technology and materials (CF_{TT}).

Table B.15. Judgement factor for the different cost items.

	Kerosene		LH_2	
factor	**conventional**	**unconventional**	**conventional**	**unconventional**
CF_{AMC}	1.00/1.08	1.10 /1.20	1.08/1.20	1.20/1.25
CF_{TF}	0.90	1.00	1.00	1.10/1.20
CF_{TT}	0.85	1.15	1.25	1.40/1.50
CF_{adv}	1.00	1.05	1.10/1.15	1.10/1.15
CF_{unc}	1.00	1.10	1.00	1.10

B.6.2.3 Cost of Spares

The initial aircraft price used in the evaluation of depreciation will usually include an allowance for the capital required to provide for spares holding. Therefore

aircraft initial price = factory cost of the aircraft + spares cost

Two references were found containing data on the cost of the spares. In Jenkinson et al. (1999), it is indicated to use 10 % of the airframe price and 30 % of the engine price. Liebeck et al. (1995) on the other hand gives values of 6 % of the airframe price and 23 % of the engine price. In this work, an average of both values is used:

8 % of the airframe study price
27% of the engine study price

B.6.3 Cost Parameters

Depreciation, interest and insurance are annual costs while the maintenance costs are calculated per trip and the flying cost per hour of flight. All the different costs thus have to be brought back to a common base. Here, all costs are converted to hourly costs before summing them. In order to do that, the block time of the flight as well as the annual utilization of the airplane have to be defined. Both concepts are explained in the first paragraph of this section. Then, as several correlations are based on a different references, the cost escalation factor used to convert between the different years is explained.

B.6.3.1 Utilization and block time

Long-range transport aircraft usually have a fairly high annual utilization (Torenbeek, 1982). In the Cryoplane study an utilization of 550 flights per year with a range of 4000 nm was set forth for the DOC evaluation of the long range missions (Oelkers et al. (2000a) and Oelkers et al. (2000b)). Both values are adopted here too.

To convert the costs per flight cycle and the costs per hour to a common basis, the mission block time is used (Jenkinson et al. (1999) and Liebeck et al. (1995)). The block time is the total time spent from starting the engines till turning them off completely. The block time t_b is, according to Jenkinson et al. (1999, p. 322), given by:

$$t_b = t_{gm} + t_{cl} + t_d + t_{cr} + t_{am} \tag{B.60}$$

where t_{gm} is the ground maneuver time including one minute for take-off. It is taken as 0.25 hr. The time to climb t_{cl}, which includes acceleration from take-off speed to climb speed is determined from the mission profile given in Brewer (1991, pp. 411-414). t_d is the time required to descend including deceleration to approach speed. It is calculated based on a cabin pressurization rate of 300 fpm and a cruise cabin altitude[32] of 8000 ft (Jenkinson et al., 1999). t_{am} is the time for air maneuvers (no credit for distance) which is taken as 0.1 hr. Finally the cruise time is calculated as (Jenkinson et al., 1999):

$$t_{cr} = \frac{R + K_a + 20 - (R_{cl} + R_d)}{v_{cr}}$$

where all distances are given in statute miles (1.609 km). R is the range or trip distance, R_{cl} and R_d are the distance to climb and to descend respectively. K_a is an airway distance increment which is according to Jenkinson et al. (1999) taken as 2% of the trip distance when the trip distance is higher than 1400 statute miles. As recommended in Jenkinson et al. (1999) all DOC calculations assume a zero wind speed and standard temperature.

B.6.3.2 Cost Escalation Factor

As the different correlations for the cost items use different years they need to be converted to a common base to take inflation into account. All prices are converted here to 2008 values as further data is not available at the time of writing. In order to convert data from one year to another, a so-called Cost Escalation Factor (CEF) needs to be defined. Following (Roskam, 1989c, pp. 19-20), the Consumer Price Index (CPI) is taken in this work as the CEF. The CEF's for the different years used in the correlations can be found in Table B.16. They were derived from reference USBoLS (2009).

Table B.16. Values for the Consumer Price Index of different years, derived from USBoLS (2009).

Year	CEF
1970	0.205
1989	0.656
1993	0.765
1994	0.784
2004	1.000
2008	1.140

---

[32] The cabin altitude is the pressure altitude to which the cabin pressure is held. It is a compromise between passenger comfort (volumetric oxygen content) and fuselage mass.

APPENDIX C

Turbofan Design and Performance Analysis Tool

A library of aero-engine components has been developed to enable the simulation of the different turbofan cycles investigated in this work on an equal basis. The library is implemented in the high-level object-oriented language Ecosimpro^{TM}(Empresarios Agrupados, 2009). An object-oriented environment was chosen due to the modular nature of the gas turbine engine. Creating an object for each of the physical components of the engine namely enables the quick buildup of the particular engine configuration under consideration. The different objects only exchange information through the interface, named ports in Ecosimpro^{TM}. The methods used to calculate the performance of each component are thus hidden for the other components, which is called encapsulation. This enables the gradual extension and development of the software. For specific investigations, a more sophisticated and/or detailed model of one object could be introduced. This is further simplified as the objects can inherit information from previously developed models. Finally, object-oriented modeling was preferred because of its polymorphism, which allows the coexistence of different models with the same name, that can be called depending on the context of the particular simulation.

Besides these general advantages of any object-oriented programming environment, Ecosimpro has additional interesting features. The "tool" namely looks after the complex programming and mathematical aspects of the problem, which allows the "developer" to concentrate on the phenomena whose physics he can describe completely freely. This is particularly useful for the development of a gas turbine performance analysis tool (Kurzke, 1992). As the tool furthermore offers wizards for boundary condition selections and several more advanced features, Ecosimpro^{TM} is retained here for the development of the gas turbine components library. In the VIVACE project, Ecosimpro^{TM} is also chosen for the development of a similar but far more detailed performance tool, called PROOSIS (Alexiou & Mathioudakis (2005) and Alexiou et al. (2007)).

As the thermodynamic model utilized to describe the thermodynamic fluid properties is a critical part of any gas turbine performance tool, the model adopted here is described in the first section of this appendix. A second section then tackles the ports through which those fluid properties are passed on from one component to another. The component blocks in which the models for each gas turbine component are stored are introduced in a third section. After all components are described, the boundary conditions to be specified in the model of a complete gas turbine are explained and the component maps used in the off-design calculations in the work are given. Finally, the gas path analysis is presented.

C.1 Thermodynamic Fluid properties

Accurate cycle calculations require a good description of the gas properties, which is even more the case for this work. After all engines using hydrogen and kerosene will be modeled and the difference in engine performance is a consequence of the dissimilar thermodynamic properties of hydrogen combustion gases. Here, the working fluid in the different components is assumed to behave like a half ideal gas as proposed in Kurzke (1992), Kurzke (2004b) and RTO-AVT (2007). The specific heat, the enthalpy, the entropy and the gas constant are function of temperature and gas composition only, but not dependent from pressure.

The gas properties and the temperature increase due to combustion are stored in tables, created using the computer code CEA, described in Gordon & McBride (1994a) and Gordon & McBride (1994b). As set forth in Kurzke (2004b), the specific heat, enthalpy, entropy and gas constants are calculated considering only H_2O and CO_2 as combustion products. For the calculation of the temperature increase due to combustion, however, all sorts of combustion products as well as the pressure influence are considered. The effects of dissociation on the combustion temperature increase are thus taken into account. The effects of CO, NO_X and unburned hydrocarbons are on the other hand neglected, following (Kurzke, 2004b, p. 104).

For both kerosene and hydrogen, the gas constant is stored in a table in function of the fuel-to-air ratio (FAR), The specific heat, the enthalpy and the entropy function are stored in function of total temperature and FAR. The entropy function Ψ^1 is defined as (Jackson (2004) and Kurzke (2004b)):

$$\Psi(T, FAR) = \int_{T_{ref}}^{T} \frac{c_p(T, FAR)}{T} dT \tag{C.1}$$

As for enthalpy calculations, the reference can be arbitrarily selected. The calculations of isentropic compression and expansion processes use namely only differences of entropy function values, not absolute values themselves. An isentropic change of state between pressures p_{t2} and p_{t1} is then given by the following equation:

$$\Psi(T_{t,2}) - \Psi(T_{t,1}) = R \cdot \ln\left(\frac{p_{t,2}}{p_{t,1}}\right) \tag{C.2}$$

---

[1] Although both the enthalpy and the entropy function depend on the temperature of the fluid as well as the fuel-to-air ratio, from here on the dependency on the fuel-to-air ratio is not explicitly mentioned anymore. The functions are written with only the temperature as an argument as the fuel to air ratio does not vary within the component (except for the combustion chamber). This is done to simplify the writing.

where R is the gas constant.

In the calculations, the use of the specific heat is avoided as much as possible. The enthalpy and entropy function are used to the fullest to increase the accuracy of the calculations. As the specific heat allows a quick comparison of the thermodynamic influence of both fuels, Figure C.1 nonetheless shows the specific heat of air and combustion gases for both fuels. The fuel to air ratios on the plot are chosen so that the energy added by the fuel is roughly similar for both fuels. As the lower heating value of hydrogen is roughly 3 times bigger than that of kerosene, a FAR of approximately a third of the FAR for kerosene leads to a similar 'energy injection' from the fuel.

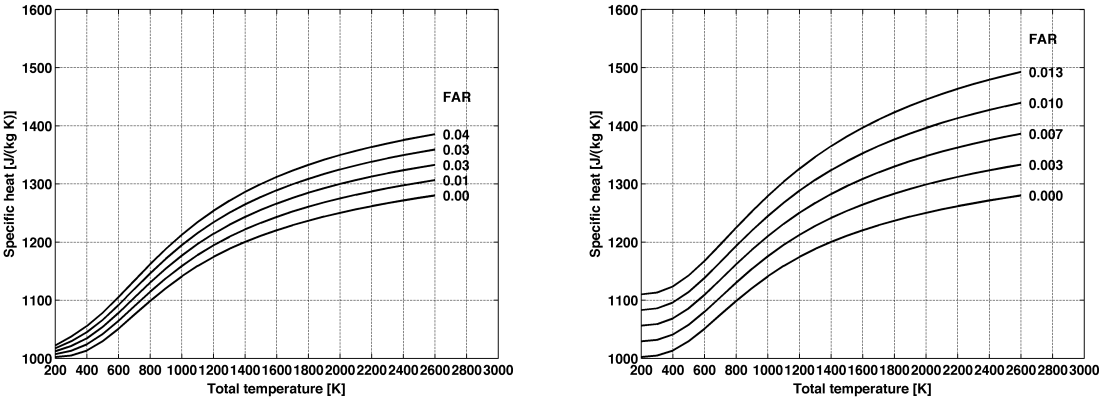

(a) kerosene (b) hydrogen

Figure C.1. Specific heat in function of temperature for different fuel to air ratios.

C.2 Ports

In an object-oriented environment, the building blocks (components) only exchange data through the connected ports, which serve as an interface. For the gas turbine design and performance analysis tool a port is created for gas (air and combustion gases, for fuel, for forces, for shafts and two feedback ports. Their properties are described below.

The **gas** port contains the thermodynamic properties of the gas entering or exiting the components. The port passes the following properties on:

- the mass flow rate $\dot{m}$
- the total pressure p_t
- the total temperature T_t
- the enthalpy of the fluid h_t
- the fuel to air ratio FAR

The port is modeled so that temperature and enthalpy are linked through the tables, explained in the previous section. The port furthermore ensures that incoming mass flow rates are added to simplify the modeling of the 'injection' of the cooling air back into the main flow.

The **fuel** port contains the thermodynamic properties of the fuel. It holds the fuel flow, and the fuel lower heating value.

The **shaft** port is used to connect compressor and turbines. It holds the mechanical power of the shaft P_m and the rotational speed N_s.

The **force** port passes the force and the mass flow on to the monitor. It is used to pass the ram drag on from the inlet to the monitor. The thrust from the nozzles is also communicated to the monitor.

The final two ports are feedback ports used in the modeling of some specific concept. The **temperature** port is used to pass the temperature from the combustion chamber, the outlet of the nozzle guide vanes, . . . back to the cooling air component. After all, this information is needed for the calculation of the amount of cooling air needed to keep the turbine metal temperature to a specified limit. The **cooling air fraction** port passes on the cooling air fractions to the turbines to adjust the polytropic efficiency of the turbine to the amount of cooling air needed. The losses generated by injecting the cooling air are namely estimated through a simple model. This is explained in detail in section C.3.9.

C.3 Component Building blocks

Below, a brief description of the main building blocks in the gas turbine component library is given. They are shown on Figure C.2. Only the components used in this work are shown and commented upon. Several other components were also developed for specific studies outside the scope of this work (see for instance Rayee et al. (2008) and Verstraete et al. (2007)).

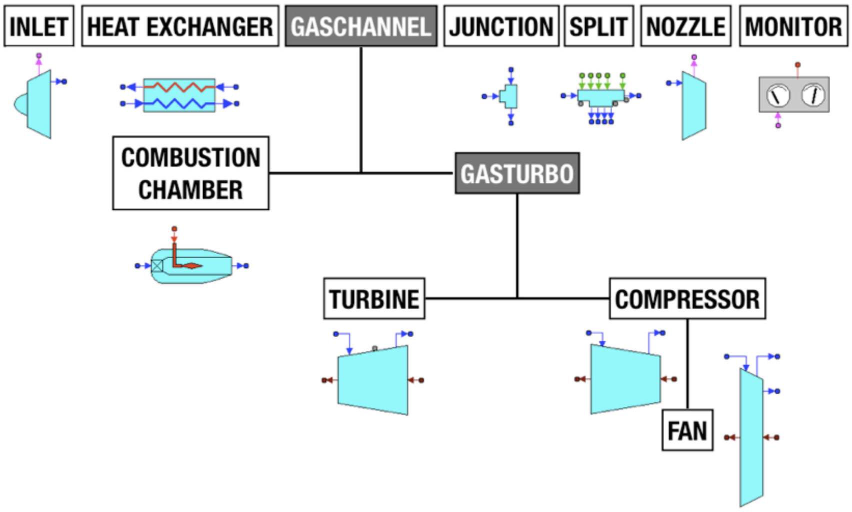

Figure C.2. The main components of the developed library.

The figure also shows two abstract components: gaschannel and gasturbo. They store methods common to other components and are used as 'parents' from whom the 'children' inherit the methods. The gaschannel component for instance holds the definition of the pressure ratio, whereas the definition of corrected speed and mass flow rate are defined in the gasturbo component.

C.3.1 Inlet

The inlet component converts the flight Mach number and altitude, which are boundary conditions to the simulations to a total temperature and pressure. The atmosphere is simulated as the international standard atmosphere after Eshelby (2000). The total temperature $T_{t,out}$ is determined through an inverse interpolation of the enthalpy table from the atmospheric temperature T_a and the flight Mach number M,

$$h(T_{t,out}) = h(T_{t,a}) + \frac{M^2}{2} \cdot \left(\gamma \cdot R \cdot T_a\right)$$

The entropy function is on the other hand used to determine the total pressure for the flight conditions under investigation:

$$\Psi(T_{t,out}) = \Psi(T_{t,a}) + R \cdot \ln \frac{p_{t,out}}{p_a}$$

As the real inlet can be considered as adiabatic but not reversible, the ram recovery is introduced to account for viscous friction pressure losses. The inlet ram recovery or pressure recovery is defined as:

$$RR = \frac{p_{t,out}}{p_{t,in}} \tag{C.3}$$

For design point calculations it is set as input to the routine. For off-design calculations, the ramrecovery can either be kept constant or varied in function of flight Mach number and relative corrected flow which is defined as

$$\left(\frac{\dot{m} \cdot \sqrt{T_t}}{p_t}\right)_{rel} = \frac{\left(\frac{\dot{m} \cdot \sqrt{T_t}}{p_t}\right)}{\left(\frac{\dot{m} \cdot \sqrt{T_t}}{p_t}\right)_{DP}}$$

where DP denotes the design point. The off-design variation of the ramrecovery is shown on Figure C.3 for 3 different Mach numbers representative of take-off, climb and cruise.

Finally, the inlet momentum drag is determined as

$$F_{ram} = -\dot{m}_{in} \cdot v_a \tag{C.4}$$

where v_a is the flight speed of the aircraft. The ram drag is passed on to the monitor through a force port.

C.3.2 Compressor

The design point performance of the compressor is calculated from the pressure ratio and the efficiency, either polytropic or isentropic, which are input to the simulations.

$$\pi = \frac{p_{t,2}}{p_{t,1}} \tag{C.5}$$

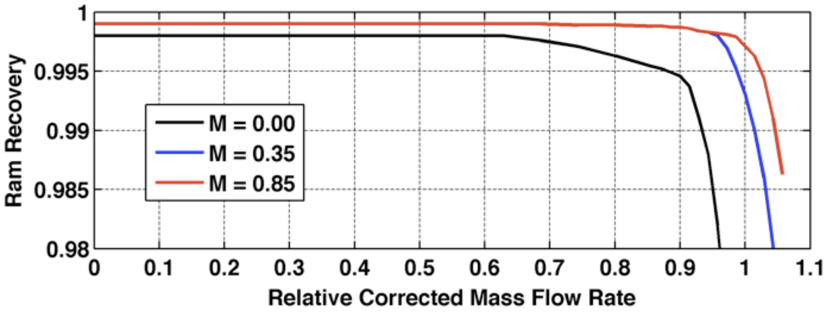

Figure C.3. The off-design variation of inlet ram recovery, derived from Jackson (2004, Fig. 2.3.1).

$$\eta_{is} = \frac{h(T_{t,2_{is}}) - h(T_{t,1})}{h(T_{t,2}) - h(T_{t,1})} \tag{C.6}$$

$$\eta_{pol} = \frac{R \cdot \ln \pi}{\Psi(T_{t,2}) - \Psi(T_{t,1})} \tag{C.7}$$

where the isentropic outlet temperature is defined as:

$$\Psi(T_{t,2_{is}}) - \Psi(T_{t,1}) = R \cdot \ln \pi$$

For off-design compressor calculations, the compressor characteristics are used. In order to do so, the relative corrected speed off the design point needs to be specified together with the β variable (amongst others Jackson (2004), Kurzke (2004b), Ramsden (2004a) and Walsh & Fletcher (2004)). The relative corrected speed is defined as

$$\left(\frac{N}{\sqrt{T_t}}\right)_{rel} = \frac{\left(\frac{N}{\sqrt{T_t}}\right)}{\left(\frac{N}{\sqrt{T_t}}\right)_{DP}}$$

β lines on the other hand are employed to facilitate loading a compressor map into an off-design performance computer model. They are arbitrary lines, drawn approximately even spaced and usually parallel to the surge line (Walsh & Fletcher, 2004). Figure C.4 shows β-lines on the fan map. They are given as black dashed lines. The black full lines are lines of relative corrected speed whereas the surge line is given as a thick blue line on the figure. Lines of constant isentropic efficiency are on the other hand indicated as red dashed lines. As the β-lines are useful to store the compressor maps on the computer but have no physical meaning, they are omitted on all other component map plots in this work.

The map of Figure C.4 is shown in normalized form. All values shown are given relative to their design point value, which is for this figure taken at a relative corrected speed of 1.0 and a β of 0.5. For this point the relative pressure ratio and relative corrected mass flow rate are thus 1.0. A normalized form is chosen here as the design point values for pressure ratio, corrected mass flow and efficiency are used to scale the turbomachinery maps for

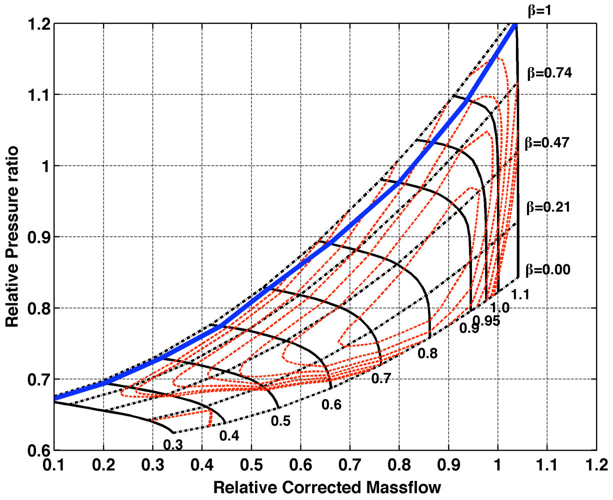

Figure C.4. The β lines for the fan map.

each specific design. This is done by using scaling factors SF:

$$
\begin{aligned}
\pi &= SF_{\pi} \cdot \left(\pi_{map} - 1\right) + 1 && \text{(C.8)} \\
\eta_{is} &= SF_{\eta} \cdot \eta_{is,\,map} && \text{(C.9)} \\
\frac{\dot{m} \cdot \sqrt{T_t}}{p_t} &= SF_{\frac{\dot{m} \cdot \sqrt{T_t}}{p_t}} \cdot \left(\frac{\dot{m} \cdot \sqrt{T_t}}{p_t}\right)_{map} && \text{(C.10)}
\end{aligned}
$$

where the subscript *map* denotes the values read in the map at the relative corrected speed and β under investigation. The scaling factors are determined in the design point calculations and the maps are adjusted using these constant factors during off-design.

In Ecosimpro, the turbomachinery characteristic is stored in 3 different tables. The first table tabulates the corrected mass flow rate in function of corrected speed and β. The second table holds the values for pressure ratio whereas the third stores the isentropic efficiency in function of the same variables. For the compressor a fourth table is added to pass the surge line information to the cycle deck. The surge pressure ratio is stored in function of the corrected mass flow rate. Figure C.5 gives a graphical representation of the table for pressure ratio and efficiency of the HP compressor. The x values on both subfigures are the relative corrected speeds whereas the y values are the β lines. The maps used in this work for the different components are described in section C.4.2.

C.3.3 Fan

Fans require a slightly different treatment from other compressors because they give a larger pressure rise at the tip than at the root. This effect stems from the blade speed which is much lower at the hub of the fan than at the tip. Especially for large civil turbofan engines, a set of characteristics is normally required for each stream. Multiple characteristics are needed which are coupled to the set of characteristics of the other stream

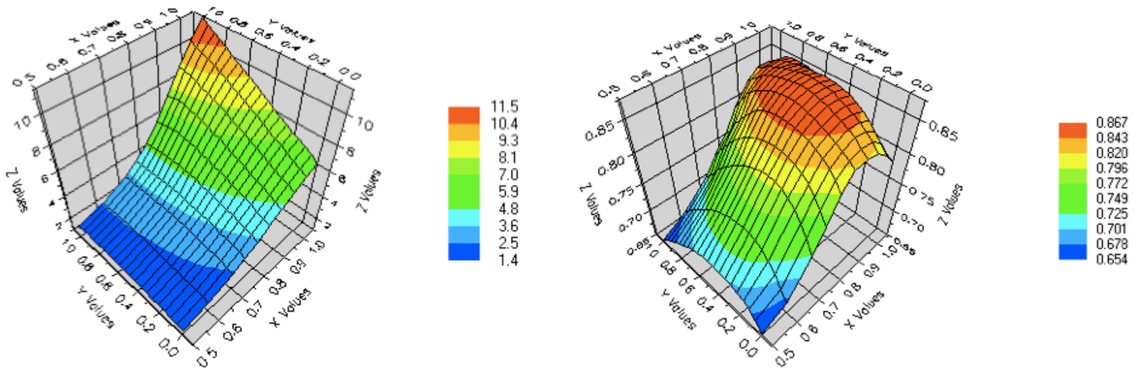

(a) Pressure ratio (b) Isentropic efficiency

Figure C.5. HP compressor pressure ratio and isentropic efficiency as stored in Ecosimpro^{TM}.

by common values of speed and bypass ratio (Jackson, 2004). As Jackson (2004) indicates, simplified assumptions can be made in early project stages. Kurzke (1992, p. 144) for instance proposes the use of one single map as adequate for high bypass ratio turbofan without booster stages. The data for the core stream are simply scaled from the map of the outer part using ratio's that are fixed by imposing pressure ratio's and efficiencies for both streams in the design point calculation. The pressure ratio and isentropic efficiency of the core are then calculated as:

$$\pi_{core} = 1 + \left(\pi_{byp} - 1\right) \cdot \left(\frac{\pi_{core} - 1}{\pi_{byp} - 1}\right)_{des} \tag{C.11}$$

$$\eta_{core} = \eta_{byp} * \left(\frac{\eta_{core}}{\eta_{byp}}\right)_{des} \tag{C.12}$$

As only a limited amount of fan maps is available from open literature, this approach is adopted here too.

The bypass ratio is finally fixed in design point calculations but is allowed to vary in off-design as needed for the compressor-turbine matching.

$$BPR = \frac{\dot{m}_{byp}}{\dot{m}_{core}}$$

C.3.4 Combustion chamber

In design point calculations, the combustion chamber efficiency and the pressure drop are imposed. The efficiency is defined as:

$$\eta_{cc} = \frac{\left(\dot{m}_a + \dot{m}_f\right) \cdot h(T_{t,2}) - \dot{m}_a \cdot h(T_{t,1})}{\dot{m}_f \cdot LHV} \tag{C.13}$$

where LHV is the lower heating value of the fuel. $\dot{m}_a$ represents the airflow rate entering the combustion chamber, $\dot{m}_f$ gives the fuelflow rate.

Off-design calculations on the other hand use the pressure loss factor PLF and the combustion chamber loading Θ_{300} to determine the pressure loss and the efficiency respectively.

$$\begin{aligned} \frac{p_{t,in} - p_{t,out}}{p_{t,in}} &= 1.49 \cdot PLF \cdot \left(\frac{\dot{m}_{in} \cdot \sqrt{T_{t,in}}}{A_{in} \cdot p_{t,in}} \right)^2 && \text{(C.14)} \\ \Theta_{300} &= \frac{p_{t,in}^{1.75} \cdot V_{cc} \cdot e^{T_{t,in}/300}}{\dot{m}_{in}} && \text{(C.15)} \end{aligned}$$

where the pressure loss factor is composed of an aerodynamic (cold) loss and a hot loss due to the combustion temperature rise (Jackson, 2004, pp. 22-24):

$$PLF = 40 + 2.4 \cdot \left(\frac{T_{t,out}}{T_{t,in}} - 1 \right)$$

The design point is again used to scale the geometry of the combustion chamber. The volume V_{cc} and inlet section of the combustion chamber A_{in} are then held constant for off-design calculations and the efficiency and pressure loss vary according to the flow conditions. Evolution of combustion chamber efficiency with loading is found in Jackson (2004) and Rollin (2003). The curves from Jackson (2004) are adopted here.

C.3.5 Turbine

The turbine is modeled in the same way a compressor with regards to scaling of the maps. The selection of the correct turbine maps is however less critical for the correct representation of engine off-design than compressor maps as the turbine is usually choked over most of the operating domain of the engine, which fixes the operating line of the turbine to a single point on the turbine map. Similar to the compressor maps, the turbine maps are specified as a set of 3 tables. The corrected flow, the turbine basic uncooled polytropic efficiency and the expansion ratio are stored in function of corrected speed and β.

For the design point, only the basic uncooled polytropic efficiency needs to be specified. The expansion ratio is determined from the power required by the compressor(s) that are driven by the turbine. Design point values are used to scale the maps for the off-design calculation.

The polytropic efficiency of the turbine, read from the scaled map and called here basic uncooled efficiency is corrected to account for the mixing pressure loss from discharging the coolant flow to the mainstream. According to Horlock et al. (2001), this pressure loss can be modeled as either an additional pressure drop, as an efficiency loss converted from the pressure loss, or as a combustion chamber pressure loss resulting in virtually identical performance outcomes. Here, the pressure drop is converted into an efficiency loss for the turbine through the following equation (Horlock et al., 2001).

$$\frac{\Delta\eta_t}{\eta_t} = -0.125 \cdot \psi \tag{C.16}$$

with the coolant flow fraction ψ is determined as specified in section C.3.9. This method is preferred here over the more complex method proposed in Wilcock et al. (2005) and Young & Wilcock (2002b) for its simplicity and as it avoids additional assumptions on where the cooling air is injected. After all, cooling air injected in the leading edge region will have a different effect on efficiency than cooling air injected on the pressure or suction surface for instance (Kurzke (2003) and Walsh & Fletcher (2004)).

C.3.6 Nozzle

Depending on the flight conditions and engine rating, the propelling nozzles of the engine are either choked or adapted (as only convergent nozzles are considered here seen the envisaged application). When the nozzle is choked, the outlet flow is sonic and the pressure can not adapt to the ambient conditions. If the nozzle pressure ratio drops below a critical value however, the nozzle unchokes and the pressure at outlet is equal to the ambient pressure. The Mach number at the nozzle outlet is as a consequence less than one.

As suggested in Jackson (2004) and Kurzke (2004b), the nozzle is modeled as an ideal (isentropic) one-dimensional flow device. Corrections to the ideal case are then applied through flow and thrust coefficients, which account for losses due to boundary layer growth, pressure and temperature profiles and the nozzle shape. The discharge or flow coefficient is defined as:

$$C_{dis} = \frac{A_{out,eff}}{A_{out}}$$

and is consistent with isentropic flow calculations (Jackson, 2004, p. 38). The thrust coefficient C_F on the other hand, accounts for the loss in thrust due to the nozzle losses and is assumed to apply only to the velocity term of the gross thrust (Kurzke, 2004b):

$$F_G = C_F \cdot \dot{m}_{out} \cdot v_{out} + A_{out} \cdot \left(p_{s,out} - p_a\right) \tag{C.17}$$

For an adapted nozzle, the outlet static pressure is equal to the ambient pressure so the second term of the gross thrust disappears. The need to determine whether the nozzle is choked or adapted is bypassed by setting the outlet static pressure to the maximum of the ambient pressure and the static pressure after expansion to sonic conditions.

$$p_{s,out} = \max\left(p_a, p_s^*\right)$$

where p_s^* is the static pressure for which sonic conditions are attained after an isentropic expansion. It is calculated from the corresponding static temperature T_s^* through the enthalpy and entropy function:

$$\begin{aligned} h(T_s^*) &= h(T_{t,in}) - \frac{\gamma}{2} \cdot R \cdot T_s^* \\ \ln\left(\frac{p_s^*}{p_{t,in}}\right) &= \frac{\Psi(T_s^*) - \Psi(T_{t,in})}{R} \end{aligned}$$

If the obtained static pressure is lower than ambient pressure, the nozzle outlet pressure is set to the atmospheric pressure and $T_{s,out}$, $p_{s,out}$ and v_{out} are calculated with use of the enthalpy and entropy function tables in a similar way.

C.3.7 Monitor

The monitor receives the momentum drag from the inlet(s) and the gross thrust from the nozzle(s) and calculates the net thrust F_N and the specific net thrust $F_{N,spec}$

$$F_N = F_G + F_{ram} \tag{C.18}$$

$$F_{N,spec} = \frac{F_N}{\dot{m}_a} \tag{C.19}$$

The thrust specific fuel consumption SFC is the calculated from the net thrust and the fuel mass flow rate

$$SFC = \frac{\dot{m}_f}{F_N} \tag{C.20}$$

To allow a comparison between kerosene and hydrogen, the energy specific fuel consumption $ESFC$ is adopted as a metric for the energy efficiency of the engine:

$$ESFC = \frac{\dot{m}_f \cdot LHV}{F_N} = SFC \cdot LHV \tag{C.21}$$

C.3.8 Heat exchanger

The design and performance of a heat exchanger performance is typically assessed using either a logarithmic mean temperature difference (LMTD) or a heat exchanger effectiveness ϵ (Lienhard & Lienhard, 2004). As the LMTD method requires knowledge about in- and outlet temperature of both streams in the calculation, an iteration is required for design problems. The ϵ-NTU (number of transfer units) method in the other hand only requires knowledge about the inlet conditions of both streams. As the method has been developed for use in compact heat exchangers, it should only be applied in conditions where the overall heat transfer coefficient is likely to remain fairly uniform (Lienhard & Lienhard, 2004, p. 121). Seen the need for compactness for aero-engine heat exchangers, the method is deemed to be applicable for this work.

The HEX effectiveness is defined as:

$$\epsilon = \frac{C_h \cdot \left(T_{t,hin} - T_{t,hout}\right)}{C_{min} \cdot \left(T_{t,hin} - T_{t,cin}\right)} = \frac{C_c \cdot \left(T_{t,cout} - T_{t,cin}\right)}{C_{min} \cdot \left(T_{t,hin} - T_{t,cin}\right)} \tag{C.22}$$

where the subscript h is used for the hot flow and c for the cold flow. The total heat capacities of the flows are on the other hand defined as

$$C_h = \left(\dot{m} \cdot c_p\right)_h \qquad C_c = \left(\dot{m} \cdot c_p\right)_c$$

and C_{min} is the smaller of C_h and C_c.

As equation (C.22) shows, the effectiveness is the ratio between that actual amount of heat transferred to the maximum heat that could potentially be transferred between both streams. It follows that the amount of heat transferred Q is given as

$$Q = \epsilon \cdot C_{min} \cdot \left(T_{t,hin} - T_{t,cin}\right) \tag{C.23}$$

The effectiveness can be related to the number of transfer units which is defined as

$$NTU = \frac{U \cdot A}{C_{min}} \tag{C.24}$$

where U is the overall heat transfer coefficient and A is the heat transferring area of the HEX.

Depending on the configuration of the heat-exchangers, expressions can be derived for the effectiveness in function of the total heat capacities of the flows and the NTU. A different expression is obtained for cross-flow, counterflow or parallel flow configurations (Lienhard & Lienhard, 2004). In order not to impose a heat exchanger configuration, the number of transfer units is not calculated in this work. After all, the evaluation of the number of transfer units requires a calculation of the overall heat transfer coefficient as well as the heat transferring area, which are both hard to assess without detailed knowledge of the heat exchanger. The effectiveness is simple assumed to be known and typical values for aero-engine HEX are adopted. These values are significantly lower than values found in stationary applications due to the stringent limitations on HEX size (Walsh & Fletcher, 2004).

In part load conditions the effectiveness increases as the mass flow reduces while the heat transfer areas remains constant (Walsh & Fletcher, 2004). According to Svensson (2005) this will however only have a small effect on the off-design performance. As it is furthermore conservative, leading to a slightly lower performance for the advanced engine cycles, the variation in effectiveness is neglected here. Guidelines for inclusion of this variation in later calculations can be found in Walsh & Fletcher (2004).

Besides the heat exchanger effectiveness, the pressure drop through the channels also needs to be imposed in the model. For both flows, classical values are adopted. Again, in off-design calculations are neglected, which is conservative.

C.3.9 Cooling air fraction

Using different fuels in the combustion chamber will not only alter the performance of the turbofan engines, it will also influence the amount of cooling air needed to keep the turbine metal temperature below a specified limit. After all, the difference in combustion gases will affect radiative as well convective heat transfer properties in the hot engine section. As the turbine inlet temperature is furthermore extensively used in the engine tradeoff studies, a relatively detailed engine cooling model is required.

A full calculation of the heat transfer properties in a turbine environment lies outside the scope of this work. After all, it requires knowledge of several specific geometrical characteristics of both the turbine blades as well as the cooling passages for internal convective blade cooling and the size, location and number of holes for film cooling (Rubini, 2005). Several empirical simplified models are found in literature[2]. The model described

---

[2] Models are amongst others found in Horlock et al. (2001), Kurzke (2003), Kurzke (2008), Rubini (2005), Wilcock et al. (2005) , Young & Wilcock (2002a) and Young & Wilcock (2002b).

in Young & Wilcock (2002b) and Wilcock et al. (2005) is adopted here as it accounts for several factors despite its simplicity and can be adapted to hydrogen fuel.

As the adopted model calculates the required cooling fraction for each blade row individually, the amount of nozzle guide vane and rotor cooling air needs to be determined separately, which is normal practice in preliminary design (Kurzke (2004b) and Kurzke (2008)). It is hereby assumed that the NGV cooling air does work in the turbine and the rotor cooling air does not (Kurzke (2004b) and Kurzke (2008)). In reality, additional cooling flows are however present, as shown on Figure C.6. As proposed in Kurzke (2004b), it is assumed here that platform cooling air (stream c) and disk rim sealing air (stream d) are added downstream of the turbine as they do not have sufficient momentum to do work in the rotor. The rotor cooling air (stream D) and liner cooling air (stream a) also do not perform useful work and are thus mixed downstream of the turbine (Kurzke, 2008). This is consistent with the model from Wilcock et al. (2005). It furthermore yields accurate results for single stage cooled turbines (Kurzke, 2008). As only the HPT and IPT are cooled this assumption is thus valid. As the NGV cooling air is mixed before the turbine, the turbine entry temperature is lowered by the cooling air, leading to a reduced turbine work potential. The rotor inlet temperature, or stator outlet temperature, is namely used as temperature at the turbine inlet.

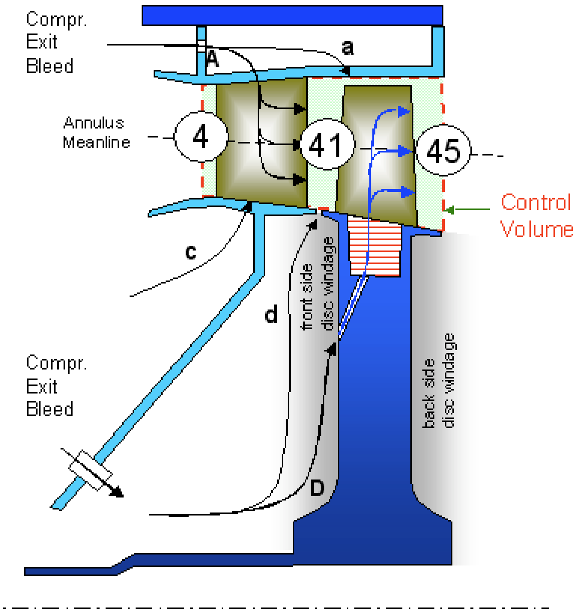

Figure C.6. The different cooling air flows, adopted from Kurzke (2004b).

As described in Wilcock et al. (2005), the cooling air fraction ψ can be calculated as:

$$\psi = \frac{\dot{m}_c}{\dot{m}_{tot}} = \frac{K_{cool}}{1+B} \cdot \left(\frac{\epsilon_0 - \epsilon_f \cdot \left[1 - \eta_{int} \cdot (1-\epsilon_0)\right]}{\eta_{int} \cdot (1-\epsilon_0)} \right) \tag{C.25}$$

ϵ_0 is the blade cooling effectiveness, K_{cool} the cooling flow factor, η_{int} the internal cooling efficiency, ϵ_f the film cooling effectiveness and B a factor to account for the Biot number of both the blade metal Bi_{met} and the thermal barrier coating (TBC) Bi_{TBC} and is given by

$$B = Bi_{TBC} - \left(\frac{\epsilon_0 - \epsilon_f}{1 - \epsilon_0}\right) \cdot Bi_{met}$$

with the Biot number defined as:

$$Bi = \frac{h_g \cdot l}{k}$$

with h_g the gas-side convective heat transfer coefficient, l a characteristic length and k the heat transfer coefficient for conduction. The blade cooling effectiveness ϵ_0 is defined by

$$\epsilon_0 = \frac{T_{t,g} - T_{met,ext}}{T_{t,g} - T_{t,c,in}} \tag{C.26}$$

where $T_{t,g}$ is the relative total temperature of the mainstream gas, $T_{t,c,in}$ is the relative total temperature of the cooling air and $T_{met,ext}$ is the allowable external surface metal temperature, which is assumed to be constant over the blade (Wilcock et al., 2005). The cooling flow factor on the other hand is given by

$$K_{cool} = \left(1 + \chi\right) \cdot \frac{A_{surf}}{A_g} \cdot \frac{c_{p,g}}{c_{p,c}} \cdot St_g$$

A_{surf} denotes the blade surface area, A_g the exit flow area normal to the axial direction, $c_{p,g}/c_{p,c}$ is the gas to coolant specific heat ratio and St_g is the Stanton number of the gas flow:

$$St_g = \frac{h_g \cdot A_g}{\dot{m}_g \cdot c_{p,g}}$$

In both the Stanton and the Biot number, the gas-side convective heat transfer coefficient h_g is taken as the blade surface *mean* coefficient. χ is a factor to allow for other primary cooling flows (mainly end wall cooling), but does not consider secondary cooling flows for sealing, ... (Wilcock et al., 2005). K_{cool} is "tuned" to engine data in Wilcock et al. (2005) and values are proposed for several levels of technology (see Table C.2).

The internal cooling efficiency η_{int} of equation (C.25) is defined by

$$\eta_{int} = \frac{T_{t,c,out} - T_{t,c,in}}{T_{met,int} - T_{t,c,in}}$$

where $T_{t,c,out}$ is the relative total temperature of the cooling air at exit from the internal blade passage and $T_{met,int}$ the internal surface metal temperature. η_{int} represents the quality of internal cooling and a value is proposed for it in order to bypass the difficult internal heat transfer calculation (Wilcock et al., 2005).

Finally, the film cooling effectiveness ϵ_f is given by

$$\epsilon_f = \frac{T_{recov} - T_{ad,w}}{T_{recov} - T_{t,c,out}}$$

T_{recov} is the mainstream recovery temperature. For nozzle guide vanes, it is taken as the total gas temperature. For rotor blades the recovery temperature depends on the velocity triangles of the turbine blade. According to El-Sayed (2008), Kurzke (2003), Kurzke (2008) and Philpot (1995), a fraction of the total gas temperature can be used in preliminary design. The fraction suggested in Philpot (1995) is slightly higher than the ones proposed in Kurzke (2003) and Kurzke (2008). In order to be slightly conservative, the highest value is retained here:

$$T_{recov} = 0.93 \cdot T_{t,g}$$

The film cooling effectiveness ϵ_f is a surface-area-averaged value which is difficult to estimate as it depends on the geometry and layout of the injection holes and the possible interactions between the different cooling jets (Rubini (2005) and Wilcock et al. (2005)). Similar to the internal efficiency, the values proposed by Wilcock et al. are retained here. They can be found in Table C.2.

When the mass-averaged total temperature is used for $T_{t,g}$, the predicted coolant flow rate found from equation (C.25) is lower than that used in a real engine (Wilcock et al., 2005). Allowance must namely be made for the temperature non-uniformity of the combustor outlet flow. According to Wilcock et al. (2005), this can be done by replacing $T_{t,g}$ by a temperature $T_{t,g,max}$ defined as

$$T_{t,g,max} = T_{t,g} + K_{comb} \cdot \Delta T_{comb}$$

where ΔT_{comb} is the temperature rise in the combustion chamber and K_{comb} is a "pattern factor" depending on the type of combustor and the position of the blade row (Kawaike et al. (1984) and Rollin (2003)). Following both references, the values of K_{comb} of Table C.1 are adopted. For the nozzle guide vanes (NGV) the values represent a radial variation in temperature. For the rotor blades, on the other hand, the values are representative for a circumferential variation in temperature from the combustion chamber. As suggested by Kawaike et al. (1984), the rotor pattern factor is assumed to be maintained throughout all stages, as shown in Table C.1.

Table C.1. Values for the combustion chamber pattern factor K_{comb}.

Turbine blade row	**K_{comb}**
HPT NGV	0.10
HPT rotor	0.06
IPT NGV	0.05
IPT rotor	0.06

As mentioned earlier, different cooling technology levels can be simulated by adapting the parameters of equation (C.25). They were mainly introduced to bypass the need for geometric details (Wilcock et al., 2005). Their utilization however allows to account for different technologies and different combustion gas composition. Wilcock et al. (2005) propose values for 3 different aeroderivative technology levels. Here, the advanced level is assumed as the baseline.

Table C.2. Values for different cooling technology levels, as given in Wilcock et al. (2005).

Cooling Technology	$\mathbf{K_{cool}}$	$\eta_{\mathbf{int}}$	$\epsilon_{\mathbf{f}}$	$\mathbf{Bi_{met}}$	$\mathbf{Bi_{TBC}}$
Current	0.045	0.70	0.40	0.15	0.30
Advanced	0.045	0.75	0.45	0.15	0.40
Super-advanced	0.045	0.80	0.50	0.15	0.50

C.3.10 Junction

The junction component is used to mix the cooling air with the main stream. As the pressure losses due to mixing of the cooling and main stream gas are taken into account in the turbine efficiency, they are not considered here. The cooling air component therefore only assures conservation of energy.

$$\dot{m}_g \cdot h(T_{t,g}) + \dot{m}_c \cdot h(T_{t,c}) = \left(\dot{m}_g + \dot{m}_c\right) \cdot h(T_{t,out}) \tag{C.27}$$

where the subscript g denotes the combustion gases (main stream), c the cooling air and out the mix of combustion gases and cooling air. Obviously conservation of mass for both the fuelflow and the airflow are also respected.

C.4 Design point and off-design modeling

As indicated in the description of the component models, a different input, called boundary conditions in Ecosimpro^{TM}, is required for design point and off-design calculation. As Ecosimpro^{TM} deals with the mathematical aspects of solving the governing equations, the boundary conditions cannot be selected completely freely. However, the different component models have been set up so that a logical choice is supported as described below. The choice for both design point and off-design calculations is described below. As component maps are mandatory for off-design calculations, the maps adopted in this work are given next.

C.4.1 Boundary conditions

To solve the mathematical set of equations of the gas turbine performance model, the proper choice of variables and boundary conditions is of great importance to both the usage as well as the mathematical stability of the routine. Ecosimpro^{TM} offers the possibility to define any parameter of the model as a variable. As the mathematical problem needs to be well-conditioned, adding extra variables however requires extra boundary conditions. A careful balance is thus required.

For design point simulations a 'classical' set of boundary conditions is selected as shown in Table C.3 whereas the variables are chosen so that the chosen boundary conditions can be properly calculated. As the table shows, the ram recovery is chosen as the boundary condition for the inlet. The corrected relative flow is then automatically set to the corresponding value from Figure C.3. For the compressor on the other hand, the polytropic efficiency and the pressure ratio need to be specified for design point calculations. The β value and the relative corrected speed are needed in addition to those so that the map can be scaled. For the fan, the BPR needs to be specified on top of that. The turbine module requires similar boundary conditions. However, as shown in the table, the pressure ratio is not specified as input. It is determined from the power balance of the spool. As such the turbine delivers the power required by the compressor[3]. To close the mathematical set of equations, the nozzle exit area finally needs to be set as a variable so that it is adapted to the massflow rate under investigation. Obviously, the flight altitude and Mach number also need to be given.

Table C.3. Boundary conditions for design point simulations.

	Boundary Conditions	**Variables**
Inlet	RR	$\left(\frac{\dot{m}\cdot\sqrt{T_t}}{p_t}\right)_{rel}$
Compressor	η_{pol}	SF_η
	π	SF_π
	β	$SF_{\frac{\dot{m}\cdot\sqrt{T_t}}{p_t}}$
	$\left(\frac{N}{\sqrt{T_t}}\right)_{rel}$	$\left(\frac{N}{\sqrt{T_t}}\right)_{DP}$
Combustion Chamber	$\frac{p_{t,out}}{p_{t,in}}$	A_{in}
	η_{cc}	V_{cc}
Turbine	η_{pol}	SF_η
		SF_π
	β	$SF_{\frac{\dot{m}\cdot\sqrt{T_t}}{p_t}}$
	$\left(\frac{N}{\sqrt{T_t}}\right)_{rel}$	$\left(\frac{N}{\sqrt{T_t}}\right)_{DP}$
Nozzle		A_{out}

As the scaling of the maps needs to stay constant for off-design calculations, a different approach is needed. The map scaling factors are taken here as boundary conditions and only one variable needs to be selected to allow the specification of the engine rating. The relative corrected speed of any of the spools, the turbine inlet temperature and the fuel flow rate are all viable variables. In this work, the turbine inlet temperature is chosen for most calculations, however any of the aforementioned candidates are also possible.

Besides the boundary conditions and variables Ecosimpro^{TM} requires tearing variables to solve iterative loops. The program proposes the most adequate variables from a mathematical point of view. However, within limits, other variables can also be chosen but they

---

[3] To allow future off-design calculations the dynamic equations are also implemented so it must be specified that the derivative of the spool speed is zero. As inertia moments of the components are needed and volume dynamics and heat soakage effects need to be taken into consideration for a proper transient calculation, this is considered outside the scope of this work.

might prohibit convergence of the calculations. As the tearing variables strongly depend on the type of engine investigated, they are omitted here.

C.4.2 Component maps

In order to simulate off-design behavior of engines, adequate usage of the correct component maps is of vital importance. This is especially true for compressor maps. Turbine maps have less influence on the outcome of the off-design simulations as turbines are usually chocked throughout a wide operating range. Ideally, compressor maps derived from tests would have to be used. As this data usually is not available in the preliminary design phase, theoretical performance maps obtained through stacking of compressor stage characteristics can also be used (Lewis (1996) and Rizvi (2007)). Even though the AAXIALB1 software from Cranfield University is capable of generating component maps for a specific compressor design, this is considered to be outside the scope of this work seen the significant amount of engines under consideration. In this work, compressor and turbine characteristics from the public domain are therefore retained. The fan map is derived from Freeman (1992). For the IPC and the HPC, the characteristics are taken from Plencner (1989). The same characteristic is assumed to apply to both compressors (scaled differently). The compressor characteristics are shown on Figure C.7. Again, the maps are shown normalized by the design point values as the scaling of the map will be different for each design study carried out.

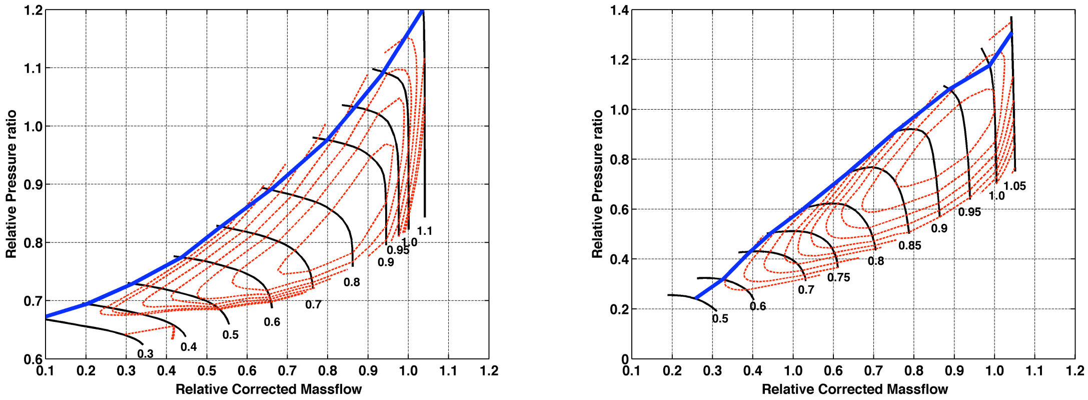

(a) Fan map (b) HPC map

Figure C.7. Normalized fan and HPC compressor characteristics.

The HP turbine characteristic is on the other hand obtained from Stabe et al. (1984) and is also used for the IPT. The LPT map finally is taken from Serovy (1976). All map data was converted from (Kurzke, 2004a) and Kurzke (2004b), as they have been prepared specifically for gas turbine performance simulations (Kurzke, 2004a). The turbine maps used in this work are shown on Figure C.8.

The maps chosen in the work are also adopted as "standard maps" in the Gasturb software. Their utilization leads to a good general representation of the engine operating line over a wide range of operating conditions (Verstraete & Hendrick, 2006), which is the

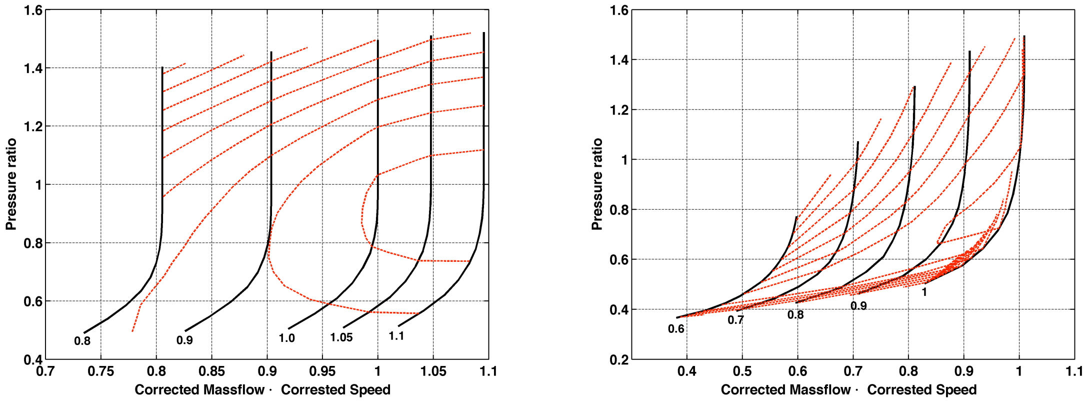

(a) HPT map

(b) LPT map

Figure C.8. Normalized HP and LP turbine characteristics.

primary reason for which they are retained here. Obviously, when component specific issues such as surge and bleed air to avoid surge are tackled, more specific component data is required. As this is not intended in this work, the utilization of the selected maps is believed to be suitable.

C.5 Gas Path Analysis

In a tradeoff study between turbofans having a different BPR, the engine mass and size play a key role. A gas path analysis of the engine is therefor considered indispensable. Here, a rudimentary gas path analysis is made at the mean radius of the different components. Several simplifying assumptions are made as is often done in preliminary design (Cumpsty (1997), Ramsden (2005a), Ramsden (2005b), Rizvi (2007), Saravanamuttoo et al. (2001) and Walsh & Fletcher (2004)). For both compressor and turbines for instance a constant axial velocity is assumed at the entrance and exit of each stage, which is often not far from reality (Cumpsty, 1997, p. 91). The designs of the turbomachinery is also made for either constant hub or constant tip radius whereas on the Trent engines for instance, slight deviations are made from this approach. All in all the choices made lead to a representative engine layout and some room is available for modifications in later steps in the design. Possible steps to cure problems later on are for instance a deviation from a constant axial velocity, adopting a slightly higher stage loading for the mid compressor stages, keeping the annulus area constant for the last stages of compressors and LP turbine, ...

The gas path analysis described below essentially boils down to sizing the annulus area of compressors and turbines. For the compressors no attempt is made to calculate the angles of the different stages. For the LP turbine on the other hand, some angles of the velocity diagram are calculated as they are needed to determine the number of LPT stages for a given fan. Top of climb is selected as the design point as it is the highest non-dimensional operating point of the engine and as such leads to the highest pressure ratios and massflow rates. The temperatures and pressures at the in- and outlet of the different components are derived from the simulations in Ecosimpro^{TM}.

The annulus sizing methods for each of the components are described consecutively from the front to the rear of the engine. In a last section the calculation of the engine length is detailed.

C.5.1 Fan

The fan dimensions can be calculated by specifying the hub to tip ratio and the fan face axial Mach number. After all the required airflow rate is set by the thrust demanded by the aircraft and the specific thrust as determined from the turbofan cycle calculations for the atmospheric conditions and flight Mach number of the design point. A given axial fan face Mach number $M_{ax_{ff}}$ thus enables the calculation of the fan face area can from the "Q function":

$$Q = \frac{\dot{m} \cdot \sqrt{T_t}}{A_{ff} \cdot p_t} = M_{ax_{ff}} \cdot \sqrt{\frac{\gamma}{R}} \cdot \left(1 + \frac{\gamma - 1}{2} \cdot M_{ax_{ff}}^2\right)^{-\frac{\gamma+1}{2\cdot(\gamma-1)}} \tag{C.28}$$

as T_t, p_t and γ are set by the flight conditions.

Walsh & Fletcher (2004, p. 188) propose an axial fan face Mach number between 0.50 and 0.65. The higher value of this range is in line with Cumpsty (1997, p. 91) where it is stated that the mass flow per unit area of the fan is approximately 88% of that required to choke the annulus. Williams (2007, p. 43) quotes similar values as Walsh & Fletcher (2004) but indicates nonetheless that with sophisticated very thin fan blades an inlet Mach number up to around 0.72 can be tolerated and suggests that the nacelle forebody annulus for advanced projects could consider almost zero net diffusion of the inlet nacelle[4]. A slightly diffusing sector nevertheless helps to reduce the amount of turbulence at the fan face and as such also the tolerance of the fan to pressure distortions. The axial fan face Mach number is therefore set slightly lower than the nacelle throat Mach number. A value of 0.70 is chosen to reflect the advances in engine technology by the time of the entry into service of the engines.

The speed in the fan duct is set as a compromise between turbofan frontal area and duct pressure losses. Walsh & Fletcher (2004, p. 189) propose a range between 0.30 and 0.35 as a good balance between those requirements. Occasionally fan exit Mach numbers up to 0.40 can be found (Walsh & Fletcher, 2004, p. 189). The latter number is retained here to yield a reasonable hub to tip ratio for the fan exit.

To reduce the engine frontal area the fan face hub to tip ratio should namely be set as low as possible. However the circumference of the fan disc should be large enough to attach the blades which places a lower limit on achievable hub to tip ratios. For very low hub to tip ratio's secondary losses will also be higher (Walsh & Fletcher, 2004). A hub to tip ratio of 0.35 is adopted here, since higher bypass ratio fans which inherently have heavy blades are investigated, which is the lower limit indicated in Cumpsty (1997, p. 91).

This value for the hub to tip ratio is furthermore in line with the fan tip speed of 460 m/s, adopted from Rizvi (2007). Walsh & Fletcher (2004) namely indicate that fan tip speeds are

---

[4] For a zero net diffusion the fan face area would be set to the nacelle forebody throat area as the fan face Mach number is equal to the inlet throat Mach number.

limited to about 500 m/s for hub-to-tip ratios of 0.3 to 0.4, whereas higher speed might be allowed for higher ratios.

To determine the engine length, the fan chord needs to be determined. This is done by imposing a fan blade mean aspect ratio, which is defined here as the ratio of the blade height to the blade chord at mean radius. A value of 2.5 is utilized after Walsh & Fletcher (2004) where a range between 2.0 and 2.5 is suggested for fan blades without clappers.

As the BPR of the engine is fixed, the radial position of the bypass to core split is determined assuming a constant axial velocity throughout the fan. The length from the fan blade to the split and from the split to the IP compressor are on the other hand determined from a Trent 884 cross-section (Cumpsty, 1997, p. 47).

To calculate the annulus of the fan and the other compressor, the annulus boundary layer growth is accounted for by the adoption of a "blockage factor" ((Ramsden, 2004a, p. 3.48) and Rizvi (2007)). The blockage factor is used to compensate the work loss from the low speed boundary layer by increasing the annulus area.

$$K_{bl} = \frac{A_{ann}}{A_{ann,bl}}$$

where A_{ann} is the annulus area determined with the assumption of a uniform velocity. $A_{ann,bl}$ denotes the annulus area with blockage correction. As the boundary layer increases through the first stages of the compressor the blockage factor reduces throughout the compressor as shown in Table C.4. From the fifth stage onwards the axial velocity profile stays more or less constant and the same value should be used for the blockage factor of subsequent stages (Ramsden, 2004a, p. 3.48)

Table C.4. Typical values for stage blockage factors, adopted from Ramsden (2004a).

Stage	K_b
1	0.99
2	0.95
3	0.92
4	0.90
5	0.88

C.5.2 IP and HP Compressors

As is common practice in the first stages of the engine design, the axial velocity of the air is kept constant at the inlet of each of the IP and HP compressor stages (Ramsden (2004a) and Walsh & Fletcher (2004)). Walsh & Fletcher (2004, p. 163), propose an axial inlet Mach number between 0.4 and 0.6 for the core compressor. Saravanamuttoo et al. (2001, p. 189) quote a value of up to 200 m/s for advanced aero engines. As this value is also used Ramsden (2005a, p. 1), it is retained here.

As the designs in this work are 3 spool turbofans, the IPC and HPC designs are based on the Rolls-Royce Trent family. For the IPC a constant inner diameter design is therefore utilized. The radial position of the IPC is then found by imposing a hub-to-tip ratio limit of 0.88 at the outlet of the last stage. The HPC on the other hand has a constant outer diameter design which limits the number of stages for a given pressure rise (Saravanamuttoo et al., 2001, p. 218). Here an hub-to-tip ratio of 0.92 is imposed, as proposed by Walsh & Fletcher (2004, p. 164) for the last stages of HPC. If this would lead to excessive tip losses, this could be cured in later steps of the design by imposing a constant annulus area for the last stages.

The number of compressor stages is calculated for each of the compressors. For this the stage loading factor is set as:

$$\frac{\Delta H}{U^2} = 0.35$$

where ΔH is the enthalpy rise of the air and U is the mean circumferential speed of the compressor blade. This value is adopted as a reasonable compromise between number of compressor stages and stage efficiency. Walsh & Fletcher (2004, p. 273) shows that a polytropic compressor efficiency slightly higher than 90% is feasible for this stage pitchline loading. As the RPM of the IP and HP spools is set by the requirement for a single stage turbine, the temperature (enthalpy) rise per stage is set and the number of stages can be determined.

Compressor blade aspect ratios of 3.5 for the first stage IPC progressively down to 1.5 for the last stage HPC are adopted for both stator and rotor (Rizvi (2007) and Walsh & Fletcher (2004)). A spacing of 20% of the upstream chord is assumed which then fixes the length of the compressors (Onat & Klees (1979), Ramsden (2004a) and Walsh & Fletcher (2004)). As for the fan to IPC duct, the length of the IPC to HPC duct is scaled from the Trent 884 cross section.

C.5.3 Combustion chamber

The combustion chamber length for kerosene fueled turbofans is scaled from the Trent 884 cross section in Cumpsty (1997). A constant fraction of the engine length is as such assumed for the combustion chamber. In line with current practice, it is furthermore ensured that the combustion chamber axis is only slightly inclined by positioning the HP turbine at an adequate radius.

C.5.4 HP and IP turbines

As a single stage HP and IP turbine is chosen to limit engine part count, cost and turbine cooling air losses, the HP (IP) spool RPM is set by the HPT (IPT) power required. As it was done in the determination of the number of compressor stage, the RPM is determined from the HPT pitchline stage loading which is set to

$$\frac{\Delta H}{U^2} = 2.185$$

This value is judged to be high enough to enable a high work output per turbine stage to enable the single stage design, but low enough to yield a reasonably high efficiency. Increasing the stage loading namely leads to a reduced turbine stage efficiency as shown on the Smith chart (amongst others Cumpsty (1997), Lewis (1996), Ramsden (2005b), Taylor (2003) and Walsh & Fletcher (2004)). Even though the shape and more importantly the level of peak efficiency and its location on the chart (set by a combination of flow coefficient $\phi = V_{ax}/U$ and stage loading $\Delta H/U^2$) are effected by turbine design parameters as e.g. specific work (Taylor, 2003, pp. 11-12), these are neglected here as only a first-order gas path analysis is made. Despite the relatively high stage loading[5], the turbine efficiencies are nonetheless fairly high, to reflect the timeframe for which the engines are primarily intended.

The axial inlet Mach number to the HPT is kept at 0.3 as a compromise between upstream duct losses and cooling air requirements, which are proportional to the HPT nozzle guide vane size (Ramsden, 2005b). The hub-to-tip ratio also also plays a role in the selection as a too high value would lead to excessive over-tip leakage losses. A low inlet Mach number furthermore ensurse acceleration at all points along the NGV surface (Walsh & Fletcher, 2004). As the mean circumferential velocity U is set by power output requirements, the flow coefficient ϕ is fixed by imposing the axial velocity. As HPT's are often designed for flow coefficients lower than optimum (Ramsden, 2004b), the flow coefficients are typically between 0.4 and 0.65 (Cumpsty (1997) and Taylor (2003)). The designs in this work fall within that range.

For the IPT similar flow coefficients are found in literature but Ramsden (2005b) indicates that IPT are typically designed so that the flow coefficient is close to the "efficiency ridge", as Taylor calls the flow coefficient that yields the maximum efficiency at a given stage loading. Ramsden (2004b, p. 4.31) gives the following equation for the optimum flow coefficient for a given loading:

$$\frac{\Delta H}{U^2} = 6.5 \cdot \frac{V_{ax}}{U} - 2.90$$

The IPT inlet axial velocity is chosen to lie on this line here whereas the stage loading for the IPT is set to 2.2. The power generated by the turbine is corrected for annulus boundary layer growth using the work done factor (Ramsden, 2005b), which is of similar purpose and use as the blockage factor defined for the compressor stages. A work done factor of 0.98 is assumed for the HPT whereas 0.97 is utilized for the IPT and LPT (Ramsden (2005b) and Rizvi (2007)).

As is often done in preliminary design, a stage reaction of 50% is chosen for all turbines (a.o. El-Sayed (2008), Ramsden (2004b), Saravanamuttoo et al. (2001), Walsh & Fletcher (2004)). Theoretically this stage reaction namely leads to the highest attainable efficiency (Lewis (1996) and Wilson & Korakianitis (1998)). It furthermore leaves a high kinetic energy flow for subsequent stages, which makes it the preferred design for gas generator stages (Ramsden, 2004b, p. 4.26). For the HPT, Taylor (2003, pp. 5-6) indicates a typical reaction of 0.45 to yield reduced relative total temperature and pressure, reduced bearing loads and less turning required in the following nozzle. As the reaction will vary along the blade

---

[5] A typical range quoted for stage loadings is 1.5-2.0 (Taylor (2003, p. 5) and Walsh & Fletcher (2004)).

height and a more detailed calculation of the radial distribution of the velocity triangles is in any case needed in later design stages, the 50% reaction, is assumed here to apply to all turbines.

As both the stage reaction and the stage loading have been fixed, the mid radius velocity triangles can easily be drawn. Utilising the Euler's turbine equation, simplified for constant mid radius and constant axial velocity, the angular velocity change in the turbine stage Δv_w is obtained from

$$\frac{\Delta H}{U^2} = \frac{\Delta v_w}{U} \tag{C.29}$$

As a 50% reaction (symmetrical velocity triangle) is assumed the angular velocity at the stage outlet $v_{w,3}$ is given by

$$v_{w,3} = \frac{\Delta v_w - U}{2} \tag{C.30}$$

which leads to the blade outlet angle α_3 and the absolute velocity at the blade outlet v_3:

$$\tan\alpha_3 = \frac{v_{w,3}}{v_a} \tag{C.31}$$

$$v_3 = \frac{v_a}{\cos\alpha_3} \tag{C.32}$$

Even though the direction of the gas velocity at exit from the stage is not absolutely needed for the HP and IPT turbine annulus area from, the swirl angle α_3 is important for the last LPT stage, as shown in the next section. It is therefore calculated for the HP and IPT also. The magnitude of the stage exit velocity allows the calculation of the annulus area through the Q-function of equation (C.28) as the pressure and temperature are known from the cycle calculations.

The length of the turbines is calculated through the blade aspect ratio, as was done for the compressors. For the turbines, a spacing between the rotor blades and stator vanes of 25% of the upstream chord is adopted (Ramsden (2004b) and Walsh & Fletcher (2004)). The HPT NGV aspect ratio is set to 1.2 to keep the amount of nozzle guide vane cooling air to a reasonable level (Ramsden, 2004b). For the HPT rotor a value of 2.5 is on the other hand adopted. The IPT aspect ratios are set to 2.75 (Ramsden (2004b) and Walsh & Fletcher (2004)). The IPT is placed at a radial position halfway the HP and LP turbines to enable a smooth transition from one turbine to the other. As was done for the compressors, the turbine inter-ducts are scaled from the Trent 884 cross section.

C.5.5 LP turbine

Contrary to HP and IP turbines, the LPT is often designed for higher axial velocity, leading to flow ratio coefficients above the optimum value for efficiency (Ramsden (2004b) and Walsh & Fletcher (2004)). The turbine efficiency is thus slightly compromised to reduce the frontal area. According to de la Calzada (2003), flow coefficients around 0.85 are reasonable for LP turbines with a stage loading around 2.25. This leads to a turning of about 100° while maintining a reasonable efficiency.

The LPT is chosen as a constant hub design and the last 3 stages also have a constant tip radius to align the flow axially into the nozzle (Ramsden, 2004b). This practice is also found on the Trent 884. The first stage hub to tip ratio is set to 0.72. As the blade hub to tip ratio is lower for subsequent stages, this value is considered a reasonable compromise to keep the frontal area reasonable while obtaining acceptable final stage hub-to-tip ratios. According to Walsh & Fletcher (2004) the hub-to-tip ratio namely needs to stay higher than 0.5 to limit the influence of secondary losses. Finally, the hub radius of the LPT is set so that the tip of the last stages is at the same radius as the fan splitter that divides the fan outlet air into core and bypass air. This is common practice for aero-engines (Ramsden (2004a) and Rizvi (2007)).

Each turbine stage is designed for a stage loading of 2.2 and stages are added until the power required by the fan can be delivered. The last stage is then designed for a lower stage loading so that a more axial flow is obtained at the LPT outlet while the required fan power is matched. If the last stage swirl angle is higher than 25° an extra stage is added to the LPT, which is in line with the value recommended in Walsh & Fletcher (2004). A constant axial velocity is assumed as was done for the HPT and IPT and it is checked whether the outlet axial Mach number is lower than 0.35 (Walsh & Fletcher, 2004). The efficiency of the turbine stage is determined from the Smith chart provided in Ramsden (2005b) to determine the outlet pressure of the different stages.

Again the spacing between the rotor blades and stator vanes of the different turbine stages is set to 25% of the upstream chord. Blade stage aspect ratios are set to 3.0 for the first stage and increase up to 5.5 for the last stage, keeping a small margin over the upper limit of 6, indicated in Walsh & Fletcher (2004).

C.5.6 Engine length

As indicated in the previous sections, the ducts between the different compressors, as well as the combustion chamber and position of the core to bypass splitter are set to a fraction of the total engine length l_{eng} based on the Trent 884. The engine length is defined here as the distance from the fan face to the exit of the last LPT stage. The adopted fractions are indicated in Table C.5.

Table C.5. Values adopted for the length of the different engine ducts, as fraction of l_{eng}.

Component	$\mathbf{l_{comp}/l_{eng}}$ [%]
fan to IPC duct	17
IPC to HPC duct	7
HPT to IPT duct	4
IPT to LPT duct	4
combustion chamber	6
combustion chamber diffuser	2
fan to bypass duct splitter	7

A typical outcome of the gas path analysis is given on Figure C.9. The geometry of the ducts between the different components and of the inside of the bypass duct are adopted from a scaling of the Trent engine and of examples of nacelle geometry from Rolls-Royce (2005, p. 156,212). A similar practice is adopted for the nozzle cone.

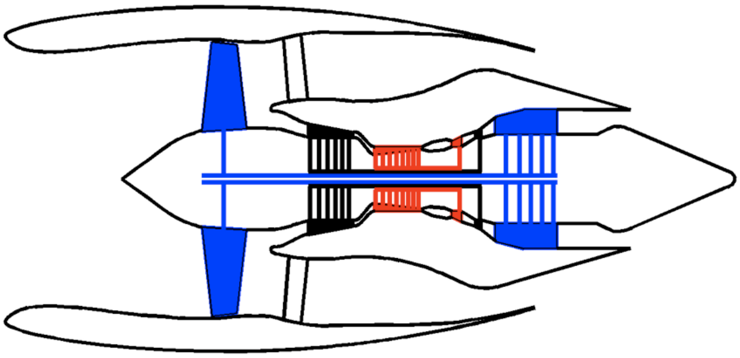

Figure C.9. A typical result of the gas path analysis.

As shown on the figure, the IPC to HPC duct seems fairly short, however, in the Trent engine the last stages of the IPC are at a lower hub radius to start the turning of the air before entering the duct. As indicated in the introduction to this section, this sort of designer solutions are not considered here due to the preliminary nature of the gas path analysis.